Studies of the Responses of Liquid and Solid Targets for Direct Dark Matter Searches

Hassan Chagani

High Energy Physics Group
Department of Physics & Astronomy

June 2008

A thesis submitted to the University of Sheffield for the degree of Doctor of Philosophy in the Faculty of Pure Science

Abstract

The quenching factor for sodium recoils in a 2-inch NaI(Tl) scintillating crystal has been measured at room temperature. The crystal has been exposed to 2.45 MeV mono-energetic neutrons generated by a deuterium-deuterium fixed target accelerator in the energy range 10 to 100 keV nuclear recoil energy. A BC501A liquid scintillator detector has been used to tag neutrons that scatter off sodium nuclei in the crystal. Cuts on pulse shape discrimination in BC501A and neutron time of flight have been performed on pulses recorded by an Acqiris DC265 digitiser with a 2 ns sampling time. A quenching factor of $25.2 \pm 6.4\%$ has been determined for 10 keV sodium recoils. Measured quenching factors range from 19% to 26% in good agreement with other experiments. From pulse shape analysis, the mean time of pulses from electron and nuclear recoils have been compared down to 2 keV electron equivalent energy.

Photon reponse measurements with the same crystal have also been taken by exposing it to gamma-ray sources with a range of energies. In agreement with results from other experiments, a dip in the photon response is seen at energies coincident with the iodine K-shell electron binding energy. This is a direct consequence of the energy of the photoelectron emitted during photoelectric absorption. An attempt to measure the non-linear electron response is also made with the Compton Coincidence Technique. Implications of this result on the quenching factor for sodium recoils in NaI(Tl) are also discussed.

The commissioning of passive neutron and gamma shielding, together with an active veto system, around the ZEPLIN-II dark matter detector is described. The preparation of neutron shielding has required the impregnation of paraffin wax with gadolinium, and the casting of this into cuboids. Tests of the veto trigger with source data yield gamma and neutron background rejection efficiencies of 21.13% and 50.44% respectively. The veto efficiency is 99.15%.

Declaration

The work described in this thesis was carried out in the Department of Physics and Astronomy at the University of Sheffield from October 2004 to June 2008. It is the original work of the author, unless otherwise acknowledged within the text. It has not been submitted previously for a degree at this or any other university.

Hassan Chagani

June 2008

Acknowledgements

For those of you who are not mentioned here, I ask you to forgive me, for there is not enough space to thank everybody.

Firstly, I must thank my supervisor Ed Daw for his guidance and encouragement over the last three-and-a-half years. There have been many times when we have not seen eye-to-eye and have had our fair share of disagreements. However, he has been very patient with me and has fought hard on my behalf whenever I wanted to do something that differed from the normal procedure. In hindsight, I have been fortunate to have him as a supervisor.

I also must thank Pawel Majewski, who deserves far more than just a simple thank you. I shudder to think what my PhD would have been like had Pawel not joined the group, and I had not had the fortune of working with him. I know I have not been the easiest person to work with, and there are countless times at which I have thought about packing it all in and taking the next train to London. However, whether he knows it or not, Pawel has stopped me. He has been very patient and supportive when nobody else was, and has always encouraged me to follow my ideas. Working with him has been a wonderful experience, and he has been a priceless source of guidance and advice. He has been an inspiration and I hope many other students will benefit from working with him in years to come.

Concerning the work in this thesis, I would like to thank Matthew Robinson (and Paul Hodgson on the rare occasions Matt has been away) for always solving my computing problems immediately, as if by magic, almost 24 hours a day. I could not have got this far without him. I also want to thank Vitaly Kudryavstev for explaining the physics behind my work, and Akira Hitachi for his help with quenching factor theory. Thank you to John McMillan for his invaluable guidance with the use of photomultipliers. I acknowledge the members of the ZEPLIN-II collaboration for their help. Financial support for this work was provided by STFC (formally PPARC) for which I am also grateful.

I would like to thank Jeremy Lloyd-Evans for sparking my interest in particle physics while I was at the University of Leeds, and Stefan Söldner-Rembold for taking this further at the University of Manchester. I also thank Fred Loebinger at Manchester who, even though he may disagree with me, took a big chance on accepting my application to read for a MSc.

As this is a culmination of over seven years in higher education, I also want to thank all the friends I have made along the way. Especially Tim from my time in Leeds, and Irina and Marta from my year in Manchester. Thank you to all the students in the particle physics group here at Sheffield. Those who deserve particular mention include Eirini for making the office a much nicer place to work in, and Kevin (who does something with semiconductors, not particles) and Mark Ward for the random conversations, about anything but physics, I would have with them in the early morning hours. Thank you to Ben and Rob too.

I also want to thank all my mates back in London, especially Greg and Chris who have remained my closest friends for many, many years. Thanks also to Nicole for introducing me to the wonders of theatre and fine dining. Thank you to Beckiiiiiiiiy for just being herself, a wonderful and amazing person.

Finally, the biggest thank you of all is to my mother. As a chemist, she has always been supportive of my decision to read physics at university and to undertake a PhD. The last few years have been very tough on me, but she has always been there for me whenever I have needed encouragement. I always try to give more than I take, but it is impossible for me to give her more than she has given me. She is the only person who has given me constant and unfailing support, and for this I am eternally grateful.

For ammi

Contents

List of Figures

List of Tables

Chapter 1

Introduction

For all the many great strides in science, it is humbling to think that the nature of most of the matter in the Universe is still unknown. Astronomical observations that point to such a conclusion, such as galactic rotation curves and gravitational lensing, have perplexed cosmologists for many decades. A possible solution to the questions asked may come from particle physics, with the introduction of new non-baryonic particles, collectively known as 'dark matter'.

Although there are a number of theories that offer explanations for these observations, the presence of a halo of dark matter that constitutes a significant fraction of galactic mass is the only one that can be verified through experimental work. Furthermore, in light of further astronomical observations, other theories have required considerable fine-tuning, unlike the dark matter halo model.

Although little is known about them, a number of assumptions can be made about the nature of dark matter particles through observations of their effect on the Universe. One of these assumptions is the fact that they must only interact through the weak and gravitational forces, otherwise they would have formed anomalous heavy isotopes that could be seen today. Of the many possible candidates, the Weakly Interacting Massive Particle (WIMP) has the most direct search experiments dedicated to its discovery. Being massive, neutral particles, their interaction mechanism in matter is equivalent to that of a neutron, in that they interact primarily with the nucleus of an atom. This is in contrast to gamma-rays where, due to their massless nature, detectable recoils are from collisions with electrons.

As the particulars of dark matter particle interactions with baryonic target atoms are

relatively unknown, there could be any number of complicated processes that are possible. However, it can be said with certainty that dark matter particles must be able to scatter elastically off target nuclei, and this is the detection principle behind the vast majority of search experiments. The main detector techniques exploit signatures from ionisation, scintillation and phonon emission. Newer hybrid detectors combine two of the above signals, resulting in better discrimination between nuclear and electron recoils.

The finite size of a nucleus means that the momentum transfer from a dark matter recoil may be larger than its inverse size. In these situations, the cross-section for scattering falls with increasing recoil energy. Therefore, the majority of detectable dark matter interactions will be of recoil energy less than 50 keV. As a result, this is the energy regime where dark matter detectors must be sensitive, and the intrinsic properties of the target material become important.

In absence of a signal, a limit on the WIMP-nucleon interaction cross-section can be determined with the detector-specific, expected differential nuclear event rate. Current experimental limits lie between 10^{-7} and 10^{-5} pb.

As a direct consequence of the low cross-section for WIMP-nucleon coupling, such search experiments must be located in areas of low radioactive background. To minimise interactions with cosmic rays, detectors are typically found in underground laboratories that provide a rock overburden. Dark matter detectors are normally encased within several layers of gamma and neutron shielding to minimise the flux of background radiation incident on the target. Additionally, a secondary detector surrounding the target is commonly used to reject events coincident with those in the primary detector. Such a system is called an active veto, and relies on the negligible probability that a WIMP will interact in both detectors. Currently, sensitivities are limited by the radiopurity of internal detector components.

Detector calibration is typically performed by exposing the target material to gamma-ray emitting isotopes of known energy. Neutron sources are not used for this purpose as prolonged exposure can lead to the generation of long-lived radioisotopes in the detector materials, hampering sensitivity. They also require significantly more shielding, which can be a problem in the limited space underground, and lack well-defined energy spectra.

However, as identified above, the processes for gamma and neutron interactions in a detector differ. Although this can be exploited to distinguish nuclear and electron recoils,

by using pulse shape discrimination in scintillators for example, it also gives rise to a problem. The degree to which light is quenched also differs, and as a result of calibration with a gamma-ray source, the measured energy from a nuclear recoil will be lower than its actual value. This results in the inaccurate calculation of the differential event rate, and therefore the setting of a false limit on WIMP-nucleon interactions. This phenomenon is corrected for by multiplying the differential cross-section by the quenching factor. The quenching factor is the ratio of scintillation light from a nuclear recoil to that from an electron interaction, and varies for different detector media and nuclear recoil energies.

Although a linear energy scale is assumed after calibration, the photon response in scintillators is non-linear. This is a direct consequence of the non-linear electron response. As the establishment of an energy scale is performed in exactly the same way to determine the quenching factor, this effect is cancelled out when the differential event rate is calculated. Therefore, electron response is of little importance in the scope of direct dark matter experiments. However, the simplest model assumes that scintillation light is the result of a recoiling nucleus transferring its energy to target electrons. Therefore, the value of the quenching factor itself is dependent on the detector response to electrons.

Outlines of the modern cosmological model and particle physics theory relevant to direct dark matter search experiments are presented in this work. The physics behind the operation of scintillation detectors is discussed in further detail, in addition to an overview of the ZEPLIN-II hybrid detector. An in-depth discussion of the commissioning of the ZEPLIN-II veto and shielding, which are important requirements for low background operation, is given. Measurements of the quenching factor for sodium recoils in a 2-inch sodium iodide (NaI(Tl)) crystal scintillator, and photon and electron responses are also presented.

Chapter 2

Dark Matter Searches

It is now widely believed that most of the matter in the Universe does not consist of the stars, planets and gas that are visible in the images from telescopes. A large body of evidence points to there being a more elusive particle population of 'dark matter', that contributes to most of the mass of galaxies. The search for such particles has required the synergy of particle physics and cosmology, together with considerable experimental effort. However, as yet, dark matter still remains unobserved.

This chapter outlines the current theories of cosmology and particle physics relevant to the dark matter problem, and describes some of the indirect evidence that implies its presence in the Universe. The second part of the chapter is dedicated to the challenges of detection, describing current experiments and experimental techniques.

2.1 Concordance Cosmology

The modern model for evolution of the Universe is based on the cosmological principle [1]. This states that no observer occupies a special position in an isotropic and homogenous Universe. Although it is clear that on small scales this assumption is far too simple, when investigating the Universe as a whole this is a reasonable approximation.

The roots of the modern model, normally termed concordance cosmology, lie in Hubble and Humason's observation of an expanding Universe [2]. Hubble measured the distances to a sample of nearby galaxies and combined his measurements with the redshifts associated with them [3], finding that there was a rough proportionality. Thus, a correlation between distance $\vec{r}$ and recession velocity $\vec{v}$ was determined:

$$\vec{v} = H_0 \vec{r} \tag{2.1}$$

where H_0 is the observed present-day rate of expansion, known as the Hubble constant. Although H varies with time, the cosmological principle makes it constant in space. The current best-fit determination of its value gives $H_0 = 70^{+2.4}_{-3.2}$ km/sMpc [4] and is derived from a combination of data from the Wilkinson Microwave Anistropy Probe (WMAP) and the Sloan Digital Sky Survey (SDSS). From Eq. (2.1), a positive value for H_0 indicates that the Universe is currently expanding rather than contracting.

The distance $\vec{r}$ can be expressed in terms of a constant comoving distance $\vec{x}$:

$$\vec{r}(t) = a(t)\vec{x} \tag{2.2}$$

where $a(t)$ is known as the scaling factor, and describes the separation of galaxies during the expansion of the Universe. The Hubble parameter can also be expressed in terms of the scaling factor:

$$H(t) = \frac{1}{a(t)} \frac{\mathrm{d}a(t)}{\mathrm{d}t} = \frac{\dot{a}(t)}{a(t)} \tag{2.3}$$

where $H(t_0) = H_0$, and t_0 is the present time.

The geometry of the Universe can be related to its matter and energy content with the Friedman equation:

$$\left(\frac{\dot{a}(t)}{a(t)}\right)^2 = \frac{8\pi G}{3}\rho(t) - \frac{k}{a^2} \tag{2.4}$$

where ρ is the average mass-energy density of the Universe and k is its spatial curvature. The spatial curvature is a constant in space and time, and hence defines the future of the Universe, as shown in Table 2.1.

From Table 2.1, in the case of a flat Universe where $k = 0$, Eq. (2.4) can be rearranged in terms of the average mass-energy density:

$$\rho_c(t) = \frac{3H^2(t)}{8\pi G} \tag{2.5}$$

where ρ_c is the critical density, and is directly proportional to the square of the Hubble parameter. Therefore, the value of ρ relative to ρ_c also defines the fate of the Universe at

Table 2.1: Summary of Possible Geometries and Scenarios for the Fate of the Universe as a function of the spatial curvature k, average mass-energy density ρ and density parameter Ω. The critical density ρ_c is obtained with Eq. (2.5).

k	ρ	Ω	Scale Factor ($a(t)$)	Geometry	Future of Universe
< 0	$< \rho_c$	< 1	$\propto t$	open	expands forever
0	ρ_c	1	$\propto t^{\frac{2}{3}}$	flat	expands forever†
> 0	$> \rho_c$	> 1	$\rightarrow 0$	closed	big crunch

†Rate of expansion will tend to 0 at infinite time

outlined in Table 2.1. The actual average mass-energy density of the Universe is usually given with respect to the critical density in the form of the density parameter Ω:

$$\Omega(t) = \frac{8\pi G}{3H^2(t)}\rho(t) = \frac{\rho(t)}{\rho_c(t)} \tag{2.6}$$

which is a function of time. The relation of Ω with time can be derived from Eq. (2.4) and Eq. (2.6):

$$|\Omega(t) - 1| = \frac{|k|}{a^2H^2(t)} \tag{2.7}$$

As the density parameter Ω depends on the spatial curvature k, it follows that its value also defines the geometry of the Universe, as shown in Table 2.1.

Although successful, the Big Bang model requires initial conditions that create problems. If the density parameter does not equal unity, Eq. (2.7) leads Ω away from a value of 1, in conflict with the flat Universe we see today. As a result, the Hubble parameter requires excessive fine tuning, which cannot be explained by the Big Bang model. A simple solution to this problem is to assume that the Universe has always been flat, and hence the density parameter has always been 1.

The zeroth law of thermodynamics states that two bodies in thermal contact with each other will eventually reach the same temperature. If the cosmological principle holds true, the temperature of different regions of sky should be the same. The Cosmic Microwave Background (CMB) bathes the Earth in isotropic radiation at a temperature of 2.726 ± 0.010 K [5]. Photons travel between regions, establishing thermal equilibrium. However,

the finite speed of a photon is too low to account for the distances travelled since the beginning of the Universe.

Finally, a large number of stable, relic particles were produced as a result of the Big Bang. However, none of these particles, such as monopoles, have been observed.

The solution to the aforementioned problems is a period of inflation in the early Universe [6]. The early Universe underwent exponential expansion at a much higher rate than expected for the Big Bang, diluting any initial curvature, resulting in the flat geometry observed today. At the start of this period of very rapid expansion, when the Universe was 10^{-35} s old, it is thought to have had a size of 10^{-32} nm. Therefore, there was enough time for photons to traverse the entire Universe, thus establishing thermal equilibrium between different regions of the sky. Additionally, the number density of relic particles is rapidly reduced during this phase, explaining why their present-day observation is so difficult.

2.2 The Dark Matter Problem

The density parameter Ω can be broken down into components:

$$\Omega = \Omega_{\mathrm{M}} + \Omega_{\mathrm{R}} \tag{2.8}$$

where Ω_{M} and Ω_{R} are the matter and radiation contributions to Ω. Apart from the scenarios listed in Table 2.1, a special case exists if the universe is dominated by vacuum energy, rather than radiation or matter. This is where the universe expands at an ever increasing rate ($a(t) \propto e^t$), and this component was dominant during the period of inflation. It is also believed to be the dominant component in the present evolutionary stage of the universe from observations of $H(t)$, where t is the lookback time of distant supernovae [4]. This results in an additional term Λ in Eq. (2.4), and a new component to the density parameter:

$$\Omega = \Omega_{\mathrm{M}} + \Omega_{\mathrm{R}} + \Omega_{\Lambda} \tag{2.9}$$

The vacuum energy contribution Ω_{Λ} is often referred to as quintessence or dark energy. As Λ is not a function of k in Eq. (2.4), a flat geometry is still possible in an accelerating universe.

Several pieces of observational evidence indicate that luminous matter does not dominate Ω_M. In fact, stars, planets and other astronomical bodies contribute a relatively small amount to the total mass of the Universe. Another type of matter dominates the matter contribution to the density parameter. As yet it remains unobserved, implying that it does not emit electromagnetic radiation. This gives it the name dark matter.

2.2.1 Galactic Rotation Curves

The earliest indication of the presence of dark matter in the Universe is the observation of rotational velocities $v(r)$ of spiral galaxies as a function of radius r. Equating Newton's law of universal gravity and the centrifugal force yields:

$$v(r) = \sqrt{\frac{GM(r)}{r}} \tag{2.10}$$

where G is the gravitational constant and $M(r)$ is the mass of a galaxy within a radius r. Therefore, as shown in Figure 2.1, the galactic velocity is expected to drop once the radius extends beyond the core, where most of the luminous mass is concentrated, proportional to $\sqrt{\frac{1}{r}}$. However, measurements of the Doppler shift in the 21 cm neutral hydrogen emission line indicate that the curve remains constant at radii far beyond the galactic core [7], as shown in Figure 2.1. Since the intial observation in 1970, the rotation curves for a large number of spiral galaxies have been taken, and the vast majority display the same properties [9].

The discrepancy between the observed rotation curves and those predicted by Eq. (2.10) points to the presence of a very large amount of non-luminous material extending to larger radii than that encompassing the visible matter. The extra matter must extend in all directions, not just in the plane of the luminous galactic disc, ensuring it remains stable out to large radii [10]. This means that the distribution of dark matter must be roughly spherical, surrounding the visible galaxy with a density distribution proportional to $\frac{1}{r^2}$, and contributing the majority of the galactic mass.

An alternative explanation of the observed phenomenon is given by Modified Newtonian Dynamics (MoND) [11], which hypothesises that very small gravitational accelerations depart from those predicted by classical Newtonian gravity. The model makes an adequate prediction of the rotation curves for many galaxies [11].

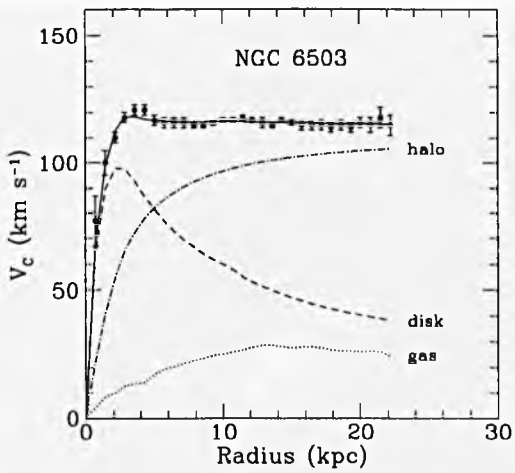

Figure 2.1: Rotation Curve for the Spiral Galaxy NGC 6503. The rotation velocity V_C increases with radius until approximately 4 kpc from the galactic centre. It then plateaus out to 23 kpc, in contrast to what would be expected if all the matter in the galaxy was luminous (labelled disk). A contribution from the dark matter halo solves this problem. Taken from [8].

2.2.2 Gravitational Lensing

Additional evidence comes from the phenomenon of gravitational lensing. The effect can be observed when a massive cluster passes between a distant galaxy and an observer; the trajectories of photons from the distant object are altered by the presence of the massive cluster in the foreground. In other words, the photons bend due the gravitational pull of the massive cluster, creating Einstein rings, arcs and multiple images of obscured objects in astronomical photographs. See for example [12] and Figure 2.2.

From such images, the mass distribution of the cluster in the foreground can be determined. Recently, strong evidence for the existence of dark matter was shown in weak lensing observations of two colliding clusters of galaxies (1E0657-558) [13]. Regions of hot X-ray emitting gas trail behind the galaxies within the merging clusters. Using gravitational lensing, the system's centre of mass is shown to differ from the centre of luminous mass. From this, a region of dark matter that lies in front of the slower X-ray gas can be inferred. Although many MoND theories cannot provide a solution, significant effort has been made to describe this effect in the absence of a dark matter halo [14].

Figure 2.2: Hubble Space Telescope Image of GC 0024 and GC 1654. Several blue, loop-shaped objects can be seen in the image, and are multiple images of the same galaxy. The duplications are due to the cluster of yellow, spiral galaxies GC 0024 and GC 1654 in the centre of the photograph. Image courtesy of W. N. Coley, E. Turner, J. A. Tyson and NASA/ESA.

2.2.3 Big Bang Nucleosynthesis

It is possible for astronomical objects to radiate so dimly that they may be classified as dark matter. Massive Compact Halo Object (MaCHO) is the general term for very dim stars that are observed through their gravitational effect only. These include red, brown and white dwarfs, and neutron stars. These are the remnants of stars once they have burned all their fuel. Although searches are in progress for MaCHOs in the Milky Way galaxy, there are far too few to account for the proportion of dark matter in the Universe [15].

Other possibilities include very large black holes that are the remnants of an early generation of stars, which were so massive that they died before many heavy elements could be produced. Additionally, small, primordial black holes created during the Big Bang may also contribute. However, the masses of the early black holes are too small and would have evaporated by this time [16].

This leaves galactic dust clouds to account for the dark matter contribution. However, Big Bang nucleosynthesis constraints [17] indicate that the dark matter component cannot

be comprised of any of the above astronomical bodies or clouds.

All stars begin their lives burning hydrogen by nuclear fusion reactions. At successive stages of their lives, the more massive stars burn heavier elements. The most massive stars continue until their cores are full of iron. At this point a supernova explosion ensues, in which elements heavier than iron are created. However, some isotopes of the lighter elements, such as ^{2}H (deuterium), ^{3}He, and ^{7}Li, cannot have been created in this manner. This means that they must have been produced at the time of the Big Bang.

Deuterium is burnt in stars at 10^6 K, which is significantly lower than the temperature of the stellar core. Therefore, ^{2}H can only be found in interstellar gas clouds and protostars that are too young to have a nuclear burning core [18]. Both ^{3}He and ^{7}Li are destroyed in stellar evolution, so their abundances are measured in regions of space in which stars are being formed [19], or in metal-poor stars [20].

The strongest constraints are imposed on the measurement of the deuterium abundance [18] inferred from spectroscopy on lyman alpha forest spectra of high redshift hydrogen emission, resulting in the vertical shaded box in Figure 2.3. This implies that the total baryonic matter in the Universe is of the order of $4.1 \pm 0.9\%$ of the critical density ρ_c [22].

This is confirmed from measurements of temperature fluctuations in the Cosmic Microwave Background (CMB) [4]. The CMB, which is briefly described in Section 2.1, was created during recombination, the time at which the Universe was cool enough to allow electrons to combine with nuclei. The WMAP observations [4] mapped out three small-scale anisotropies in the temperature fluctuations. The pressure imposed by photons travelling to the outer reaches of the early Universe countered the inward pressure imposed by gravitational attraction due to matter. This created the acoustic oscillations, or anisotropies, shown in Figure 2.4. By calculating the ratio of peak heights, a number of cosmological parameters can be determined.

The best fit to the data is from the ΛCDM model [1], assuming that the Universe has a flat geometry. The model includes contributions from vacuum energy Λ and Cold Dark Matter (CDM) to the density parameter Ω in Eq. (2.9). The fitting results in a value for the contribution to the matter density parameter from luminous material of 0.042 ± 0.004 [4]. This is in agreement with the amount of luminous material calculated from the measurements of light nuclei abundances detailed above.

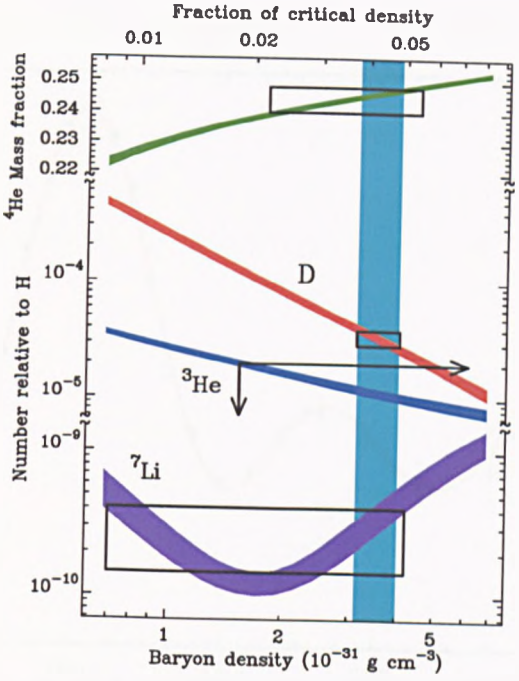

Figure 2.3: Predicted and Measured Abundances of the Light Nuclei ^{2}H (deuterium), ^{3}He, ^{4}He and ^{7}Li. Predicted abundances are shown by the shaded horizontal bands, and the boxes represent 95% confidence intervals for the measured values, except in the case of ^{3}He, where this is represented by arrows. The deuterium measurement provides the strongest constraint on the baryon density, which is represented by the vertical shaded area. The plot shows that approximately 4% of the matter in a flat Universe can be attributed to baryonic material. Taken from [21].

Therefore, it is reasonable to conclude that there is a halo of dark matter distributed throughout each galaxy, which contributes most of its mass. Additionally, this halo cannot be comprised of interstellar gas, leaving the possibility of there being an, as yet, unobserved particle that proliferates in this region.

The magnitude of contributions to the density parameter from vacuum energy, dark matter and baryons are shown in Table 2.2.

2.3 The Standard Model

Since its introduction in 1970, the Standard Model [25] of particle physics has been resoundingly successful in predicting the observations made in modern day experiments. It is a gauge theory based on the group $SU(3) \otimes SU(2) \otimes U1$, containing 12 spin-$\frac{1}{2}\hbar$ fundamental

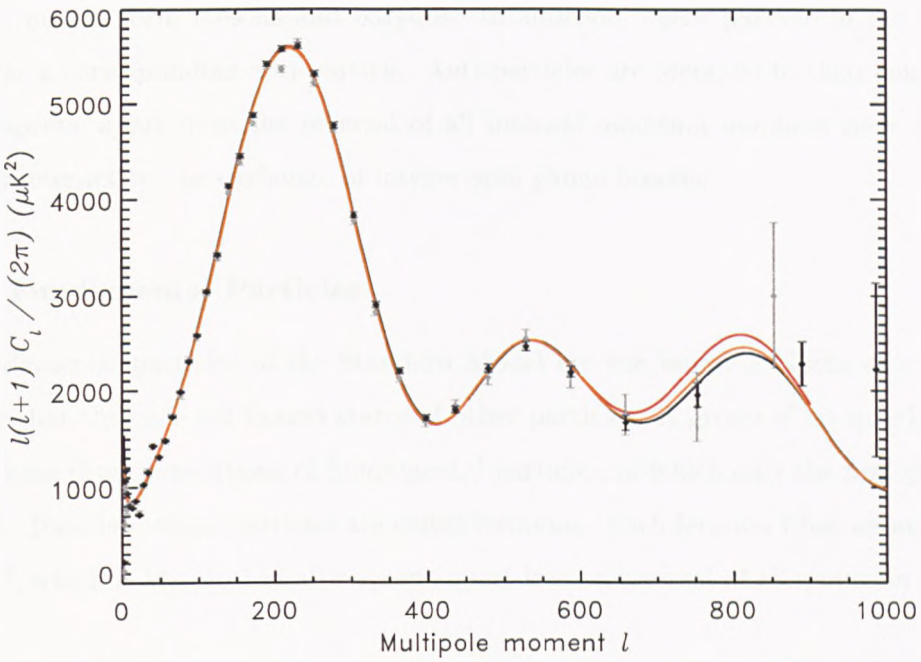

Figure 2.4: The Cosmic Microwave Background (CMB) Angular Power Spectrum from WMAP measurements. The black and red lines are the best fits to 3 and 1 year WMAP data respectively, using the ΛCDM model [1], assuming a flat Universe. The orange line is the best fit to a combination of measurements from the Cosmic Background Imager (CBI) [23] and Arcminute Cosmology Bolometer Array Receiver (ACBAR) [24]. The solid points represent the 3 year data, and the grey points the first-year data. From the ratios of the peaks, the amount of baryonic material in the Universe is found to be $4.2 \pm 0.4\%$, in agreement with that derived from Big Bang nucleosynthesis.

Table 2.2: Summary of Contributions by Different Components to the Density Parameter Ω. Values taken from observations of the CMB from WMAP [4].

Vacuum energy	0.73 ± 0.04
Dark matter	0.23 ± 0.04
Baryonic matter	0.044 ± 0.004
Total	1.02 ± 0.02

particles, which are subdivided into equal numbers of quarks and leptons. When bound together, quarks form mesons and baryons. In addition, every particle in the Standard Model has a corresponding anti-particle. Anti-particles are identical to their counterparts in all respects, apart from the reversal of all internal quantum numbers such as charge. Particles interact by the exchange of integer-spin gauge bosons.

2.3.1 Fundamental Particles

The fundamental particles of the Standard Model are the building blocks of all matter, meaning that they are not bound states of other particles. A group of six quarks and six leptons form three generations of fundamental particles, of which only the first generation is stable. Together, these particles are called fermions. Each fermion f has an antiparticle partner $\bar{f}$, which is identical in all respects apart from a reversal of all quantum numbers.

Quarks

An outline of the properties of quarks is given in Table 2.3. These spin-$\frac{1}{2}\hbar$ particles, which possess a baryon quantum number of $\frac{1}{3}$, can form bound states of mesons and baryons, collectively known as hadrons. Mesons, such as the π^0 and η particles, consist of a quark and antiquark. Baryons, such as the proton and neutron, consist of three quarks. Of all the baryons, only the proton and neutron, having valence quark compositions (uud) and (udd) respectively, are stable. Therefore, all stable nuclei formed in the early Universe are made up of protons and neutrons. Since these two baryons are over 3 orders of magnitude heavier than the next heaviest stable particle, the electron, the baryonic mass of the Universe is dominated by protons and neutrons.

Leptons

The second group of fundamental particles is the leptons, whose properties are given in Table 2.4. Each lepton carries a conserved quantum number, similar to the baryon number possessed by quarks. Each lepton generation has its own lepton conservation number. Anti-leptons have opposite charges and lepton numbers associated with them. Standard Model neutrinos are massless particles, and interact with matter only through the weak interaction, thus making them difficult to detect.

Table 2.3: Properties of Quarks in the Standard Model. All values are taken from [26], except the mass of the top quark, which is taken from current experimental data [27].

Name	Symbol	Electric Charge [e]	Mass [GeV]	Generation
down	d	$-\frac{1}{3}$	≈ 0.35	1st
up	u	$+\frac{2}{3}$	≈ 0.35	1st
strange	s	$-\frac{1}{3}$	≈ 0.5	2nd
charm	c	$+\frac{2}{3}$	≈ 1.5	2nd
beauty	b	$-\frac{1}{3}$	≈ 5.0	3rd
top	t	$+\frac{2}{3}$	172.5 ± 2.7	3rd

2.3.2 Particle Interactions

Within the Standard Model there are three classes of interactions, each mediated by the exchange of integer-spin gauge bosons.

The strong interaction affects those particles which possess a colour charge. This includes quarks and anti-quarks, and is responsible for the meson and baryon bound states. The mediating gauge boson for this force is the gluon, which carries a net colour. Hence, gluons can also interact strongly with each other, or in other words, they can couple to themselves.

Both quarks and leptons are affected by the weak interaction, which is observed in nuclear beta decay. It is mediated by the exchange of $W^{\pm}$ and Z^0 bosons.

Table 2.4: Properties of Leptons in the Standard Model. All values are taken from [26].

Name	Symbol	Electric Charge [e]	Mass [MeV]	Generation
electron	e^-	-1	0.511	1st
electron neutrino	ν_e	0	0	1st
muon	μ^-	-1	105.7	2nd
muon neutrino	ν_μ	0	0	2nd
tau	τ^-	-1	1777	3rd
tau neutrino	ν_τ	0	0	3rd

Table 2.5: Summary of Gauge Boson Properties and the Interactions they Mediate. All values are taken from [27].

Name	Symbol	Electric Charge [e]	Mass [GeV]	Spin $\hbar$	Interaction
gluon	g	0	0	1	strong
W boson	$W^{\pm}$	± 1	80.4	1	weak
Z boson	Z^0	0	91.2	1	weak
photon	γ	0	0	1	electromagnetic
graviton	G	0	0	2	gravitational

The photon is the exchange boson for electromagnetic interactions, which occur between particles with electric charge. It is responsible for holding atoms and molecules together, and at these scales, is dominant over all other interactions.

Although outside the Standard Model, the gravitational force is responsible for the shape of the Universe. By far, it is the weakest force on the scale of individual particles, and is mediated by the, as yet unobserved, graviton.

The three forces, along with the gravitational force, are summarised in Table 2.5. Apart from the graviton, all the gauge bosons are spin-$\hbar$ particles. Gauge theories predict massless exchange particles, in contradiction with the experimental evidence for W and Z bosons. This implies that there is an additional mechanism that generates particle mass, known as the Higgs mechanism [28]. The Higgs Boson H^0 [29] is the spin-0 particle associated with this mechanism, and is the only Standard Model particle yet to be observed.

All interactions in the Standard Model must conserve certain quantities. These rules are known as conservation laws, and apply to energy, momentum, angular momentum, electric and colour charges, and baryon and lepton flavour numbers.

2.4 Dark Matter Candidates

Observations of the CMB from WMAP indicate that non-baryonic dark matter accounts for $23 \pm 4\%$ of the mass-energy density of the Universe [4]. Although they are yet to be detected, a number of assumptions can be made about the properties of dark matter

particles. They must be stable, or have lifetimes of the order of the age of the Universe, otherwise they would have decayed. Additionally, they must only interact through the weak and gravitational forces, otherwise they would have become bound to protons and neutrons and would be seen today as anomalous heavy isotopes. Searches for such isotopes have proved fruitless [30]. For reasons discussed in Section 2.2, they must have a large *total* mass-energy density, as they make up a significant proportion of the Universe. In other words, they should have large masses and/or be abundant.

There is a large wealth of possible candidates for dark matter particles [31], of which the Weakly Interacting Massive Particle (WIMP) has the most direct search experiments dedicated to it. Extensions of the Standard Model, such as supersymmetry, provide promising WIMP candidates that have typical masses in the range 0.01 to 10 TeV.

2.4.1 Supersymmetry

Although the Standard Model has been successful in explaining the observations from particle physics experiments, it is not a complete theory as it leaves many questions unanswered. As mentioned in Section 2.3.2, the Higgs boson is a by-product of the Higgs mechanism, which is thought to be responsible for assigning particle masses. If the Standard Model remains valid to the Planck scale (1.2×10^{19} GeV), then the emission and reabsorption of a fermion by a Higgs boson leads to quadratically divergent mass corrections. The quadratically divergent mass of the Higgs boson is termed the mass hierarchy problem, and implies that there must be some new physics, in which the contribution from fermions is cancelled out, at energies far smaller than the Planck scale.

The theory of supersymmetry attempts to solve the mass hierachy problem. It is a high-energy extension of the Standard Model, and as such, the equations of the Standard Model remain unaltered when bosons are replaced by fermions and vice versa. In supersymmetric models, bosons and fermions are grouped together in supermultiplets, and there is an operator $\hat{Q}$ that transforms between each boson and its fermionic superpartner:

$$\begin{aligned} \hat{Q}|\text{Boson}\rangle &= |\text{Fermion}\rangle \\ \hat{Q}|\text{Fermion}\rangle &= |\text{Boson}\rangle \end{aligned} \tag{2.11}$$

The operator in Eq. (2.11) changes the spin of a particle by at least half a unit. The simplest example of a supersymmetric theory is one with a single operator. In the following

equations, the indices α and β are used to distinguish identical operators Q_α and Q_β. As $\hat{Q}$ is a symmetry operator, Q_α and its anti-commutator $\{Q_\alpha, Q_\beta\}$ must commute with the Hamiltonian H:

$$[Q_\alpha, H] = 0 \quad \text{and} \quad [\{Q_\alpha, Q_\beta\}, H] = 0 \tag{2.12}$$

In the relativistic limit, all particles can be classed as massless, and a momentum-energy tensor can be chosen such that $P_\mu = \frac{1}{4}(-1, 0, 0, 1)$. This is a four-dimensional vector that gives the particle a momentum component of $-\frac{1}{4}$ in the x-direction and energy component of $\frac{1}{4}$. The following commutation relations can be derived [32]:

$$\{Q_\alpha, Q_\beta^\dagger\} = 2\sigma_{\alpha\beta}^\mu P_\mu \tag{2.13}$$

$$\{Q_\alpha, Q_\beta\} = \{Q_\alpha^\dagger, Q_\beta^\dagger\} = 0 \tag{2.14}$$

$$[Q_\alpha, P_\mu] = [Q_\alpha^\dagger, P_\mu] = 0 \tag{2.15}$$

where $\sigma^\mu = (1, \vec{\sigma})$. The Pauli vector $\vec{\sigma}$ is defined by $\vec{\sigma} = \sigma_1\hat{x} + \sigma_2\hat{y} + \sigma_3\hat{z}$, where $\sigma_{1,2,3}$ are the Pauli matrices, and $\hat{x}$, $\hat{y}$ and $\hat{z}$ are unit vectors in the x-, y- and z-direction. The only non-vanishing relation is given by Eq. (2.13). As a result, for a massless particle in spin state $|\lambda\rangle$, only two operators will result in a non-vanishing state. These are Q_α, which raises the spin state by $\frac{1}{2}\hbar$, and $Q_\alpha^\dagger$, which has the opposite effect. Therefore, the chiral supermultiplet can be formed to relate spin-$\frac{1}{2}\hbar$ fermions with scalar bosons:

$$\begin{pmatrix} \frac{1}{2} \\ 0 \end{pmatrix} \Longrightarrow \begin{pmatrix} l\,(\text{lepton}) \\ \tilde{l}\,(\text{slepton}) \end{pmatrix} \quad \text{or} \quad \begin{pmatrix} q\,(\text{quark}) \\ \tilde{q}\,(\text{squark}) \end{pmatrix} \tag{2.16}$$

where the superpartners of the leptons and quarks are called sleptons and squarks respectively. Sleptons and squarks are also known as scalar leptons and scalar quarks. The vector or gauge supermultiplet relates fermions with spin-$\hbar$ vector bosons:

$$\begin{pmatrix} 1 \\ \frac{1}{2} \end{pmatrix} \Longrightarrow \begin{pmatrix} \text{gauge boson} \\ \text{gaugino} \end{pmatrix} \tag{2.17}$$

where the gaugino is the general name for the superpartners of gauge bosons. There is also a graviton supermultiplet, which comprises of the spin-2 graviton and the spin-$\frac{3}{2}$ gravitino.

As their quantum numbers do not match their Standard Model counterparts, these are new particles, collectively known as superparticles or sparticles. Their inclusion means that

for every fermion loop, there is a boson loop that adds counter terms to the equations for radiative corrections. The new diagrams cancel out the divergent Standard Model ones without the need for fine tuning, solving the mass hierarchy problem.

In some supersymmetric theories, all particles possess an additional quantum number called R-parity [33]. A particle with baryon number B, lepton number L and spin S has an R-parity of:

$$\mathcal{R}_p = (-1)^{3B+L+2S} \tag{2.18}$$

All Standard Model particles posses $\mathcal{R}_p = +1$, and all supersymmetric particles carry the opposite value. In many supersymmetric theories, R-parity needs to be conserved in all interactions to account for baryon and lepton number conservation. Therefore, in the case of models in which R-parity is not violated, at least one sparticle must be produced when an unstable supersymmetric particle decays. This means that the Lightest Supersymmetric Particle (LSP) must be stable, as no lighter sparticle can be produced from its decay.

Of the many supersymmetric theories in existence, the Minimal Supersymmetric Standard Model (MSSM) [34] is the simplest. The MSSM consists of 124 independent parameters, including the nineteen free parameters of the Standard Model. R-parity conservation is incorporated in the constrained model (cMSSM).

Compared to the Standard Model, an additional Higgs doublet is a necessary addition to the MSSM [35]. This leads to four new Higgs bosons, comprising of 1 scalar h^0, one pseudo-scalar A^0 and 2 charged scalars $H^{\pm}$, each of which has its own superpartner.

The commutation relationship $[Q_\alpha, P \cdot P] = 0$ can be derived from Eq. (2.15). From kinematics, the mass of a particle is given by $M^2 = E^2 - p^2$, where E and p are the energy and momentum of the particle respectively. Therefore, the commutation relationship $[Q_\alpha, M^2] = 0$ can be inferred. This means that a sparticle should have the same mass as its Standard Model counterpart. However, as superparticles are yet to be observed in particle physics experiments, there must be a symmetry breaking mechanism.

Spontaneous supersymmetry breaking is a possible mechanism induced by a vacuum state. It is favoured as it is similar to gauge symmetry breaking. There exist two primary mechanisms for transmitting supersymmetry breaking from the hidden to the visible sectors of the MSSM. In gravity mediated supersymmetry breaking [36], or the minimal SUperGRAvity (mSUGRA) model, gravitons carry messages between the hidden and visible

sectors. In Gauge Mediated Supersummetry Breaking (GMSB) [37], a separate messenger sector is used.

In addition to the superpartners of Standard Model particles, four new neutral spin-$\frac{1}{2}\hbar$ fermions are present in the MSSM. These particles are known as neutralinos, and form four mixed states comprised of two neutral higgsinos, $\tilde{H}^0$ and $\tilde{h}^0$, the photino $\tilde{\gamma}$ (superpartner of the photon) and Zino $\tilde{Z}^0$ (superpartner of the Z^0 boson). The four mass eigenstates of the neutralino are denoted by $\tilde{\chi}_i^0$, where $i = 1,\ldots, 4$, and can be calculated from the mass mixing matrix [38]:

$$M_{\tilde{\chi}^0} = \begin{pmatrix} M_1 & 0 & -M_{Z^0} s_{\theta_W} c_\beta & M_{Z^0} s_{\theta_W} s_\beta \\ 0 & M_2 & M_{Z^0} c_{\theta_W} c_\beta & -M_{Z^0} c_{\theta_W} s_\beta \\ -M_{Z^0} s_{\theta_W} c_\beta & M_{Z^0} c_{\theta_W} c_\beta & 0 & -\mu \\ M_{Z^0} s_{\theta_W} s_\beta & -M_{Z^0} s_{\theta_W} s_\beta & -\mu & 0 \end{pmatrix} \tag{2.19}$$

where $s_{\theta_W} = \sin\theta_W$, $c_{\theta_W} = \cos\theta_W$, $s_\beta = \sin\beta$ and $c_\beta = \cos\beta$. As shown in Eq. (2.19), neutralino mass is a function of the U(1) and SU(2) gaugino masses (M_1 and M_2 respectively), the ratio of Higgs expectation values $\tan\beta$ and the higgsino mass parameter μ.

In the mSUGRA scenario of the MSSM, the lightest mass eigenstate of the neutralino $\tilde{\chi}_1^0$ is the LSP. If R-parity is conserved, this makes the $\tilde{\chi}_1^0$ a possible dark matter candidate [39].

In the GMSB scenario of the MSSM, the gravitino is the LSP [40]. However, gravitinos only interact by the gravitational force, thus making them almost impossible to detect in dark matter search experiments.

2.4.2 Other Candidates

The observation of neutrino oscillations [41] simultaneously solved the solar neutrino problem [42] and disproved the Standard Model prediction of massless neutrinos. Neutrinos can satisfy all the necessary conditions outlined above, and contribute to the dark matter density. However, experimental limits on their masses [27] show that they are low mass, highly relativistic particles. N-body structure formation simulations of a Universe dominated by such hot dark matter particles as neutrinos fail to reproduce the observed

structure [43]. Therefore non-relativistic, in other words cold dark matter, particle candidates like the neutralino must dominate the mass contribution from non-baryonic matter. There is no requirement for a significant contribution to Ω_M from hot dark matter within the currently favoured ΛCDM model [44].

A number of experiments are dedicated to searching for an alternative cold dark matter candidate called the axion [45]. It provides a solution to charge-parity violation in the strong interactions, called the strong CP problem [46]. The mass of the axion is expected to lie between approximately 1 μeV and 1 meV [27], which is on the scale of neutrinos. However, they are expected to have decoupled at non-relativistic speeds, and hence, are classified as cold dark matter particles. In certain cosmological models the axino, the superpartner of the axion, could be regarded as a possible dark matter candidate [47].

Apart from those discussed above, there are many other possible candidates, such as the Lightest Kaluza-Klein (LKK) particle [49] and WIMPzillas [50]. Additionally, there are no theoretical reasons that cold dark matter is not a combination of any of these possible candidates. Theoretical predictions of masses and interaction strengths with ordinary matter for some well-motivated dark matter candidates are summarised in Figure 2.5.

The matter contribution to the density parameter Ω_M, given in Eq. (2.9), can now be written in terms of its components:

$$\Omega_M = \Omega_B + \Omega_\nu + \Omega_{CDM} \tag{2.20}$$

where Ω_B, Ω_ν and Ω_{CDM} are the baryonic, neutrino and cold dark matter contributions respectively.

2.5 Direct WIMP Dark Matter Search Experiments

There are three main WIMP detection methods currently employed by international collaborations. Detection of dark matter particles passing through the Earth is performed with Earth-based detectors, in what is referred to as the direct method. Indirect detection is the search for particles produced as a result of neutralino annihilations. Finally, dark matter can be probed through searches for production and detection in collider experiments.

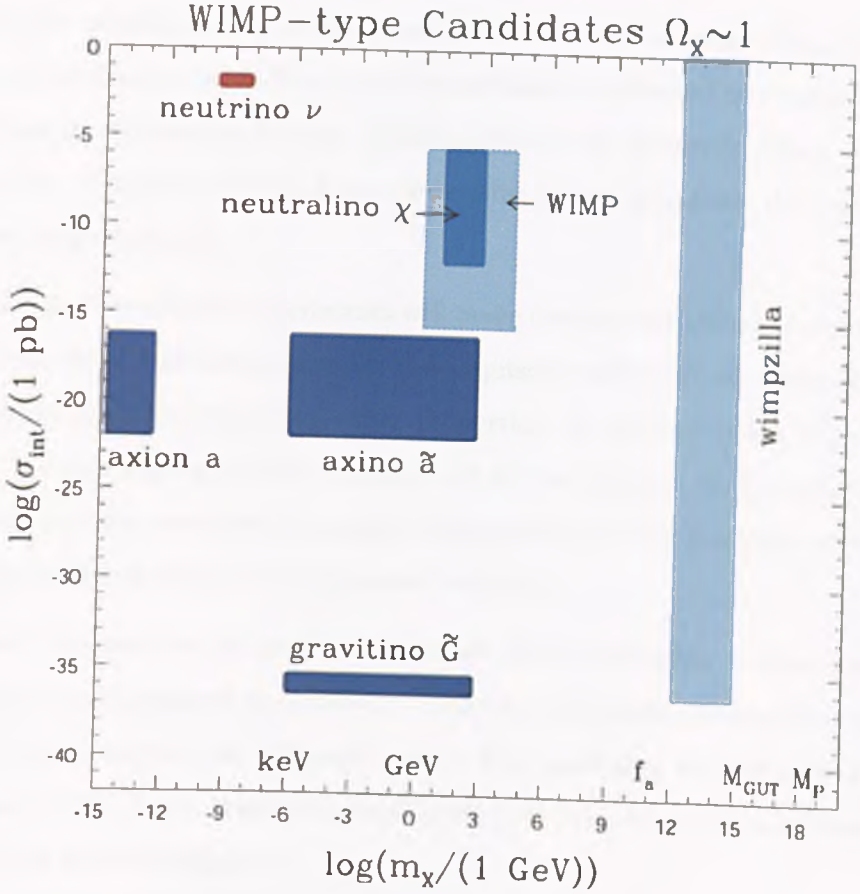

Figure 2.5: Theoretical Representation of Some Well-Motivated Dark Matter Candidates. The shaded areas signify their position in interaction strength with ordinary matter σ_{int} and candidate mass m_χ phase space. The region marked "WIMP" includes the Lightest Kaluza-Klein (LKK) particle and neutralino. Taken from [48].

It is assumed [51] that the dark matter particle density at the Earth's position in the spherical WIMP halo is 0.3 GeV/c^2/cm^3. At this radius, further assumptions are made setting the velocity required for a WIMP to escape the halo at 650 km/s and its root mean square velocity at 279 km/s. As the Earth orbits the Sun, and the Sun orbits the galactic centre, the Earth moves through this halo at a relative velocity of 235 km/s [51]. Direct dark matter searches detect the elastic recoil of an incident WIMP off a nucleus in an Earth-based target [51, 52].

Neutralinos coalesce in regions of space with strong gravitational fields, such as the galactic and solar centres. Due to their weakly interacting nature, the cross-section for neutralino annihilation is very small. However, in these high dark matter density regions, the rate of such an interaction occurring may be observable. Indirect detection experiments

are essential for calculations of the cold dark matter density parameter Ω_{CDM} in Eq. (2.20). Photons and neutrinos emitted from these interactions are detected by experiments such as the High Energy Stereoscopic System (HESS) [53] and the Antarctic Muon and Neutrino Detector Array (AMANDA) [54]. A comprehensive review of indirect dark matter search experiments is given in [55].

It is possible that collider experiments will make the first detections of supersymmetric particle production. Following discovery, the acquisition of a high statistics event sample could establish the stability, among other properties, of these particles. Thus, they can determine whether supersymmetric theories do in fact yield a dark matter candidate. Determination of the mass and interaction cross-section of this candidate would provide a sensitivity for direct dark matter detectors to aim for.

In order to determine the properties of dark matter particles, a large number need to be produced and detected in a factory. Collider experiments provide the means with which to produce particles on industrial scales. The possibility of dark matter detection at the Tevatron [56], Large Hadron Collider (LHC) [57] and International Linear Collider (ILC) [58] have been investigated.

A variety of approaches to the direct detection of dark matter are adopted by various groups around the World. The rich diversity in detection techniques is briefly outlined in this section. A more comprehensive review is given by [59].

2.5.1 WIMP Detection Signatures

A WIMP will interact elastically with target media in a model independent manner. Due to their relatively large mass, WIMPs will preferentially scatter off the target nucleus. WIMP-electron events are unlikely due to the large mass difference between these two particles, meaning that the energy transferred to the electron will be below the detectable threshold. Incident gamma-rays from background radioactivity will interact with both the target nucleus and its surrounding electrons. However, being massless, gamma-rays incident on a target nucleus will result in negligible recoil energy. Hence, gamma-electron interactions are more likely to show up in the detector. As most detection techniques are sensitive to gamma radiation, the discrimination between these events and WIMP/neutron-nucleus interactions affects the sensitivity of the detector.

The differential nuclear recoil event rate in events per kilogram per day is given by [60]:

$$\frac{dN}{dE_R} = \frac{N_0}{2M_W^2 M_A v_0^2} (M_W + M_A)^2 \, e^{-\frac{E_R(M_W+M_A)^2}{2M_W^2 M_A v_0^2}} \tag{2.21}$$

where N is the event rate per unit mass, N_0 is the total event rate, M_W is the WIMP mass, M_A is the mass of the target nucleus and v_0 is the incident velocity of the WIMP. The recoil energy E_R is given by:

$$E_R = \frac{M_W^2 M_A v_0^2}{(M_W + M_A)^2} (1 - \cos\theta) \tag{2.22}$$

where θ is the angle of the recoiled nucleus relative to the incident WIMP's direction. As mentioned above, the relative velocity of the Earth with respect to the dark matter halo is 235 km/s. Hence, expected recoil energies are typically less than 50 keV. It is also evident from Eq. (2.21), that the differential event rate is proportional to e^{-E_R}, meaning that more events are expected at lower recoil energies.

Substituting the recoil energy given by Eq. (2.22) into Eq. (2.21) yields a differential nuclear recoil event rate of:

$$\frac{dN}{dE_R} = \frac{N_0}{2M_W^2 M_A v_0^2} (M_W + M_A)^2 \, e^{-\frac{(1-\cos\theta)}{2}} \tag{2.23}$$

Due to physical constraints, a number of corrections need to be made to Eq. (2.23). The velocity of the Earth relative to the WIMP halo is not constant due to its orbit around the Sun, which in turn orbits the centre of the galaxy. This 14% variation in the Earth's relative velocity results in a 5-7% seasonal modulation in the event rate for an energy threshold of 1 keV [61]. To account for this, a function $f(v)$ needs to be included:

$$\frac{dN}{dE_R} = \frac{N_0}{2M_W^2 M_A} (M_W + M_A)^2 \, e^{-\frac{(1-\cos\theta)}{2}} \int_{v_{min}}^{v_{esc}} \frac{f(v)}{v^2} dv \tag{2.24}$$

where v_{esc} is the maximum WIMP escape velocity set by the halo model, and v_{min} is the minimum WIMP velocity that will result in a recoil of energy E_R.

An additional consideration is the number of different nuclei within the target material itself. In compounds, WIMP recoils off different elemental nuclei are analysed separately. The differential nuclear event rate in Eq. (2.24) is multiplied by the fraction f_A of total target mass contributed by element A:

$$\frac{dN}{dE_R} = f_A \frac{N_0}{2M_W^2 M_A} (M_W + M_A)^2 \, e^{-\frac{(1-\cos\theta)}{2}} \int_{v_{min}}^{v_{esc}} \frac{f(v)}{v^2} dv = N_0 S_p \tag{2.25}$$

where S_p is the modified spectral function taking the velocity of the Earth with respect to the WIMP halo and the fraction mass of the target into account.

Another complication arises from the quenching of nuclear recoil events. In scintillators, a recoiling nucleus loses energy through the electronic and atomic channels. The electronic channel results in the production of scintillation light, while atomic energy losses give rise to phonon emission. This is in contrast to electron interactions, where energy is lost through the electronic channel only. As the use of a mono-energetic neutron source is not practical in the typically hostile environments where dark matter detectors operate, energy scale calibation is performed with a gamma-ray emitting radioisotope. However, due to losses through the atomic channel, the energy detected from nuclear recoils is less than that for electron recoils of the same E_R. In other words, $E_{\text{vis}} = QE_R$, where E_{vis} is the visible energy, and Q is the degree of quenching for nuclear recoils with respect to electron interactions. This is also known as the quenching factor, and varies depending on the recoil energy and the target nucleus. In the energy range relevant to dark matter experiments (below 50 keV), the quenching factor is of the order of 0.1 to 0.3 for most target materials.

Recoils of a single energy E' will not be observed as such due to the finite resolution of the detector. With enough of these events, a Gaussian function can be fitted, the mean of which will be E'. The width of this distribution is a measure of the amount of fluctuation from E' recorded. The energy resolution Υ is typically defined as:

$$\Upsilon = \frac{\Delta E_{\text{FWHM}}}{E'} \tag{2.26}$$

where ΔE_{FWHM} is the full width of the distribution at half-maximum.

The threshold of the detector must be set just above the electric noise level, implying that events with a low enough energy to fall beneath this threshold will not be detected. The number of low energy counts may be so small that the use of a Gaussian function would lead to unphysical negative energy values for E'. Therefore, at energies close to threshold, a Poissonian function should be used.

In the non-relativistic limit, WIMPs can only couple to nuclei in spin-independent and spin-dependent interactions [62]. In the former case, a WIMP couples to the mass of the nucleus. The WIMP-quark cross-section for spin-independent interactions can be calculated with the use of the Feynman diagrams in Figure 2.6 [63]. This is then summed

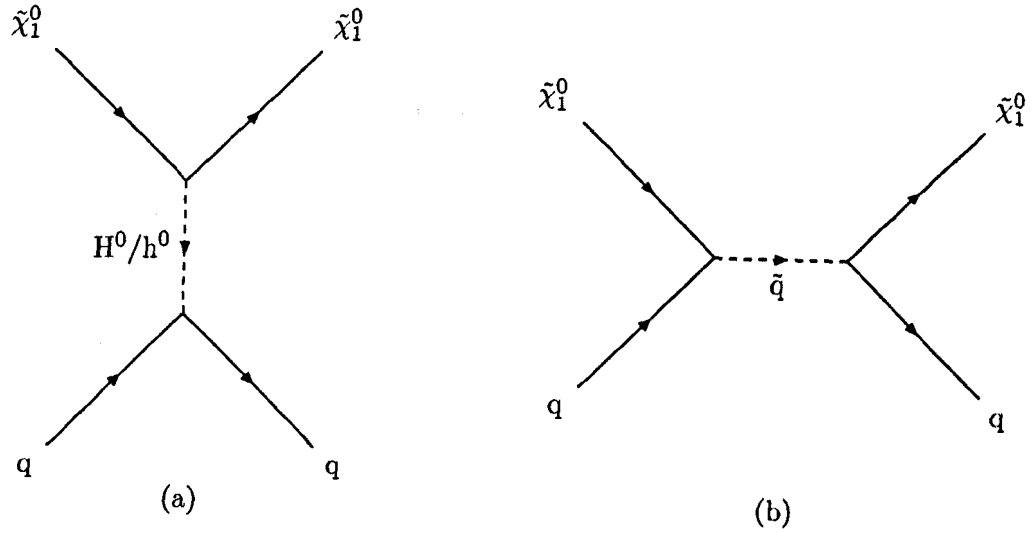

Figure 2.6: Feynman Diagrams contributing to Spin-Independent Elastic Scattering of Neutralinos off Quarks by: (a) Higgs boson exchange; and (b) squark exchange.

over all the quarks in a nucleon to give a WIMP-nucleon cross-section. The total cross-section scales with the square of the mass number A. Therefore, to compare results from experiments that utilise different target materials, the event rate should be normalised by dividing it by A^2.

WIMPs can also couple to the spin of the target nucleus. As with spin-independent interactions, the cross-section for WIMP-quark spin-dependent interactions is calculated

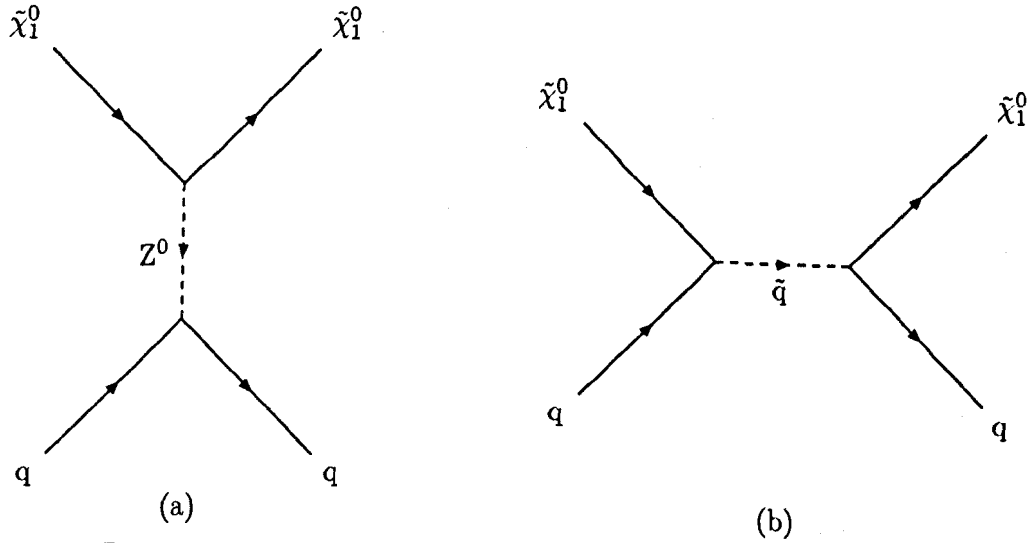

Figure 2.7: Feynman Diagrams contributing to the Spin-Dependent Elastic Scattering of Neutralinos off Quarks by: (a) Z boson exchange; and (b) squark exchange.

and summed for a resultant WIMP-nucleon cross-section. The Feynman diagrams in Figure 2.7 contribute to the spin-dependent WIMP-quark cross-section [63]. However, in spin-dependent interactions the scattering amplitude changes sign with the spin direction, and thus proton-proton and neutron-neutron pairs cancel out. Therefore, only isotopes with an odd number of protons or neutrons can undergo spin-dependent interactions. To compare experiments with different target materials, the spin factor of the target nucleus must be taken into account when calculating the differential event rate. Additionally, the spin-dependent cross-section is altered by the spin of the incident WIMP, meaning that these interactions are model dependent.

Due to the finite radius of a nucleus r_n, it is possible for the momentum transfer $q = \sqrt{2M_A E_R}$ to be larger than its inverse size. When this happens, the effective cross-section falls with increasing q, or for the same isotope, increasing recoil energy. This decline is represented by the form factor F [64]. Therefore, the cross-section for WIMP-nucleus scattering σ can be rewritten as:

$$\sigma(qr_n) = \sigma_0 F^2(qr_n) \tag{2.27}$$

where σ_0 is the cross-section when $q = 0$. Since r_n is typically given in units of fm [65], the momentum transfer can be converted to units of fm^{-1}, making the quantity qr_n dimensionless [60]:

$$qr_n = 6.92 \times 10^{-3}\sqrt{AE_R}\, r_n \tag{2.28}$$

where E_R is in units of keV. The form factor is obtained by performing Fourier transforms on different approximations for nuclei [60]. For the spin-independent case, performing a Fourier transform on a solid sphere approximates the whole nucleus:

$$F(qr_n) = \frac{3\left[\sin(qr_n) - qr_n \cos(qr_n)\right]}{(qr_n)^3} \tag{2.29}$$

In the spin-dependent case, a Fourier transform is performed on a thin shell, which serves as a model for the outer shell nucleon:

$$F(qr_n) = \frac{\sin(qr_n)}{qr_n} \tag{2.30}$$

The form factors, in the spin-independent case, for ^{23}Na and ^{127}I nuclei as a function of energy are shown in Figure 2.8. It is clear that the decrease in form factor at increasing

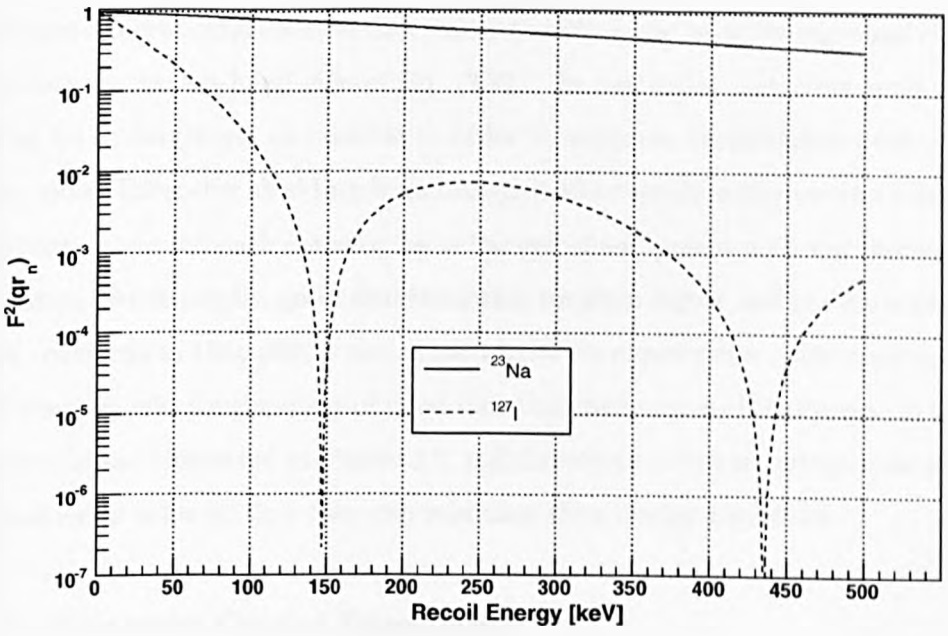

Figure 2.8: Form Factor as a Function of Recoil Energy for ^{23}Na (sodium) and ^{127}I (iodine) nuclei. The solid shell approximation outlined in Eq. (2.29) is used, and nuclear radii of 2.994 and 4.749 fm for ^{23}Na and ^{127}I are taken from [65]. It is clear that heavier elements have steeper distributions, indicating the event rate for WIMP-nucleus recoils is larger at lower recoil energies.

energies is flatter for light nuclei like ^{23}Na. From Eq. (2.27), the cross-section, and hence event rate, is directly proportional to $F^2(qr_n)$, implying that more low energy WIMP-nucleus recoils should be seen in the detector.

After these corrections have been taken into account, the differential event rate for WIMP-nucleus scattering given in Eq. (2.21) becomes [60]:

$$\frac{dN}{dE_{\text{vis}}} = N_0 S_p Q_A \mathcal{G}(E_{\text{vis}}) \epsilon(E_{\text{vis}}) F^2(qr_n) I \tag{2.31}$$

where S_p is the modified spectral function from Eq. (2.25), Q_A is the quenching factor for a nucleus of element A, $\mathcal{G}(E_{\text{vis}})$ is the correction due to detector energy resolution, $\epsilon(E_{\text{vis}})$ is the correction due to detector energy threshold, $F(qr_n)$ is the form factor, and I is the interaction function for spin-independent or spin-dependent factors.

2.5.2 Criteria for Dark Matter Detectors

Significant experimental effort is undertaken to reduce and reject background events which contribute to the left-hand side of Eq. (2.31). In particular, detectors tend to be operated as far underground as possible in order to suppress backgrounds from atmospheric cosmic rays. Extensive shielding from background neutrons and gamma radiation is also a key feature around each detector, as is the use of equipment with low radioisotope contamination. Additionally, good discrimination between signal and background events is a major requirement that affects the sensitivity of an experiment. This results in the constant research and development of novel detection techniques. Finally, due to the effect of the form factor illustrated in Figure 2.8, collaborations strive to reduce instrumental and environmental noise so that they can minimise their energy threshold.

2.5.3 Inorganic Crystal Scintillators

Scintillation is a process in which a charged particle traversing a medium loses energy through interactions with the electrons of the scintillator. The subsequent de-excitation of these electrons results in photon emission. Although WIMPs are electrically neutral, they can still collide with the target nucleus and cause excitation or ionisation. The emitted light, on de-excitation or recombination, can then be detected by a photomultiplier tube, which converts incident photons to an electric current that can be analysed.

Sodium iodide (NaI(Tl)) crystals were the first scintillators used in direct dark matter search experiments [66]. They remain a popular choice as target materials for dark matter experiments because of their high light yield and pulse shape differences between nuclear and electron recoils. Currently, the ANAIS (Annual modulation with NaI'S) [67], DAMA/NaI (DArk MAtter/NaI) [68] and ELEGANT-V (ELEctron GAmma-ray NEutrino Telescope) [69] experiments utilise these crystals. Although better discrimination can be reached with other scintillators, they remain one of the best at determining spin-dependent WIMP-nucleon limits. This is because the 100% naturally abundant stable isotopes ^{23}Na and ^{127}I have non-zero spin. Until very recently, the NaIAD (NaI Advanced Detector) experiment [70] held the best spin-dependent limit on WIMP-proton interactions [71]. A next generation NaI(Tl) detector, DAMA/LIBRA (DArk MAtter/Large sodium Iodide Bulk for RAre processes) [72], is taking data at Gran Sasso.

Caesium iodide (CsI(Tl)) crystals have a number of advantages over NaI(Tl) detectors,

such as better pulse shape discrimination and a higher light yield. They are also less hygroscopic, meaning that there is no need for encapsulation. However, CsI(Tl) crystals suffer from higher internal backgrounds in the form of ^{134}Cs, ^{137}Cs and ^{87}Rb radioisotopes. The KIMS (Korea Invisible Mass Search) Collaboration are currently using CsI(Tl) crystals in their dark matter search experiment [73].

The growing need for non-baryonic dark matter search experiments to reach greater sensitivities means better background discrimination is important. As discussed, pulse shape discrimination is possible with conventional scintillators, but this requires a large number of events. A better technique is to discriminate on an event-by-event basis, and this is possible with the new generation of hybrid detectors. These detectors combine simultaneous measurements of ionisation or heat, and light. However, this increases the complexity of these experiments.

Phonon detectors (also known as bolometers) use the fact that deposited energy in a target nucleus will eventually be converted to mechanical vibrations. Dielectric or superconducting crystals are cooled to very low temperatures (typically below 100 mK). At these temperatures, nuclei within the target material do not possess enough energy to vibrate significantly about their positions in the lattice. WIMP-nucleus collisions transfer some energy, resulting in larger vibrations. A sensitive thermometer on the surface of the crystal can detect these phonons (quantised modes of vibration).

The high sensitivity of phonon detectors, and the relatively low cost of scintillators, makes the simultaneous detection of heat and light very attractive. These experiments feature two crystals placed near each other. A particle interacting with the scintillating crystal is detected by phonon emission, and the photons emitted due to the de-excitation of the electrons of the scintillator are directed toward the second crystal. Here the emitted photons are absorbed, producing heat. Gamma-electron interactions result in higher scintillation yields when compared with nuclear recoils, allowing for event-by-event discrimination.

Possible scintillating crystals include calcium tungstate ($CaWO_4$), calcium molybdate ($CaMoO_4$), zinc tungstate ($ZnWO_4$) and aluminium oxide (Al_2O_3). The ROSEBUD (Rare Objects SEarch with Bolometers UndergrounD) Collaboration has used $CaWO_4$ in the past [74], and are currently testing the feasibility of Al_2O_3 [75]. CRESST-II (CRyogenic Rare Event Search with Superconducting Thermometers) [76] currently uses $CaWO_4$

crystals, and EURECA (European Underground Rare Event Calorimeter Array) [77] is a proposed next-generation experiment using the same detection technique.

2.5.4 Liquid Noble Gas Detectors

Better background discrimination can be achieved using liquid noble gases as scintillator media. Xenon has a high density of 3 g/cm^3 in its liquid phase, allowing greater sensitivities to be reached with lower volumes. Unlike NaI(Tl) however, not all stable xenon isotopes have non-zero spin, hence making liquid xenon less sensitive to spin-dependent WIMP couplings. However, unlike crystal-based detectors, liquid xenon experiments can be easily scaled-up. DAMA/LXe (DArk MAtter/Liquid Xenon) [78] and ZEPLIN-I (ZonEd Proportional scintillation in LIquid Noble gases) [79] are recent liquid xenon experiments, and XMASS (Xenon MASSive) [80] is a next-generation detector.

Hybrid liquid noble gas detectors look for ionisation and scintillation responses. A noble element is kept in a two-phase liquid-gas state within the same chamber. Incident WIMP particles will interact with the target nuclei in the liquid phase, resulting in the emission of scintillation light (primary pulse). The recoiling nucleus ionises a portion of the surrounding liquid. Some electrons will gain enough energy to cross the band gap and become free. The application of an electric field across the detector causes these electrons to drift toward the gas phase. The application of a stronger electric field across the liquid-gas boundary enables these electrons to cross it and accelerate, causing an avalanche within the gas phase. This avalanche gives rise to a secondary electroluminescence pulse. Gamma-rays interact with the electrons surrounding atoms in the liquid phase, resulting in different shaped secondary pulses.

Xenon is a relatively radiopure noble gas (^{85}Kr is the main impurity) and is sensitive to large WIMP masses due to the size of its nucleus. This makes it an attractive target medium, and the ZEPLIN-II [81], ZEPLIN-III [82] and XENON [83] experiments utilise it.

As an alternative to xenon, argon is used by the WARP (Wimp ARgon Programme) [84] and DEAP (Dark matter Experiment with Argon and Pulse shape discrimination) [85] Collaborations, and the next generation detectors ArDM (Argon Dark Matter) [86] and CLEAN (Cryogenic Low Energy Astrophysics with Noble gases) [87]. Compared with xenon, argon is relatively cheap and gives a higher light yield. However, argon suffers

from the presence of cosmogenically produced ^{39}Ar, although there are plans to extract underground argon from oil wells. The CLEAN collaboration are also looking into the possibility of using neon.

2.5.5 Other Techniques

As with the hybrid detectors outlined above, better discrimination can also be achieved by using targets sensitive to both ionisation and phonons. These detectors are ultra-pure semiconductor crystals, such as germanium and silicon, cooled to very low temperatures. As electron recoils in a target create more charge, the ratio between the charge collected and the phonon signal is used to discriminate on an event-by-event basis.

The CDMS-II (Cold Dark Matter Search) experiment [88] is an array of four 165 g germanium and two 100 g silicon crystals at the Soudan Underground Laboratory. Its direct competitor is the EDELWEISS-II (Expérience pour DEtecter Les Wimps En Site Souterrain) detector [89], which consists of twenty-one 320 g and seven 400 g germanium detectors installed at the Modane Underground Laboratory.

The sensitivities achievable with these relatively small mass detectors are competitive with the two-phase noble gas detectors described previously. This is accomplished through the excellent rejection of background events, which cannot be matched by any other technique.

The techniques described so far attempt to use low-background materials, shielding and various discrimination techniques to derive limits on the WIMP-nucleon cross-section. Even so, it is possible for a neutron signal from an unknown background to be detected, and hence be incorrectly identified as a WIMP. In a similar way to the hybrid detector discriminating nuclear and electron recoils on an event-by-event basis, the discrimination between WIMP and neutron events can be achieved using gas as a target medium. With a gas-filled Time Projection Chamber (TPC), an incident WIMP interacts with a nucleus and deposits some of its energy. This recoiling nucleus ionises surrounding gas atoms that lie in its trajectory. An electric field between the centre and endplates of the TPC causes the released electrons to drift to multiwire proportional chambers located at each endplate. This resultant signal can be translated to give positional information for each ionised gas atom, and hence reconstruct the path taken by the incident particle. However, gases are less dense than liquids or solids, and hence a larger volume is required to achieve

the same sensitivities as other dark matter experiments.

The DRIFT-II (Directional Recoil Identification From Tracks) experiment [90] at Boulby Mine, consists of one stainless steel vessel, holding 134 g of electronegative carbon-disulphide (CS_2) gas, occupying a total volume of 1 m^3. An electronegative gas is one that easily captures free electrons. This allows the drift of CS_2^- anions rather than electrons, reducing lateral and longitudinal diffusion of the track and maintaining fine detail features necessary for three dimensional reconstruction. A research and development study is being undertaken by the NEWAGE (NEw generation Wimp search with an Advanced Gaseous tracking dEvice) collaboration on the development of a TPC filled with carbon-tetrafluoride (CF_4) gas [91].

Metastable particle detectors include Superheated Droplet Detectors (SDDs), liquid bubble chambers and Superconducting Superheated Grains (SSGs). SDDs consist of droplets of superheated liquid in a gel matrix. A WIMP interaction causes a phase-transition from the superheated to normal states, resulting in the evaporation of these droplets to form bubbles. The properties of these bubbles are then detected acoustically. SDDs tend to be insensitive to low-energy transfer particles, such as gamma-rays, making them good target materials for direct dark matter search experiments.

The SIMPLE (Superheated Instrument for Massive ParticLE searches) experiment [92] consists of two freon-filled chambers loaded with C_2ClF_5 droplets. The PICASSO (Project in CAnada to Search for Supersymmetric Objects) detector [93] consists of three modules each of volume 1.5 l. One litre of C_4F_{10} droplets are loaded into the water-based gel.

The continuous operation of SDDs is difficult due to bubble growth over time, which leads to fractures within the gel and the depletion of freon. Their operation is also complex, and the fabrication of the detector components must be carefully done to prevent contamination with refrigerant molecules. However, a significant advantage of using this technique is the low background from gamma radiation.

The COUPP (Chicago Observatory for Underground Particle Physics) collaboration [94] intend to operate a 60 kg CF_3I bubble chamber. Unlike SDDs, the detector is relatively simple to construct and operate. However, maintaining the fluid in a superheated state for a considerable time period can prove difficult. As with other metastable particle detectors, they are relatively insensitive to the incident gamma background.

A far older technique is the use of SSGs, and ORPHEUS [95] is the only experiment

that utilises this technology. The detector consists of an array of superconducting tin granules of total mass 8 g, uniformly distributed in teflon powder, and contained within 56 pick-up coils. The total mass of the detector is 450 g, and a magnetic field of 285 G is imposed on the chamber. The granules are kept slightly below their superconducting-to-normal phase transition boundary. A recoil from an incident particle results in an increase in temperature, causing the granule to become normal conducting, and the magnetic field to pass through the interior.

2.5.6 Setting Limits on WIMP-Nucleon Interaction Cross-Sections

In the absence of a signal, experiments can set limits on the properties of WIMPs using the right-hand side of Eq. (2.31). For a stationary Earth, the simplest case, the total event rate R_0 is related to the total nuclear cross-section σ_A by [60]:

$$R_0 = \frac{D\sigma_A\,[\mathrm{pb}]}{M_\mathrm{W} M_A} \tag{2.32}$$

where D is a numerical factor dependent on the assumed dark matter density of the halo, and M_W and M_A are the masses of the WIMP and target nucleus respectively. The total nuclear cross-section is given by [63]:

$$\sigma_A = 4G_F^2 \frac{M_\mathrm{W} M_A}{(M_\mathrm{W} + M_A)} C \tag{2.33}$$

where G_F is the Fermi coupling constant, and C depends on the type of interaction. The differential cross-section takes the general form [63]:

$$\frac{d\sigma}{dq^2} = G_F^2 \frac{C}{v^2} F^2(qr_\mathrm{n}) \tag{2.34}$$

where q is the momentum transfer. For spin-independent interactions [63]:

$$\frac{d\sigma}{dq^2} = \frac{1}{\pi v^2} \left[Zf_\mathrm{p} + (A-Z)f_\mathrm{n}\right]^2 F^2(qr_\mathrm{n}) \tag{2.35}$$

Therefore, Eq. (2.34) and Eq. (2.35) give:

$$C_\mathrm{SI} = \frac{1}{\pi G_F^2} \left[Zf_\mathrm{p} + (A-Z)f_\mathrm{n}\right]^2 \tag{2.36}$$

where f_p and f_n are the values of the proton and neutron couplings to WIMPs respectively, and A and Z are the mass and atomic numbers of the target nucleus.

For spin-dependent interactions [63]:

$$\frac{d\sigma}{dq^2} = \frac{8G_F^2}{\pi v^2}\left[a_p\langle S_p\rangle + a_n\langle S_n\rangle\right]^2 \frac{(J+1)}{J} F^2(qr_n) \tag{2.37}$$

Therefore, Eq. (2.34) and Eq. (2.37) give:

$$C_{SD} = \frac{8}{\pi}\left[a_p\langle S_p\rangle + a_n\langle S_n\rangle\right]^2 \frac{(J+1)}{J} \tag{2.38}$$

where a_p and a_n are the model dependent values of the WIMP-proton and WIMP-neutron couplings respectively, and $\langle S_p\rangle$ and $\langle S_n\rangle$ are the spin expectation values of protons and neutrons within the nucleus. The resultant spin of the nucleus is given by J.

It is common for σ_A to be converted to a WIMP-nucleon cross-section σ_{W-N}, so that different target materials and theoretical predictions can be compared. In the case of spin-independent interactions, this is accomplished with [60]:

$$\sigma_{W-N_{SI}}\,[\text{pb}] = \left(\frac{M_p\,(M_W + M_A)}{AM_A\,(M_W + M_p)}\right)^2 \sigma_A\,[\text{pb}] \tag{2.39}$$

where M_p is the mass of the proton. WIMP-nucleon spin-independent exclusion limits from some of the experiments described earlier are shown in Figure 2.9. Currently, the XENON10 experiment [83] holds the best limit.

For spin-dependent interactions, the WIMP-proton and WIMP-neutron cross-sections are calculated separately. The WIMP-proton σ_{W-p} and WIMP-neutron σ_{W-n} cross-sections are given by [96]:

$$\sigma_{W-p}\,[\text{pb}] = \frac{4}{3}\sigma_A\,[\text{pb}]\left(\frac{M_p\,(M_W + M_A)}{M_A\,(M_W + M_p)}\right)^2 \frac{J}{\langle S_p\rangle\,(J+1)} \tag{2.40}$$

$$\sigma_{W-n}\,[\text{pb}] = \frac{4}{3}\sigma_A\,[\text{pb}]\left(\frac{M_n\,(M_W + M_A)}{M_A\,(M_W + M_n)}\right)^2 \frac{J}{\langle S_n\rangle\,(J+1)} \tag{2.41}$$

where M_n is the mass of the neutron. WIMP-proton and WIMP-neutron spin-dependent exclusion limits from some of the experiments described earlier, are shown in Figures 2.10(a) and 2.10(b) respectively. Currently, the KIMS [97] and CDMS-I [107] experiments hold the best spin-dependent WIMP-proton and WIMP-neutron limits respectively.

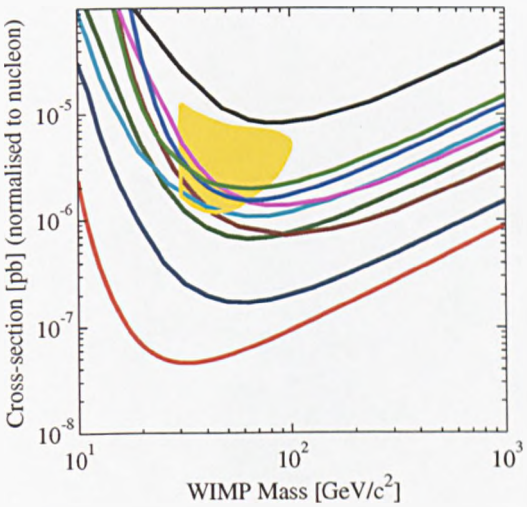

Figure 2.9: Current Experimental Exclusion Limits on Spin-Independent WIMP-Nucleon Cross-Sections as a Function of WIMP Mass. Limit curves from top to bottom are from: NaIAD [71] (black line), KIMS [97] (light green line), CRESST-I [98] (blue line), EDELWEISS-I [99] (purple line), ZEPLIN-I [79] (light blue line), WARP [100] (brown line), ZEPLIN-II [101] (dark green line), CDMS-I [102] (dark blue line) and XENON10 [83] (red line). The seasonal modulation signal from DAMA/NaI [103] is also shown (yellow area). Generated with [104].

2.6 Summary

Concordance cosmological theory hypothesises that the early history of the Universe is that of a violent birth followed by a brief period of very rapid expansion. A flat geometry is theoretically well-motivated, and under this assumption almost 30% of the Universe consists of matter. The majority of the remainder is from dark energy, which is causing the Universe to expand at an accelerating rate. Observational evidence from galactic rotation curves and gravitational lensing indicate that the contribution from matter is dominated by some non-baryonic particles, commonly referred to as dark matter. Big bang nucleosynthesis and measurements of the cosmic microwave background imply that the baryonic matter contribution is approximately 4% of the critical density.

Although there are many dark matter candidates, the Weakly Interacting Massive Particle (WIMP) has the most direct search experiments dedicated to it. From a particle physics perspective, if stable, the lightest supersymmetric particle is a well-motivated WIMP candidate. In the context of the simplest supersymmetric model, the Minimal

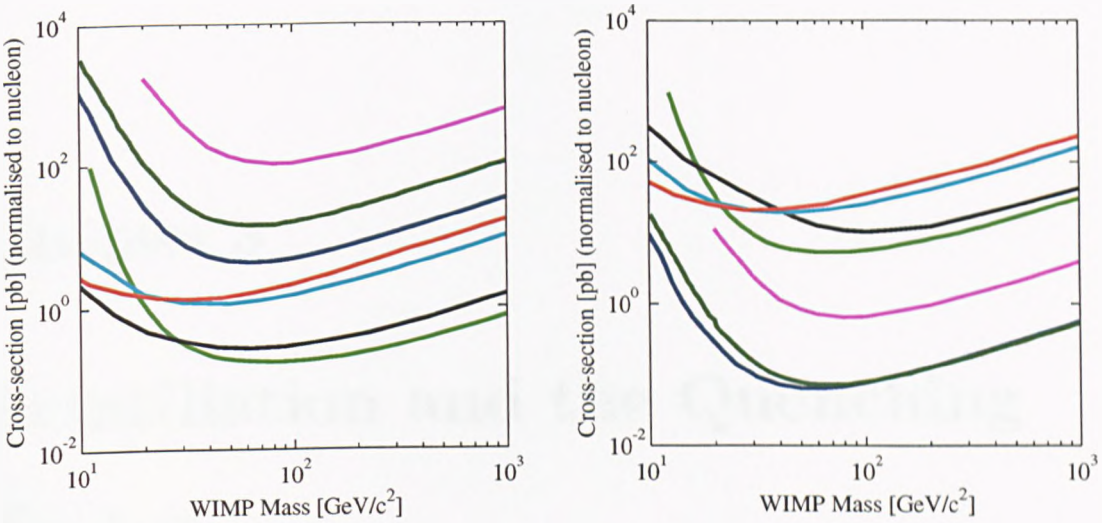

Figure 2.10: Current Experimental Exclusion Limits on Spin-Dependent (a) WIMP-Proton and (b) WIMP-Neutron Cross-Sections as a Function of WIMP Mass. Limit curves are from: EDELWEISS-I [105] (purple line), ZEPLIN-II [106] (dark green line), CDMS-I [107] (dark blue line), PICASSO [108] (red line), SIMPLE [109] (light blue line), NaIAD [71] (black line) and KIMS [97] (light green line). Generated with [104].

Supersymmetric Standard Model, the neutralino is a suitable candidate for detection in direct and indirect searches, and production on industrial scales in colliders.

The direct detection of dark matter is a rich and diverse field, and the recent introduction of hybrid detectors allows for better signal-background discrimination. The main backgrounds are from detector internal and external gamma and neutron sources, of which the latter is indistinguishable from a WIMP signal. Significant experimental effort is undertaken to reduce the contribution to background through shielding and the use of radiopure materials during detector fabrication. In the absence of a signal, a limit on the WIMP-nucleon cross-section can be derived from the differential event rate at recoil energies of interest. These are typically below 50 keV due to the form factor, which results in the sharp decrease in the event rate at higher recoil energies.

Chapter 3

Scintillation and the Quenching Factor

A charged particle traversing a medium can interact with target electrons, depositing some or all of its energy. The absorbed energy can then be released through de-excitation of these electrons, and detected. In scintillating media, the excess energy is lost through the process of photon emission, and these quantised particles of light can be detected with instruments such as Photomultiplier Tubes (PMTs). These instruments convert the light signal to an electric current, through a chain of resistors, and the resulting voltage pulse can be analysed to derive information about signal photons.

The process of scintillation varies significantly depending on the target medium. In the scope of dark matter experiments, three types of scintillators are used. Organic scintillators are typically used in liquid form as active veto systems around the main detector. Inorganic crystals and, more recently, liquid noble gases are primarily used as target materials. The first section of this chapter outlines the scintillation processes in these materials.

Traditionally, dark matter experiments that make use of scintillators as target materials use PMTs to detect photoemission. However, recent research and development efforts have been made to determine the suitability of an alternative light detection device, the photodiode, in dark matter searches. The operating principles behind these two devices are also discussed in this chapter.

Gamma-rays and neutrons are the major sources of background for dark matter experiments. Neutrons are especially difficult to separate from WIMP events, as they both induce nuclear recoils, and hence the subsequent scintillation light pulses are similar. Due

to the importance of these particles as potential backgrounds in all dark matter experiments that use scintillators as their active medium, the different interaction mechanisms of neutral particles are also discussed.

Finally, a discussion of light quenching in scintillators is given, together with a discription of the quenching factor correction, which was introduced in Section 2.5.1. Theoretical results for the value of this correction are presented, in addition to the author's calculation from a Monte Carlo simulation.

3.1 Scintillation in Organic Liquids

The chemical structure of organic molecules is dependent on the electronic configuration of the carbon atom in its ground state, which is ($1s^2 2s^2 2p^2$). The indices represent the number of electrons that form each shell. The valence electrons, which form chemical bonds with other atoms, are on orbitals 2s and 2p. To form an organic compound, one of the electrons on orbital 2s is excited into a 2p state, giving rise to a new electronic configuration of ($1s^2 2s 2p^3$). Carbon atoms can then bond with hydrogen to form saturated hydrocarbons such as methane (CH_4), doubly-bonded molecules such as ethene (C_2H_4), or triply-bonded molecules such as acetylene (C_2H_2).

Saturated hydrocarbons are composed of single bonds between carbon and hydrogen atoms. They are formed when at least one valence orbital forms a bond with the valence electron in a hydrogen atom. The other bonds can either be with other carbon or hydrogen atoms. These are collectively known as σ-bonds, and do not form excited states that emit light on de-excitation to the ground state. Hence, saturated hydrocarbons do not scintillate.

Alternatively, an extra carbon-carbon bond can be formed between valence electrons in the p-orbital. This is known as a π-bond. The electrons that form the π-bond in doubly-bonded molecules, interact to form two completely delocalised orbitals. Luminescence originates from the excited states of these orbitals.

Finally, a carbon atom can form a triple bond with another of carbon, in which three valence electrons from each carbon atom are shared. As two of the shared pairs must be from electrons in the p-orbital, triply-bonded molecules consist of two π-bonds, and so they also scintillate.

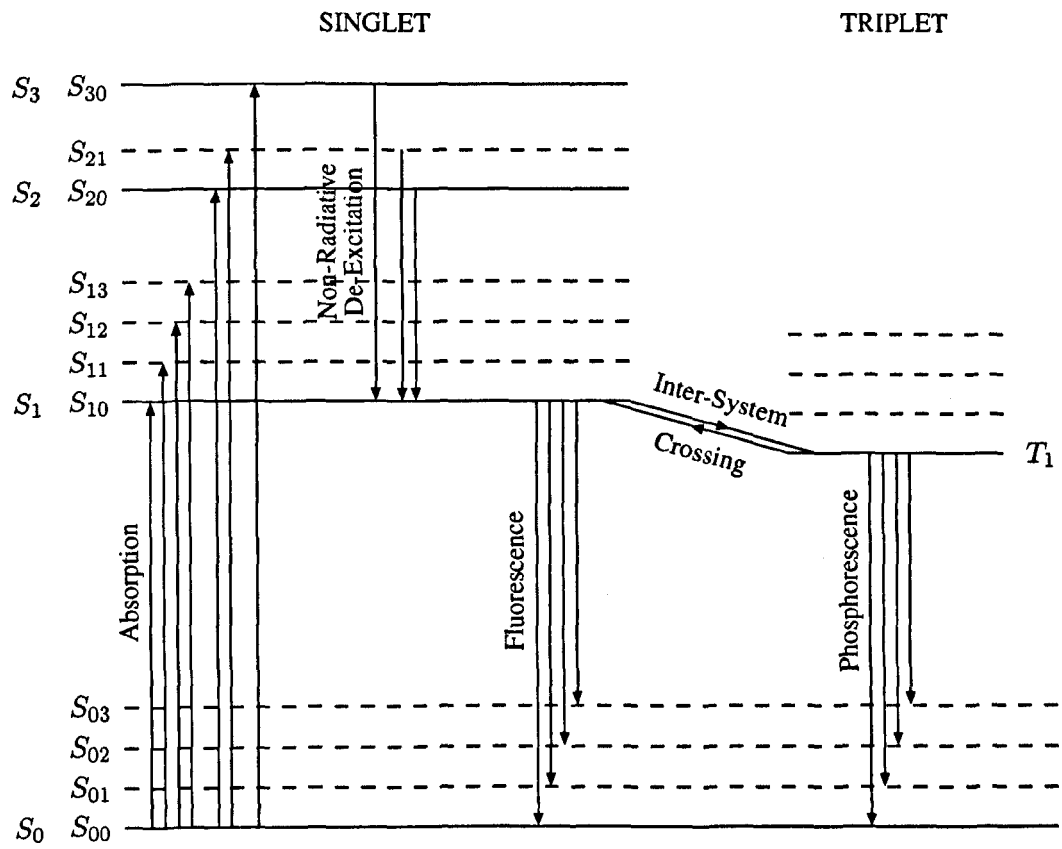

Figure 3.1: π-Electronic Energy Levels of an Organic Molecule. S_0 is the ground state; S_1, S_2 and S_3 are the excited spin-0 singlet states; and T_1 is an excited spin-$\hbar$ triplet state. Each level is divided into substates. The absorption of kinetic energy leads to the excitation of electrons. Electrons in singlet states higher than S_1 de-excite through radiationless transitions. Scintillation photons are released through S_1 to S_0 transitions. Alternatively, a transfer to T_1 can result in phosphorescence, or the restoration of the S_1 state, and hence delayed fluorescence.

The π-electronic energy levels are shown in Figure 3.1, where S_0 is the ground state, S_1, $S_2, \ldots S_n$ are the excited spin-0 singlet states and T_1, $T_2, \ldots T_n$ are the excited spin-$\hbar$ triplet states. Each of these levels is subdivided into substates that correspond to the vibrational states of the molecule. These are represented by the second subscript j in S_{ij}.

A particle traversing the medium results in the absorption of kinetic energy, and the subsequent excitation of electrons as shown in Figure 3.1. Higher singlet electron states quickly de-excite to the S_{10} level though non-radiative transfers. Scintillation light is released when an electron returns to one of the substates at ground level from S_{10}. The

intensity $I(t)$ of scintillation light released by this process decays exponentially with time t:

$$I(t) = I_0 e^{-\frac{t}{\tau}} \tag{3.1}$$

where I_0 is the intensity at time $t = 0$, and τ is the decay constant.

Alternatively, the electron can transfer to the triplet state T_1 by inter-system crossing, as shown in Figure 3.1. Although the transition from T_1 to the ground state singlet S_0 results in the emission of phosphorescence, interaction with another excited molecule can result in the restoration of a S_1 state. This results in delayed fluorescence emission on the time scale of the interaction. This delayed scintillation light also decays exponentially, and assuming that its intensity is equal to that of the prompt component, it can be factored into Eq. (3.1):

$$I(t) = I_0 \left(e^{-\frac{t}{\tau_1}} + e^{-\frac{t}{\tau_2}} \right) \tag{3.2}$$

where τ_1 and τ_2 are the decay constants for the prompt and delayed fluorescence respectively. Due to their relative speeds, the prompt and delayed scintillation pulses are called the fast and slow components of the scintillator.

Excitatation to the triplet state is a two stage process, implying that it is less probable than the simple excitation to and de-excitation from a singlet state. So the intensity of light from the fast component is larger than that from the slow component. As explained above, two excited molecules in a triplet state can result in the emission of phosphorescence and delayed scintillation light. The cross-section for this process increases in relation to the number of molecules that occupy a triplet state. Therefore, particles that deposit more of their energy over a shorter distance (in other words, they have a large $\frac{dE}{dx}$ ratio, where E is the energy deposited and x is the distance travelled), will result in more of these reactions. This in turn leads to more enhanced emission in the slow component [110]. The intensities of the fast and slow component, A and B respectively, can be factored into Eq. (3.2):

$$I(t) = Ae^{-\frac{t}{\tau_1}} + Be^{-\frac{t}{\tau_2}} \tag{3.3}$$

where the ratio $\frac{B}{A}$ will be greater for particles with a higher $\frac{dE}{dx}$ ratio, such as neutrons, than for those with a lower ratio, such as gamma-rays. This is known as pulse shape

discrimination, and can be used to discern high energy electron and nuclear recoils in organic scintillators.

3.2 Scintillation in Inorganic Crystals

Although the cross-section for neutron capture in organic scintillators is very high and they are relatively inexpensive, there are significant disadvantages with using them as target materials in direct dark matter searches. They are not favoured due to their poor light yield (number of photons emitted per unit energy deposited), and the significant quenching of light from nuclear recoils. For example, the Nuclear Enterprise NE224 scintillator (C_6F_6) has a carbon recoil efficiency relative to electron recoil of 0.7% at 1220 keV [111]. This means that, if energy calibration is performed with a source of 1220 keV gamma-rays, a nuclear recoil of the same energy will be measured as one of energy 8.54 keV. This makes pulse shape discrimination harder at the lower energies that are relevant to dark matter searches. They are also difficult to deploy underground due to the low flashpoint of most scintillators. However, those liquid organic scintillators with a higher flashpoint are typically installed in containers around an underground detector for the purpose of neutron rejection.

The first practical inorganic crystal scintillator was created by adding a trace of thallium iodide to crystalline sodium iodide [112]. This resulted in a significant improvement over the light yield obtained from the traditional organic scintillators used at the time. Sodium iodide (NaI(Tl)) remains prevalent in the field, and was the first scintillator to be used in dark matter search experiments [66].

With reference to Figure 3.2, in an inorganic crystal, electrons located in the valence band are bonded at lattice sites, whereas those in the conduction band are free to move around the crystal. Absorption of energy, from a particle passing through and depositing some of its energy in the crystal, results in some electrons in the valence band receiving energy to break free from the covalent bonds between neighbouring atoms. Some will have enough energy to cross the band gap, and this process is known as ionisation. This leaves a hole in the valence band, which is filled when an electron de-excites and releases a photon.

However, in inorganic crystals this is a very inefficient process, and the band gap tends to be too large to result in photon emission within the visible range. To enhance

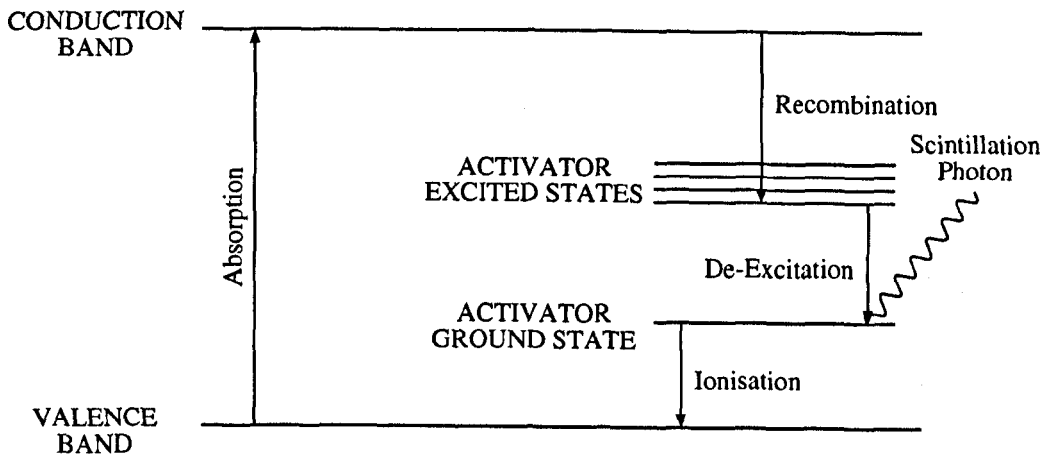

Figure 3.2: Energy Band Structure of a Doped Inorganic Scintillation Crystal. The absorption of kinetic energy results in electrons receiving enough energy to migrate to the conduction band. An electron from the activator ground state moves to fill the positive hole in the valence band, leaving the activator site ionised. A free electron in the conduction band drops into the activator site and de-excites through photon emission.

the number of visible photons emitted, small amounts of an impurity are added to the scintillator to create special sites in the crystal lattice at which the normal bond structure is modified. This results in new energy states created between the valence and conduction bands, in what is termed the forbidden gap. As the energy is less than that between the valence and conduction bands, an electron can now de-excite through these forbidden states, giving rise to a visible photon as shown in Figure 3.2. These impurities are called activators, and are written in brackets after the chemical formula for the crystal. For example, NaI(Tl) is thallium activated sodium iodide.

Positive holes, from the electron-hole pairs created by an incident particle, drift toward the location of the activator sites and ionise them, as the ionisation energy of the impurity is less than that of a lattice site. Electrons in the conduction band drift throughout the crystal until they come into contact with an ionised activator. An electron can then drop into the activator site, and de-excite, releasing a photon [113].

A second process leading to visible scintillation photons exists. An electron, upon arrival at an activator site, can create an excited configuration whose transition to the ground state is forbidden. The electron then requires additional energy to excite it to a slightly higher state, from which transitions to the ground level are possible. This process

gives rise to the slow component seen in some inorganic crystals, and can also cause after-pulsing [114].

3.3 Scintillation in Liquid Noble Gases

Radiation incident on liquid noble gases, such as xenon (Xe) and argon (Ar), can interact with a target particle. When the deposited energy is sufficient, this recoiling primary particle can undergo secondary collisions with other atoms, resulting in their subsequent excitation or ionisation.

Electric and nuclear recoils result in the emission of scintillation light through the de-excitation of the two lowest excited molecular states [115]:

$$\begin{aligned} {}^1\Sigma_u^+ &\longrightarrow {}^1\Sigma_g^+ \\ {}^3\Sigma_u^+ &\longrightarrow {}^1\Sigma_g^+ \end{aligned} \tag{3.4}$$

where ${}^1\Sigma_u^+$ is the singlet state of an excited dimer and ${}^3\Sigma_u^+$ is its triplet state. These states can be produced through either excitation or ionisation.

Primary charged particles, or secondary electrons, interact with noble gas atoms exciting electrons to higher energy states. Excited electrons leave behind a hole in the shell they were previously occupying. These electron-hole pairs are bound together by the Coulomb force, and are known as excitons (for example, Xe^* in xenon). In crystals, such as germanium and silicon, these excitons are free to move around and transport energy. However, in liquid noble gases the mean lifetime of these electrons is much shorter, at around 1-4 ps [116] in liquid xenon, whereupon they form the metastable excimer state Xe_2^*. This process is known as self-trapping. The two lowest lying electronic energy levels of this excimer decay to the ground state are shown in Eq. (3.4), resulting in the emission of photons [117]:

$$\begin{aligned} Xe^* + Xe &\longrightarrow Xe_2^* \\ Xe_2^* &\longrightarrow 2Xe + h\nu \end{aligned} \tag{3.5}$$

where $h\nu$ represents an ultraviolet photon. This is the process for excitation.

As primary particles, or secondary electrons, interact with the detector medium, they can also ionise the target atoms producing electron-hole pairs. This results in the formation of the ion Xe^+ and subsequent released electron e^-. The ion then interacts with a nucleus,

forming the molecular ion Xe_2^+ and the released electrons lose kinetic energy through the production of excitons (electron-hole pairs), and heat. These electrons recombine with the molecular ion to form the double-exciton state Xe^{**}. This then loses heat through non-radiative transfer processes, resulting in the excimer Xe^*. Scintillation light is then produced in the same way as described above [117]:

$$\begin{aligned} Xe^+ + Xe &\longrightarrow Xe_2^+ \\ Xe_2^+ + e^- &\longrightarrow Xe^{**} + Xe \\ Xe^{**} &\longrightarrow Xe^* + \text{heat} \\ Xe^* + Xe &\longrightarrow Xe_2^* \\ Xe_2^* &\longrightarrow 2Xe + h\nu \end{aligned} \tag{3.6}$$

The extra steps preceding the emission of ultraviolet photons in the ionisation mechanism mean that the radiative lifetime for this process is longer than that for excitation.

In xenon, the two lowest excited molecular states $^1\Sigma_u^+$ and $^3\Sigma_u^+$ decay with radiative lifetimes of 4.5 ns and 103 ns respectively [118]. In xenon, measured lifetimes for the fast $^1\Sigma_u^+$ and slow components $^3\Sigma_u^+$ are 4.3 ± 0.6 ns and 22 ± 2 ns respectively from alpha-induced recoils [119], and 2.2 ± 0.3 ns and 27 ± 1 ns for recoiling electrons [117]. Additionally, as electrons receive more kinetic energy from a direct particle interaction, a longer recombination time of approximately 15 ns results [117]. Combining this information, it is possible to use pulse shape analysis to discriminate between nuclear (decay constant of approximately 20 ns) and electron recoils (decay constant of approximately 40 ns). The exact values of these decay constants depend on the fitting methods employed.

In the presence of an electric field, as with two-phase detectors where the liquid and gas phases co-exist, this behaviour changes. Free electrons can now be removed from the interaction site, meaning that some will fail to undergo recombination, and hence the intensity of the scintillation signal from an event decreases. It has been shown that an increasing electric field strength results in more electrons drifting through the liquid phase [120]. Hence, the expected intensity of the scintillation signal from events is smaller in the presence of an electric field. Additionally, as electrons receive more kinetic energy from direct particle interactions, the expected scintillation signal for these events decreases with increasing electric field strength [121]. Nuclear recoils are affected to a lesser degree [121].

The supression of recombination also implies that decay times should be shorter, re-

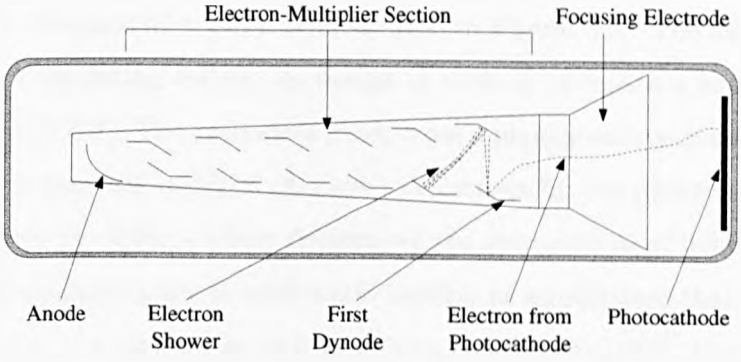

Figure 3.3: Schematic of a Typical Photomultiplier Tube. The first stages of an electron shower are shown.

sulting in scintillation pulses of smaller width. Thus, effective discrimination with the scintillation pulse only in two-phase detectors becomes difficult.

The higher the electric field strength at the liquid-gas boundary, the greater the probability of extracting an electron. This directly affects the magnitude of the signal from electroluminescence, which is effectively a measure of the ionisation of the event. This is a more powerful discriminant than the pulse shape technique outlined above. Due to the sustained presence of this field, once extracted, these electrons continue to drift through the gas phase on their original trajectory, ionising surrounding atoms. Electroluminescence occurs in the same way outlined in Eq. (3.6).

3.4 Devices for Detection of Scintillation Light

In order to take advantage of the properties of scintillators, an appropriate device needs to be selected to detect photoemission. Additionally, this device must convert a scintillation signal into one that can be sent through wires to hardware electronics. In this section, two light collection devices that are the mainstay of particle physics experiments are briefly described.

3.4.1 Photomultiplier Tubes

The most widely used light collection devices in particle physics are Photomultiplier Tubes (PMTs). They are, in essence, evacuated glass tubes that detect a light signal and convert it to an electric current that can be collected by data acquisition systems.

A schematic diagram of a PMT is illustrated in Figure 3.3. The dynodes are maintained at a fixed operating voltage by means of a chain of resistors known as a Voltage Divider Network (VDN). The cathode is made from a photosensitive material, such as caesium (Cs), which converts incident photons to electrons by the photoelectric effect. The optical transmissivity of the window determines the wavelengths of light that the tube is sensitive to. Borosilicate glass is used when looking at scintillators that emit photons in the visible band of the electromagnetic spectrum, such as NaI(Tl). However, special ultraviolet transmissive glass is required for the transmission of xenon scintillation photons, and magnesium fluoride is typically used in liquid argon experiments.

Incident photons need to be of a minimum energy to induce electron emission in the photocathode layer:

$$h\nu \geq \phi \tag{3.7}$$

where the energy of the photon is given by the product of its frequency ν and Planck's constant h. The work function ϕ is the minimum energy required to remove an electron from the photocathode, and differs between materials.

With reference to Figure 3.3, the electrons accelerate as a result of the potential difference between the cathode and first dynode. Upon impact, the electron transfers some of its energy to the electrons that form this dynode, resulting in the emission of secondary electrons. These electrons accelerate toward the next dynode, and the process is repeated, resulting in an avalanche of electrons arriving at the anode. At the anode, the total electron charge is collected and converted to an electric current that can be amplified. The measure of charge collected at the anode from one incident photon causing the emission of one electron from the photocathode is called the single photoelectron response.

The degree to which the charge is amplified can be quantified as the gain. The gain G of a PMT and VDN configuration is the ratio of the charge generated over the length of the dynode chain by one photoelectron Q to the electron charge C:

$$G = \frac{Q}{C} = \frac{1}{C}\int I(t)\cdot dt = \frac{1}{CR}\int V(t)\cdot dt \tag{3.8}$$

where $C = 1.6 \times 10^{-19}$ C, the current is $I(t) = \frac{V(t)}{R}$, and $V(t)\cdot dt$ is the area underneath a single photoelectron pulse. The resistance of the load is given by R.

Once measured, the gain of the PMT can be compared with the manufacturer's value to determine if the tube is working correctly at this operating voltage. It is clear from Eq. (3.8) that increasing the operating voltage results in higher gain. However, this comes at the price of increased noise as a result of the stronger electric fields between the dynodes. This can lead to electrical breakdown, resulting in electrons being stripped off the electrodes and accelerated through the chain, causing excess current. These are called dark pulses, and affect the linearity of the photomultiplier.

Not all incident photons will give rise to electron emission. The ratio of incident photons resulting in the emission of electrons to the total number of photons is the quantum efficiency of the PMT. For most PMTs, this is typically in the order of 30%.

3.4.2 Photodiodes

As an alternative to PMTs, photodiodes are semiconductor devices that consist of p-n junctions typically made from silicon or germanium. A p-n junction is formed by placing a semiconductor with an excess number of free positive charge carriers (p-type) next to that with an excess number of free negative charge carriers (n-type). In the junction between them, electrical charge carriers from both semiconductors attract each other and recombine, hence creating an insulator. This area is known as the depletion region or zone. As the p-type semiconductor has lost its free positive charge carriers to the depletion zone, it is now negatively charged. The opposite is true for the n-type semiconductor.

When a photon strikes the diode's depleted region, it can excite an electron as long as it has enough energy to do so via the photoelectric effect (Eq. (3.7)). This creates an electron-hole pair. Due to the presence of positively and negatively charged regions on either side of the depletion zone, the electron will move towards the n-type semiconductor, and the positive hole will drift in the opposite direction. This results in a current, which can be harnessed by connecting an external circuit between the n- and p-layers.

The signal can be amplified by using avalanche photodiodes. Connecting the p-layer to the negative terminal of a power supply pulls the free positive holes in the p-type semiconductor away from the depletion zone. If this is done while connecting the n-layer to the opposite polarity of the power supply, the size of the depletion zone increases. Applying a higher voltage causes the depletion region to widen, increasing the electric field until the junction breaks down. This electrical breakdown occurs when the electric

field across an insulator is so strong, that the few free electrons available are accelerated to such an extent that they can excite other electrons to the conduction band. These newly generated electrons serve to amplify the signal.

Photodiodes compare favourably with PMTs. They are relatively inexpensive, have a larger range of spectral responses and much higher quantum efficiency (typically 80%). However, even the gain of avalanche photodiodes cannot match those of photomultiplier tubes, and they have smaller sensitive areas, meaning that many need to be used to cover a large area, which can complicate data collection. Although direct dark matter search experiments do not currently make use of photodiodes, they have been investigated in liquid xenon by the XENON collaboration [122]. Additionally, signals from low energy electron recoils have been investigated in inorganic crystals [123].

3.5 Interaction of Neutral Particles in Matter

Charged particles traversing a detector will interact with target atoms via the Coulomb force, slowing down gradually through continuous collisions. Electrons traversing a material will primarily ionise and excite target electrons in this way. Due to their identical masses, a large fraction of the initial electron energy can be lost in a single collision, resulting in a very tortuous and eratic path through a detector. They quickly dissipate all their energy within a very short distance.

As neutral particles carry no electric charge, they cannot interact in matter by means of the Coulomb force. As a consequence, they tend to have longer path lengths before colliding with target atoms. In the context of the direct dark matter searches outlined in Section 2.5, the neutral gamma-ray and neutron particles are the major sources of background for most experiments. The interaction mechanisms for these particles in the energy regime relevant to these experiments is outlined here.

3.5.1 Gamma-Rays

There are three main mechanisms that lead to some degree of energy loss in matter for gamma-rays: photoelectric absorption; Compton scattering; and pair production. These are illustrated in Figure 3.4, and their typical cross-sections as a function of energy in sodium iodide and xenon are shown in Figure 3.5. In marked contrast to the mechanisms

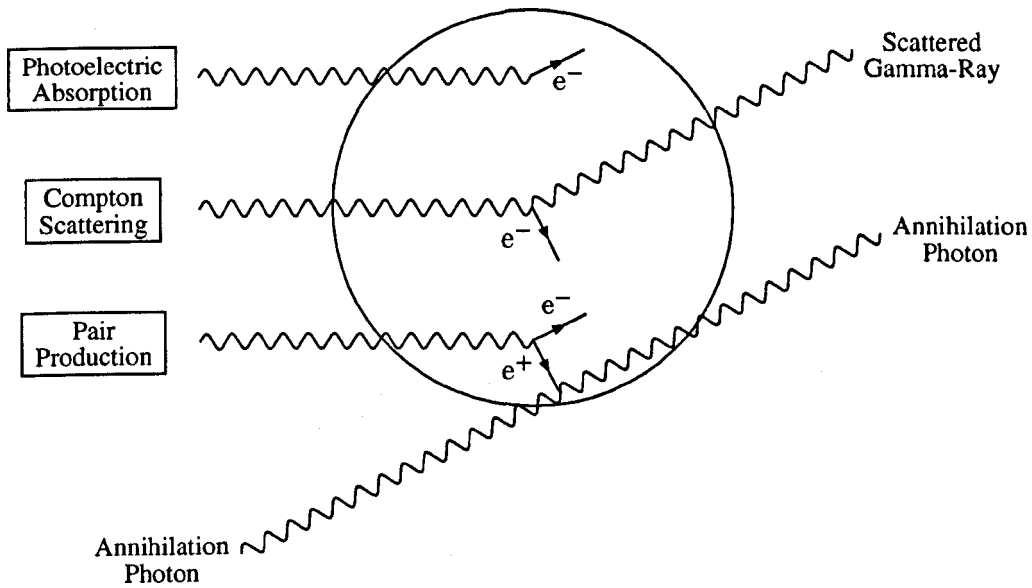

Figure 3.4: Interaction of Gamma-Rays in Matter. The process of photoelectric absorption results in the entire energy of the incident photon being transferred to an atom, leading to photoelectron emission. The incident photon deposits some energy in the target in Compton scattering, altering its trajectory. For gamma-rays of sufficient energy, an electron-positron pair can be created due to the strong electric field present near a target nucleus. The positron travels a short distance before annihilating with a target electron, resulting in two almost back-to-back photons.

responsible for charged particle interactions in a target, gamma-rays interactions tend to cause the destruction of the gamma-ray, or its scattering at a sharp angle.

Photoelectric Absorption

All the energy of an incident photon can be transferred to an electron in one of the target atom's shells. This results in the disappearance of the photon, and for gamma-rays of sufficient energy a photoelectron of energy E_e can be ejected from the atom:

$$E_e = h\nu - E_b \tag{3.9}$$

where $h\nu$ is the incident photon energy and E_b is the binding energy of the photoelectron in its orginal shell. This process is known as photoelectric absorption, and is shown in Figure 3.4.

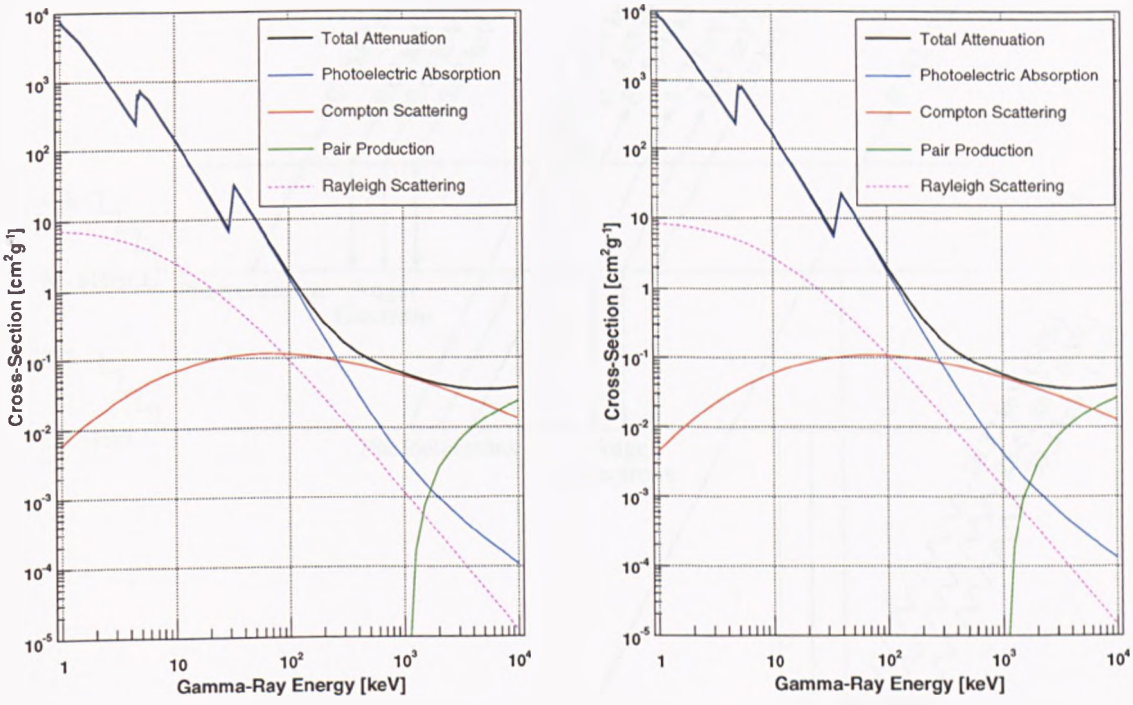

Figure 3.5: Cross-Sections for Gamma Interactions in: (a) Sodium Iodide; and (b) Xenon. Abrupt edges can be seen at the L- and K-shell binding energies for: (a) iodine; and (b) xenon. Gamma-rays of energy less than approximately 200 keV undergo photoelectric absorption in the target. At higher energies, Compton scattering dominates until the cross-section for pair production eventually overtakes it. The cross-section for gamma-rays is dependent on the atomic number of the target element, and hence electrons surrounding iodine nuclei dominate in (a). As the atomic numbers of iodine and xenon are similar, the behaviour seen in both plots is almost identical. Data taken from [124].

The photoelectron leaves behind an ionised atom, which results in the capture of a free electron and/or the internal rearrangement of electrons from other shells. With reference to Figure 3.6, electrons moving from the L- and M-shells to the K-shell in iodine atoms will make the transition through K_α and K_β X-ray emission respectively. These X-rays are of low enough energy to undergo photoelectric absorption in the detector. Alternatively, they can escape detection, resulting in some missing energy.

In some cases, another electron may be emitted instead, as shown in Figure 3.6. The excitation energy of an atom can be transferred to an electron in an outer shell, resulting

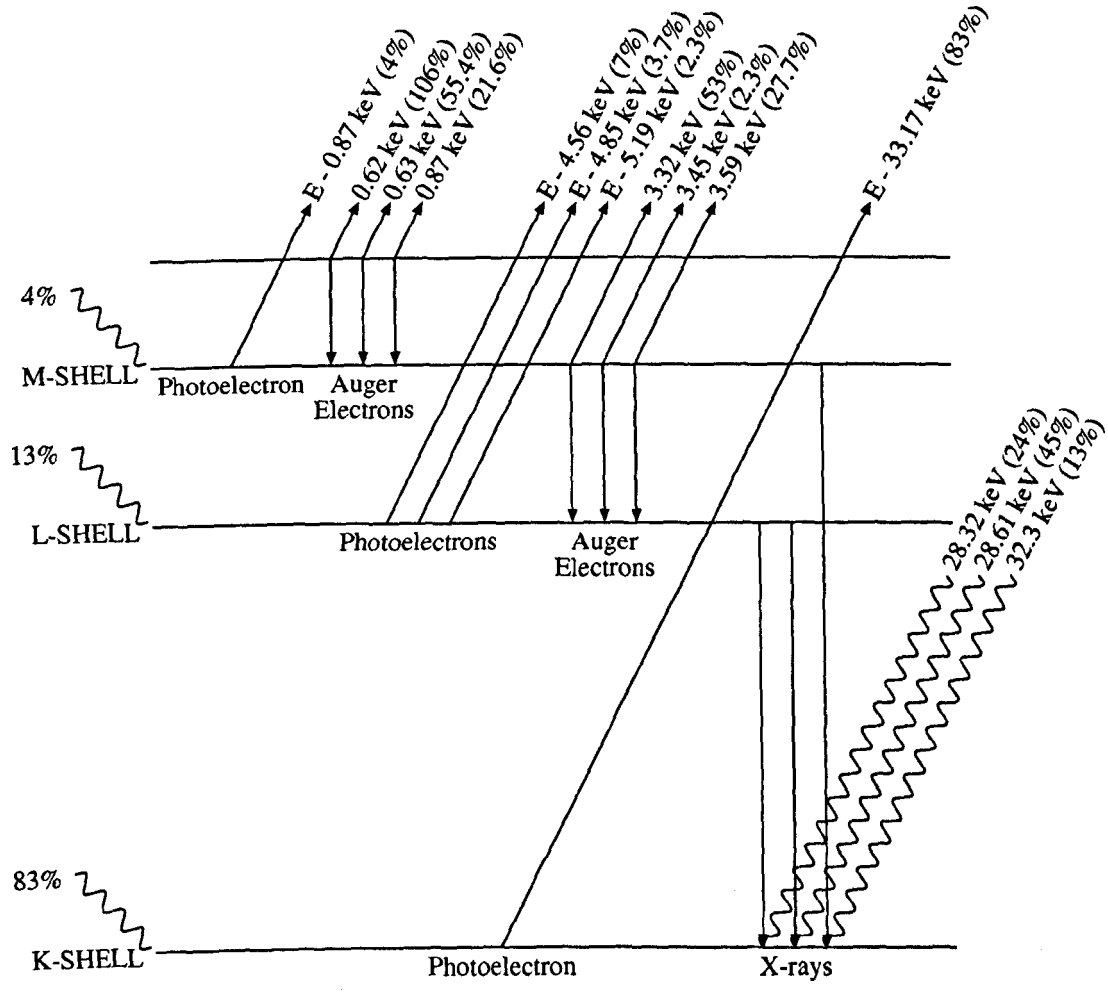

Figure 3.6: Photoelectric Absorption of an Incident Gamma-Ray in NaI(Tl). All the possible origins and electron and photon emission following the photoelectric absorption of a gamma-ray with energy greater than the K-shell binding energy of iodine (33.17 keV) are shown. Percentage probabilities and energies are taken from [125].

in its ejection. This is called an Auger electron.

The complexity of this process is clearly shown in Figure 3.6, where gamma-rays of energy greater than the K-shell binding energy of iodine (33.17 keV) have many different final states. For comparison, 86% of energetic gamma-rays above the K-shell binding energy of xenon (34.56 keV) will interact with the K-shell. Of these interactions, 87.5% will result in X-ray emission, while the remainder will de-excite through Auger electrons [126].

There are two abrupt edges in the photoelectric cross-section spectra at low energies in Figure 3.5. These correspond to the respective L- and K-shell binding energies in iodine (Figure 3.5(a)) and xenon (Figure 3.5(b)). At each binding energy, the emission of a

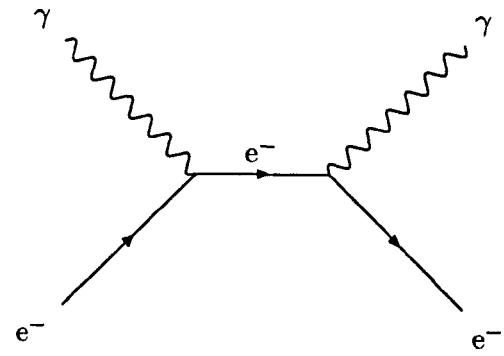

Figure 3.7: Feynman Diagram for Compton Scattering. An incident gamma-ray will scatter off a target electron elastically, depositing some its energy, as shown in the s-channel process here.

photoelectron becomes possible, resulting in a sharp increase in the cross-section.

Compton Scattering

Alternatively, at higher incident energies, the path of the gamma-ray can be altered as it recoils off a target electron. Some of the initial energy is deposited in the target material as a result of the collision. As shown in Figure 3.5, the cross-section for this process dominates at gamma-ray energies typical of radioactive isotopes. The Feynman diagram for this process is shown in Figure 3.7.

With reference to Figure 3.8, the energy of the scattered gamma-ray $h\nu'$ is a function of the scattering angle θ:

$$h\nu' = \frac{h\nu}{1 + \frac{h\nu}{m_e c^2}(1 - \cos\theta)} \tag{3.10}$$

where $h\nu$ is the energy of the incident gamma-ray, and $m_e c^2$ is the rest mass energy of the electron.

Unlike photoelectric absorption, where all of the incident gamma energy is deposited in the target, Compton scattering results in a wide continuum of possible energy depositions. Using Eq. (3.10), the kinetic energy of the recoil electron E_e in Figure 3.8 is:

$$E_e = h\nu - h\nu' = \frac{\frac{(h\nu)^2}{m_e c^2}(1 - \cos\theta)}{1 + \frac{h\nu}{m_e c^2}(1 - \cos\theta)} \tag{3.11}$$

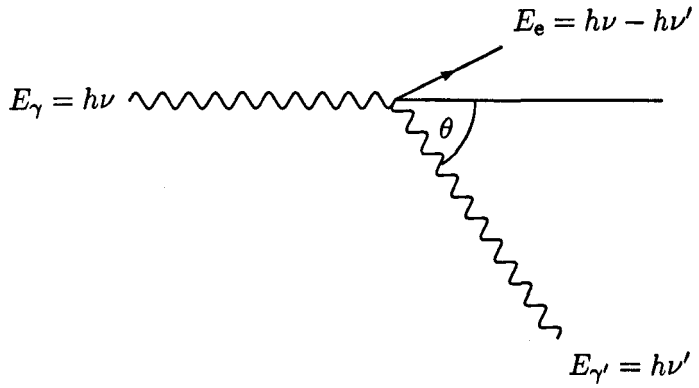

Figure 3.8: Illustration of Compton Scattering. An incident photon of energy $h\nu$, scatters off a target electron. As a result of the collision, the scattered photon changes direction relative to its original path, and now has energy $h\nu'$. From conservation of energy, the energy of the recoil electron is the difference between the intial and final energy of the photon.

The distribution of Eq. (3.11) for gamma-rays of different incident energies is shown in Figure 3.9. The change in the energy of the recoil electron is far more pronounced for gammas of higher initial energy. The maximum energy is transferred to the recoil electron when the scattering angle is 180°, or π radians, which sends the scattered photon back toward its direction of origin. Substituting this value for θ into Eq. (3.11) yields:

$$E_{e_{max}} = \frac{\frac{(h\nu)^2}{m_e c^2}}{1 + \frac{h\nu}{m_e c^2}} \tag{3.12}$$

Therefore, the largest amount of energy that a single Compton scatter can deposit in a detector is given by Eq. (3.12). This is also known as the Compton edge.

The cross-section for Compton scattering increases with the number of available electrons in a target material, or in other words with the atomic number Z. The angular distribution is predicted with the Klein-Nishina differential scattering cross-section formula:

$$\frac{d\sigma}{d\Omega} = \frac{Zr_e^2}{2}\left(\frac{1}{1+\alpha(1-\cos\theta)}\right)^2\left(1+\cos^2\theta+\frac{\alpha^2(1-\cos\theta)^2}{1+\alpha(1-\cos\theta)}\right) \tag{3.13}$$

where $\alpha = \frac{h\nu}{m_e c^2}$ and r_e is the classical electron radius. This distribution is shown graphically in Figure 3.10, and is clearly not isotropic. Gamma-rays with higher initial energies

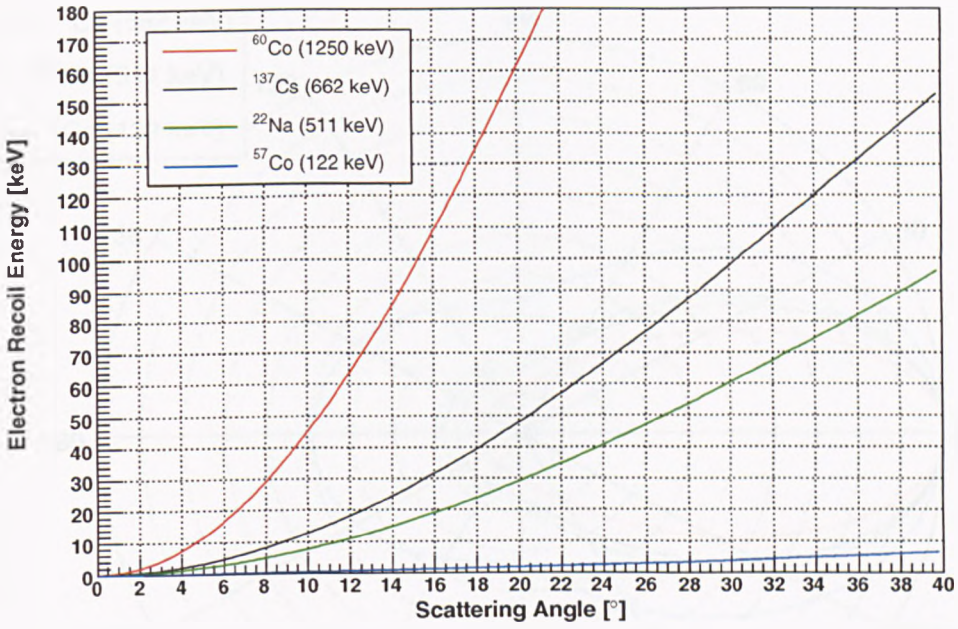

Figure 3.9: Electron Recoil Energy as a Function of Compton Scattering Angle. The distributions of Eq. (3.11) show that the electron recoil energy increases with scattering angle. Additionally, this effect is more pronounced with gamma-rays of higher intial energy.

are more likely to scatter in the forward direction, and this bias increases with energy.

Pair Production

When the energy of the incident gamma-ray exceeds twice the rest mass of the electron ($2m_ec^2$), pair production of electron-positron pairs becomes kinematically possible. This occurs when such a gamma-ray is exposed to the intense electric field near the protons in a target nucleus. As is clear from Figure 3.5, pair production begins to dominate at energies of the order of several MeV. The emitted positron has a very short mean free path before encountering a target electron and annihilating to create two photons of energy m_ec^2 each. The entire process is shown in Figure 3.4, and the Feynman diagram for electron-positron annihilation is illustrated in Figure 3.11.

As a minimum energy of $2m_ec^2$ is required to create an electron-positron pair, the kinetic energies of the resultant electron E_{e^-} and positron E_{e^+} are given by:

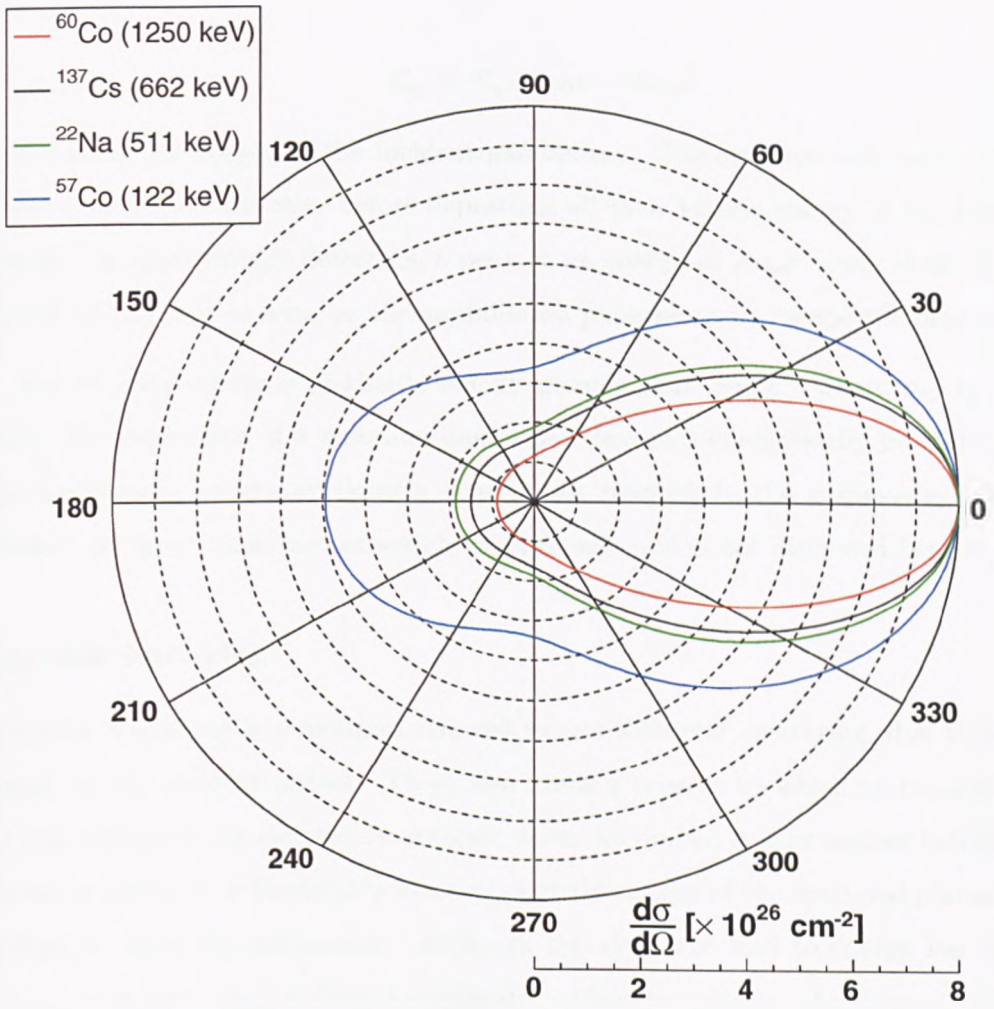

Figure 3.10: Directional Characteristics of Compton Scattering in Hydrogen (atomic number $Z = 1$). Incident gamma-rays from various radioisotopes can be scattered in any direction. However, at higher incident gamma-ray energies, they are preferentially scattered in the forward direction, as defined by Eq. (3.13).

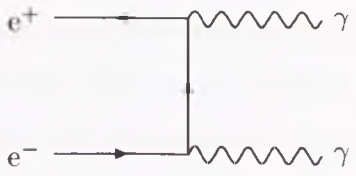

Figure 3.11: Feynman Diagram for Electron-Positron Annihilation. If the energy of an incident gamma-ray is greater than twice the rest mass of an electron ($2m_ec^2$), it becomes kinematically possible for it to split into a positron-electron pair. The positron then travels a short distance before interacting with a target electron in the t-channel process shown here.

$$E_{e^-} + E_{e^+} = h\nu - 2m_e c^2 \tag{3.14}$$

where $h\nu$ is the energy of the incident gamma-ray. The electron and positron typically travel a very short distance before depositing all their kinetic energy in the detector. As a result, in small enough detectors, a peak at an energy of $2m_e c^2$ lower than the incident photon energy can be seen, as the annihilation photons easily escape the detector.

For incident photons of kinetic energy greater than $2m_\mu c^2$, where m_μ is the muon mass, the production of a muon-antimuon pair becomes energetically possible. However this happens in an energy domain that is not relevant to the gamma-ray background incident on direct dark matter search experiments, and is not discussed here.

Rayleigh Scattering

Compton scattering is sometimes referred to as incoherent scattering, due to the loss of energy by the incident photon. There also exists a process by which an incident gamma-ray can scatter off the electrons in a target atom, leaving no energy deposit behind. This is known as coherent or Rayleigh scattering, and the energy of the scattered photon remains unchanged after the interaction. Although this does not lead to energy loss, the angle of the gamma-ray can be altered significantly after its collision. As shown in Figure 3.5, Rayleigh scattering does not dominate at any incident photon energies.

3.5.2 Neutrons

Like gamma-rays, neutrons are electrically neutral particles that cannot interact in matter by the Coloumb force. Additionally, they may not interact at all while traversing through a detector. In contrast with gamma-rays, neutrons penetrate the electron clouds and interact with the nucleus of a target atom. As a result of which they can either be scattered or absorbed. The total scattering and absorption cross-sections for ^{1}H (hydrogen), ^{23}Na (sodium) and ^{131}Xe (xenon) are shown in Figure 3.12.

Scattering

A neutron can collide with a nucleus and transfer some of its energy to it. The maximum energy that can be deposited by a neutron occurs in a collision with another neutron or

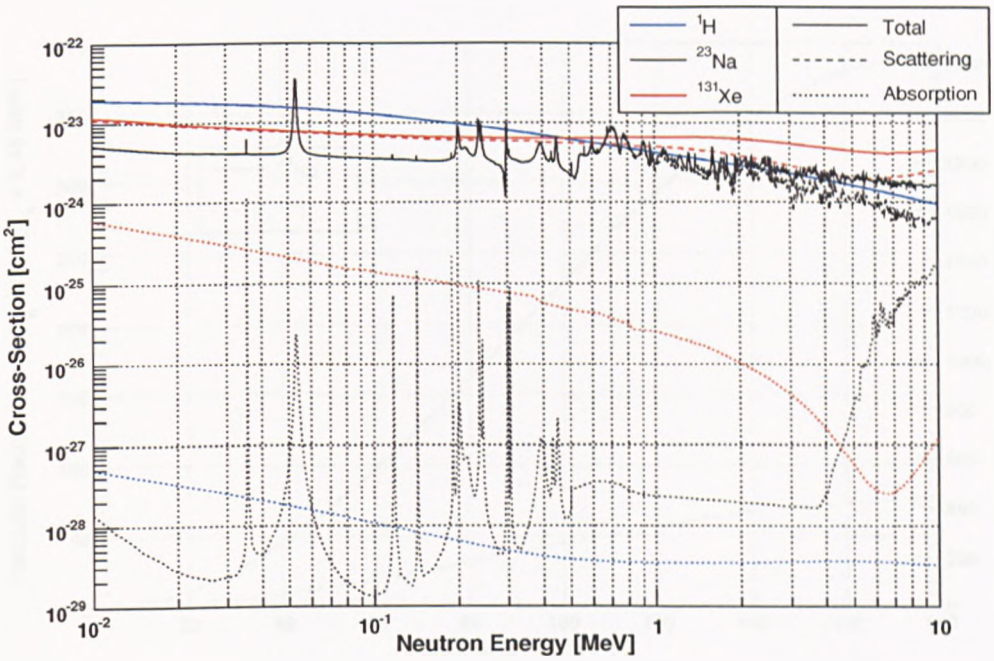

Figure 3.12: Cross-Sections for Neutron Interactions with ^{1}H, ^{23}Na and ^{131}Xe Nuclei in the Energy Range Relevant to Dark Matter Search Experiments. The total, scattering and absorption cross-sections for these isotopes are also shown. Data taken from [127].

proton due to their similar sizes and masses. Therefore, organic scintillators make excellent neutron detectors due to the abundance of hydrogen atoms.

Neutron scattering is akin to Compton scattering, and the photon and electron in Figure 3.8 can be replaced with a neutron and nucleus respectively. However, the deposited and final neutron energy cannot be calculated in the same way. Neutrons that interact with target nuclei scatter off at an angle that is dependent on the deposited energy E_R:

$$E_R \approx \frac{2m_A E_\mathrm{n} m_\mathrm{n}}{(m_A + m_\mathrm{n})^2} \cdot (1 - \cos\theta) \tag{3.15}$$

where m_A is the mass of the target nucleus, E_n is the energy of the incident neutron, m_n is the mass of the neutron and θ is the scattering angle. The distribution of Eq. (3.15) for mono-energetic 2.45 MeV and 14.0 MeV neutrons scattering off sodium and iodine nuclei is shown in Figure 3.13. It is clear that the change in energy with scattering angle is far more pronounced for lighter nuclei. Additionally, the recoil energy is more sensitive to scattering angle the higher the incident neutron energy. The recoil energy is a maximum when the scattering angle is 180°, and substituting this value into Eq. (3.15) yields:

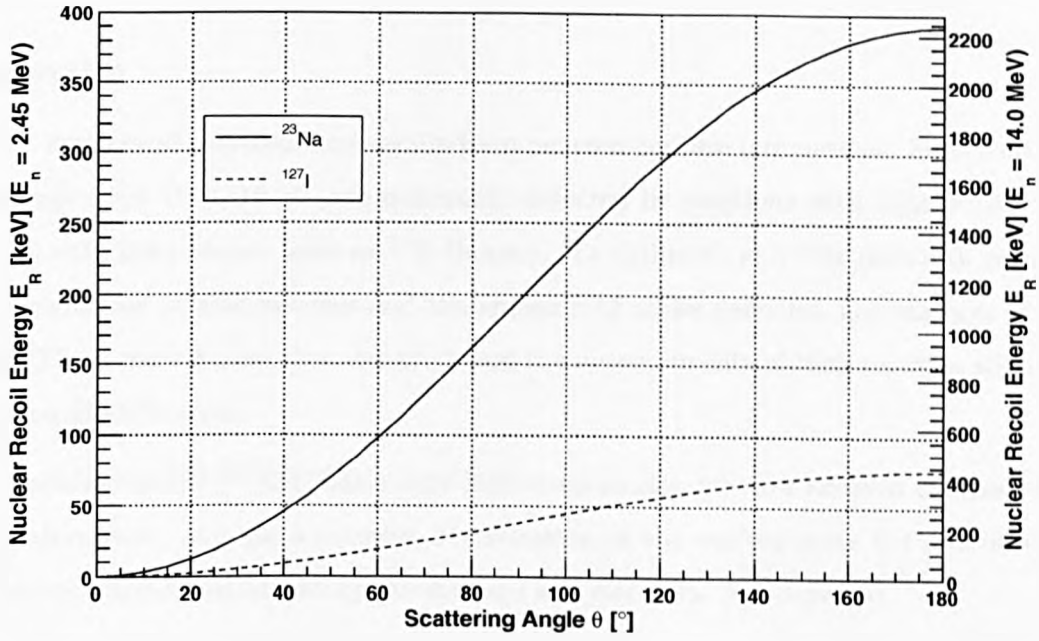

Figure 3.13: Nuclear Recoil Energy as a Function of Scattering Angle for ^{23}Na and ^{127}I Nuclei. The distributions of Eq. (3.15) are shown for incident neutron energies E_n of 2.45 and 14.0 MeV. Recoil energies of lighter nuclei are more senstive to changes in scattering angle. Additionally, the maximum recoil energy is lower for heavier nuclei.

$$E_{R_{max}} \approx \frac{2m_A E_n m_n}{(m_A + m_n)^2} \tag{3.16}$$

where the mass of the target nucleus m_A becomes the dominant variable. The inverse proportional relationship of the deposited energy E_R to m_A explains why organic scintillators that have high hydrogen-to-carbon ratios are commonly used for neutron detection.

Unlike Compton scattering, where the angular distribution (Eq. (3.13)) is dependent solely on the initial recoil energy, the preferential direction for scattered neutrons also depends on the target nucleus [128]. At incident neutron energies below 10 MeV, neutron-proton scattering is isotropic. However, at energies above this threshold, and with heavier nuclei, distortions in the angular distribution start to appear.

For incident neutrons of sufficient energy, inelastic scattering can take place, where a recoil nucleus is excited to a higher energy state as a result of a collision. The neutron loses significantly more energy in such an interaction, and the nucleus de-excites, emitting a gamma-ray. Such reactions are an important background to the population of elastic

neutron scattering events.

Absorption

There are several processes and results from neutron capture interactions. Slow neutrons, of energies less than 0.5 eV, are commonly detected by reactions with light nuclei. Collisions with light nuclei, such as ^{10}B (boron), ^{6}Li (lithium) and ^{3}He (helium), result in the production of new isotopes and the emission of alpha particles, gamma-rays or protons. These particles are then detected, and the measurements of their energies allows for neutron identification.

Gadolinium-157 (^{157}Gd) has a very high cross-section for slow neutron capture. Neutron absorption, and the successive de-excitation of the excited state Gd*, results in a variety of interactions including gamma-rays and electrons. For example:

$$\mathrm{n} + \mathrm{Gd} \rightarrow \mathrm{Gd}^* \rightarrow \mathrm{Gd} + \gamma_1 + \gamma_2 + \ldots + \gamma_n \tag{3.17}$$

where the total energy of gamma-rays γ_i, where $i = 1, 2, \ldots n$, is 8 MeV.

Gadolinium can be dissolved in organic liquid scintillators, allowing for the detection of these particles [129]. Alternatively, a second detector can be used [130]. The conversion efficiency for interactions with ^{157}Gd is higher than for any of the light nuclei discussed above [131].

Nuclear fission can be induced by neutron capture, and this is exploited in nuclear reactors. For slow neutrons, the cross-section for this process in elements with atomic mass greater than 90 amu is relatively large.

3.6 Quenching Mechanisms

The scintillation efficiency of a scintillator is the fraction of deposited energy that is converted to light. Alternative de-excitation modes compete with photon emission, thus decreasing the scintillation efficiency. These radiationless de-excitation processes contribute to the quenching of light.

The potential energy system of a diatomic molecule OA is shown in Figure 3.14. The lower curve aa' determines the vibrational amplitudes of atom A relative to atom

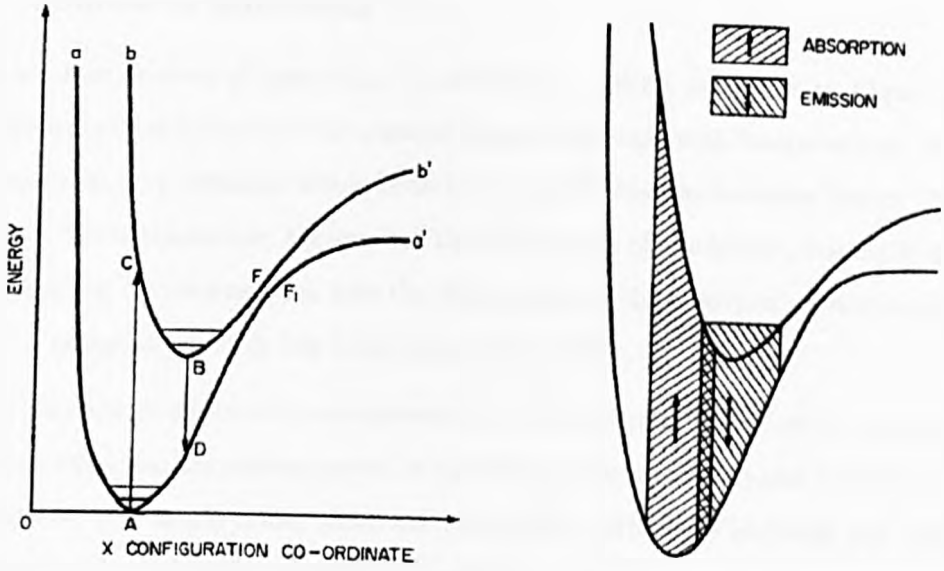

Figure 3.14: Potential Energy Diagrams of Luminescence Process for a Diatomic Molecule OA. Energy is plotted against the interatomic distance. Taken from [132].

O for all vibrational energies of the neutral molecule in the ground state. The upper curve bb' determines the vibrational amplitudes in an excited state. Due to the increase in bond length as a result of excitation, the minimum B is to the right of A. Photon absorption causes a transition from the ground state aa', to the excited state bb'. The Franck-Condon principle states that electronic change is faster than atomic movements, and hence excitation will follow the path of a straight vertical line. In the transition A to C, dissociation will occur if C is of higher energy than the limit set by b'. Otherwise, it will move to position B, releasing its excess vibrational energy as heat. It can then return to the ground state through the transition B to D, resulting in photon emission.

The widths of the absorption and emission spectra in Figure 3.14 correspond to those of the first few enery levels of A and B respectively. Due to the displacement of B in relation to A, photons from emission are of a longer wavelength. Self-absorption, when the scintillator absorbs the light it has emitted, occurs where the two bands overlap.

Alternatively, an excited electron at F, moving to F_1 is more efficient than de-excitation to B. This transition will result in no photon emission, as the electron will dissipate its energy as heat. Such transitions reduce the intensity of emitted light, and this process is called quenching.

3.6.1 Sources of Quenching

There are four sources of quenching in scintillators. With reference to Figure 3.14, the population of states just above the minima A and B increase with temperature. As a result, the absorption and emission bands broaden, and the overlap becomes larger. Therefore, the higher the temperature, the greater the percentage of luminous photons lost through self-absorption. Extensive work into the dependence of light output on temperature for a variety of inorganic crystals has been performed [133].

The presence of impurities can decrease the transmittance of a crystal. Extensive effort is made to minimise the concentration of impurities in inorganic crystal scintillators during manufacture, and liquid noble gases are constantly purified to expunge any undesirable substances. The scattering of light by impurities in liquid noble gases accounts for the difference in calculated [134] and experimental measurements [135] of the attenutation length due to Rayleigh scattering.

In the case of doped scintillation crystals, the light intensity is at a maximum for a certain activator concentration. This has been investigated for NaI(Tl) crystals over a wide range of temperatures, and a concentration of 0.03 wt.% of thallium was found to be optimal [136].

The radiationless de-excitation mechanisms mentioned so far affect both electron and nuclear recoils. Therefore, they can be said to contribute to the absolute quenching factor of a target material. However, as mentioned in Section 2.5.1, energy calibration of direct dark matter search detectors is performed with a gamma source.

This is done for a number of reasons. Energy scale calibration is typically conducted on a daily basis, and the use of a neutron source would lead to the generation of long-lived isotopes within the detector materials. This would make a significant contribution to the internal background, and hence hamper sensitivity. Additionally, energy spectra from gamma-ray emitting radioisotopes are more well defined than those from neutron sources, which tend to consist of a wide spectrum of energies. Therefore, gamma-ray sources allow for precise energy calibration. Finally, the shielding needed for the safe handling of gamma-ray sources is minimal compared with that required for neutron emitters. This makes them easier to handle, which is important in the underground environments that are home to most dark matter detectors.

The light intensity per unit energy loss $\frac{dL}{dE}$ rises with increasing ionisation density $\frac{dE}{dx}$

up to a certain point. Once this optimum ionisation density is reached, there is a sharp drop in $\frac{dL}{dE}$ with increasing $\frac{dE}{dx}$. This was first observed in inorganic crystals by [137].

Therefore, when the energy loss per unit length is large, as is the case in nuclear recoils, the dense ionised ions lead to overlapping excitations. This results in reduced light emission. Lightly ionising particles, such as electrons, lead to successive ionisations several molecular distances apart. As a consequence, any interactions between the ionisation sites is negligible, and a higher light yield for the same deposited energy is expected. This is known as ionisation quenching [132, 138].

The quenching factor correction outlined in Section 2.5.1 is a measurement of the relative ionisation quenching between nuclear and electron recoils rather than the absolute scintillation efficiency. For the purpose of dark matter experiments, the absolute quenching factor is of little importance.

An additional quenching mechanism takes place in the two-phase noble gas target detectors outlined in Section 2.5.4. This is due to the presence of an electric field, allowing electrons released from ionisation to drift toward the gas phase. With reference to Section 3.3, the larger the electric field, the fewer the number of electron-hole pairs that recombine to release scintillation light. The relationship between electric field strength and light yield has been investigated in xenon [121]. As mentioned in Section 3.3, this affects electron recoils more than nuclear ones.

3.6.2 The Quenching Factor

As mentioned above, an important measurement to determine a scintillating target's sensitivity to dark matter particles is the ratio of light induced by a nuclear recoil S_{nr} to that by an electron of the same energy S_{er}. This is known as the quenching factor Q:

$$Q = \frac{S_{nr}}{S_{er}} \tag{3.18}$$

Alpha-particles, ions and neutrons all induce nuclear recoils in materials. As alpha-particles and ions are strongly ionising, most interactions occur on the target surface. However, neutrons interact uniformly throughout the bulk of the target, making them the best choice for nuclear recoil experiments.

Neutron beams are small fixed target linear accelerators. An isotope of hydrogen (such as deuterium ^{2}H or tritium ^{3}H) is accelerated towards a metal hydride target. At a high

enough energy, the isotopes fuse together to form a helium ion and neutron. A deuterium ion striking a deuterium target results in 2.45 MeV mono-energetic neutrons:

$$^2\mathrm{H} + ^2\mathrm{H} \longrightarrow ^3\mathrm{He} + ^1\mathrm{n} \tag{3.19}$$

Similarly, a deuterium ion striking a tritium target produces 14.0 MeV mono-energetic neutrons:

$$^2\mathrm{H} + ^3\mathrm{H} \longrightarrow ^4\mathrm{He} + ^1\mathrm{n} \tag{3.20}$$

From Eq. (3.15), it is clear that the knowledge of initial neutron energies is essential. Neutron beams are relatively small and inexpensive mono-energetic neutron sources, making them ideal for quenching factor experiments.

A gamma source, such as ^{57}Co, is used to measure the detector response to electron recoils. By calibrating the detector to the gamma line (122 keV in the case of ^{57}Co) and scaling to lower energies, an electron equivalent energy E_{ee} is established. Using the nuclear recoil energy E_R calculated in Eq. (3.15) and the measured detector response to these recoils E_{Ree}, Eq. (3.18) becomes:

$$Q = \frac{E_{Ree}}{E_R} \tag{3.21}$$

3.6.3 The Lindhard Theory

After a nuclear interaction, a recoiling nucleus will lose energy as it moves through a target material through collisions with both electrons and other nuclei. As most detectors, including scintillators, are sensitive to electronic energy loss only, the quenching factor can be calculated through an understanding of these mechanisms. In other words, scintillation light can be understood to be a result of the electronic energy loss mechanisms, while non-radiative transfers, such as heat, are due to collisions with other nuclei. The Lindhard theory [139, 140] attempts to separate the electronic and nuclear energy loss mechanisms, and quantify these interactions from first principles. The points relevant to the theoretical determination of the quenching factor are discussed here.

In the following equations, the atomic numbers are denoted by Z_i, where $i = 1$ for the penetrating particle (recoiling nucleus), and $i = 2$ for the atoms of the medium. The same notation is used for the mass numbers A_i.

The energy loss mechanisms through the electronic and nuclear channels can be understood as the electronic and nuclear stopping powers respectively. These can be defined by rescaling the range R and energy E of a recoiling nucleus to the respective non-dimensional variables ρ and ϵ [139]. In such a way, the nuclear energy loss $\left(\frac{d\epsilon}{d\rho}\right)_n$ can be defined as a universal function $f(\epsilon)$ that can be calculated numerically [139].

The expression for ϵ in terms of the atomic and mass numbers of the penetrating particle and atoms of the medium, and the nuclear recoil energy E_R in units of keV is:

$$\epsilon = \frac{32.5A_2}{Z_1Z_2(A_1+A_2)\sqrt{Z_1^{\frac{2}{3}}+Z_2^{\frac{2}{3}}}}E_R\,[\text{keV}] \tag{3.22}$$

When the penetrating particle and atoms of the medium are the same (in other words, when $Z = Z_1 = Z_2$ and $A = A_1 = A_2$), Eq. (3.22) simplifies to:

$$\epsilon = \frac{11.5}{Z^{\frac{7}{3}}}E_R\,[\text{keV}] \tag{3.23}$$

The electronic energy loss is defined by $\left(\frac{d\epsilon}{d\rho}\right)_e = \kappa\sqrt{\epsilon}$, where κ is given by:

$$\kappa = \frac{0.0793Z_1^{\frac{1}{2}}Z_2^{\frac{1}{2}}(A_1+A_2)^{\frac{3}{2}}}{\sqrt[4]{\left(Z_1^{\frac{2}{3}}+Z_2^{\frac{2}{3}}\right)^3}A_1^{\frac{3}{2}}A_2^{\frac{1}{2}}}\xi_e \tag{3.24}$$

where $\xi_e \approx Z_1^{\frac{1}{6}}$ [139]. When the penetrating particle and the atoms of the medium are the same, Eq. (3.24) becomes:

$$\kappa = \frac{0.133Z^{\frac{2}{3}}}{\sqrt{A}} \tag{3.25}$$

Assuming that the electronic and nuclear collisions are uncorrelated, the total energy given to electrons and that given to atoms can be expressed as the two separate quantities η and ν respectively. The non-dimensional variable ϵ can now be written in terms of these:

$$\epsilon = \eta + \nu \tag{3.26}$$

For large ϵ, the mean energy given to the atoms of the medium $\bar{\nu}$ is inversely proportional to κ [140]. However, this does not hold when $\epsilon < 1$, in which case $\bar{\nu} \approx \epsilon$ [140]. A single formula that combines these results is:

$$\bar{\nu} = \frac{\epsilon}{1+\kappa g(\epsilon)} \tag{3.27}$$

where the function $g(\epsilon)$ [140] is well fitted by [60]:

$$g(\epsilon) = 3\epsilon^{0.15} + 0.7\epsilon^{0.6} + \epsilon \tag{3.28}$$

From Eq. (3.26), the mean energy given to electrons $\bar{\eta}$ in terms of ϵ can be written as:

$$\bar{\eta} = \epsilon - \bar{\nu} \tag{3.29}$$

Therefore, an estimation for the quenching factor can be obtained by dividing the average contribution from electronic energy losses $\bar{\eta}$ by the total recoil energy E_R through a combination of Eq. (3.26), Eq. (3.27) and Eq. (3.29):

$$\frac{\bar{\eta}}{E_R} = \frac{\epsilon - \bar{\nu}}{\epsilon} = \frac{\epsilon(1 + \kappa g(\epsilon)) - \epsilon}{\epsilon(1 + \kappa g(\epsilon))} = \frac{\kappa g(\epsilon)}{1 + \kappa g(\epsilon)} \tag{3.30}$$

By substituting Eq. (3.23), Eq. (3.25) and Eq. (3.28) into Eq. (3.30), the quenching factor as a function of nuclear recoil energy can be plotted for sodium recoils in $^{23}_{11}$Na, as shown in Figure 3.15. There is no clear way to solve Eq. (3.30) when the target material is a compound. Additionally, $^{23}_{11}$Na and $^{127}_{53}$I have significantly different mass and atomic numbers, implying that the quenching factors of sodium recoils in sodium and those in iodine cannot be similar. In the case of sodium recoils in iodine, where $Z_1 \neq Z_2$, the evaluation of the quenching factor is more complicated, and Eq. (3.30) can no longer be used. In fact, the original theory [140] can only approximate the quenching factor in such cases at very low energies. As such, the Lindhard curve in Figure 3.15 is an upper limit for the quenching factor of sodium recoils in NaI(Tl).

The main drawback of the Lindhard theory is the assumption that electronic and nuclear collisions can be separated. However, the repulsion between two interacting nuclei makes part of the parameter range unavailable for transfering energy to electrons. As a result, the electronic stopping power is suppressed when $\epsilon \ll 1$, leading to the non-proportionality of $\left(\frac{d\epsilon}{d\rho}\right)_e$ with $\sqrt{\epsilon}$ in this energy range [143]. This can be corrected for by replacing ξ_e in Eq. (3.24) with the function $\tau\left(\epsilon, \frac{Z_1}{Z_2}\right)$, given in [143]. The impact of this correction on light nuclei, such as sodium, is very small, and as such it is not evaluated here.

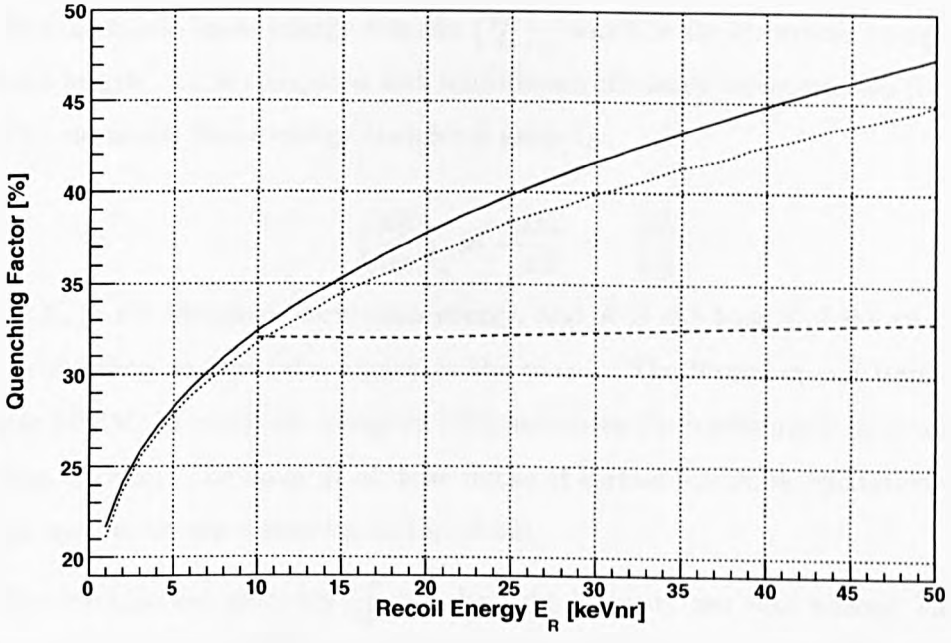

Figure 3.15: Theoretical Curves for the Quenching Factor of Sodium Recoils. The solid black curve represents the quenching factor of sodium recoils in sodium derived from the Lindhard theory [139, 140] (Section 3.6.3, Eq. (3.30)). The upper limit from Hitachi [141] (Section 3.6.4, Eq. (3.31)) is illustrated by the dashed line. Finally, the result derived from SRIM/TRIM [142] (Section 3.6.5) is shown by the dotted line.

3.6.4 Quenching Factor in Scintillators

In semiconductors, the measured quenching factor agrees well with that given by Eq. (3.30). For scintillators, however, some degree of quenching also affects the intensity of scintillation light from electron recoils, as do escaping electrons [144]. As explained previously, the absolute quenching factor for nuclear recoils q_n given by Eq. (3.30) is not what is measured by neutron scattering experiments, and is not the required correction factor Q_A in Eq. (2.31). The measured quenching factor Q for scintillators can be approximated by [144]:

$$Q = \frac{q_n q_e}{S_\gamma} \tag{3.31}$$

where q_e is the electronic quenching factor and S_γ is the scintillation efficiency for electron interactions. If the quenching factor for sodium recoils in Na from Eq. (3.30) is defined as q_n in Eq. (3.31), the resulting solution will only set an upper limit for sodium recoils in

NaI(Tl).

The electronic linear energy transfer $\left(\frac{dE}{dx}\right)_e$, which is the electronic energy deposition per unit length, can be compared with scintillation efficiency measurements [137] to obtain q_e. The electronic linear energy transfer is given by:

$$\left(\frac{dE}{dx}\right)_e = -\frac{dE_e}{dR} = -\frac{\delta E_e}{\delta R} \tag{3.32}$$

where E_e is the electronic excitation energy, and R is the length of the track produced by the recoiling nucleus (also known as the range). The Stopping and Range of Ions in Matter (SRIM) Monte Carlo program [142] simulates the tracks made by recoiling ions in a target medium. The range R of these tracks at certain electronic excitation energies E_e can be used to obtain a solution to Eq. (3.32).

The scintillation efficiency $\frac{dL}{dE}$, or the light intensity per unit energy, has a flat-tip region over a range of $\left(\frac{dE}{dx}\right)$ [145]. By assuming that $q_e = 1$ in this region, values for the electronic quenching factor can be obtained from this curve.

The response of NaI(Tl) to electron recoils is known to be non-linear [146–149]. In other words, the light intensity is not completely proportional to the energy deposited by an electron recoil. Therefore, the choice of gamma source for detector calibration plays some role in the final quenching factor, as a linear energy distribution in assumed both in dark matter and quenching factor experiments. Using the response curve from [146], the scintillation efficiency S_γ of 122 keV gamma-rays from a ^{57}Co source is approximately 0.923. Hitachi approximates $S_\gamma = 0.9$ when calculating his limit [141], which is shown in Figure 3.15.

3.6.5 Calculation of the Quenching Factor in NaI(Tl) with SRIM/TRIM

As mentioned previously, the Stopping and Range of Ions in Matter (SRIM) package [142] simulates the process of ions impinging onto various target materials. In elastic neutron scattering, an incident neutron will recoil off a target nucleus, leading to ionisation as discussed in Section 3.5.2. The recoiling ionised nucleus will travel through the crystal, dissipating its energy among the atoms of the target material until coming to rest. The program calculates the stopping power and range of ions in matter using a quantum mechanical treatment of ion-atom collisions.

The Bragg rule states that the stopping power of a compound can be estimated by the linear combination of the stopping powers of the individual elements. Although this is a reasonably accurate approximation, corrections are required due to the nature of bonding between target elements. However, in the case of NaI(Tl), the bonding between sodium and iodine atoms is that of a single-bond structure, and hence the uncorrected Bragg rule is used by SRIM in this case.

The TRansport of Ions in Matter (TRIM) program [142] reads the values for the nuclear and electronic stopping powers calculated by SRIM, and calculates the final distribution of the ions. All the energy loss mechanisms associated with ion-atom collisions, such as target damage, sputtering, ionisation and phonon production, are also evaluated.

Quenching factors for silicon recoils in Si, argon in Ar, germanium in Ge and xenon in Xe have been derived from SRIM and TRIM by [150], and compared with predictions from Lindhard theory and experimental data where available. The nuclear stopping powers predicted by the Lindhard theory and calculated by SRIM differ by 15% at most, although bigger discrepancies are present for the electronic stopping power. When compared with experimental data, the original Lindhard theory is closest to giving an accurate prediction [150].

A sodium iodide crystal, of density 3.67 g/cm^3, is defined as the solid target. Sodium ions are given an intial energy (in other words, a recoil energy) and propagated through the crystal at a normal incidence angle. Recoil energies are varied between 1 and 50 keVnr, in 1 keVnr steps, and 4000 ions are simulated at each energy.

Tracks made by 10 keVnr and 50 keVnr sodium ions in NaI(Tl) are shown in Figures 3.16(a) and 3.16(b) respectively. The percentage energy loss from the original ions and the resultant recoiling atoms induced by ion-atom collisions is calculated by TRIM. This is then subdivided into energy loss from ionisation, vacancies from un-filled holes left behind after a recoil atom moves from its original site, and phonon emission. Light emission is a result of ionisation, and hence, the sum of the energy loss due to ionisation from the original ion and recoiling atoms is the quenching factor. The mean of these contributions over 4000 events is calculated by TRIM, and the result for 10 keVnr sodium ions is given in Table 3.1 as an example.

The results from SRIM and TRIM over a range of nuclear recoil energies are shown in Figure 3.15. Unlike the prediction of an upper limit from Hitachi, the result from TRIM

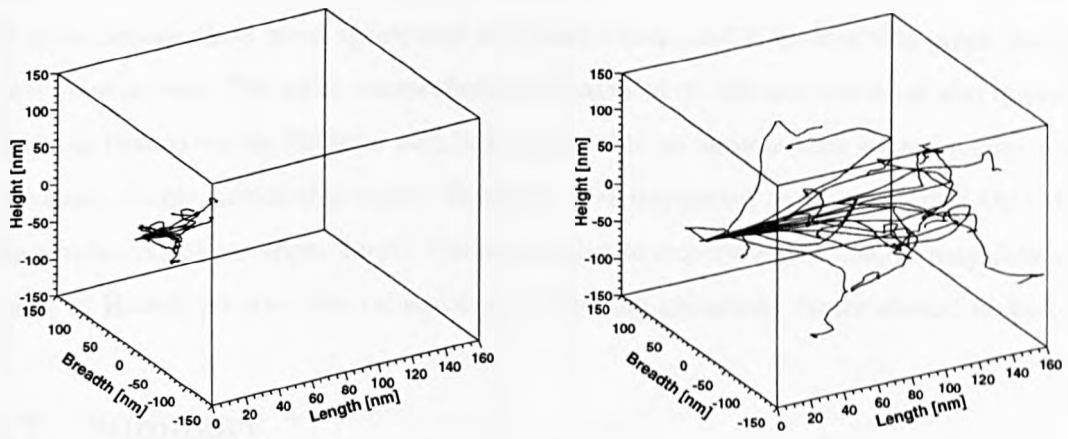

Figure 3.16: Tracks made by Sodium Ions in NaI(Tl) of Initial Energies: (a) 10 keVnr; and (b) 50 keVnr. Sodium ions are propogated through the crystal from the origin, at a normal incidence angle. Ion-atom collisions cause the ion to scatter off target atoms at different angles, depositing energy at each interaction point, before finally coming to rest once it has dissipated all of its kinetic energy. A sample of twenty tracks are shown in each graph.

Table 3.1: Simulated Percentage Energy Losses for 10 keVnr Na Ions in NaI(Tl). The values shown are the mean percentage contributions calculated by TRIM [142] over 4000 events. The sum of percentage energy losses from the original ion and successive recoiling atoms is the quenching factor. In the case of the results shown here for a 10 keVnr nuclear recoil energy, a quenching factor of 31.75% is determined. Results over a range of energies are illustrated in Figure 3.15.

Energy Loss	Mean Energy Loss From:	
Mechanism	Ions [%]	Recoiling Atoms [%]
Ionisation	19.02	12.73
Vacancies	0.69	2.40
Phonon emission	2.95	62.21

follows the shape of the Lindhard curve. However, although they display similar values at low energies, the two curves diverge from each other with increasing energy. At 10 keVnr, all three results show good agreement with each other, and it is after this point that they start to separate. The most comprehensive treatment to the evaluation of the quenching factor is that given by Hitachi, and it is reasonable to assume that experimental results will more closely match this curve. However, it is important to bear in mind that this is the prediction of an upper limit. Even though the experimental results may follow the shape of Hitachi's curve, the values obtained for the quenching factor should lie below it.

3.7 Summary

Photoemission occurs when an electron in its ground state is excited to that of a higher energy, and subsequently de-excites releasing quantised particles of light called photons. Although this process is a common trait in all scintillating materials, the specific mechanics can vary. In organic scintillators, only the electrons in π-bonds can form excited states. In inorganic crystals, free electrons in the valence band are excited to the conduction band. Their subsequent de-excitation is through activator excited states such that visible photons are emitted. In liquid noble gases, the recoiling primary particle can undergo secondary collisions with neighbouring atoms, resulting in excitation and ionisation. Two-phase detectors suppress the recombination of electron-hole pairs by extracting excited electrons into the gas phase by means of an electric field. This enables the direct measurement of ionisation, and is a more powerful discriminant of nuclear and electron recoils than pulse shape analysis.

Photomultiplier tubes are the typical light collection devices used in dark matter scintillation detectors, although photodiodes are a possible alternative.

Gamma-rays and neutrons are the main backgrounds in most dark matter detectors. Gamma-rays can deposit energy in target electrons through photoelectric absorption, Compton scattering and electron-positron pair-production. Neutrons are either absorbed by or scattered off target nuclei. Although other interactions are possible, only these result in a detectable response.

As energy calibration of dark matter detectors is typically performed with gamma sources, the phenomenon of ionisation quenching makes the ratio of light from a nuclear recoil to that of an electron recoil an important correction factor. Lindhard theory states

that the energy loss of a recoiling nucleus can be separated into the electronic and atomic channels. Scintillation light is a result of energy loss to target electrons, and therefore a prediction of the quenching factor of sodium recoils in NaI(Tl) can be made. Results from the SRIM/TRIM Monte Carlo code agree with the shape of the curve from Lindhard theory, although they diverge from each other at higher nuclear recoil energies. Both approaches neglect the quenching of light in the electronic channel, and the scintillation efficiency of gamma-rays used to define the energy scale. For a more accurate result, these two factors must be taken into account. Additionally, in the case of a compound like NaI(Tl), the difficulty of predicting the nuclear quenching factor from Lindhard theory when the target atoms and recoiling nucleus are different means that this calculation can only be regarded as an upper limit. Actual experimental results may match the shape, but should lie below the prediction.

Chapter 4

The ZEPLIN-II Dark Matter Detector

The ZEPLIN-II (ZonEd Proportional scintillation in LIquid Noble gases) detector is a two-phase xenon-based direct dark matter search experiment at Boulby Mine, North Yorkshire, United Kingdom. The collaboration has recently published its first limit on WIMP nuclear recoil signals [101]. A schematic of the ZEPLIN-II detector is shown in Figure 4.1. The detection principles of two-phase noble gas experiments are discussed in Sections 2.5.4 and 3.3.

The components of the detector are discussed at the beginning of this chapter, together with the data acquisition system. The second part of this chapter is dedicated to the commissioning of the veto and neutron shielding, in which the author made a significant contribution. This includes a calculation of the background rejection efficiency of the veto. All work performed on the veto was done with the aid of Dr. Ed Daw, Mr. Trevor Gamble, Dr. Phil Lightfoot and Dr. John McMillan. Neutron shielding was constructed and installed with the help of Dr. Phil Lightfoot.

4.1 The Inner Vessel

The inner vessel consists of two hollow copper chambers that bolt together, one sitting on top of the other, as shown in Figure 4.1. The copper vessel is evacuated to a pressure of 10^{-4} mbar, and this is maintained with a gold wire seal between each chamber. An IGC PFC330 Polycold refigerator feeds cooling fluid through pipes into a copper cold

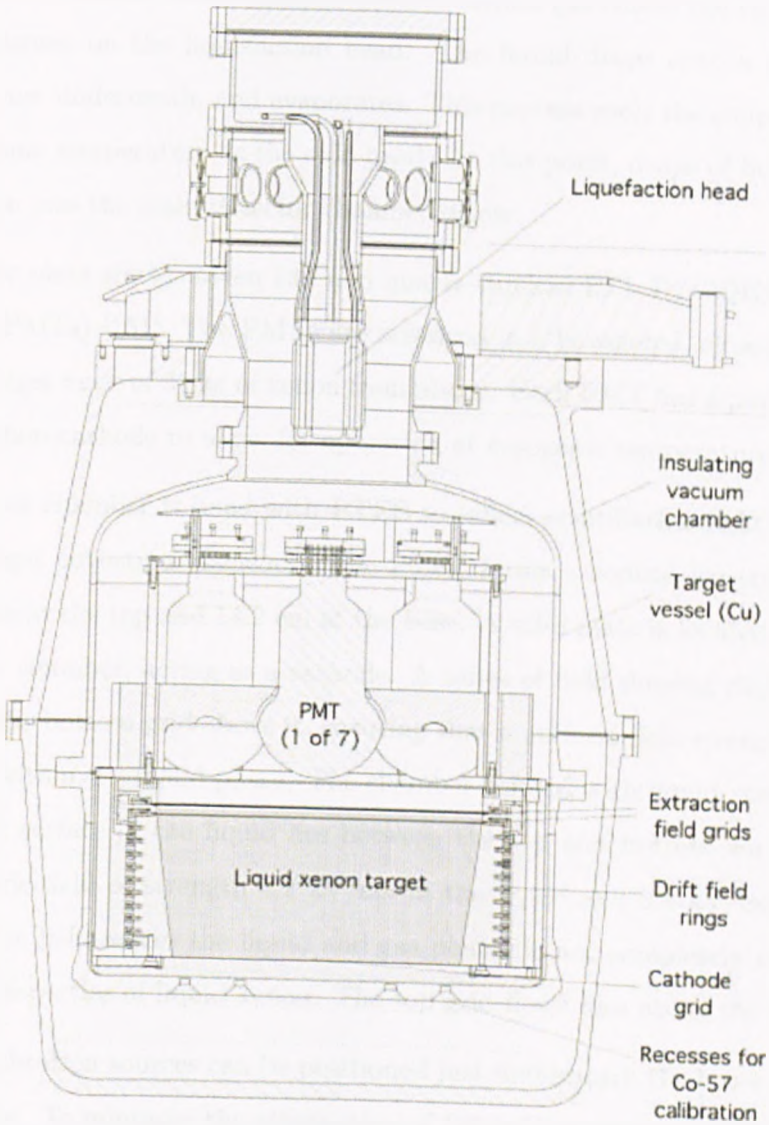

Figure 4.1: Schematic of the ZEPLIN-II Detector. The detector consists of a copper inner vessel surrounded by an evacuated stanless steel vacuum jacket. The liquid xenon volume is viewed from above by seven photomultiplier tubes. The electron drift region lies between the cathode and lower extraction field grids. The electron extraction region, where electroluminescence occurs, lies between the liquid xenon surface and upper extraction field grid. Xenon gas condenses on the liquefaction head, and drips onto a copper plate, shielding the photomultipliers. The bottom of the inner vessel has recesses for calibration with a gamma source, such as ^{57}Co, placed just beneath the base using a source dropper. The source dropper is not shown. Taken from [101].

head within the vessel. This cold head is located at the top of the inner vessel, and is maintained at a constant temperature of 163 K. Xenon gas enters the chamber from the top and condenses on the liquefaction head. The liquid drops onto a relatively warm copper plate just underneath, and evaporates. This process cools the copper plate until it reaches the same temperature as the cold head. At this point, drops of liquid xenon slide down the plate into the main detector chamber below.

The copper plate shields seven 130 mm quartz-window ETL D742QKFLB photomultiplier tubes (PMTs) [151]. The PMTs are arranged in a hexagonal, close-packed pattern viewing the target mass of 31 kg of xenon from above. Each PMT has a platinum underlay beneath the photocathode to allow for operation at cryogenic temperatures.

The detector chamber is lined with PTFE to reflect scintillation light in an effort to improve the light collection efficiency. The PTFE forms a conical frustrum, with inner radii of 16.2 cm at the top and 14.2 cm at the base. A solid plate is located at the bottom of the detector chamber, acting as a cathode. A series of field shaping rings separate the cathode from the bottom grid above it, ensuring that a uniform field strength of 1 kV/cm is maintained within the liquid phase. The chamber is filled with liquid xenon to a height of 14 cm. The surface of the liquid lies between the top and bottom wire grids, across which an electric field of strength 4.2 kV/cm in the liquid and 8.4 kV/cm in the gas is maintained. The field across the liquid and gas phases is not completely uniform due to the dielectric properties of liquid xenon. The top grid lies 9 mm above the bottom grid.

Gamma calibration sources can be positioned just underneath the lower chamber with a source dropper. To minimise the attenuation of 122 keV gamma-rays from ^{57}Co as they pass through the copper wall, recesses have been drilled into the base of the inner vessel.

4.2 The Outer Vessel

As shown in Figure 4.1, a stainless steel outer vessel evacuated to a pressure of 10^{-3} mbar, insulates the copper inner vessel, allowing for minimal heat loss. It is attached to the top of the inner vessel, and also consists of two chambers bolted together. These chambers are sealed with a PTFE seal to maintain the roughing vacuum.

4.3 Xenon Purification

Impurities within the liquid phase will prevent some electrons reaching the gas phase. In turn, this could lead to the misidentification of events and affect the sensitivity of the experiment. Hence, maintaining a high level of purity is essential. As shown in Figure 4.2, xenon gas is initially purified by passing it through SAES PS11-MC500 getters while circulating it between two storage bottles. These filters remove carbon dioxide (CO_2), water (H_2O) and oxygen (O_2) molecules from the gas. Each bottle can hold gas at a pressure of 68 bar, and pressure sensors are attached to indicate when they are full.

Many non-metallic compounds are highly soluble in liquid xenon. Even if clean xenon is introduced into the detector, xenon-soluble impurities within the inner vessel can cause contamination. Therefore, it is prudent to circulate the xenon continuously through a purification rig. This mechanism is provided by the recirculator system attached to ZEPLIN-II, as shown in Figure 4.2.

A heater is contained within a stainless steel tube that is immersed in the liquid phase. Liquid xenon within the tube is gently heated, forming xenon gas. This gas bubbles to the surface and is extracted with a Tokyo Garasu Kikai MX-808-ST diaphragm pump at a rate of 3 slpm (standard litres per minute, ie. litres per minute at standard temperature and pressure). It is then passed through the filter system and returned to the gas phase.

Over the lifetime of the detector, it is important to assess the level of xenon purity on a regular basis. This is done by assessing the mean free path of electrons in the liquid. Liquid xenon is fed into a small chamber (the electron lifetime monitor in Figure 4.2), which is maintained at a thermal gradient such that both the liquid and gas phases co-exist. An americium-241 (^{241}Am) source is located at the top of the chamber, emitting 4 MeV α-particles into the gas phase. Their passage through the gas results in ionisation and the mean production of 2×10^5 electrons per α-particle. A uniform electric field is maintained across the chamber, directing the produced electrons toward the liquid phase. The number of electrons that remain after traversing through the liquid is proportional to the level of purity. Cold temperatures are maintained by a cold finger extending from the bottom of the chamber into a dewar of liquid nitrogen. The temperature is adjusted with heaters embedded within the cold finger.

Additionally, a mass spectrometer is attached to the ZEPLIN-II detector, as shown in Figure 4.2, to perform residual gas analysis. This enables the identification of impurities

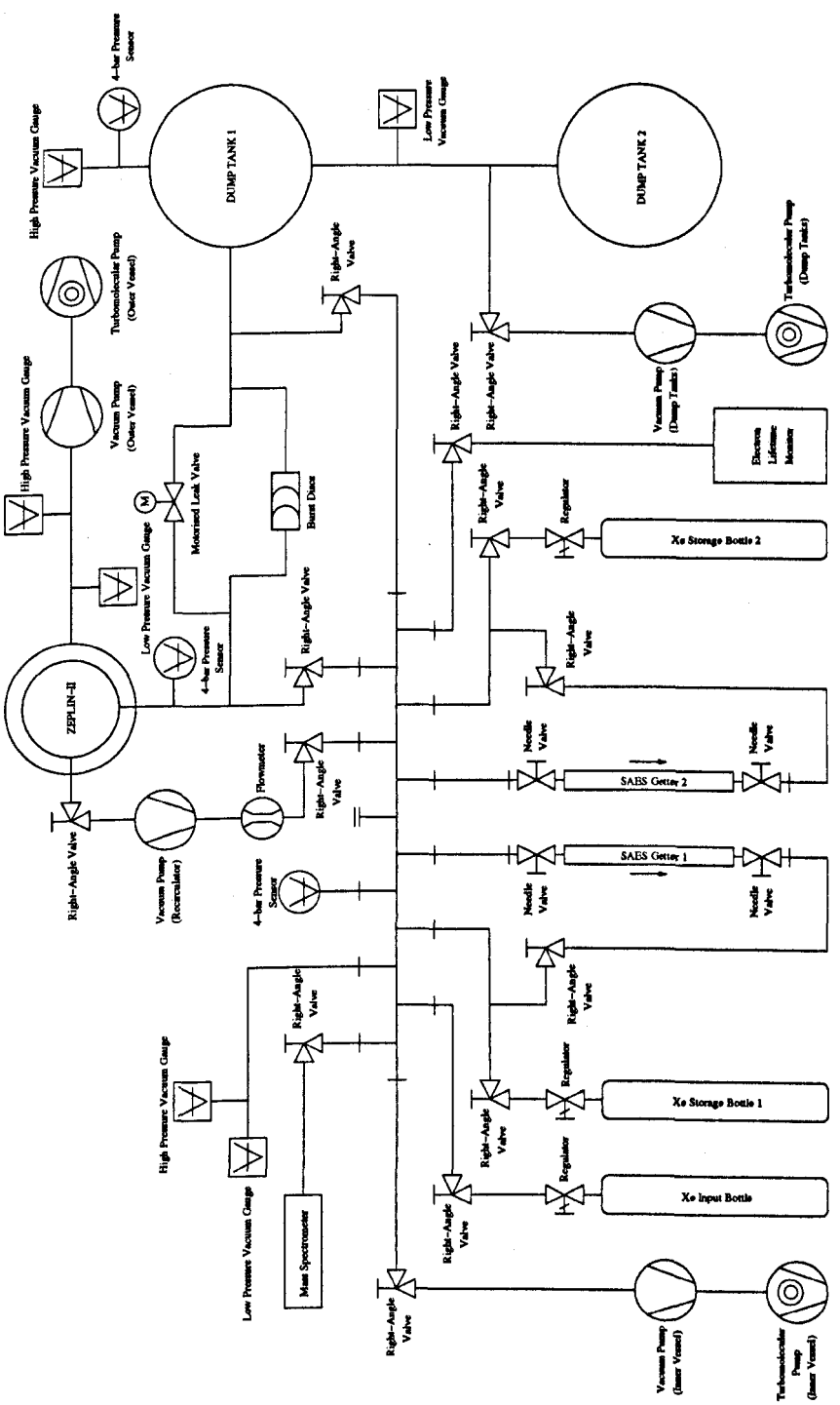

Figure 4.2: Schematic of the ZEPLIN-II Vacuum System. Xenon gas is fed into the system from an input bottle, and purified by continuous circulation through two SAES getters. Purified xenon gas is stored in two pressurised stainless steel bottles. The gas is then fed into the detector where it is liquified. During operation, xenon can be extracted for recirculation and further purification. A mass spectrometer and the electron lifetime monitor are used to measure the relative purity of the gas and liquid respectively. In case of overpressure in the target, excess xenon can be stored as a gas in the dump tanks.

in the gas phase.

Over the course of the experiment, the mass spectrometer has been found to be of limited use as impurity levels have been far below those that could be detected, and hence identified. Radon contamination in the liquid itself has unexpectedly enabled the assessment of purity levels within the target itself. The area of secondary pulses from these events have been found to fall off exponentially with drift time, or in other words the time difference between the primary and secondary pulses. The decay time constant of this exponential gives the lifetime of electrons that drift to the gas phase. The values of electron lifetime from these events could never be reconciled with those measured by the electron lifetime monitor, which were always higher. This could be due to impurities from internal components within the inner vessel, that would not evaporate with the xenon, and hence were absent in the electron lifetime monitor. As a result, purity is measured through the analysis of high energy alpha events in the target vessel itself.

4.4 Dump Tanks

As a safety system, dump tanks are also incorporated into the design. Overpressure within the detector could result in an explosion, and the subsequent loss of xenon gas. With reference to Figure 4.2, two pressure sensors are connected to the line that feeds the detector. In case of relatively small excess pressures, one of the pressure sensors activates a motorised leak valve, bleeding excess xenon gas into the dump tanks. If the pressure exceeds 3 bar, the second pressure sensor causes the splitting of a diaphragm that separates the intake pipe from the dump tanks. This enables the flow of xenon into the dump tanks, where it is stored as a gas at a pressure of 1 bar within stainless steel containers. The dump tanks are maintained at a pressure of 10^{-7} mbar during operation.

4.5 Data Acquisition System

Full details of the data acquisition system (DAQ), reduction procedure and analysis are given by [152]. Figure 4.3 shows the signal path from target PMTs to the DAQ via the trigger electronics.

The signal from each PMT in the target is split by a Suhner 4901.01.A 2 GHz 50 Ω power divider. One signal is fed into a $\times 10$ amplifier, and then a discriminator (D1 in

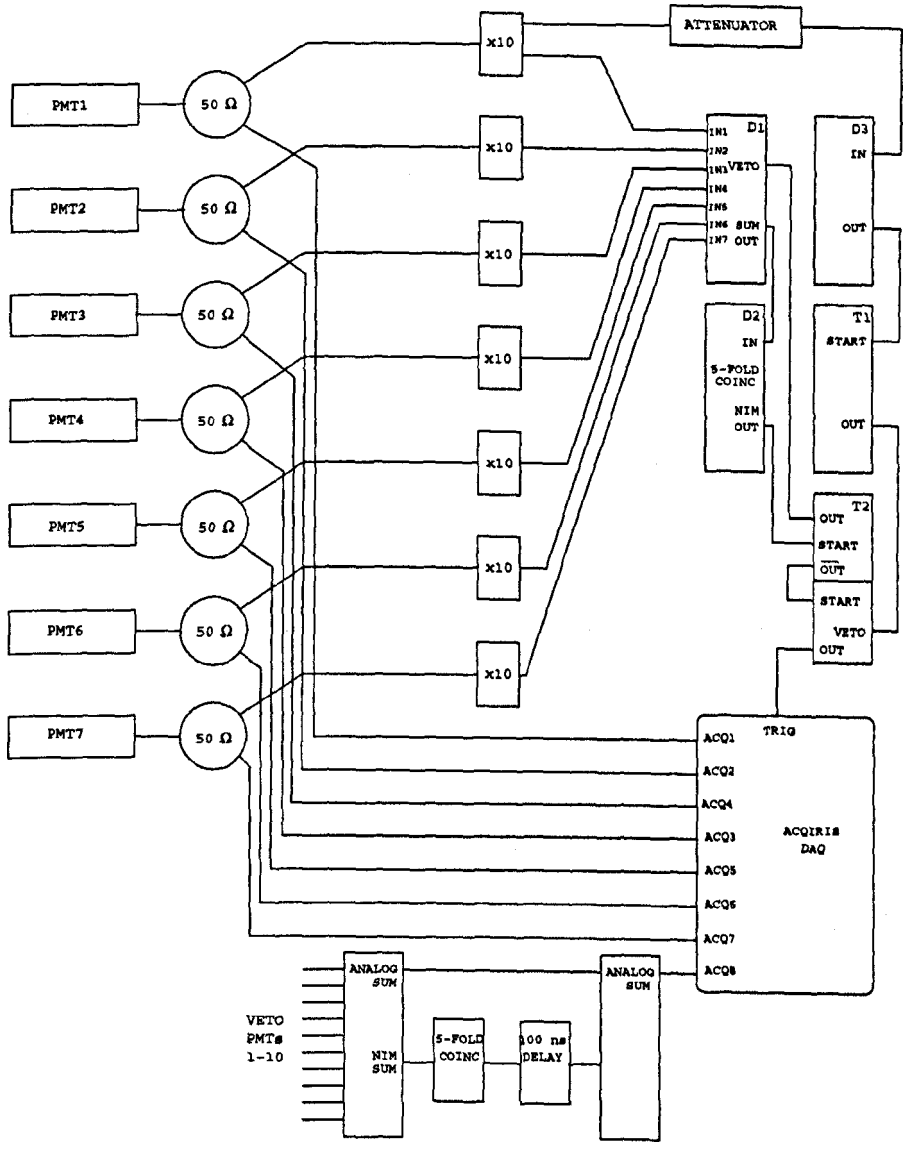

Figure 4.3: Hardware Trigger Electronics for Signals from ZEPLIN-II Photomultiplier Tubes. The signals from each target PMT (PMT 1 to PMT 7) are split by a 50 Ω power divider and sent to an amplifier and an input channel on the DAQ (ACQ 1 to ACQ 7). The amplified signals are sent to discriminator D1 set at a threshold of 17 mV amplitude, and passed to a 5-fold coincidence unit D2. A dual timer T2 prevents other pulses triggering the electronics for 100 μs, and provides the external trigger to the DAQ should the attenuated ampltude of the signal from PMT 1 not exceed 200 mV (determined by discriminator D3). However, if this happens, dual timer T1 prevents the DAQ from acquiring data for 1 ms. Trigger electronics for signals from the veto are also shown. Taken from [152].

Figure 4.3). This discriminator outputs a logic pulse for each signal that satisfies the threshold of approximately 40% of the single photoelectron amplitude of 50 mV. The logic pulses are sent to a 5-fold coincidence unit (D2 in Figure 4.3), and if this condition is satisfied, a logic pulse is sent to a dual timer (T2 in Figure 4.3). A 100 μs square-wave pulse is sent from the dual timer T2 to the veto input of discriminator D1, preventing further triggers until the whole waveform is read by the DAQ.

As discussed in Section 4.1, the PMTs are arranged in a hexagonal pattern, with PMT 1 in Figure 4.3 in the centre. As a result, this central PMT sees a much larger signal than the others on average. Large amplitude signals can cause optical feedback effects, thus giving rise to noise pulses of long duration. Therefore, the amplified signal from PMT 1 is attenuated before being sent to a discriminator (D3 in Figure 4.3) with threshold set at 200 mV. If this condition is satisfied, a logic pulse is sent to a dual timer (T1 in Figure 4.3), which sends a 1 ms square-wave pulse to the veto channel on dual timer T2.

After each PMT signal is split, the other signal goes to a channel (labelled ACQ 1 to ACQ 7 in Figure 4.3) of an 8-bit, 500 MHz sampling rate cPCI-based DC265 Acqiris digitiser [153]. If the conditions for the hardware trigger outlined above are satisfied, a logic pulse is sent to the DAQ, and the PMT pulses are digitised. The resultant waveforms are stored on a computer for later analysis. At a later date, the ZEPLIN-II reduction code can be run over these files to extract waveform parameters. Files containing these parameters are stored on a central computer system at the University of Sheffield. The reduction code also allows users to view the raw waveforms.

Sample gamma and neutron waveforms from ZEPLIN-II are shown in Figures 4.4(a) and 4.4(b) respectively. Both events correspond to 16 keVee energy deposition in the target vessel. As outlined in Section 2.5.4, event-by-event discrimination can be achieved by comparing the ratios of secondary to primary pulse areas at the same deposited electron equivalent energies. In Figure 4.4(a), the area of the secondary pulse from the gamma event is roughly 300 times that of the primary pulse. By comparison, this ratio falls to 100 for the neutron event in Figure 4.4(b).

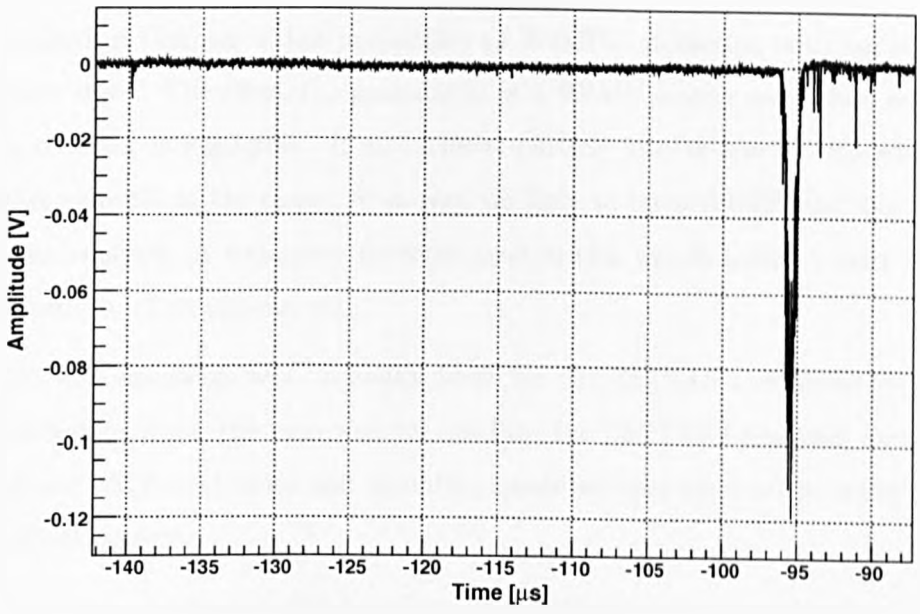

(a)

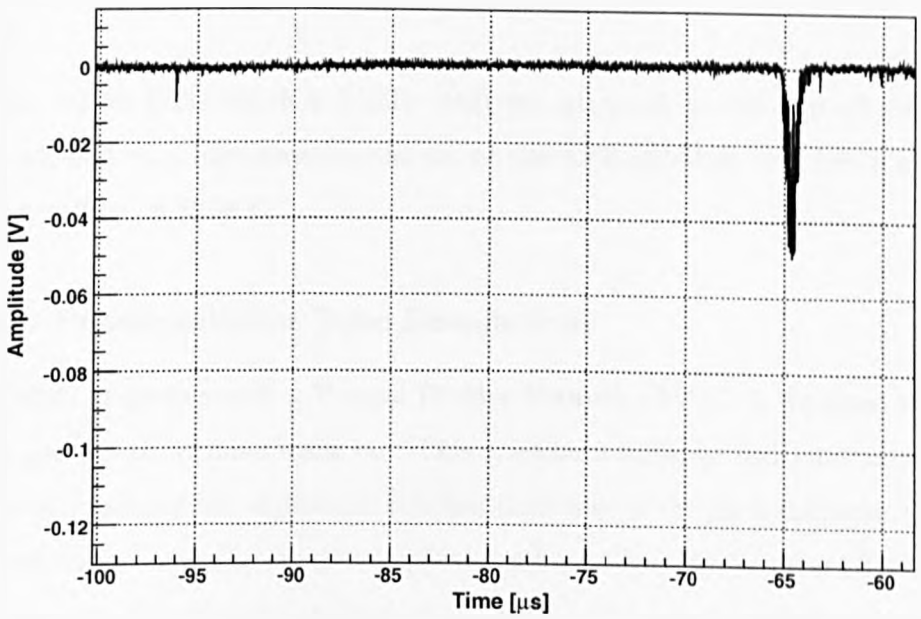

(b)

Figure 4.4: Typical 16 keVee (a) Gamma and (b) Neutron Events from ZEPLIN-II. Event-by-event discrimination is achieved by comparing the ratio of secondary to primary pulse areas at the same deposited electron equivalent energies. The area of the secondary pulse from gamma events in this example is roughly 300 times that of the primary pulse. For the neutron event, this ratio is roughly 100.

4.6 Commissioning of the Veto

As outlined in Chapter 2, the probability of WIMPs interacting with baryonic matter is relatively small. Therefore, the probability of a WIMP having more than one interaction in the detector is negligible. If an incident particle also interacts with some secondary detector external to the target, it is very unlikely to be a WIMP, and can be safely cut from the analysis. A secondary detector used in this way is called a veto, and increases the sensitivity of an experiment.

The veto hardware was originally built for the ZEPLIN-I experiment [79]. Due to hardware difficulties, the veto was not used for the ZEPLIN-I analysis, and an extensive refit of the PMT electronics and mounting hardware was undertaken before use with the ZEPLIN-II detector.

The veto is filled with 960 kg of liquid scintillator, which comprises of a mixture of 80% mineral oil and 20% phenylxenylethane ($C_{16}H_{18}$). This liquid is contained within a roughly hemispherical stainless steel shell that surrounds everything but the top of the target.

Ten 8-inch ETL 9354KA PMTs [151] are attached to the top of the veto. The ETL 9354KA is a high-pressure variant of the ETL 9354KB, and has a maximum operating voltage of 2350 V.

4.6.1 Photomultiplier Tube Installation

Each PMT, together with a Voltage Divider Network (VDN), is wrapped in 2 black bin liners and placed within a black bin. This provides a suitably dark environment, ensuring that a minimal number of photons will find their way to the photocathode. Histograms of the area under each pulse are drawn quickly with a LeCroy Waverunner LT342 oscilloscope to assess the operational potential of the tube. The supply voltage for each PMT is adjusted to determine the lowest value at which the noise and single photoelectron peaks can be resolved, thus establishing the minimum operating voltage of the tube.

It was not possible to resolve the noise and single photoelectron peaks for tubes 097195 and 074976, so these were replaced.

The original photomultiplier mounting system made use of a polymethyl methacrylate (PMMA, $C_5O_2H_8$) split-ring, which was tightened onto the glass neck of the PMT with

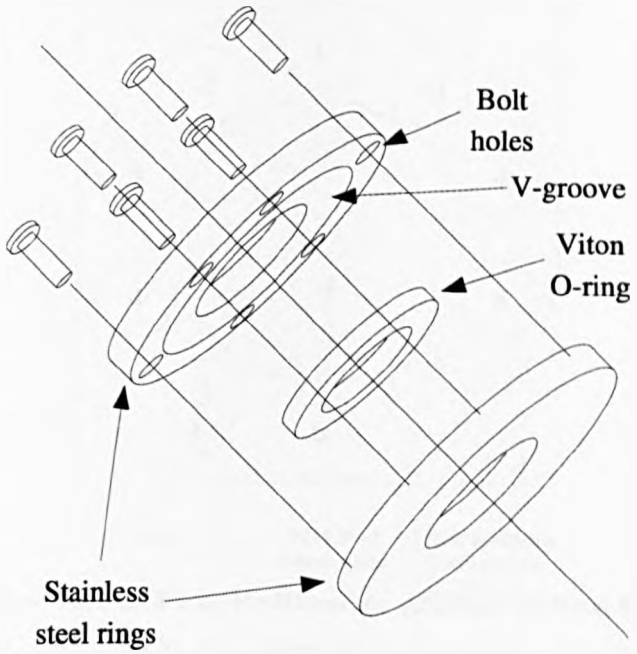

Figure 4.5: Schematic of a New ZEPLIN-II Veto PMT Support. The stainless steel rings and Viton O-ring are placed around the glass neck of the PMT. The stainless steel rings are attached to each other with six bolts, compressing the Viton O-ring, which in turn grabs onto the neck of the PMT. The bolts are screwed in uniformly with a hex key to ensure that the entire Viton O-ring is securely fixed to the PMT. To prevent excess strain being placed on the glass neck, the bolts are gently fastened until their progress starts to be impeded by the resistance of the glass neck. They are then tightened by quarter of a turn.

a single through-bolt. This split-ring was pinned to the stainless steel mounting plate with six bolts uniformly spaced round it. Therefore, when tightened to the plate, only a small section of the split-ring could flex and nip the photomultiplier. Upon opening the emptied veto for the first time after the decommissioning of ZEPLIN-I [79], one of the clamps had failed to the point that the photomultiplier would have been hanging in the liquid, supported only by its cables. Additionally, liquid scintillators are known to degrade PMMA over time, particularly when the material is under stress. Most of the PMMA split-rings showed signs of crazing round the bolt holes, and two of them had completely broken at the point where the tightening through-bolt passes.

To address these problems, it was decided to completely redesign the physical mounting system. The mechanism chosen is illustrated in Figure 4.5, in which a Viton [154] O-ring

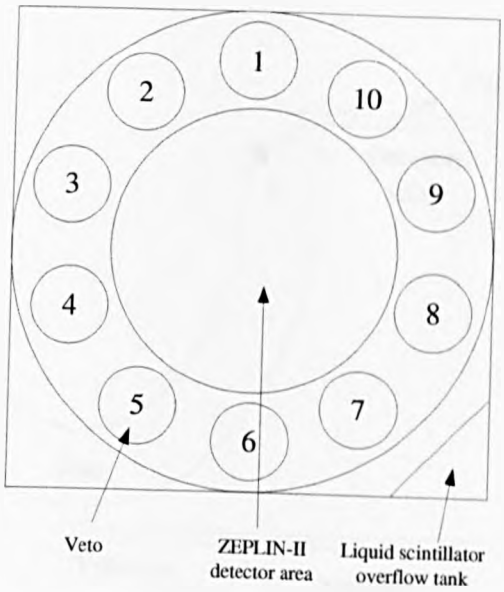

Figure 4.6: Bird's Eye View of Final Positions for ZEPLIN-II Veto PMTs relative to the Liquid Scintillator Overflow Tank. The ZEPLIN-II detector is placed in the middle of this arrangement, surrounded by the Veto.

is compressed in a V-groove such that it uniformly presses onto the glass neck of the PMT. Ten stainless steel rings are produced and machined to match the O-ring. Viton is chosen due to its resistance to aggressive solvents. Additionally, this mounting mechanism allows the use of the existing bolt holes on the mounting plate, minimising the additional machining required.

The original design also had black rubber gaskets between the mounting plates and the top of the scintillator tank, and again between the mounting plates and the copper can that protected the backs of the tubes sticking out of the veto. These gaskets had deteriorated badly, to the point that they crumbled when disturbed. This was presumably a result of the hydrogen sulphide (H_2S) attack sustained by the detector during underground operation, in addition to liquid scintillator corrosion. These were replaced with new gaskets made from Viton. An oversized Viton O-ring filled the gaps between each copper can and mounting plate in an effort to prevent light leakage.

The stainless steel rings and Viton O-ring, shown in Figure 4.5, are placed around the glass neck of each PMT. The Viton O-ring is compressed onto the neck of the PMT by fastening the bolts between the stainless steel rings with a hex key. Significant effort is made to tighten each bolt uniformly, ensuring that the entire inner area of the Viton O-ring bites into the glass neck. The bolts are gently tightened until resistance is felt

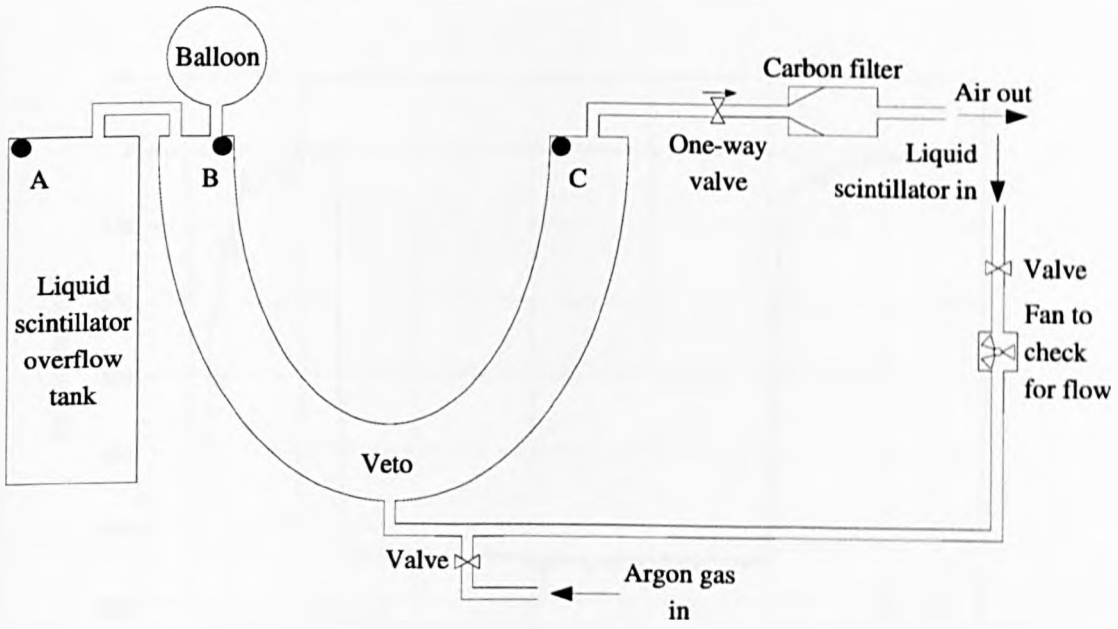

Figure 4.7: Illustration of Filling Procedure for the ZEPLIN-II Veto. Liquid scintillator is pumped into the bottom of the veto chamber, and trapped air is forced out through a one-way valve and carbon filter. A balloon is also placed on the opposite side to this outlet for collecting any excess trapped air towards the end of the procedure. A liquid scintillator overflow tank collects any excess liquid scintillator, and sensor A indicates when it is full. Sensors B and C are contained within the veto itself. An additional input for argon gas is built into the system in an effort to remove impurities from the liquid once filling is complete.

between the glass neck and Viton O-ring. The clamp is then secured by tightening each bolt by quarter of a turn only, preventing excess strain being placed on the glass neck. The mounts are then fastened to the mounting plate, and placed into one of the ten holes at the top of the tank, as shown in Figure 4.6. Finally, the protective copper can is attached.

4.6.2 Filling

After all the PMTs are fitted around the veto, it is filled with liquid scintillator, as illustrated in Figure 4.7. Liquid scintillator is pumped into a series of pipes that connect to the bottom of the veto. It passes through a transparent piece of pipe containing a fan, providing a visual indication of its motion through the pipework. This process leads to air being forced to the top of the chamber, and this is extracted through a one-way valve and carbon filter to the air of the laboratory. Additionally, a balloon constructed from

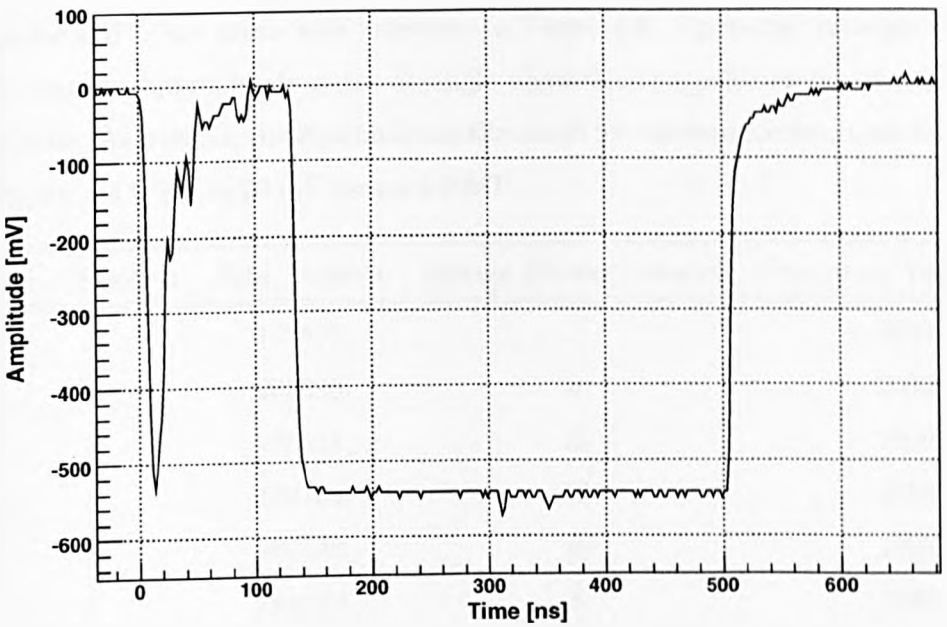

Figure 4.8: Typical Output Pulse from Veto Hardware Electronics. The hardware trigger electronics are shown in Figure 4.3. The first pulse is a sum of the analogue signals of all ten PMTs, and is always present if at least one signal satisfies the hardware discriminator threshold. The second logic pulse only appears if 5-fold coincidence is satisfied.

a black bin liner is placed on the opposite side to collect any trapped air towards the end of the procedure. Sensors are placed within the veto and liquid scintillator overflow tank, indicating when the respective chambers are full. The sensors are connected to a wall-mounted readout box. Any excess liquid scintillator should drain into the overflow tank, so there is no danger of overpressurising the vessel, and hence destroying the photomultiplier tubes. An inlet for argon gas is also built into the system so that it can be bubbled through the liquid scintillator once filling is complete. This is done in an attempt to flush out any impurities, such as air or water molecules, that may have contaminated the liquid scintillator, and as such reduced the light collection efficiency.

4.6.3 Calibration

The final stage of commissioning the veto involves assigning PMT operating voltages such that they can operate in coincidence, and establishing the light collection efficiency.

The hardware trigger electronics for the veto are shown in Figure 4.3. Signals from

Table 4.1: Calibration of ETL 9354KA PMTs Installed on ZEPLIN-II Veto. Final positions for PMTs are given with reference to Figure 4.6. Operating voltages are adjusted such that the approximate mean of single photoelectron pulse amplitudes is 30 mV for each tube. As a result, the discriminator threshold for the veto hardware electronics shown in Figure 4.3 is set to 20 mV for each PMT.

Final Position	Tube Number	Voltage Divider Network	Operating Voltage [V]
1	133510	1	1986
2	233296	0	2035
3	238514	11	1800
4	169704	10	1650
5	167733	6	1590
6	230250†	8	1990
7	226006‡	4	1680
8	167932	5	1670
9	167990	9	2110
10	161258	3	1640

†Replacement for tube number 097195
‡Replacement for tube number 074976

each tube are sent to an adder. If each signal satisfies the discriminator threshold, the total analogue signal is sent to channel 8 of the Acqiris DAQ and a logic signal is sent to a coincidence unit. If 5-fold coincidence is achieved, then the logic pulse is sent through a 15 m cable that acts as a delay, fed into the adder, and then sent to DAQ channel 8. As a result, an analogue pulse is always present if there is a signal in the veto. However, the second logic pulse, of width 375 ns, only appears 100 ns after the analogue pulse if five PMTs have seen a signal within 100 ns of each other. Such a configuration allows for some degree of flexibility when assessing the rejection efficiency of nuclear recoils. An example of an output pulse that satisfies 5-fold coincidence is shown in Figure 4.8.

In order to achieve 5-fold coincidence, the amplitude for the single photoelectron pulse from each PMT must be similar. Therefore, the supply voltages are adjusted to ensure that the mean position of the single photoelectron peak is approximately 30 mV for each tube. The most accurate way of achieving this is to record single photoelectron pulses

from each tube with the Acqiris DAQ, and analyse them offline. However, this procedure is very time consuming, and such accuracy is not required.

Instead, a LeCroy Waverunner LT342 oscilloscope records single photoelectron pulse amplitudes and displays histograms in real time. An initial operating voltage of 1900 V is supplied to a PMT, and the signal is sent to the oscilloscope. Software internal to the oscilloscope records any pulses that are of amplitude greater than 5 mV, and draws a histogram of their heights. Data are acquired until a peak becomes evident. Cursors are then used to find the approximate position of this peak, and if it lies below 30 mV, the supply voltage to the PMT is increased and the measurement is repeated. If the position of the peak is greater than 30 mV, the operating voltage is decreased. This continues until the approximate peak position of single photoelectron pulse amplitudes is 30 mV. Although sacrificing accuracy, this procedure allows for quick measurements when changing operating voltages, and hence is more efficient. The measurements are conducted on each tube, and the resulting operating voltages for PMTs in relation to their final position on the veto is given in Table 4.1. As a consequence, a discriminator threshold of 20 mV ($\approx 66\%$ of the single photoelectron pulse amplitude) is set on the veto hardware trigger electronics.

Although an accurate method of defining the single photoelectron peak is not required for the trigger electronics, it is necessary in order to obtain a value for the number of photons expected as a function of the deposited energy. This is known as the light yield, and single photoelectron pulses from each PMT attached to the veto have been recorded with the Acqiris DAQ. An internal DAQ hardware discriminator of threshold 5 mV has been used, and the recorded pulses have been analysed to obtain height and area distributions for each tube.

The light yield L can be determined by exposing the detector to a source of gamma-rays of energy E_γ, and fitting a Gaussian function to the resultant distribution to determine the mean amplitude H_γ. The light yield is given by:

$$L = \frac{H_\gamma}{H_{\text{spe}} E_\gamma} \tag{4.1}$$

where H_{spe} is the mean amplitude from a single photoelectron in the tube in question.

However, inspection of individual pulses shows that photons do not arrive at each PMT at the same time. This is because the position of the event determines the time taken for

photons to reach each PMT. With reference to Figure 4.6, photons from an event that occurs close to the PMT in position 1 will take less time to arrive at this PMT than that in position 6. Placing a gamma-ray source next to PMT 1 shows that there is as much as a 16 ns gap between the start times of pulses in tubes 1 and 6. The significance of this result lies in the fact that the adder does not take pulse start times into account when it sums the waveforms. This means that only the PMTs closest to the position of the event contribute to the amplitude of the summed signal. The rest are lost in the tail of the pulse. Therefore, using Eq. (4.1) in this case results in an underestimation of the light yield.

As an alternative, the pulse areas from single photoelectron distributions A_{spe} and the mean pulse area from the gamma-ray source A_γ can be used:

$$L = \frac{A_\gamma}{A_{\text{spe}} E_\gamma} \tag{4.2}$$

This solves the problem incurred when using amplitudes, as all PMTs contribute to the light yield rather than only those closest to the event. The single photoelectron pulse area distributions for each veto PMT are shown in Figures 4.9 and 4.10. The mean value of these distributions is 0.223 ± 0.007 nVs.

An emitter of gamma-rays of sufficient energy to be distinguished from a noise peak is required. The β^--decay source cobalt-60 (^{60}Co) satisfies this condition, and its distribution is shown in Figure 4.11. Two prominent gamma lines are emitted from ^{60}Co, at 1.17 MeV and 1.33 MeV. It is clear from Figure 4.11 that the energy resolution of the liquid scintillator is too poor to distinguish these lines. As a result, the mean value of $E_\gamma = 1.25$ MeV is substituted into Eq. (4.2). Using the mean value of the fit in Figure 4.11, a light yield of 0.0191 ± 0.0007 pe/keV (photoelectrons per keV) is derived.

The poor light yield can be attributed to impurities in the liquid scintillator. As mentioned in Section 4.1, gamma-ray sources are placed just underneath the inner target vessel with a source dropper. With reference to Figure 4.12, most electron recoils induced by gamma-rays from ^{60}Co will occur about half-way up the veto. The scintillation photons need to traverse a relatively long distance to reach the PMTs at the top of the chamber. Therefore, there is ample opportunity for light loss through absorption by impurities. Possible solutions include re-designing the veto such that PMTs are also located in the middle and base of the vessel, and distilling the liquid scintillator to remove these impurities [155].

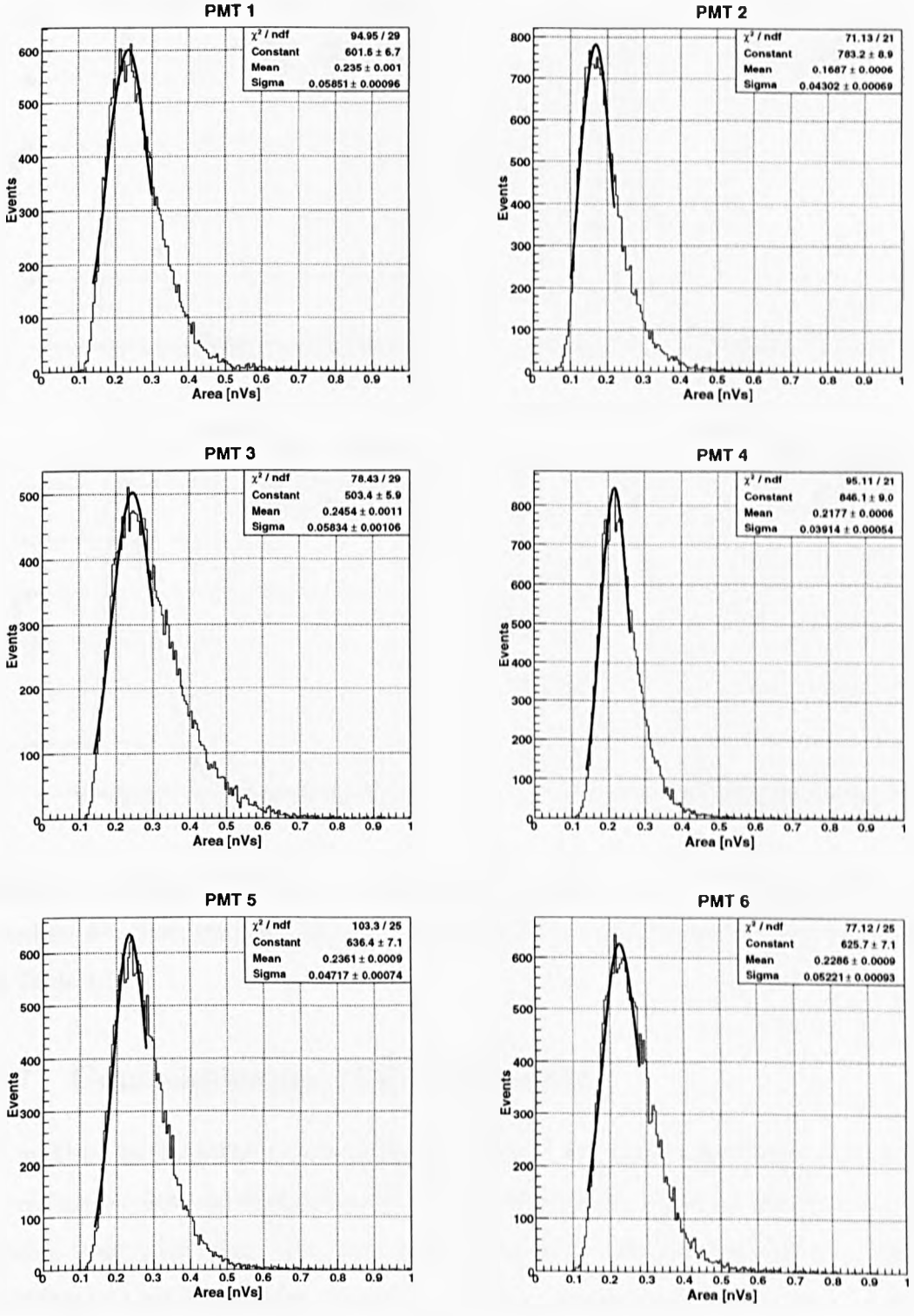

Figure 4.9: Single Photoelectron Pulse Area Distributions for Veto PMTs 1 to 6. Tube numbers are given according to their final position around the veto (Figure 4.6), as listed in Table 4.1.

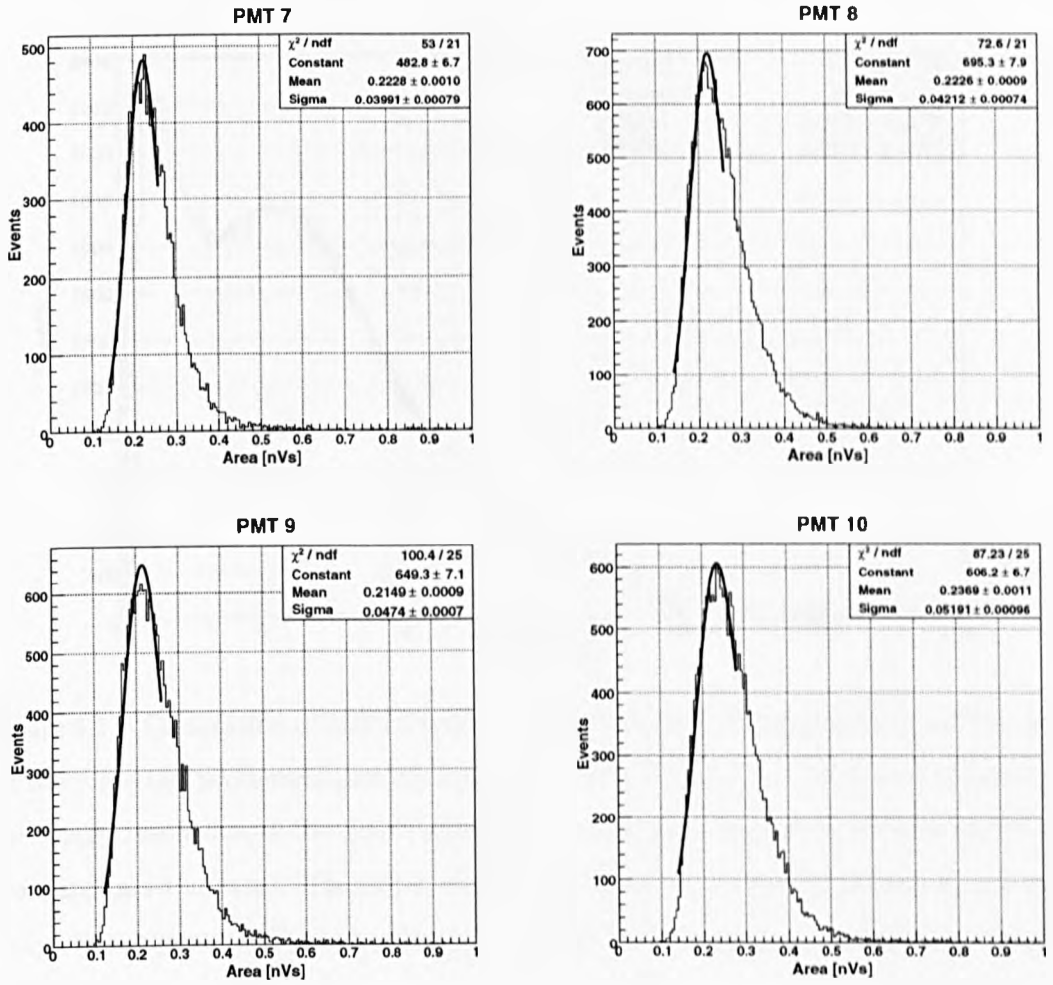

Figure 4.10: Single Photoelectron Pulse Area Distributions for Veto PMTs 7 to 10. Tube numbers are given according to their final position around the veto (Figure 4.6), as listed in Table 4.1.

4.7 Commissioning of the Shielding

In addition to the active veto described in Section 4.6, passive shielding is also required to reduce the external background to a level low enough to prevent the data acquisition system from saturating. The term passive indicates that any interactions within this shielding will not be recorded. Due to the different properties and interactions of gamma-rays and neutrons in matter (Section 3.5), there is no material that will provide adequate shielding for both. As a compromise, passive shielding from background radiation generally comprises of two or more different materials. As the gamma-ray interaction cross-section is proportional to the atomic number of a target atom, dense, high Z materials are the

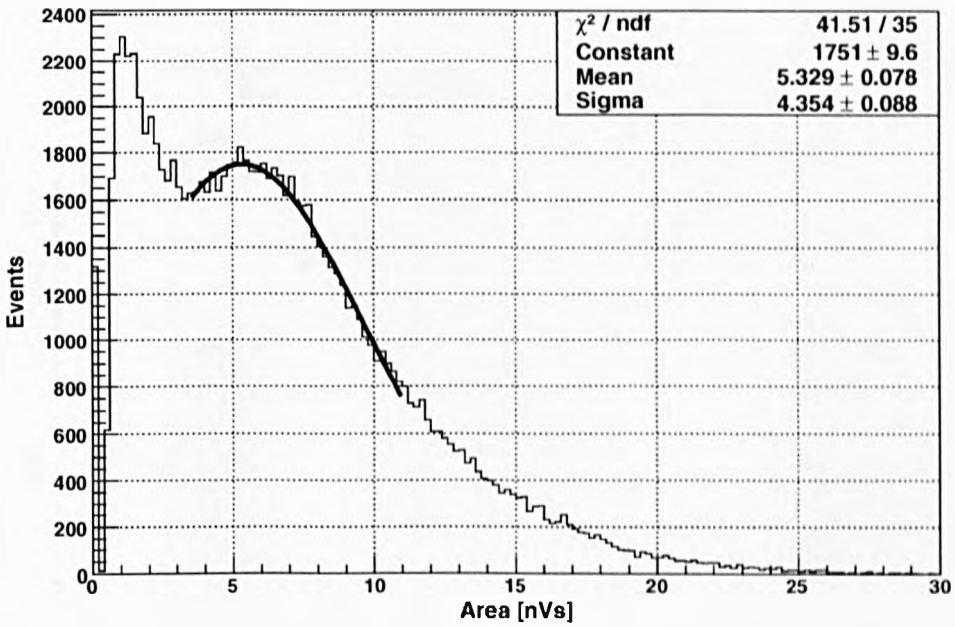

Figure 4.11: Calibration of ZEPLIN-II Veto with 1.25 MeV Gamma Line from ^{60}Co Source. As there are two prominent gamma lines emitted by ^{60}Co at 1.17 MeV and 1.33 MeV, and the energy resolution of the liquid scintillator is not good enough to distinguish them, the peak appears the same. Therefore, a mean of these two values is defined as the gamma energy of the peak. A Gaussian function is fitted to the peak corresponding to the gamma line.

best for attenuating such particles. In contrast, neutron-proton interactions result in the highest possible fractional energy loss in a single nuclear recoil, and therefore materials with a large hydrogen content are the most suitable for passive neutron shielding.

An illustration of the dimensions and positioning of the passive shielding with respect to the target and veto is given in Figure 4.12.

4.7.1 Gamma-Ray Shielding

Lead is the densest commonly available material, making it the best choice for shielding of gamma radiation. Lead ingots recycled from the NaIAD [70] and ZEPLIN-I [79] experiments surround the detector. Due to the dusty environment at Boulby Mine, the cleaning of these ingots was necessary to remove any traces of radioactive particles, thus maintaining a low gamma-ray background.

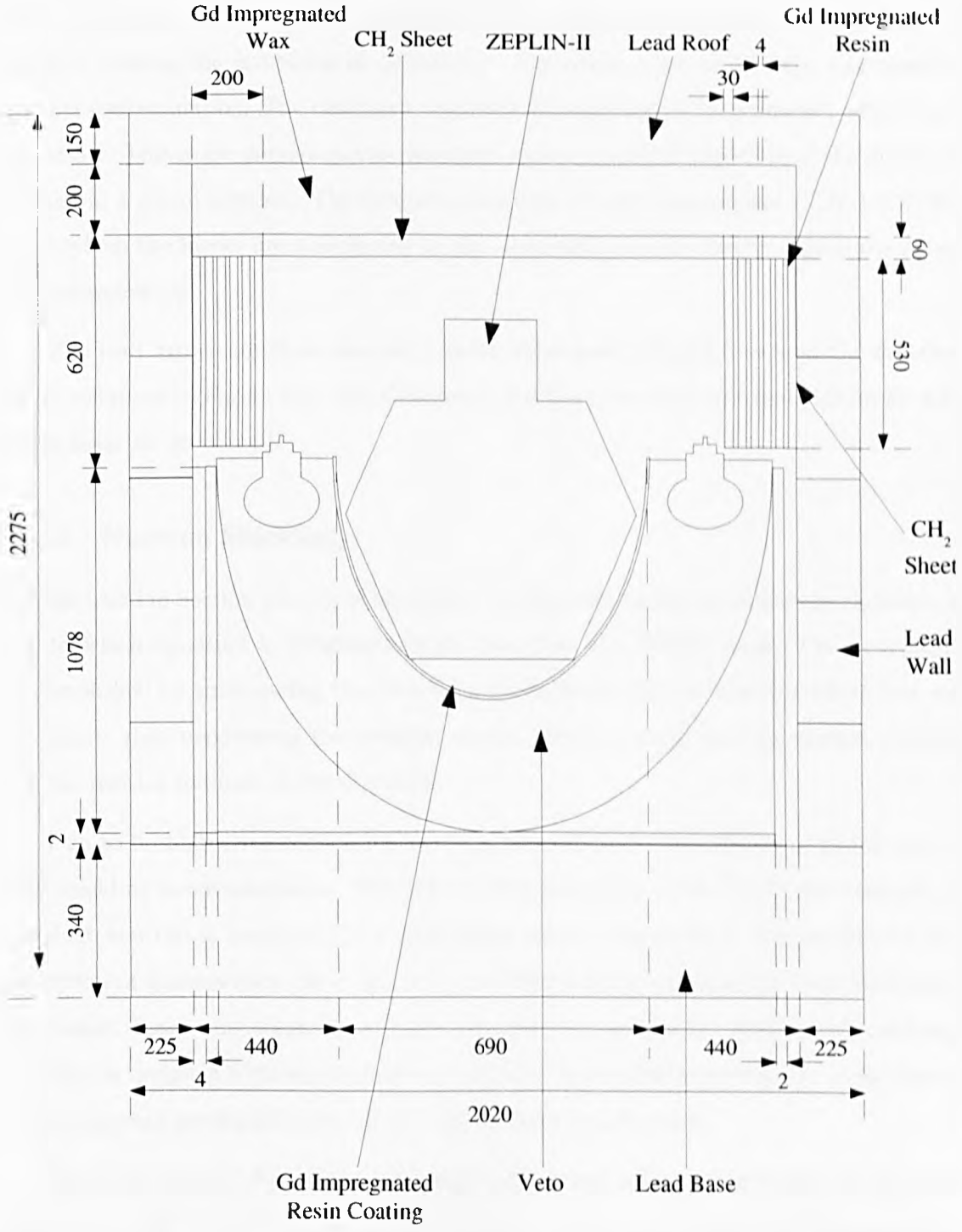

Figure 4.12: Sketch of Gamma-Ray and Neutron Shielding surrounding ZEPLIN-II. Dimensions are in mm.

The top layer of lead on each ingot can be removed by soaking it in a detergent that contains either sodium carbonate (Na_2CO_3) or sodium hydroxide (NaOH). The detergent should not be strongly alkaline as this will dissolve the layer of lead oxide (Pb_2O) on the surface, causing the formation of plumbates. Plumbates, such as $KPbO_2$, can result in further contamination. The detergent used was 'Lemon Flash - All Purpose', which has a pH of 8.5. This is low enough not to cause any major problems, especially if the ingots are soaked in a dilute solution. The detergent is wiped-off with isopropanol ($(CH_3)_2CHOH$), after which the ingots are transferred to the clean area and covered to reduce the extent of contamination.

The lead ingots are then stacked in steel boxes and positioned around the detector. With reference to Figure 4.12, the detector and veto system are surrounded from all sides by at least 15 cm of lead.

4.7.2 Neutron Shielding

As discussed in Section 2.5.1, it is important to eliminate background neutron radiation as its detection signature is indistinguishable from that of a WIMP event. This is typically accomplished by surrounding the detector with hydrogen-rich materials such as wax and polymers, thus maximising the possible energy loss in a single neutron-nucleus collision for the reasons outlined in Section 3.5.2.

Due to its high cross-section for slow neutron capture, the addition of gadolinium to any shielding is advantageous. Through the reaction given in Eq (3.17), for example, an incident neutron is captured by a gadolinium nucleus resulting in the production of a spectrum of gamma-rays. As it is possible to discriminate gamma-rays from neutrons in the target vessel, this results in an increased possible sensitivity. Additionally, although the veto is designed with an emphasis on neutron background rejection, the large number of gamma-rays produced in Eq. (3.17) will improve its efficiency.

The roof consists of a volume of gadolinium impregnated wax of height 20 cm with a square base of 157 cm. The wax is placed in five 1 cm thick steel boxes, and surrounded by lead to provide additional gamma shielding. Around 493 l of wax of density 0.89 g/cm^3 has been cast in wooden boxes, and 3.782 kg of gadolinium is uniformly distributed throughout. Gadolinium granules are diluted in a solvent, added to the molten wax at a temperature of 363 K, and mixed to ensure an even distribution.

Large quantities of the solvent are found to weaken the structure of the cast. Hence, a solvent with a high dilution efficiency and boiling point below the temperature of molten wax is required. A dilution efficiency of 33% is comfortably achieved with isopropanol. Additionally, isopropanol has a boiling point of 355 K, meaning that most of the solvent boils-off when the mixture is added to the wax. Although water is a better solvent, it is immiscible with wax so could not be used.

Adequate neutron shielding is provided by the veto up to 63 cm below the roof. An inner shield wall is constructed and installed around the remaining volume. A polypropylene sheet is cut into triangles, which are assembled to a height of 110 cm in the four corners within the veto's housing. The inner walls are supported by this structure. They comprise of a sandwich of 3 cm thick polypropylene sheets and 0.4 cm thick gadolinium impregnated resin. Around 1.06 kg of gadolinium was diluted in water to form 3.04 kg of gadolinium nitrate hexahydrate ($Gd(NO_3)_36H_2O$). A further 13.75 kg of water is added to the compound, together with 41.25 kg of resin (styrene monomer $C_{10}H_8O_4$). This is mixed well and a catalyst is added to aid polymerisation. The mixture is placed on a flat surface to polymerise. Once hardened, they are drilled into polypropylene sheets of thickness 3 cm. A total of 480 kg of polypropylene sheets are used during construction, meaning that the average gadolinium loading for the whole inner wall is around 0.2%.

Due to the impracticalities of adding gadolinium to the liquid scintillator housed within the veto, 2.76 kg of gadolinium nitrate hexahydrate is mixed with 1.92 kg of styrene monomer. A small amount of catalyst is added, and this mixture is painted onto the inside of the veto.

A 6 cm thick sheet of polypropylene is located directly underneath the roof sections to provide additional shielding. It sits on the neutron shielding that forms the inner wall. A hole of diameter 10 cm has been drilled through the sheet to facilitate the insertion of a neutron source for detector calibration.

The positioning of neutron shielding around the target and veto is shown in Figure 4.12.

4.8 Background Rejection Efficiency of the Veto

In order to maximise the background rejection potential of the veto, an associated cut needs to be implemented in the ZEPLIN-II dark matter search analysis. The parameters of this

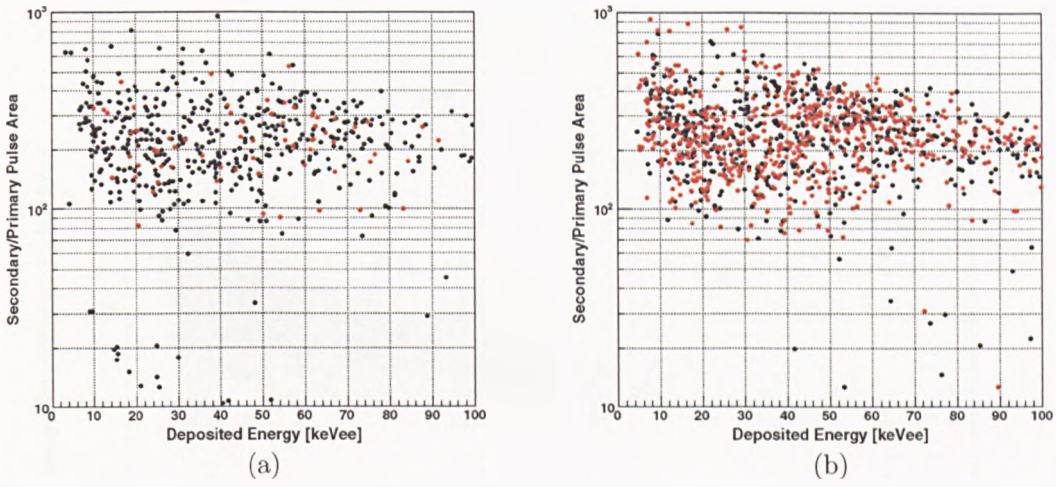

Figure 4.13: Secondary-to-Primary Pulse Area Ratio vs. Deposited Energy in ZEPLIN-II for Sample (a) Background; and (b) ^{60}Co Events. Events that survive the standard cuts are shown on both plots. Those that are rejected by the veto cut are coloured red. From Figure 4.4 it is clear that, at the same electron equivalent energy, the secondary-to-primary pulse area ratio for electron recoils is greater than that for nuclear recoils. This is clearly seen when drawing comparisons between (b) and Figure 4.14. Plots are for comparison only. Some vetoed events cover those that are accepted.

cut, and its efficiency, are defined here. Samples of data from background, and gamma-ray (^{60}Co) and neutron (americium beryllium (AmBe)) source runs are considered.

Preliminary fiducialisation cuts are performed on each data set as described in [101]. In addition, events that deposit an energy greater than 100 keVee in the target are rejected as the differential rate for dark matter interactions drops off in this domain (see Section 2.5.1 for details).

Scatter plots of the discrimination factor, secondary-to-primary pulse ratio, against the energy deposited in the target for events that satisfy these cuts are shown in Figures 4.13(a), 4.13(b) and 4.14 for background, gamma-rays and neutrons respectively. As expected from Figure 4.4, the low secondary-to-primary pulse ratio band of nuclear recoils is absent in gamma-ray runs, but present in the neutron data set.

The ZEPLIN-II reduction code scans the veto waveform from each event, searching for scintillation pulses and flagging any that have a 5-fold coincidence logic signal associated with them as shown in Figure 4.8. Therefore, by defining a time interval of -500 ns to

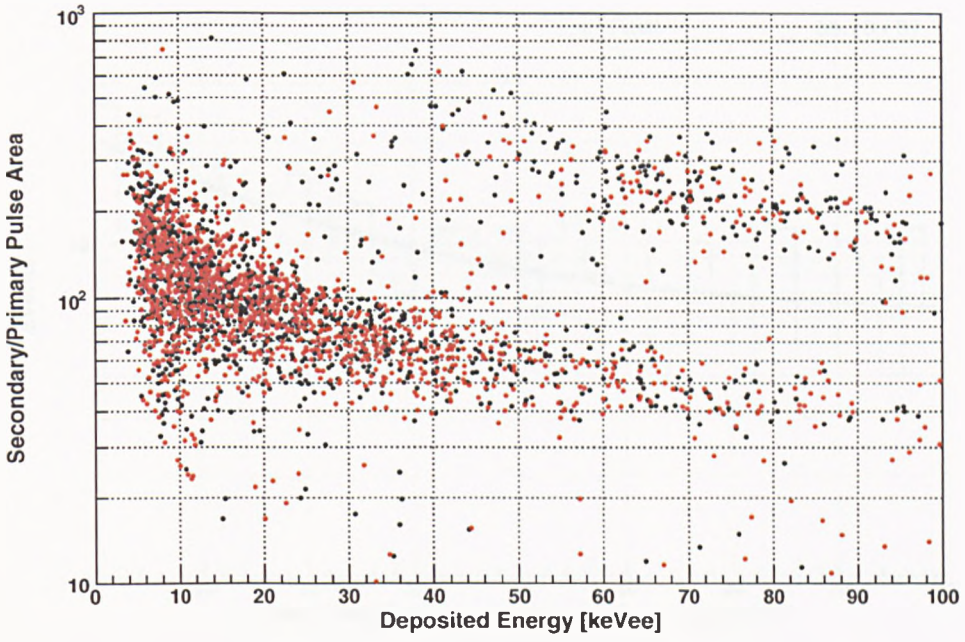

Figure 4.14: Secondary-to-Primary Pulse Area Ratio vs. Desposited Energy in ZEPLIN-II for Sample AmBe Events. As with Figure 4.13, events that survive the standard cuts are shown, and those that are rejected by the veto cut are coloured red. With reference to Figure 4.13(b), the secondary-to-primary pulse area ratio for nuclear recoils is smaller than that for electron recoils at the same electron equivalent deposited energy. This forms the basis of discrimination in two-phase xenon detectors. Plot is for comparison only. Some vetoed events cover those that are accepted.

+100 μs relative to the start of the primary pulse in the target, the number of vetoed events in each data set can be determined as listed in Table 4.2.

As the primary purpose of the veto is to reject the nuclear background, features of the time delay distribution between veto and target pulses from the AmBe source run reveal the origins of vetoed events. Approximately 75% of vetoed events occur between 0 ns and 100 ns after the start time of the target pulse. These are from neutrons that scatter off target nuclei and interact in the veto.

There is a larger time delay associated with neutron capture by gadolinium nuclei, and the subsequent emission of gamma-rays that are detected in the veto. To obtain this, a function can be defined and fit to the difference between the start times of a 5-fold veto trigger and a primary scintillation pulse in the target. The time delay between veto and

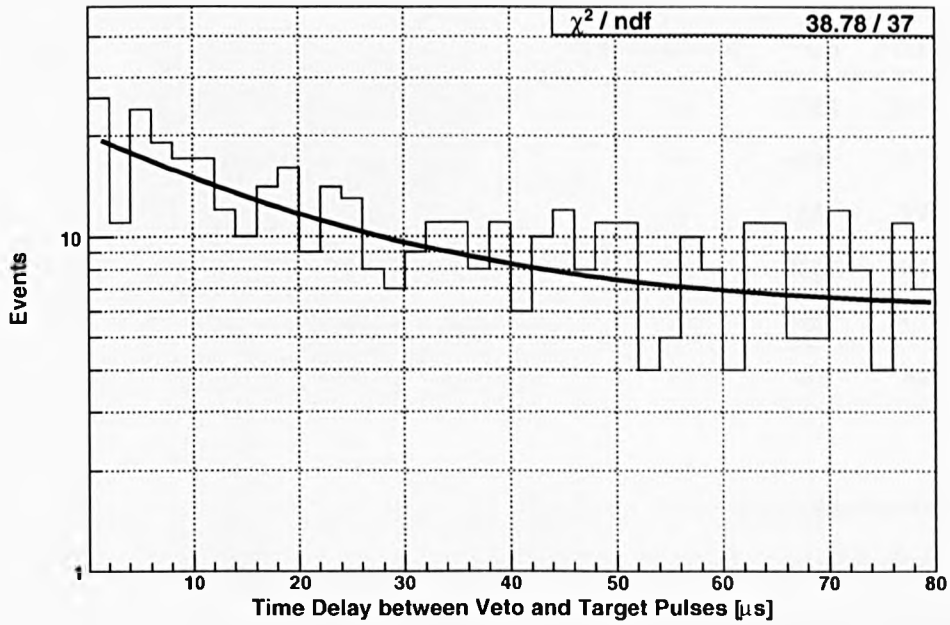

Figure 4.15: Fit to Time Delay between Veto and Target Pulses in the interval 150 ns to 80 μs. The data is best fit with an exponential decay plus a flat background function, given in Eq. (4.3). The mean lifetime of the exponential decay component is 22 μs. The exponential is from neutron capture by gadolinium nuclei and the delayed emission of gamma-rays, while the flat background comes from accidental coincidences.

target pulses from the AmBe source run, 150 ns to 80 μs after the target pulse is shown in Figure 4.15. The distribution of $N(t)$, the number of events at time t, is best fit by the sum of exponential decay and flat background terms:

$$N(t) = N_0 e^{-\frac{t}{\tau}} + A \tag{4.3}$$

where N_0 is the number of vetoed events 150 ns after the primary scintillation pulse in the target vessel, and τ is the decay time of the exponential function. The flat background is given by the constant A. The function given by Eq. (4.3) is fit to the data in Figure 4.15, providing a decay time of 22 μs. The exponential term represents the portion of events in this run due to neutron scattering in the target. The flat background comes from accidental coincidences.

Vetoed events in the scatter plots shown in Figures 4.13 and 4.14 are highlighted in red. First indications show that a large proportion of events are rejected by the veto cut

Table 4.2: Results of Tests on the Veto Trigger for Background and Source Data.

	Background	^{60}Co	AmBe
Number of events selected	550	1184	2679
Number of vetoed events	76	626	1573
Vetoed events [%]	14	53	59
Background rate [Hz]	85	3800	860
False coincidence probability [%]	0.85	32	8.3
Rejection efficiency of veto [%]	14	31	54

in both the AmBe and ^{60}Co data runs. However, there is no consideration of the false coincidence rate factored into these figures, and thus, they are misleading.

Extending the distribution in Figure 4.15 to a time interval of -80 μs to $+80$ μs indicates that, as expected, such an exponential as that defined by Eq. (4.3) is not present. The distribution is flat, implying that these events are from background sources. By counting the number of vetoed pulses from the beginning of the waveform to 500 ns before the start of the primary pulse, and dividing this by the total pre-trigger time, the background veto rate R for each run can be determined. These are given in Table 4.2.

Therefore, the mean number of interactions μ in a time interval T is given by:

$$\mu = RT = R(t_2 - t_1) \tag{4.4}$$

where t_1 and t_2 are the start and end of the time interval relative to the primary pulse. Obeying Poissonian statistics, the probability $P(\mu; n)$ of n interactions occuring is given by:

$$P(\mu; n) = \frac{\mu^n e^{-\mu}}{n!} \tag{4.5}$$

Therefore, the false coincidence probability, in other words the probability of one or more interactions $P(\mu; 1+)$ occuring over time interval T, is:

$$\begin{aligned} P(\mu; 1+) &= 1 - P(\mu; 0) \\ &= 1 - e^{-\mu} \end{aligned} \tag{4.6}$$

where μ is given by Eq. (4.4). Using the background veto rates calculated separately for each run, and $t_1 = -500$ ns and $t_2 = +100$ μs, the false coincidence probability from Eq. (4.6) is given in Table 4.2.

As random coincidences can occur at the same time as good veto events, the rejection efficiency of the veto ϵ_v is not simply the difference between the percentage of vetoed events and false coincidence probability. The probability of a non-vetoed event in the ZEPLIN-II detector $P(\not{\text{v}})$ is given by the product of $P(\mu;0)$ and the probability that the veto accepts an event $(1-\epsilon_v)$:

$$\begin{aligned} P(\not{\text{v}}) &= (1-\epsilon_v)(1-P(\mu;1+)) \\ &= 1-\epsilon_v - P(\mu;1+) + \epsilon_v P(\mu;1+) \end{aligned} \tag{4.7}$$

Therefore, the probability of an event being vetoed $P(\text{v})$ is given by:

$$\begin{aligned} P(\text{v}) &= 1-P(\not{\text{v}}) \\ &= \epsilon_v + P(\mu;1+) - \epsilon_v P(\mu;1+) \end{aligned} \tag{4.8}$$

By rearranging Eq. (4.8), the background rejection efficiency is given by:

$$\epsilon_v = \frac{P(\text{v}) - P(\mu;1+)}{1-P(\mu;1+)} \tag{4.9}$$

The rejection efficiencies of the veto for background and source data are given in Table 4.2.

Due to the very high background rate during the ^{60}Co run, the probability of false coincidence is relatively high. This explains why the percentage of vetoed events is comparable with that for the AmBe data set, yet the rejection efficiency of gamma-rays is $\approx 60\%$ of that for neutrons. This is expected from the large number of hydrogen atoms in the liquid scintillator, which provoke a greater energy loss from incident neutrons rather than gammas.

By comparison, the neutron background rejection efficiency is 54%, which is in agreement with a previous calculation from another data set [156]. The figure is also consistent with simulation studies [157].

The veto efficiency, which is the probability of the acceptance of a WIMP signal, is simply the probability of there being no false veto triggers over the time interval T in background data set. This is given by $P(\mu;0)$ in Eq. (4.6), and comes out to be 99%.

4.9 Summary

The ZEPLIN-II detector is a two-phase xenon-based dark matter detector at Boulby Mine, North Yorkshire, United Kingdom. A liquid xenon target of mass 31 kg is viewed by seven photomultiplier tubes, and contained within a PTFE conical frustrum to aid light collection. A uniform electric field strength of 1 kV/cm is maintained across the liquid phase such that electrons from electron-hole pairs, formed by interactions with particle radiation, drift to the liquid-gas boundary. A higher electric field strength at the liquid surface enables the extraction of these electrons into the gas phase, producing a secondary electroluminescence pulse. This acts as a direct measurement of the ionisation, and the ratio of this pulse to that from scintillation enables event-by-event discrimination of nuclear and electron recoils.

The inner vessel is thermally insulated by a roughing vacuum. Xenon purity levels are assessed from the observation of high energy alpha events from radon contamination in the target. In the event of overpressure in the target vessel, xenon is automatically stored in its gas phase in the dump tanks at a pressure of 1 bar. Waveforms are digitised with an 8-channel Acqiris data acquisition system, seven channels of which are connected to the target photomultipliers. The final channel is the sum of the signals from the ten veto photomultiplier tubes.

The cross-section of WIMP-nucleon interactions is relatively small, thus an interaction in the target in coincidence with one in an external detector is unlikely to be a WIMP event. The liquid scintillator filled veto is such an external detector that surrounds everything but the top of the ZEPLIN-II target. Due to the damage inflicted during its operation with the previous ZEPLIN-I detector, an extensive refit of the PMT electronics and mounting hardware has been performed. Single photoelectron distributions have been calibrated such that 5-fold coincidence operation is possible, and this is recorded as an analogue pulse followed by a logic pulse 100 ns later. Neutron and gamma shielding complement the veto, and reduce the intensity of backgrounds external to the main target. Tests of the veto trigger with source data yield gamma and neutron background rejection efficiencies of 31% and 54%. This is in good agreement with a previous analysis on a different data set, and results from simulations. The efficiency of the veto for the acceptance of a WIMP signal has been determined to be 99%.

Chapter 5

Quenching Factor Measurements in Sodium Iodide

Inorganic crystal scintillators are popular choices as target materials for direct dark matter search experiments (Section 2.5.3). The high light yield and pulse shape differences between nuclear and electron recoils explain why thallium activated sodium iodide (NaI(Tl)) crystals are the oldest scintillators used in such experiments [66]. They still remain the best at determining spin-dependent WIMP-nucleon limits, and the ANAIS [67], DAMA/NaI [68] and ELEGANT-V [69] direct search experiments utilise them. The DAMA/NaI experiment is the only one that has claimed to witness the annual modulation of a WIMP signal [68, 103], and until very recently, NaIAD [70] held the best spin-dependent limit on WIMP-proton interactions [71]. DAMA/LIBRA [72] is a next generation NaI(Tl)-based detector currently taking data at Gran Sasso. Hence, NaI(Tl) remains an important detector material in non-baryonic dark matter searches. Its relevant properties are outlined in Table 5.1.

As described in Section 3.6.2, the quenching factor is the ratio of light induced by a nuclear recoil S_{nr} to that by an electron of the same energy S_{er} (Eq. (3.18)). Dark matter experiments are calibrated with gamma-lines, such as the 122 keV line from ^{57}Co, to determine an energy scale. Nuclear recoils emit less light due to the reasons outlined in Section 3.6.1, and hence such an event appears to be of lower energy than it actually is. If the detected energy is multiplied by the reciprocal of the quenching factor, this effect can be corrected for. As neutrons do not have the same interaction cross-sections in different materials, for reasons given in Section 2.5.1, it is necessary to determine the quenching

Table 5.1: Properties of Sodium Iodide (NaI(Tl)) Relevant to its Scintillation. Values taken from [158].

Density	3.67	g/cm^3
Refractive Index	1.85	
Peak Emission Wavelength	415	nm
Decay Time	230	ns
Absolute Light Yield	38	photons/keV

factor for each scintillating dark matter target material independently. Additionally, the scintillation efficiency changes depending on the recoil energy, highlighting the importance of measurements at energies relevant to dark matter searches (below 50 keVee).

The characteristics of scintillation pulses from BC501A and NaI(Tl), and optimisation of the analysis code are detailed in the first part of this chapter. This is essential background to undertaking the quenching factor experiment described in the second part of this chapter. The work outlined in here was presented at the Sixth International Workshop on the Identification of Dark Matter 2006 [159], and has been recently published [160]. The experiment was conducted with the aid of Dr. Pawel Majewski at the University of Sheffield.

5.1 The Neutron Facility

Two Sodern GENIE 16 neutron generators are housed within a dedicated neutron laboratory at the University of Sheffield. The deuterium-deuterium and deuterium-tritium accelerators produce an isotropic distribution of mono-energetic neutrons by the reactions outlined in Eq. (3.19) and Eq. (3.20) respectively. All electronics and data acquisition equipment are located in the control room, which is isolated from the experimental hall by 3 ft of concrete shielding. During operation, the beam is placed into a concrete castle to provide additional shielding.

A diagram of the detector arrangement is shown in Figure 5.1. The deuterium-deuterium neutron beam is used for these measurements. Neutrons of energy 2.45 MeV are funneled through a hole in the concrete castle. They travel 50 cm before reaching the

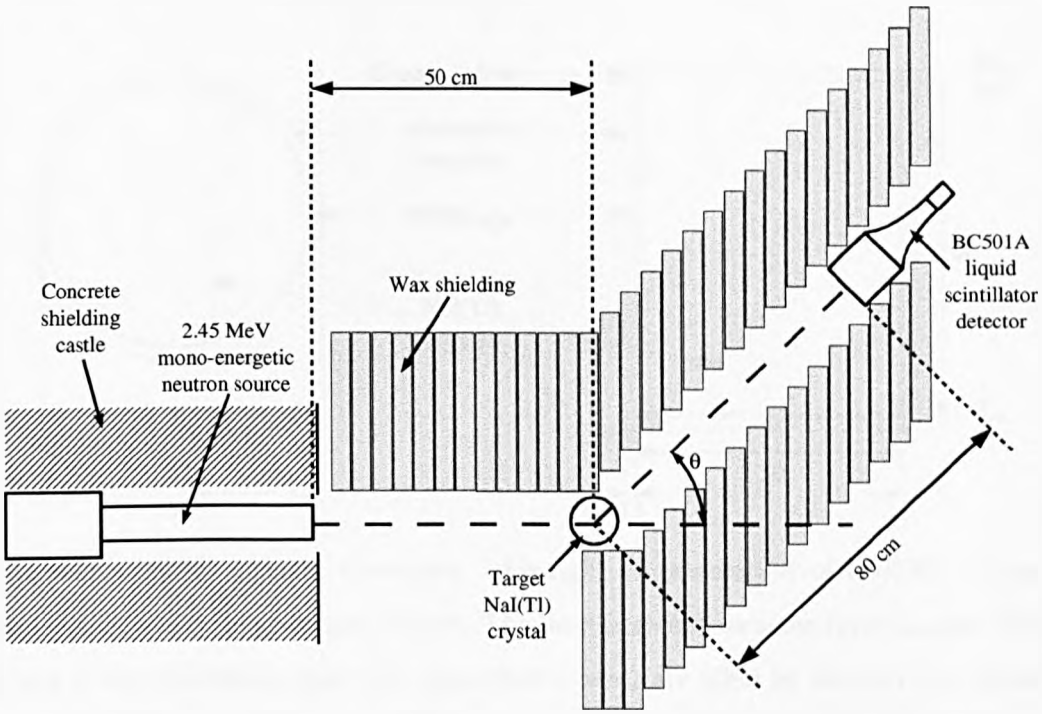

Figure 5.1: Schematic View of the Detector Arrangement used to Measure Scintillation from Nuclear Recoils in NaI(Tl).

centre of the NaI(Tl) crystal. The energy deposited E_R as a function of the scattering angle θ is given by Eq. (3.15), which can be rearranged in terms of θ:

$$\theta = \cos^{-1}\left(1 - \frac{E_R(m_A + m_\mathrm{n})^2}{2m_A E_\mathrm{n} m_\mathrm{n}}\right) \tag{5.1}$$

where m_A is 22.990 for ^{23}Na and E_n is 2.45 MeV. Using Eq. (5.1), scattered neutrons are detected by a secondary detector of BC501A liquid scintillator, which is placed at an angle θ for the recoil energies of interest E_R. It is moved for each measurement, and wax blocks line the path of the neutrons to provide additional shielding.

With reference to Figure 5.1 and Eq. (5.1), the distance between the neutron source and BC501A detector c in terms of the scattering angle θ is given by the cosine rule:

$$c = \sqrt{a^2 + b^2 - 2ab\cos\left(180° - \theta\right)} \tag{5.2}$$

where the distance between the neutron source and NaI(Tl) crystal is $a = 50$ cm and that from the target to the liquid scintillator is $b = 80$ cm. The distance c is altered until Eq. (5.2) is satisfied for each scattering angle θ investigated.

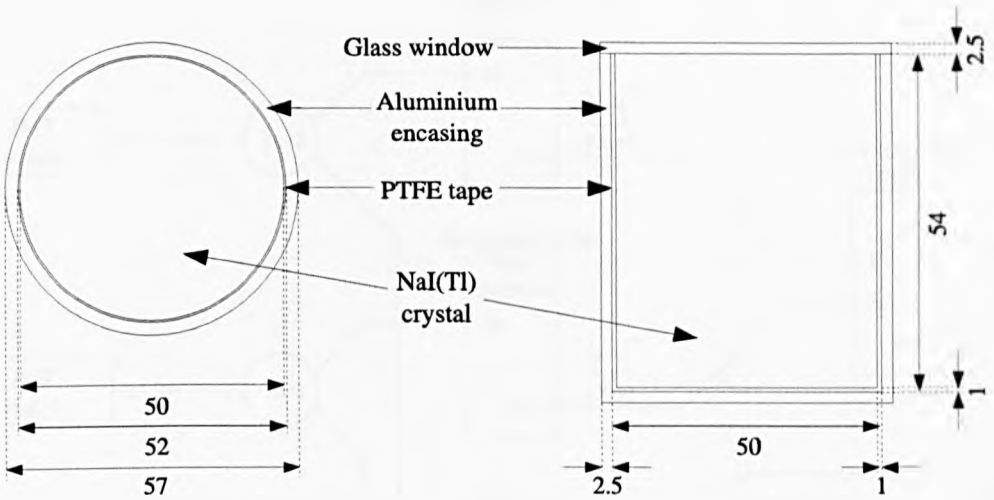

Figure 5.2: NaI(Tl) Crystal Geometry. Air-tight encapsulation of NaI(Tl) crystals is essential due to their hygroscopic nature. The interfaces between the crystal, glass window and face of the photomultiplier tube (not shown here) are filled by silicon oil of refractive index 1.46. This is close to the refractive index of borosilicate glass (1.49), and hence ensures that little light is lost through reflections. Dimensions are in mm.

NaI(Tl) crystals are hygroscopic and need to be encased within an air-tight container. The 5 cm diameter, 5.4 cm long, cylindrical NaI(Tl) crystal used for this work is encased within a hollow aluminium cylinder of wall thickness 2.5 mm, as shown in Figure 5.2. A glass window, of thickness 2.5 mm and diameter 5 cm, allows a light detector to view scintillation light from the crystal. The crystal is optically coupled to the glass window with silicone oil to aid light collection. The reflection of light off the internal walls is increased by the wrapping of 1 mm thick PTFE tape around the crystal.

The secondary detector consists of a cylinder of BC501A liquid scintillator, of diameter 7.8 cm and height 8.0 cm. This active volume is viewed by an ETL 9288B PMT [151] at an operating voltage of -1300 V. The body of liquid and PMT is encased within an aluminium vessel of wall thickness 5 mm.

Analogue photomultiplier signals from the NaI(Tl) crystal and BC501A detector are split with a 50 Ω power divider as shown in Figure 5.3. The signal from each PMT is then sent simultaneously to a discriminator set at a threshold of 5 mV, and a channel of the Data Acquisition system (DAQ). The hardware trigger is two signals coincident within a 100 ns time window. The analogue pulses are converted to digitised waveforms, and stored

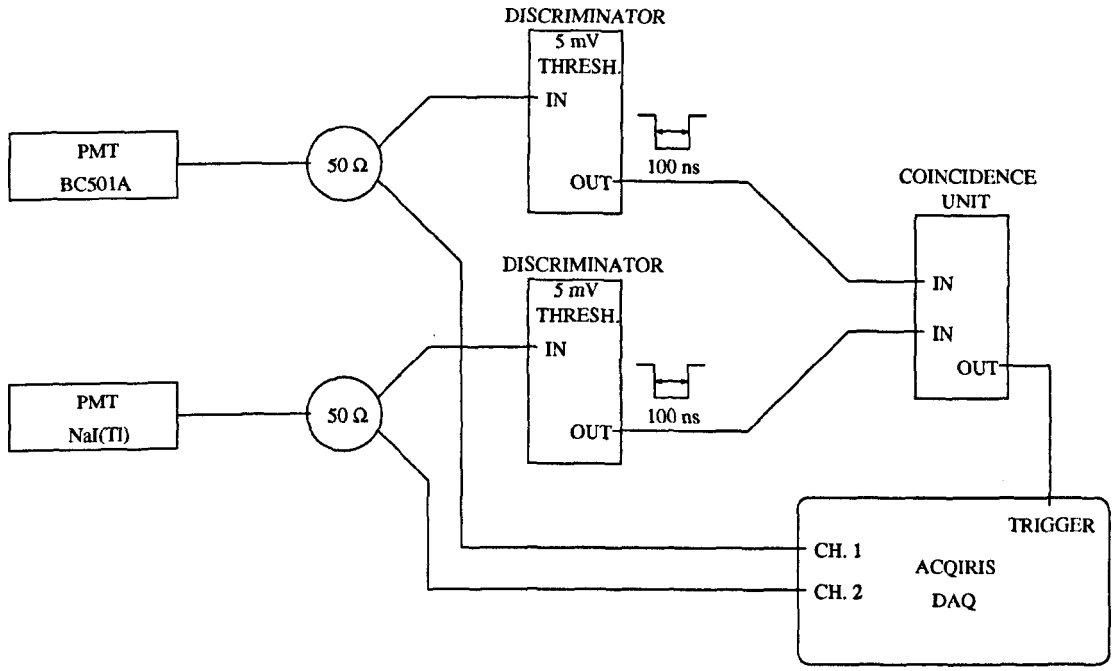

Figure 5.3: Hardware Trigger Electronics for Quenching Factor Experiment. Analogue photomultiplier signals from the BC501A detector and NaI(Tl) crystal are split with a 50 Ω power divider, and sent to a discriminator and an input channel on the Data Acquisition system (DAQ). The discriminator is set at a threshold of 5 mV, and a 100 ns wide NIM pulse is sent to a 2-fold coincidence unit. If the signals are coincident, a NIM pulse provides the external trigger to the DAQ.

on computer for later analysis.

5.2 Neutron Scattering Simulations

Only events with a single interaction in the crystal contribute to the recoil energy E_R at a given scattering angle θ given by Eq. (3.15), and hence by association Eq. (5.1). Multiple interactions lead to neutrons depositing a range of possible energies in the crystal before being detected by the secondary BC501A detector, thus contributing to the background. The mean number of interactions μ is given by:

$$\mu = \sigma \eta dx \tag{5.3}$$

where σ is the cross-section per atom, η is the number density of atoms in the target and dx is the thickness of material. Obeying Poissonian statistics, the probability $P(\mu; n)$ of

n interactions occuring is given by Eq. (4.5). Therefore, the probability of two or more interactions $P(\mu; 2+)$ taking place is:

$$\begin{aligned} P(\mu; 2+) &= 1 - P(\mu; 0) - P(\mu; 1) \\ &= 1 - e^{-\mu} - \mu e^{-\mu} \end{aligned} \tag{5.4}$$

where μ is given by Eq. (5.3). From Figure 3.12, the cross-section σ for neutrons of incident energy 2.45 MeV scattering off sodium nuclei is 2.61×10^{-24} cm^2. As the cross-section is given per atom, the number density η of sodium atoms in NaI(Tl) needs to be calculated with:

$$\eta = \frac{N_{\mathrm{A}} m_A \rho}{A} \tag{5.5}$$

where $N_{\mathrm{A}} = 6.022 \times 10^{23}$ mol^{-1} is the number of atoms in one mole (Avogadro's number), $m_A = 0.15$ is the fraction mass of sodium nuclei in NaI(Tl), ρ is the density of NaI(Tl) (from Table 5.1) and A is the mass number of ^{23}Na. Substituting these values into Eq. (5.5) yields $\eta = 1.47 \times 10^{22}$ cm^{-3}.

The maximum distance a neutron can traverse is given by the diameter of the crystal (2.5 cm). Therefore, using Eq. (5.4), approximately 0.43% of incident neutrons will scatter off two or more sodium nuclei.

However, due to the cylindrical geometry of the crystal illustrated in Figure 5.2, a Monte Carlo simulation is required in order to obtain an accurate probability for multiple interactions. Additionally, an incident neutron may scatter off multiple iodine nuclei, especially as the fraction mass of iodine atoms in NaI(Tl) is five to six times larger than that for sodium.

The geometry of the experiment is described within the GEANT4 framework [161] as illustrated in Figure 5.4. The materials used to construct the geometry are outlined in Table 5.2. As shown in Figure 5.4, 2.45 MeV neutrons are generated at the face of the neutron source, and are fired towards the NaI(Tl) crystal. The simulation is performed at scattering angles associated with 10 and 100 keVnr sodium recoil energies as given by Eq. (5.1). A total of 10^8 events are generated at each scattering angle, and the simulation only records parameters for those that deposit energy in both the crystal and BC501A detectors. Approximately 0.13% and 0.05% of events generated, at scattering angles associated with 10 and 100 keVnr sodium recoil energies respectively, satisfy this condition.

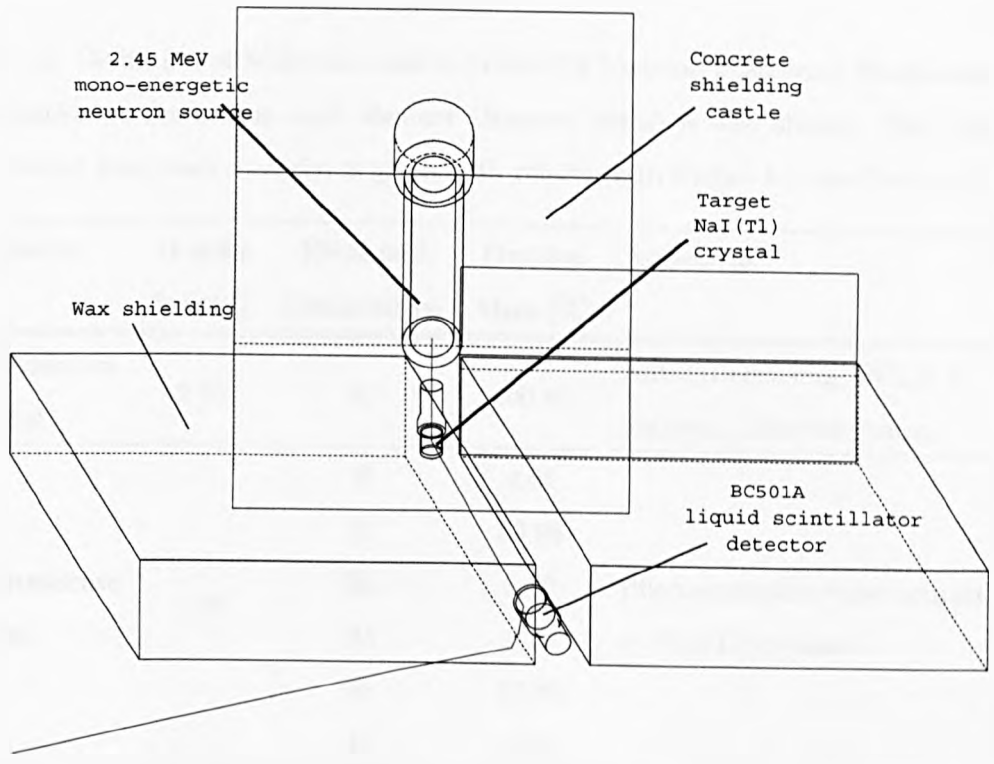

Figure 5.4: Sample Event from 10 keVnr Neutron Scattering Simulations. The geometry of the experiment is shown in reference to Figure 5.1 and materials are constructed as outlined in Table 5.2. An example of a neutron emerging from the face of the neutron source and recoiling off a single sodium nucleus is shown. The neutron then travels to the secondary detector, deposits some of its energy, and scatters within a block of wax before leaving the area.

The reason for this asymmetry is the non-isotropic cross-section for neutron scattering at higher recoil energies and for heavier target nuclei, which was briefly mentioned in Section 3.5.2.

Results at 10 keVnr nuclear recoil energy are shown in Figure 5.5. It is immediately clear from Figure 5.5(a) that the probability of multiple scattering is higher than that calculated above. However, the simulation also includes recoils off iodine nuclei, and as iodine contributes to the majority of crystal mass, this is expected. However, the deposited energy spectrum from these multiple interactions, illustrated by the shaded histogram in Figure 5.5(b), is featureless in comparison with the total recoil energy spectrum in the same Figure. Therefore, it is safe to assume that there is no preferential energy deposition, and the number of multiple interactions should make no difference to the final result.

Table 5.2: Definition of Materials used in GEANT4 Neutron Scattering Simulations. The contribution to mass from each element (fraction mass) is also shown. The apparatus constructed from each material is given with reference to Figure 5.1 and Section 5.1.

Material	Density [g/cm^3]	Elemental Composition	Fraction Mass [%]	Apparatus
Aluminium metal	2.70	Al	100.00	NaI(Tl) encasing, BC501A encasing, Neutron source
Borosilicate glass	2.23	B	4.01	Photomultiplier tube coupled to NaI(Tl) crystal
		O	53.96	
		Na	2.82	
		Al	1.16	
		Si	37.72	
		K	0.33	
Concrete	2.30	H	1.00	Concrete shielding castle
		C	0.10	
		O	52.91	
		Na	1.60	
		Mg	0.20	
		Al	3.39	
		Si	33.70	
		K	1.30	
		C	4.40	
		Fe	1.40	
Liquid scintillator	0.87	H	9.51	BC501A liquid scintillator
		C	90.49	
Paraffin wax	0.93	H	14.86	Wax shielding
		C	85.14	
PTFE	2.20	C	24.02	Light reflector wrapped around NaI(Tl) crystal
		F	75.98	
Sodium iodide	3.67	Na	15.34	NaI(Tl) crystal
		I	84.46	

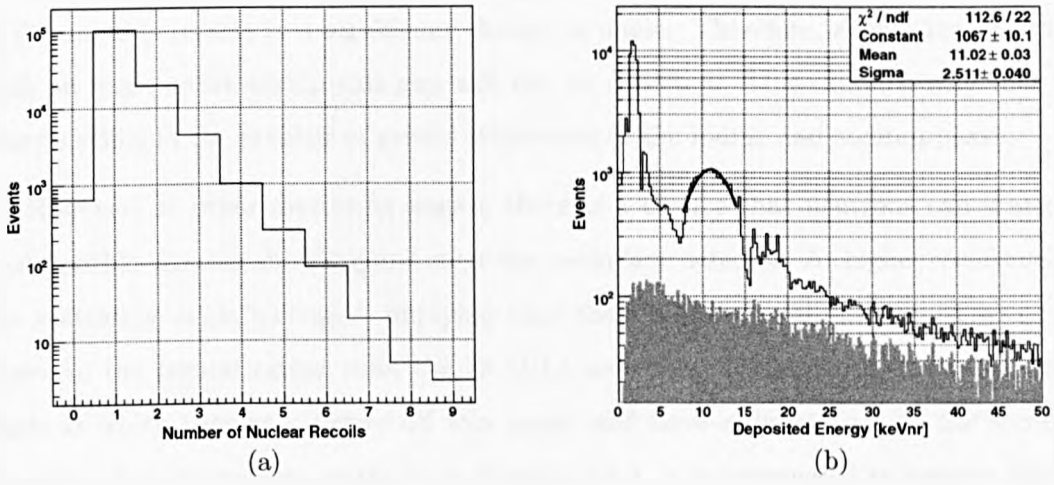

Figure 5.5: Pre-Cut Results from 10 keVnr Neutron Scattering Simulation: (a) Number of Nuclear Recoils; and (b) Total Energy Deposited in NaI(Tl) Crystal. A significant proportion of events do result in multiple scattering, as shown in (a). However, the deposited energy spectrum for events as a result of two or more nuclear recoils (shaded area in (b)) is featureless, implying that their contribution to the background should not interfere with signal peak position.

As a point of interest, the number of events that do not result in a nuclear recoil in Figure 5.5(a) arise from inelastic scattering in the aluminium encasing that surrounds the crystal. Compared with multiple scattering, the resultant gamma-ray does not make a significant contribution to the background.

The inclusion of nuclear recoils off iodine nuclei also results in a low energy peak at approximately 2 keVnr, as shown in Figure 5.5(b), from single scattered neutrons. This is expected from the deposited energy against scattering angle curve for iodine shown in Figure 3.13.

The peak at approximately 10 keVnr in Figure 5.5(b) is due to recoils off sodium nuclei. The peak is quite wide as the BC501A detector is not point-like. Hence, a range of angles is covered, rather than solely the one of interest. As long as this is taken into consideration when deriving the error in the final result, it is perfectly acceptable.

Although multiple scattering explains the origin of some of the events that do not lie in these peaks, it is evident from Figure 5.5(b) that they are not the only factor contributing to the background. With reference to Figures 5.1 and 5.4, there is a small gap of the order

of a few milimetres between the wax shielding and the BC501A detector. Over a distance of 80 cm, this results in a significant change in angle. Therefore, events that scatter at such an angle to fit within this gap will not be detected. This explains why there is a sharp decline in the number of events either side of the iodine and sodium peaks.

However, at other scattering angles, there is a chance that neutrons can scatter off nuclei within the wax shielding and enter the secondary detector. At higher recoil energies, the scattering angle increases, implying that these neutrons will scatter off wax nuclei closer to the crystal rather than the BC501A detector. These neutrons have a smaller angle at which they can scatter off wax nuclei and have a direct path to the secondary detector. For the reasons outlined in Section 3.5.2, it is reasonable to assume that the angular distribution of neutrons recoiling off the nuclei in wax is approximately isotropic at these energies. Therefore, as the deposited energy increases, fewer events will reach the secondary detector through this indirect path. This is the reason behind the shape of the spectrum in Figure 5.5(b).

5.3 Development of the Reduction Code

Analogue-to-digital conversion of PMT pulses is performed by an 8-bit, 2-channel, Acqiris DC265 digitiser [153] with a 500 MHz sampling rate. Data acquisition software running on a linux computer, similar to that used by ZEPLIN-II [152], reads out the digitised waveforms and writes them to disc.

An analysis program has been written in C++ to read the binary data output of the digitiser. The program goes through each event, extracting the amplitude at each 2 ns sampling point and placing the numbers in an array. The baseline is calculated on an event-by-event basis for each waveform:

$$V_i = \left(\sum_{j=1}^{100} \frac{A_j}{100} - A_i \right) \cdot \frac{R}{256} \tag{5.6}$$

The average value of the first 100 samples (200 ns) of each waveform is subtracted from the amplitude in counts A for each sampling point i to reconstruct the new baseline at 0 counts. The conversion of the new amplitude from counts to Volts at each sampling point V_i is achieved by multiplying the result by the least significant bit. For an 8-bit digitizer, this is calculated by dividing the full range R by 256 bits.

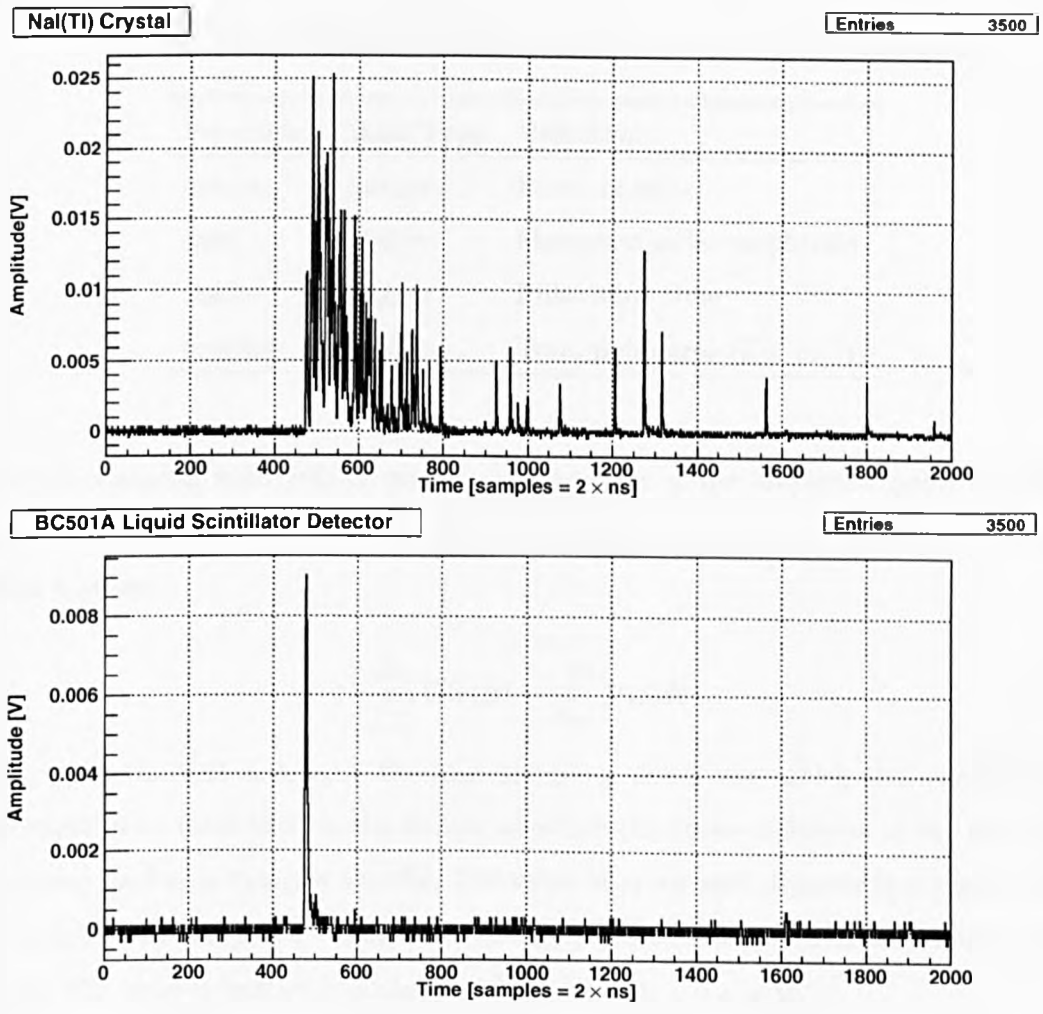

Figure 5.6: Event Viewer for Waveforms from Acqiris DC265 Digitiser. Data were taken with back-to-back coincident 511 keV gammas from a ^{22}Na gamma source. The analysis program converts digitised waveforms stored in binary files to histograms, and outputs them to a viewer. Event parameters are extracted from these histograms, within the ROOT framework, and stored in a ROOT tree for offline analysis.

The amplitudes at each sampling point given by Eq. (5.6) are written to a new array. An event viewer is implemented within the ROOT framework [162], filling histograms with the values stored in this new array, thus producing waveforms as shown in Figure 5.6. Parameters are then extracted from these waveforms and stored in a ROOT tree for later analysis.

Four initial parameters are chosen, as shown in Table 5.3. The pulse start time is defined as the time at which the pulse reaches 10% of its maximum amplitude. This is

Table 5.3: Initial Waveform Parameters Calculated by Reduction Code.

Parameter	Data Type	Definition
evnum	integer	Event number
max	double	Maximum pulse amplitude
starta	integer	Pulse start time
surf_tot	double	Total pulse area (Eq. (5.7))

found by scanning from 100 ns prior to the position of the maximum pulse amplitude until this criteria is satisfied. The total pulse area is the sum of the digitized bin contents within a range:

$$\sum_{i=s_1}^{s_2} V_i(t)\Delta t = \int_{t_1}^{t_2} V(t)dt \tag{5.7}$$

where s_1 is the first and s_2 is the final sampling point over which the summation is performed. The value of s_1 is the sample at which the above definition of the start time is satisfied, and s_2 is detector specific. The value of s_2 for each detector is discussed later. The amplitude in each bin i is denoted by $V_i(t)$, and with a 500 MHz sampling rate, Δt is 2 ns. The start t_1 and stop times t_2 are defined as $t_{1,2} = s_{1,2}\Delta t$.

5.4 Preparation of the NaI(Tl) Crystal

The light detector used in this experiment is a 3-inch ETL 9265KB Photomultiplier Tube (PMT) [151]. As outlined in Section 3.6.2, the crystal is calibrated with a gamma source of energy significantly higher than that of the nuclear recoil energies in this experiment. As a result, an appropriate Voltage Divider Network (VDN) for this tube needs to be constructed. Large pulses from a relatively high-energy gamma source cause an increase in the density of electrons at the upper stages of the VDN, leading to space charge effects, and thus a degradation of the electron current. This leads to a non-linear response, and high-energy pulses appear smaller than they actually are. This results in inaccurate calibration, and hence false results for the quenching factor of nuclear recoils. This can be corrected by increasing the voltage gradient between those electrodes that are closer to the anode, achieved by increasing the values of resistors in the upper stages of the VDN. This

is known as a tapered VDN, and the network chosen and constructed for this experiment is shown in Figure 5.7.

5.4.1 Assessment of the Light Yield

Single photoelectron distributions were taken at operating voltages from 1600 to 2100 V. The pulse amplitude and area distributions for an operating voltage of 1800 V are shown in Figure 5.8, and it was decided to use this value for several reasons. Excessive voltage causes electrical breakdown, meaning that electrons may be emitted from the electrodes by strong electric fields, thus causing dark pulses. It is best to operate the PMT at a voltage around 200 to 300 V lower than its maximum, which in the case of the ETL 9265KB is 1800 to 1900 V [151]. Additionally, Figure 5.8(a) indicates that single photoelectrons will have a mean amplitude of 6.0 mV at this operating voltage, and thus will be sufficient to trigger the 5 mV hardware trigger threshold described in Section 5.1. This is important for low energy recoils, which will emit a relatively low number of scintillation photons over a time period of the order of microseconds. This is the typical width of a NaI(Tl) scintillation pulse [163].

To assess whether the PMT is working correctly at this operating voltage, the gain can be calculated using Eq. (3.8), and compared with the manufacturer's value. From Figure 5.8(b), the mean area under a single photoelectron pulse is 0.024 nVs. The tube is coupled to a 50 Ω shielded coaxial cable, which provides the resistance R of the circuit. From Eq. (3.8), the gain is 3.0×10^6, which is the value expected for the tapered VDN configuration used on this tube at this voltage [151].

As mentioned in Section 5.1, the crystal is optically coupled to the glass window with silicone oil to aid light collection. Similarly, it is shown in Figure 5.9 that optically coupling the PMT's glass face to the window also increases the light collection efficiency. The results from ^{57}Co calibration without coupling gel are shown in Figure 5.9(a). The peak position is significantly lower than in Figure 5.9(b), where coupling gel was used between the window and PMT interfaces. Therefore, a minimum of photons are lost while traversing across the crystal-PMT boundary. To quantify this, the light yield L for both setups can be calculated in units of photoelectrons per keV (pe/keV) with Eq. (4.2), where the area under a single photoelectron pulse A_{spe} is 0.024 nVs from Figure 5.8(b). For a ^{57}Co source, the energy of the emitted gamma-ray E_γ is 122 keV, and the area under the

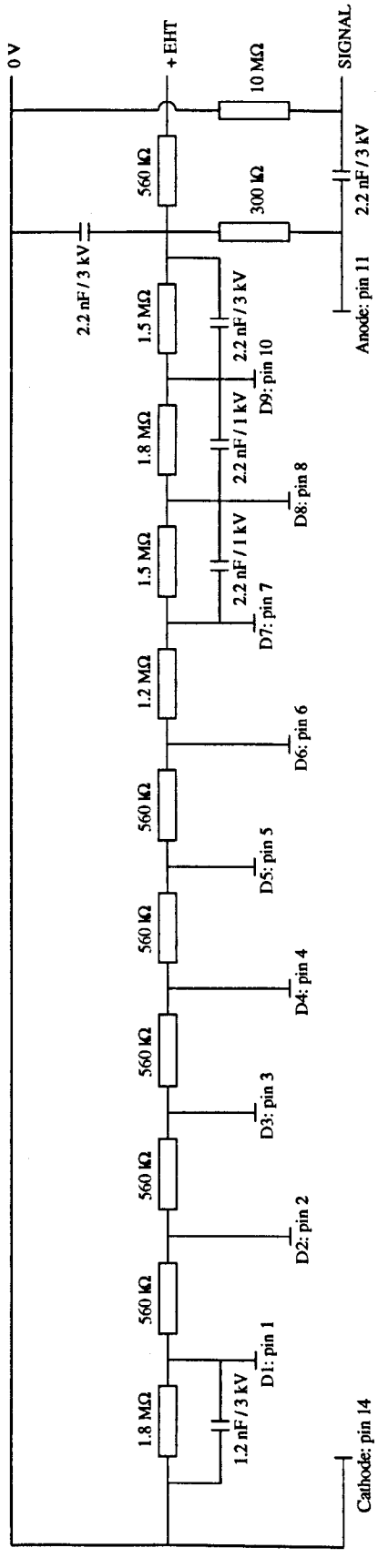

Figure 5.7: Voltage Divider Network (VDN) Design for ETL 9265KB Photomultiplier Tube coupled to NaI(Tl) crystal, based on the tapered version recommeded by Electron Tubes Ltd. [151]. The resistor values increase towards the anode, reducing space charge effects that can lead to non-linearity when dealing with large pulses. This is important for accurate energy calibration of the crystal, as such high energy pulses may saturate the tube. The operation principles of a photomultiplier tube are described in Section 3.4.1.

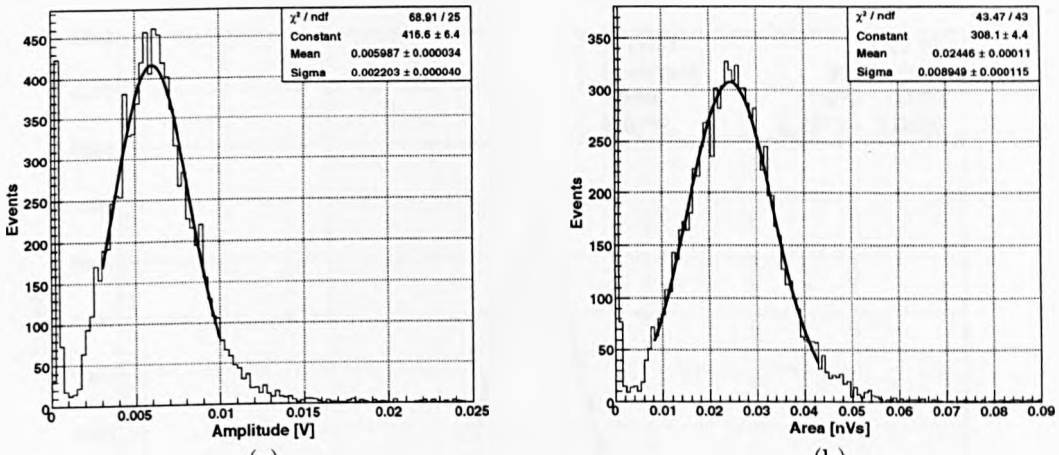

Figure 5.8: Single Photoelectron Distributions for the ETL 9265KB PMT which is coupled to the NaI(Tl) Crystal: (a) amplitude; and (b) area.

pulse A_γ is taken from Figure 5.9 for each configuration. The use of silicone oil to optically couple the PMT's glass face to the window results in a factor of seven improvement in light collection (from 0.7 pe/keV to 5.1 pe/keV).

As a significant amount of light is lost between an air-glass boundary, a simple procedure is used to ensure that there are no air bubbles trapped in the silicone oil after coupling. A ball of coupling gel of approximate diameter 5 mm is placed in the middle of the glass window surface, and the crystal is rotated onto the PMT glass face until the oil leaks out of the sides. The air-tightness is checked quickly by trying to pull the crystal off the PMT, which should not be possible without significant effort due to the lack of an air gap.

The light yield provides a lower limit to the nuclear recoil energies that can be investigated. For this crystal, which as described above has a light yield of 5.1 pe/keV, an electron recoil energy of 10 keV will release 51 detectable photons on average. However, as nuclear recoil energies are quenched in relation to electron recoils (Section 3.6.1), fewer electrons will be released for a nuclear interaction at this energy. The degree of quenching can be estimated using the Lindhard theory [139, 140], outlined in Section 3.6.3. From Figure 3.15, the quenching factor for a 10 keV nuclear recoil is expected to be 33%. Therefore, a nuclear recoil of 10 keV energy will emit 17 detectable photons. It is important that there are enough photons detected at each energy to conduct pulse shape discrimination

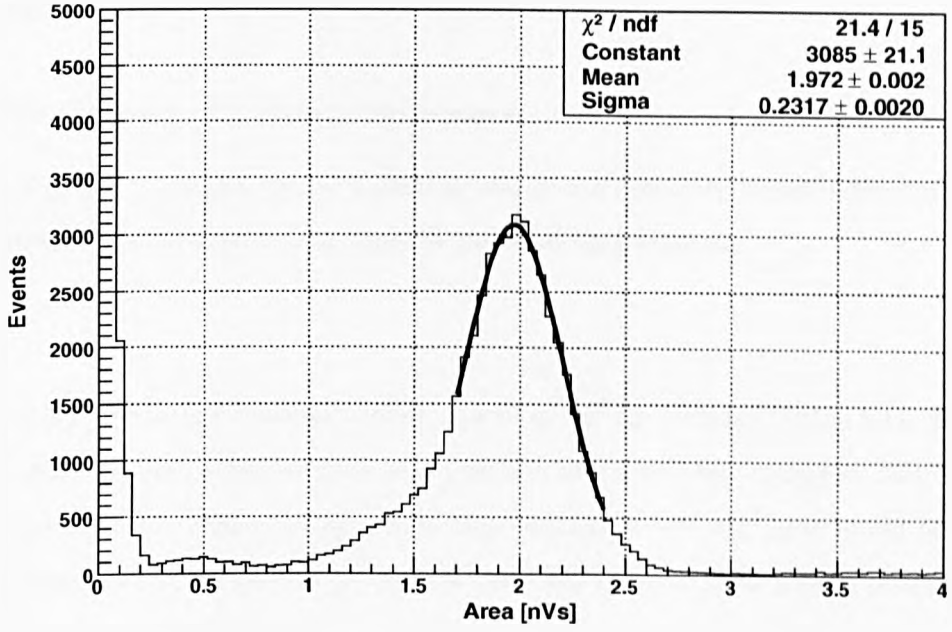

(a)

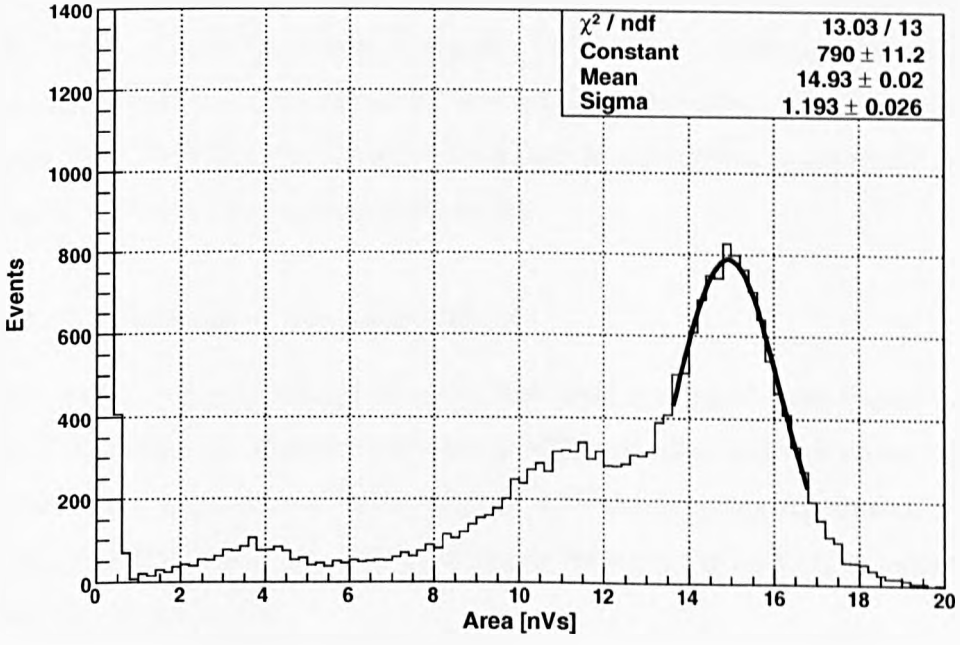

(b)

Figure 5.9: Calibration of NaI(Tl) Crystal Detector with 122 keV Gamma Line from ^{57}Co Source: (a) without; and (b) with silicone oil between PMT glass face and crystal window. In (b) three clear peaks are visible, corresponding to X-ray, photoelectron and total absorption at approximately 3.5 nVs, 11.5 nVs and 15 nVs respectively (Section 3.5.1).

in the target material itself. A measurement at 10 keV nuclear recoil energy satisfies this requirement, and hence is the lower limit.

5.4.2 Choice of Calibration Source

The distance s gamma-rays of a certain energy will typically travel before interacting is a function of their cross-section σ in the material they traverse:

$$s = \frac{1}{\sigma\rho} \tag{5.8}$$

where ρ is the material density, which is 3.67 g/cm^3 for NaI(Tl) (Table 5.1). The distribution of interaction cross-sections as a function of gamma-ray energy in NaI(Tl) is shown in Figure 3.5(a). Using this graph, a cross-section of 1.01 cm^2/g is found for a 122 keV ^{57}Co gamma-ray. Substituting this value into Eq. (5.8) yields a typical penetration depth of 2.7 mm before interaction.

This means that most of the interactions will be on the surface of the crystal, and hence may be affected by defects on the surface. To check for deformities, the light yield at 30° angles around the crystal is checked. The results of this analysis in Figure 5.10 show that all but one point lie within one standard deviation of the mean light yield of 4.14 pe/keV. Therefore, the use of a ^{57}Co source for calibration is acceptable, as there are no major defects on the surface of the crystal.

5.4.3 Variations in the Light Yield

Figure 5.10 shows a significant drop in light yield compared with Figure 5.9(b). The data used in these two figures were taken on different days, and this shows that the light yield is affected by environmental conditions. Therefore, for this experiment, calibration is performed approximately every three hours, as shown in Figure 5.11, to reduce any errors caused by this variation.

The first measurement is performed at a nuclear recoil energy of 10 keV, and each measurement is conducted over two working days. With reference to Figure 5.11, the light yield on the first day varies significantly between calibrations, ranging from 5.4 to 5.9 pe/keV. Environmental changes would not result in such erratic behaviour. Instead, the thickness of the coupling between the viewing window and the PMT's glass face varies over time, as there is nothing to hold the PMT in place over the crystal. As a result,

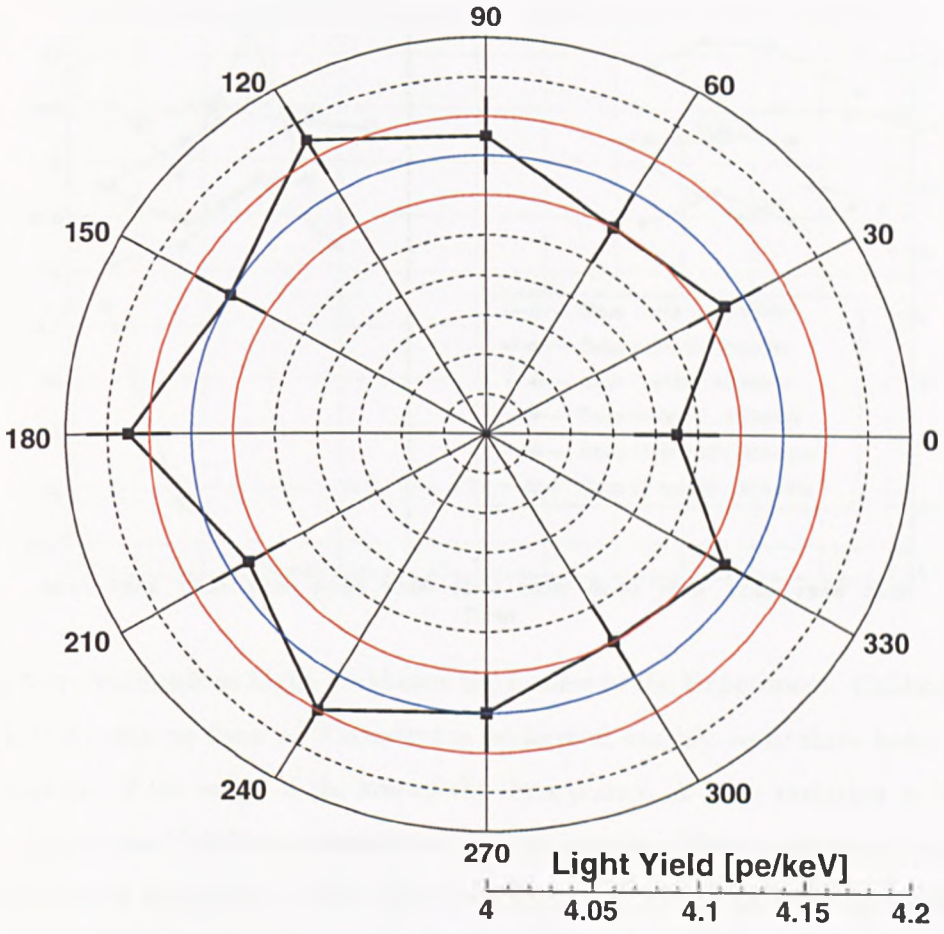

Figure 5.10: Angular Distribution of Light Yield from NaI(Tl) Crystal. Data taken with ^{57}Co gamma source. The blue circle represents the mean light yield of 4.14 pe/keV, and the red lines show the standard deviation from the mean. Within errors, all points bar one lie within one standard deviation from the mean, indicating that there are no major defects in the surface of the crystal.

it can slide, changing the light yield over the course of a measurement. This is more apparent when the coupling gel is applied for the first time, as it is still wet. To combat this problem a clamp has been designed, as shown in Figure 5.12, which holds the PMT in place. The use of this clamp results in less variation over the course of the second day of this measurement, as shown in Figure 5.11.

However, over the time scale of days, the clamp is not sufficient to prevent the degradation of light collection as the coupling gel between the crystal and PMT is attacked by moisture in the air. This trend can be seen in Figure 5.11, where the light yield for

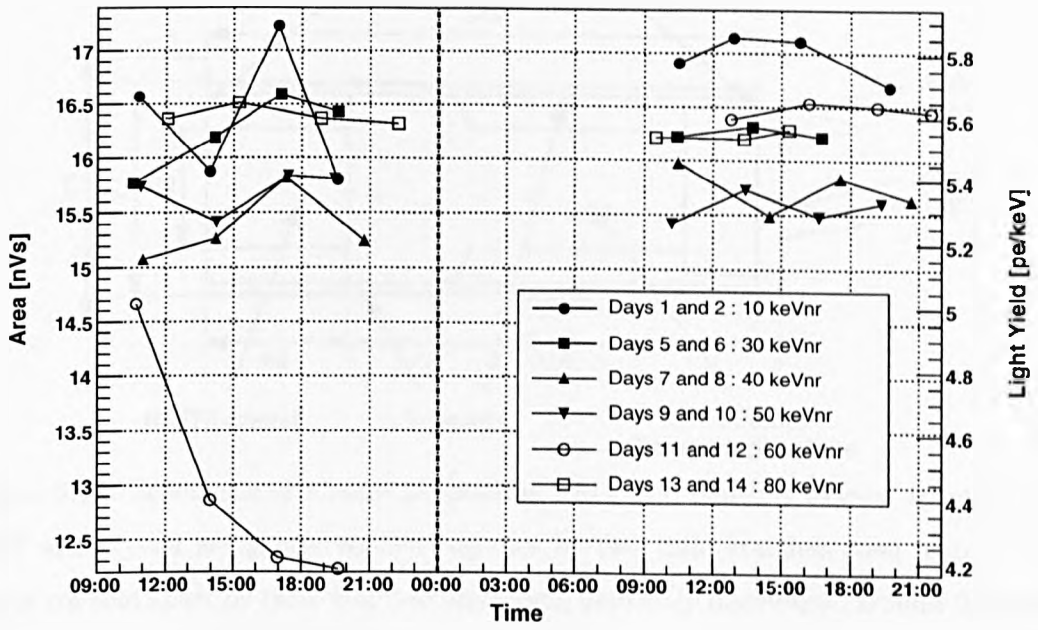

Figure 5.11: Variation in Light Yield over the Course of the Experiment. Calibration with a 122 keV gamma ray from a ^{57}Co source is performed roughly every three hours. Vertical error bars are of the order of the size of the data points. A large variation in light yield is seen during the 10 keVnr measurement on the first day. This is corrected by using the clamp shown in Figure 5.12. The light yield degrades over time and the coupling gel is reapplied once the light yield drops significantly.

measurements at 40 and 50 keV are lower than that at 30 keV nuclear recoil energy. This effect is seen far more clearly during the first day of measuring the crystal's response at 60 keV nuclear recoil energy. Once such a sharp drop in light yield is seen, the crystal is recoupled to the PMT and the measurement is repeated. This recoupling results in a much improved light collection efficiency on the second day.

5.5 Algorithm for NaI(Tl) Scintillation Pulses

From the assessment of the light yield in Section 5.4.1, low energy nuclear recoils in NaI(Tl) will result in a small number of detectable photons. Therefore, a suitable algorithm needs to be implemented for these pulses such that a minimum number of photoelectrons is lost when extracting parameters from the waveforms with the reduction code outlined in Section 5.3. This includes the determination of pulse integration boundaries such that

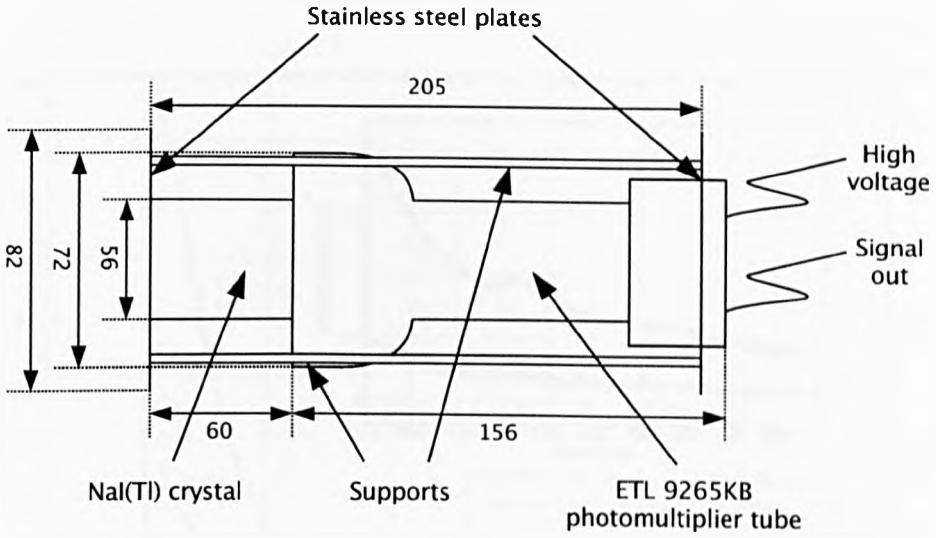

Figure 5.12: Schematic of Clamp for holding PMT and NaI(Tl) Crystal together. The PMT and crystal are gently pushed together by two thin, stainless steel plates. These plates are held apart by three stainless steel rods, uniformly distributed around the crystal. A gap in the upper plate allows for access to the voltage divider network. Once clamped together, the detector is wrapped in black tape to ensure light tightness. The use of the clamp has been found to reduce the drift in light yield over the course of a measurement, as illustrated in Figure 5.11.

Eq. (5.7) yields an accurate total pulse area, and hence pulse energy. Additionally, the removal of any inherent noise from the PMT and a more thorough calculation of the baseline than that given by Eq. (5.6) will also help to achieve this.

5.5.1 Determination of Total Pulse Area Integration Boundaries

As stated in Section 5.3, the upper integration boundary for the area under the pulse in Eq. (5.7) is dependent on the target material. It is clear from Figure 5.6 that the widths of NaI(Tl) waveforms are far greater than those from BC501A. Therefore, a suitable value for s_2, or in other words t_2, in Eq. (5.7) needs to be determined.

However, it is difficult to determine a suitable value for t_2 from Figure 5.6, as the position at which the pulse stops is unclear. After the main pulse ends at around 800 samples (1600 ns), isolated scintillation pulses appear thoughout the waveform. These pulses could arise from noise in the PMT, and hence may not be the result of a recoil and can be safely ignored.

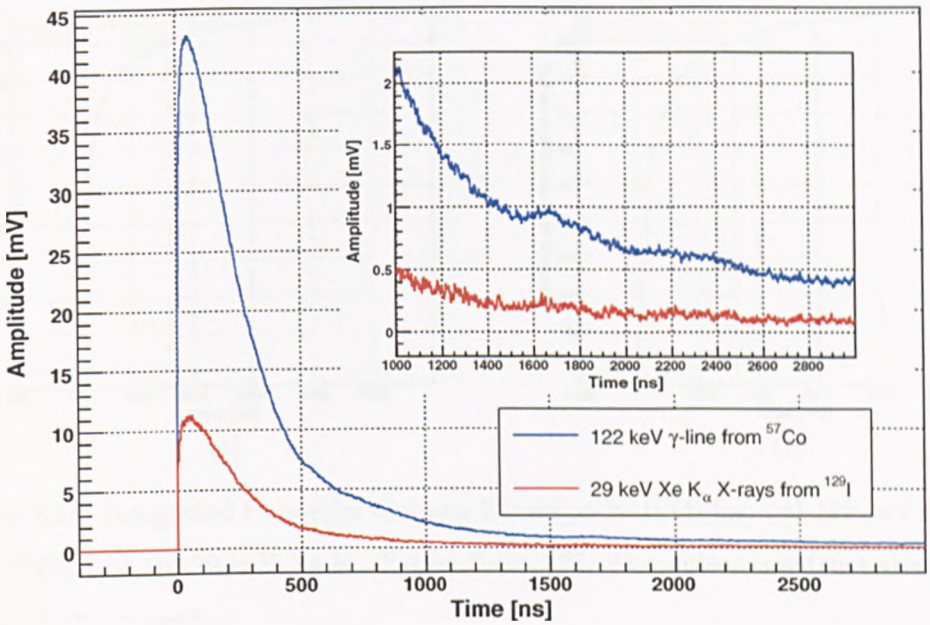

Figure 5.13: Pulse Shapes for Gamma Events in NaI(Tl) for 122 keV gamma-rays from ^{57}Co and 29 keV Xe K_α X-rays from ^{129}I. Pulses that contribute to the corresponding energy peak position are extracted and their amplitudes are summed. Both pulses are normalised to 1 event.

In an attempt to confirm this, a scintillation pulse is built with 10000 122 keV gamma-ray events from ^{57}Co, as shown in Figure 5.13. The amplitudes are normalised to reproduce the typical shape of such a pulse. The same thing is done with 10000 29 keV Xe K_α X-ray events from ^{129}I. As expected, the energy deposited is proportional to the amplitude of the pulse.

It can be seen that photons from scintillation light continue well beyond 2600 ns. Even though the pulses are averages of 10000 electron recoil events, the tail (at times greater than 1000 ns) is far from the smooth exponential expected. By contrast, the start of the pulse at times less than 1000 ns, gives rise to a clear exponential. This is a result of the random nature of scintillation signals at these time periods, which can be seen from the typical electron recoil pulse in Figure 5.6. More events would need to be analysed in order to smooth out this section, making up for the low statistics in this region. However, the purpose of this is to ascertain a value for t_2, and not to make a fit to the pulse, so such an analysis is not performed.

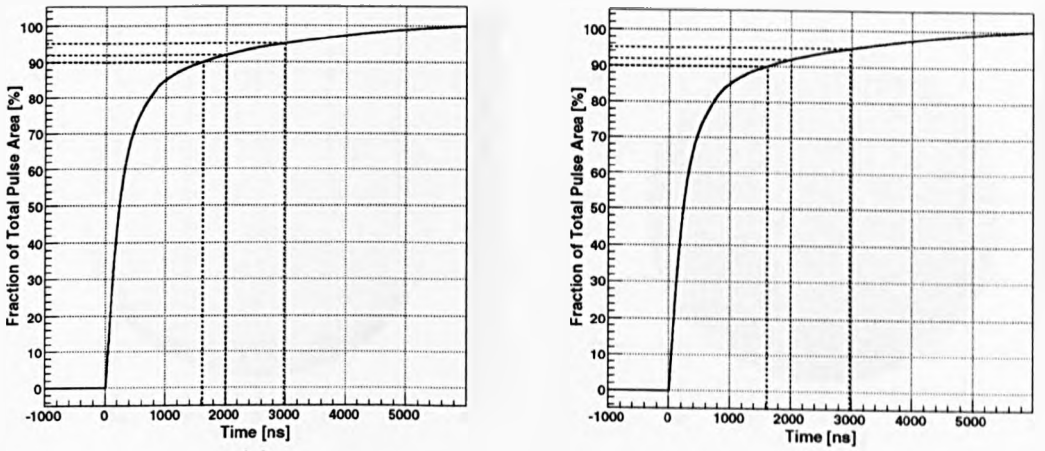

Figure 5.14: Integrated Pulses for Gamma Events in NaI(Tl) for: (a) 122 keV gamma-rays from ^{57}Co; and (b) 29 keV Xe K_α X-rays from ^{129}I. The pulses constructed and shown in Figure 5.13 are used.

Electrical noise in the tail region makes it difficult to choose a relatively large value for t_2, as this would cause the actual area of the pulse to be overestimated. In contrast, by ignoring this region completely, approximately 15% of the pulse is rejected as shown in Figure 5.14. A balance needs to be reached, and a compromise of 1800 ns after the start of the pulse was used by [163]. From Figure 5.14, this corresponds to roughly 90% of the total waveform.

Additionally, selecting an appropriate value for t_2 is necessary for good pulse shape discrimination between electron and nuclear recoils in NaI(Tl). Although there is a vast array of pulse shape discrimination techniques, the simplest to implement with digitised waveforms utilises the mean time $\langle t \rangle$:

$$\langle t \rangle = \frac{\sum_{i=s_1}^{s_2} A_i t_i}{\sum_{i=s_1}^{s_2} A_i} \tag{5.9}$$

where A_i is the amplitude of the digitised pulse and t_i is the time after the start of the pulse at sampling point i. From [163], the mean time of electron recoils should decrease with decreasing energy when compared with that of nuclear recoils, which remain roughly constant.

A suitable gamma source needs to be chosen in order to investigate the effect a pulse finding algorithm has on the mean time distribution of electron recoils. As stated in

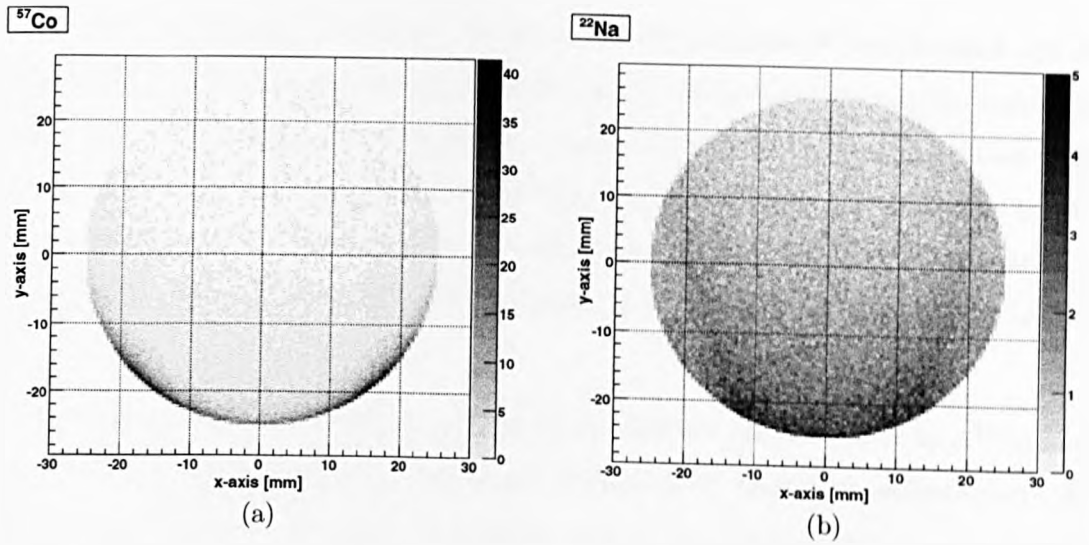

Figure 5.15: Simulated Positions of 2 to 26 keV Events in NaI(Tl) Crystal from: (a) ^{57}Co; and (b) ^{22}Na Sources. Both scatter plots contain 10000 events. Compton recoils from ^{57}Co 122 keV gamma-rays mainly occur on the surface of the crystal, unlike those as a result of 511 keV from ^{22}Na, which occur throughout.

Section 5.4.2, the typical penetration depth of a 122 keV gamma-ray in NaI(Tl) before interacting is 2.7 mm. Although this is acceptable for calibration, neutrons will interact throughout the bulk of the crystal, and hence a source of higher energy is preferable. Additionally, from Figure 3.5(a), the interaction gamma cross-section at 122 keV in NaI(Tl) is dominated by photoelectric absorption rather than Compton scattering. This means that the majority of interactions will result in the gamma-ray depositing all its energy in the crystal. Although useful for calibration, good pulse shape discrimination is required at much lower energies.

From Figure 3.5(a), Compton scattering begins to dominate at energies greater than 300 keV. For a 511 keV gamma-ray from ^{22}Na, the total attenuation cross-section is 0.0933 cm^2/g. Substituting this value into Eq. (5.8), the typical penetration depth is 29 mm, which is close to the centre of the crystal. This is confirmed with a GEANT4 simulation, where Compton recoils that deposit between 2 keV and 26 keV in the crystal are recorded. It is clear from Figure 5.15(a) that most of these interactions happen on the surface of the crystal when a ^{57}Co source is used. Gamma-rays from a ^{22}Na source however, as shown in Figure 5.15(b), leave low energy depositions throughout the entire volume of the crystal.

Another advantage of using a ^{22}Na source is the emission of back-to-back 511 keV gamma-rays. This property is exploited by placing the source between the crystal and another detector, and operating them in coincidence using the electronics shown in Figure 5.3. The width of NIM pulses from the discriminator is reduced from 100 ns to 10 ns, as coincident gammas will arrive at the same time at each detector. This enables the discriminator threshold settings to be decreased to 2 mV, without noisy events polluting the data.

As with the neutron scattering experiment, the 122 keV gamma-line from a ^{57}Co source was used for energy calibration. Histograms of mean time against deposited energy show little change when the upper limit of the pulse area integration boundary is varied between 1600 and 2400 ns. The results for a t_2 of 1800 ns and 2000 ns are shown in Figures 5.16(a) and 5.16(b) respectively. Closer inspection shows that there is an increase in the number of low energy pulses with large mean times, in relation to the time window used. This is due to additional scintillation pulses at the end of the waveform contributing to the mean time. It is unlikely that a scintillation pulse with amplitude of the order of the first pulse that triggered the DAQ would arise from the same event.

To try to improve the spread of values, the total area until the end of the waveform is calculated by the reduction code. The program then integrates this pulse, and determines the time at which a certain percentage of the total area has been achieved. It then recalculates the area, using this time as the upper integration boundary. Therefore, the value of t_2 is not fixed as in the case above, but varies depending on the waveform.

This technique gives rise to an even bigger spread as seen in Figures 5.16(c) and 5.16(d), where an upper integration boundary of 90% and 95% of the total area respectively are chosen. This effect is more pronounced in the low energy region for the reasons outlined above. This is in contrast with Figure 5.14, which indicates that little change should be seen between Figures 5.16(a) and 5.16(c). It is important to consider that the pulses used in Figure 5.14 are averaged from 10000 similar pulses, and this can vary between waveforms. Additionally, Figure 5.13 shows that the tail of these scintillation pulses is not well reconstructed, and this is the root of the problem with the spread of results in Figures 5.16(c) and 5.16(d). The resolution worsens as the boundary is increased to 95% of the waveform in Figure 5.16(d). Therefore, this technique is not suitable for this application.

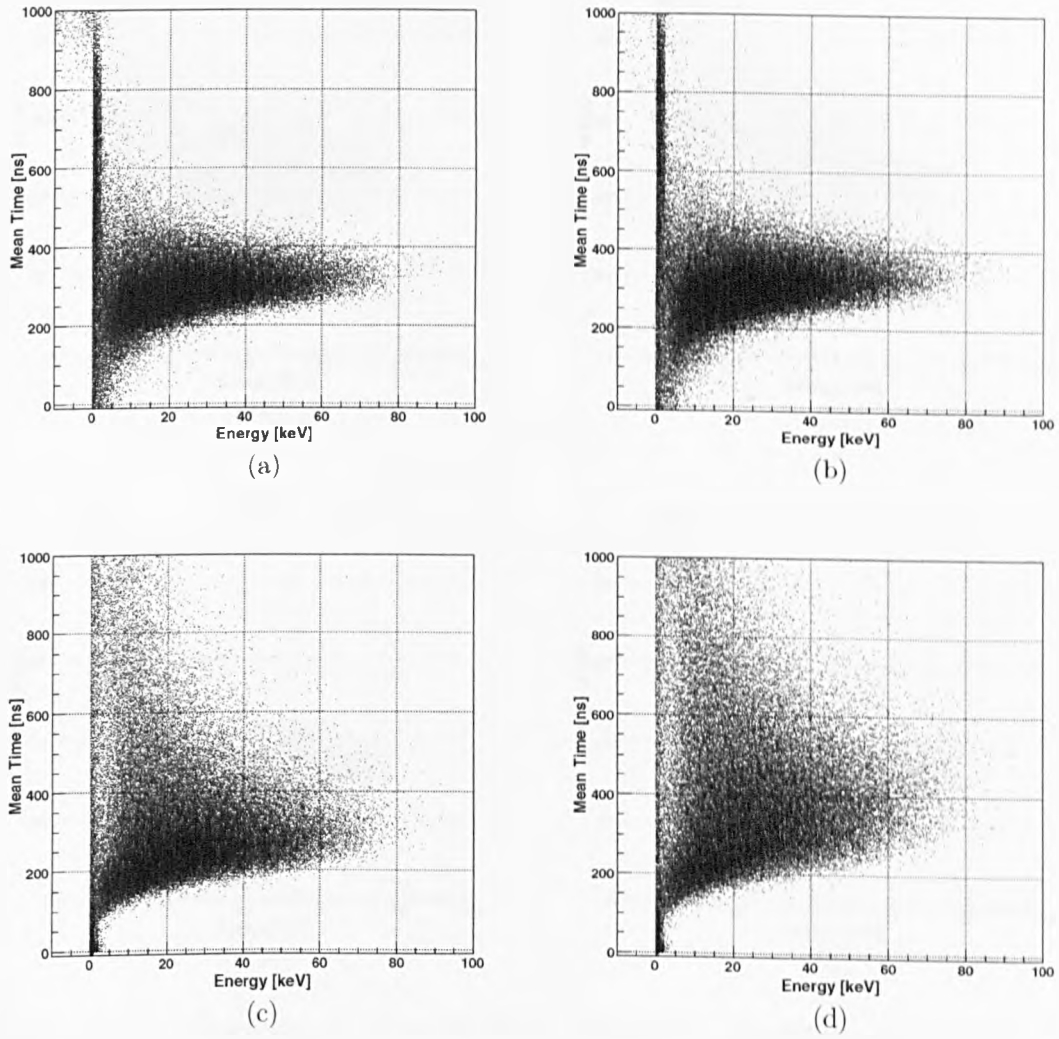

Figure 5.16: Comparison of Simple Pulse Integration Algorithms for NaI(Tl) Waveforms. Scatter plots of mean time against energy are shown. A suitable algorithm would minimise the spread in mean time seen at low energies. Total pulse integration limits over a time period of (a) 1800 ns and (b) 2000 ns from the start of the waveform are shown. Also shown are the results using total pulse integration limits from 10% to (c) 90% and (d) 95% of the integrated waveform.

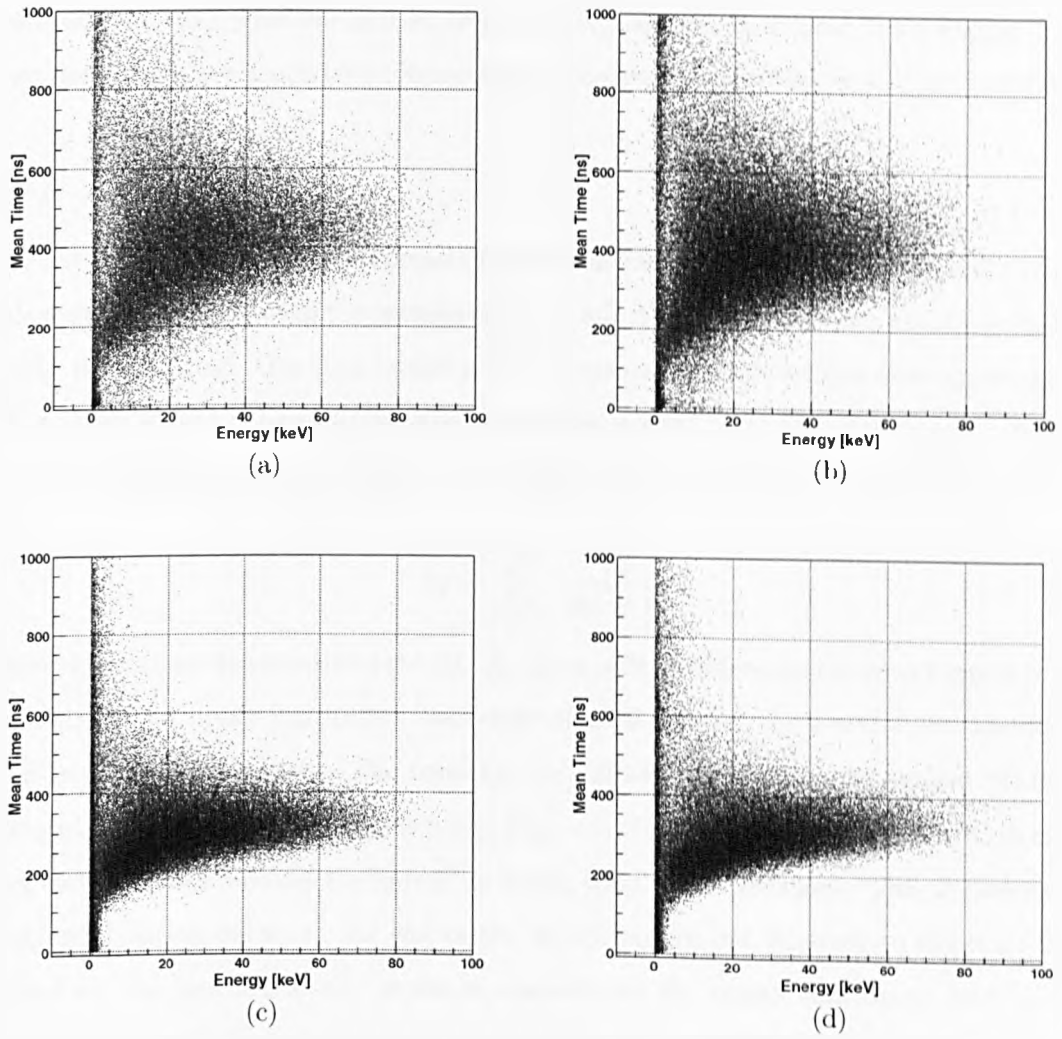

Figure 5.17: Comparison of Advanced Pulse Integration Algorithms for NaI(Tl) Waveforms. As with Figure 5.16, a suitable algorithm would minimise the spread in mean time seen at low energies. (a) A search for the last pulse to pass a threshold of 10% of the maximum peak height is performed, up to a limit of 2000 ns after the start of the waveform. (b) Data are smoothed over 10 ns using a moving average. (c) All bins contributing to the waveform that are less than the height of the maximum bin in the first 200 ns are excluded. (d) All bins that are of amplitude less than 3 standard deviations (3σ) from the mean noise, calculated from the first 200 ns of the waveform, are excluded.

As an alternative to this technique, the end of the pulse is searched for by performing a reverse search for the point at which the pulse reaches 10% of its maximum amplitude. In other words, the reduction code starts at a time of 2000 ns after the start of a pulse, and decreases the time window until such a point is reached. It is clear from Figure 5.17(a) that this results in a much larger spread when compared with Figures 5.16(c) and 5.16(d).

5.5.2 Noise Reduction

The major contribution to the spread of mean time at low energies is the presence of noise pulses over the timescale of the waveform. In an effort to curb this effect, several techniques can be implemented. One such technique is to smooth the data using a moving average. In other words, once the baseline has been calculated according to Eq. (5.6), a new amplitude V at each sampling point i is derived by taking the average of the surrounding points:

$$V_i = \sum_{j=i-n}^{i+n} \frac{V_j}{(2n+1)} \tag{5.10}$$

where n points are taken either side of i. As there is little difference between Figures 5.16(a) and 5.16(b), an upper integration boundary of 2000 ns after the start of the waveform is used to determine the area. The resultant distribution of mean times against energy for smoothing over 10 ns ($n = 2$), is shown in Figure 5.17(b). The smoothing algorithm clearly does not help to minimise the spread of mean time at low energies. This is because the noisy scintillation pulses at the end of the waveform are not inherent to the main pulse. Therefore, the procedure only serves to smooth out the pulses that occur later in time, rather than combatting the problem of reducing their contributions.

In an effort to achieve this, small noise pulses can be ignored by excluding them from the waveform. The simplest way to attain such a waveform is to extract the amplitude of the largest bin in the first 100 samples that are used to calculate the baseline (Eq. (5.6)). Then the amplitude V at each sampling point i can be scanned, and cut if it falls below this threshold. As with the moving average, the upper total pulse area integration boundary is fixed at 2000 ns after the start of the waveform. The results for this technique are shown in Figure 5.17(c), and show a slight improvement over Figure 5.16(b).

However, there is always the danger of a large pulse appearing in the first 200 ns of the waveform. This would result in a higher threshold that would not paint an accurate

picture of the level of noise. This overestimation results in the purging of good pulses, and hence is undesirable.

As an alternative, the standard deviation from the mean can be calculated over the first 100 samples, and a threshold can be set according to that. As long as there are not a large number of bins with big amplitudes in the first 200 ns of the waveform, the standard deviation provides a fairer assessment of the actual noise. The standard deviation σ over the first 100 samples is calculated by:

$$\sigma = \sqrt{\sum_{i=1}^{N} \frac{(V_i - \bar{V})^2}{(N-1)}} \tag{5.11}$$

where V is the amplitude at sampling point i, and the mean value over N samples is $\bar{V}$. The random nature of noise means that 99.7% of amplitudes should lie within three standard deviations of the mean. Therefore, setting this as the new threshold, Figure 5.17(d) is plotted. This results in a very slight improvement over Figure 5.17(c).

There is little to distinguish Figure 5.17(d) from Figures 5.16(a), 5.16(b) and 5.17(c). All four options are acceptable, although removing bins with amplitude less than 3σ from the baseline does result in a slight improvement in discrimination. To look for further improvements, individual pulses are observed with the event viewer described in Section 5.3 to look for any problems that may arise.

5.5.3 Calculation of the Baseline

The calculation of the baseline described in Section 5.3 and defined by Eq. (5.6), is a very simple determination of the mean of the first 100 samples in each waveform. As mentioned previously, incorrect calculations of the baseline are possible if a pulse is present in the first 200 ns. This would result in a skewed determination of the mean, and systematic errors in pulse parameters such as energy.

An example of an event that would cause a problem with the baseline calculation outlined in Eq. (5.6) is shown in Figure 5.18. The integration boundaries for total pulse area are of fixed width 2000 ns, and begin from the start time of the pulse. The presence of a pulse in the first 200 ns of the waveform results in an overestimation of the baseline voltage. This leads to the reduction code calculating a lower energy than that actually deposited.

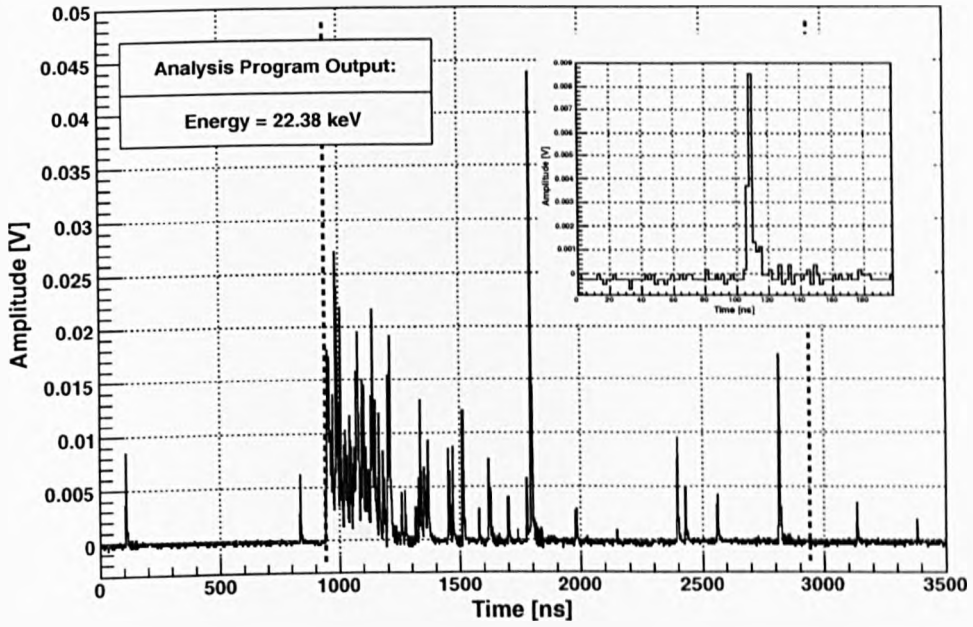

Figure 5.18: Illustration of the Baseline Problem with Original NaI(Tl) Waveform. The integration boundaries are shown by dotted vertical lines, and span a time period of 2000 ns from the start of the pulse. The baseline is calculated by averaging bins within the first 200 ns of the waveform. It is evident that an event in the first 200 ns, unrelated to the main pulse, causes the baseline voltage to be overestimated. Hence, this leads to the underestimation of the energy calculated by the reduction program.

As described above, removing all bins that are less than the maximum amplitude in the first 200 ns of the waveform results in Figure 5.19. As with the original waveform above, the total pulse area integration limits are set to a fixed width of 2000 ns. The presence of this pulse at the beginning of the waveform results in a large removal of the original signal. The degree of purging is so extreme in this case, that the energy calculated drops to 60% of the value found for the original pulse. This technique is too prone to simple errors like this and, as a consequence, it is unviable.

As described above, as opposed to excluding bins with amplitudes less than that of the maximum bin among the first 100 samples, the standard deviation for the first 200 ns of the waveform can be calculated (Eq. (5.11)). Bins with amplitudes less than 3σ from the mean baseline are excluded to produce the pulse shown in Figure 5.20. The new waveform compares favourably with Figure 5.19. However, closer inspection of the unrelated pulse

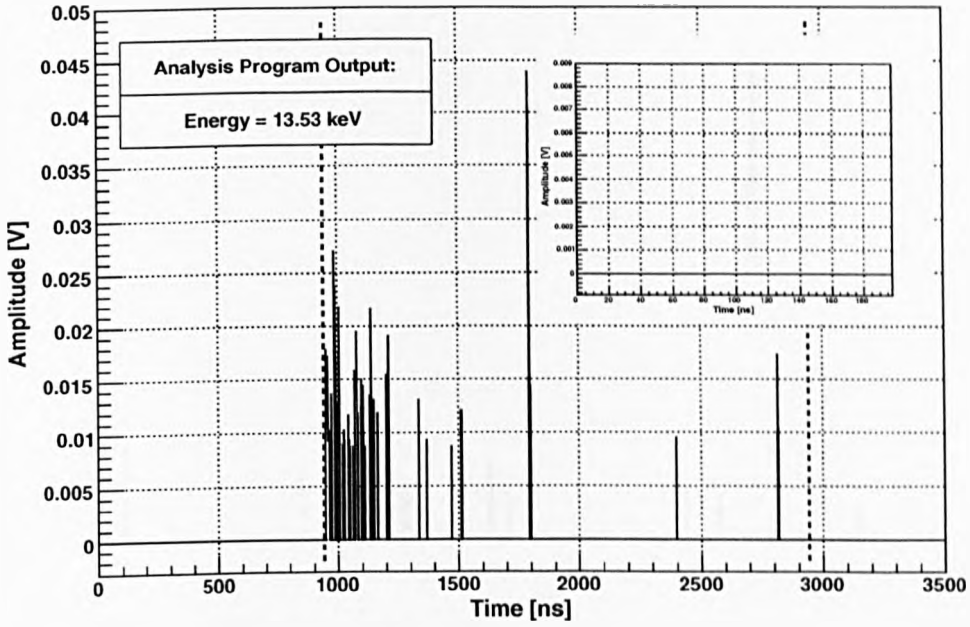

Figure 5.19: Implementing Maximum Base Noise Cut as a Solution to the Baseline Problem. The integration boundaries are shown by dotted vertical lines, and span a time period of 2000 ns from the start of the pulse. The baseline is calculated in the same way as in Figure 5.18. Bins of amplitude less than the maximum noise bin are rejected. This cut does not work well in this case, as the maximum noise bin is clearly an event rather than noise. This leads to a further underestimation of the energy when compared with Figure 5.18.

at the beginning of the waveform in Figure 5.18 indicates that this technique does not reconstruct the pre-trigger pulse correctly. Therefore, this pulse has a stronger effect on the standard deviation than desired. The integration boundaries for the total pulse area remain unchanged, and a slightly lower deposited energy is calculated. This acts as an additional indication that, although this is an improvement, the recoil energy is still underestimated.

The problem lies with the miscalculation of the baseline. As it is known that the standard deviation from the mean is affected by the presence of a pulse in the pre-trigger region, it is clear that this needs to be ignored when determining the baseline. One way to accomplish this is to find the mean and standard deviation in the same way as done for Figure 5.20. Then repeat the process excluding any bins of amplitude greater than 3σ to

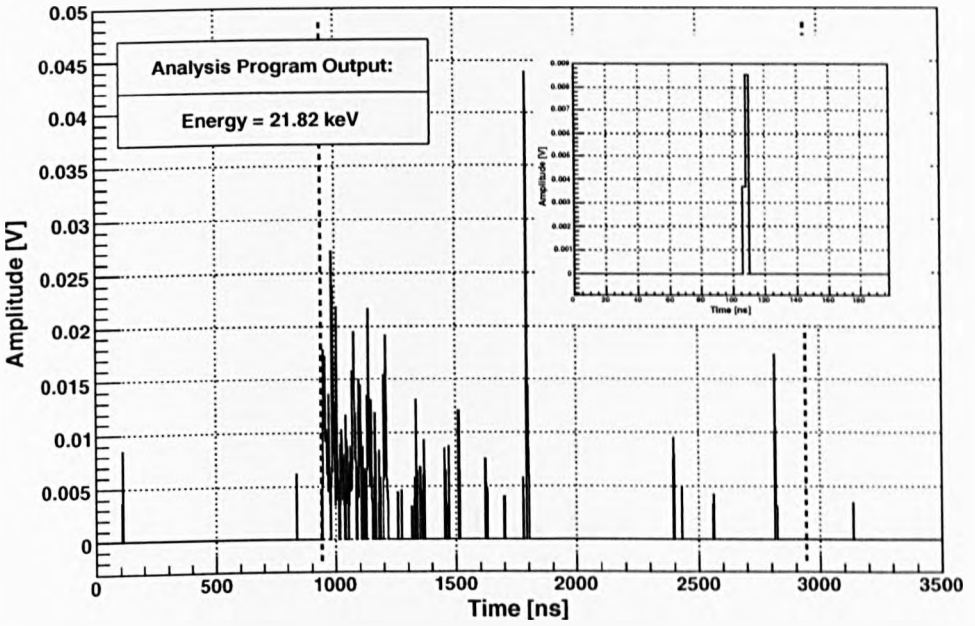

Figure 5.20: Implementing 3σ Noise Cut as a Solution to the Baseline Problem. The integration boundaries are shown by dotted vertical lines, and span a time period of 2000 ns from the start of the pulse. The baseline is calculated in the same way as in Figure 5.18. Rather than exclude bins of amplitude less than the maximum noise bin, as in Figure 5.19, the standard deviation of the first 200 ns is calculated. Bins of amplitude less than 3 standard deviations (3σ) from the mean noise are rejected. An improvement over Figure 5.19 is seen. However, the standard deviation is still affected by the unrelated event in the first 200 ns.

find a new mean and standard deviation. The new value for the mean gives an improved baseline estimation, and the standard deviation can be used in the same way as above to remove any bins of amplitude less than 3σ over the whole waveform. The resultant pulse is shown in Figure 5.21. When compared with Figures 5.19 and 5.20, the pre-trigger pulse is reconstructed to a better extent. Additionally, the baseline problem is now solved relative to Figure 5.18, evident from the higher calculated energy.

5.6 Initial Cuts

Before any higher level cuts to discriminate neutrons from gammas are conducted, a series of basic cuts are implemented to improve the signal-to-background ratio.

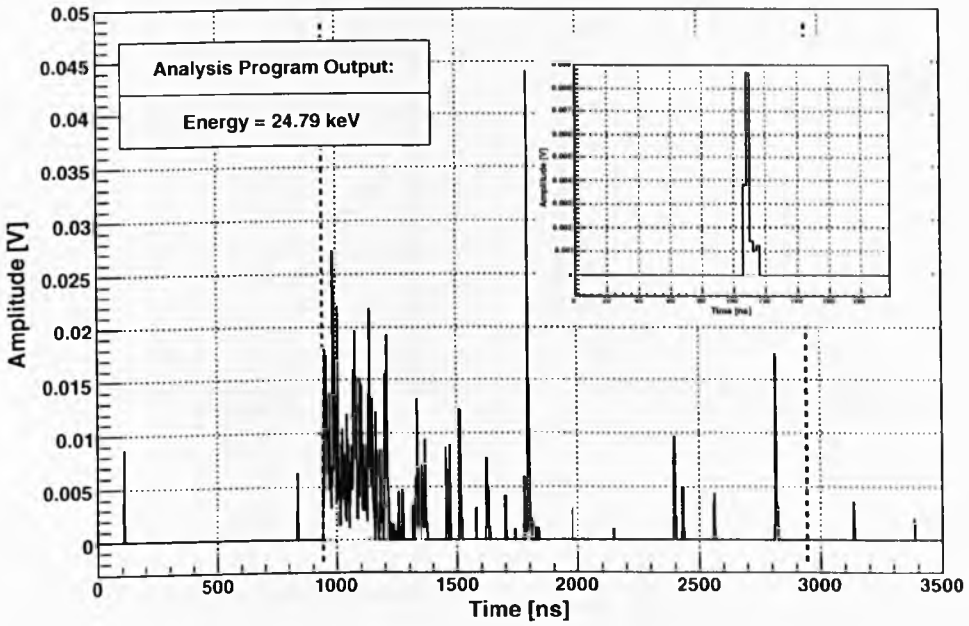

Figure 5.21: Improvement on 3σ Noise Cut Solution to the Baseline Problem. The integration boundaries are shown by dotted vertical lines, and span a time period of 2000 ns from the start of the pulse. Unlike Figures 5.19 and 5.20, the baseline is not calculated in the same way as in Figure 5.18. Instead, the baseline is determined by excluding the unrelated event in the first 200 ns, and averaging over the other bins. This is achieved by calculating the standard deviation and mean noise in the same way as in Figure 5.20. The process is then repeated over the first 200 ns, and bins of amplitude greater than 3σ from the mean noise are excluded. The new value for the standard deviation is used to reject bins of amplitude less than 3σ in the main waveform as in Figure 5.20. The result is an improvement on the energy calculated by the reduction program.

A suitable full scale (range) over which to digitise the signal needs to be chosen. An 8-bit digitiser will give a maximum of 256 counts over this range, and the Acqiris DC265 has a minimum and maximum full scale of 50 mV and 5 V respectively. Using the Lindhard curve for sodium recoils in sodium, given in Figure 3.15, all nuclear recoil energies of interest for dark matter searches will be quenched by 48% at the very most. Therefore, a 50 keV nuclear recoil will result in a 25 keV electron equivalent pulse. This is equivalent to a pulse close to that from a 29 keV Xe K_α X-ray from ^{129}I shown in Figure 5.13. With an amplitude of just over 11 mV, a range of 50 mV will be adequate for this experiment,

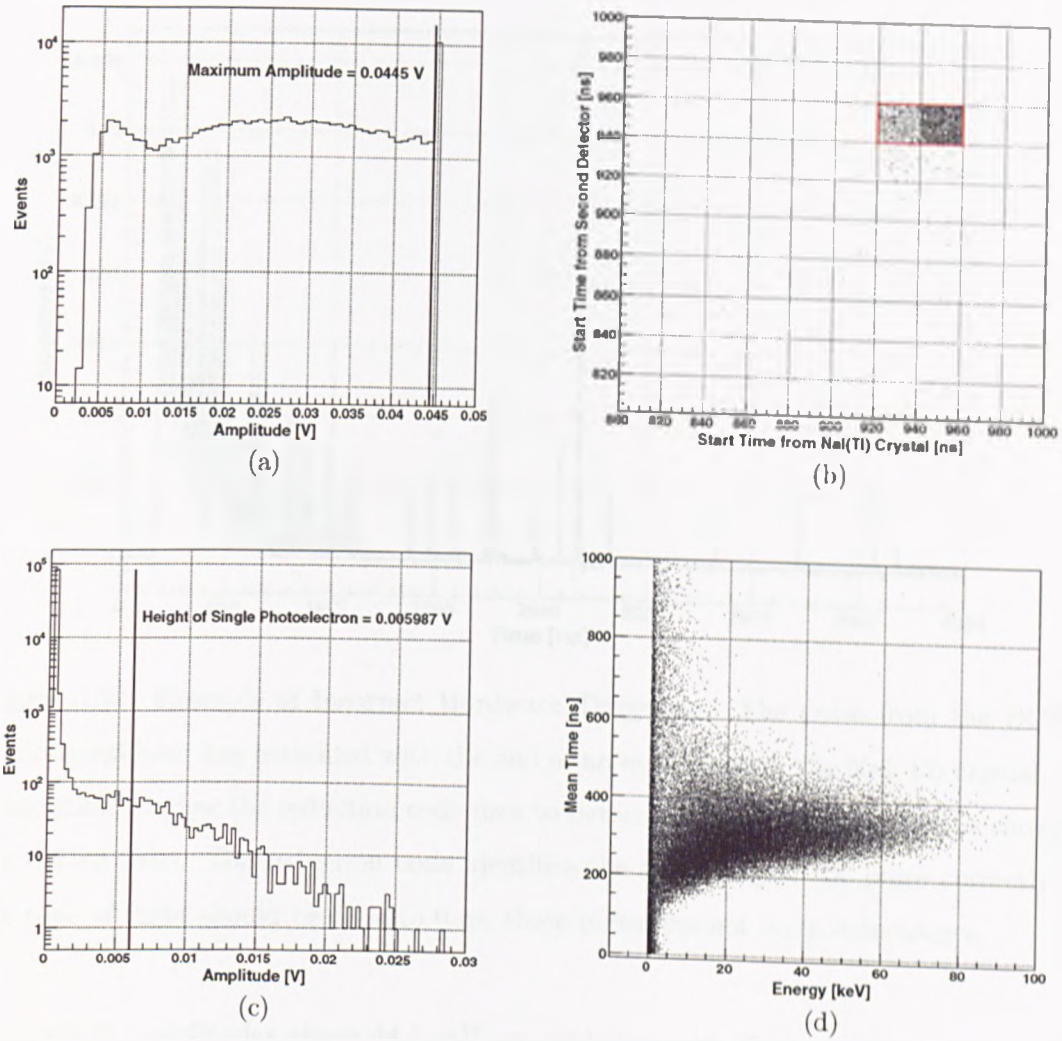

Figure 5.22: Outline of Low Level Cuts Implemented: (a) Saturation cut of 0.0445 V; (b) Coincidence cut; (c) Cut on events where 3σ exceeds the single photoelectron amplitude of 0.005987 V; and (d) Final distribution of mean time against deposited energy after the new baseline is calculated as discussed in Section 5.5.3 and all initial cuts are performed. The data used is from the ^{22}Na 511 keV gamma-ray coincidence run.

providing the best possible resolution.

As shown in Figure 5.22(a), a significant number of events exceed the full range of the digitiser. As none of these events are of an amplitude we expect for the low energy recoils being investigated, they can safely be discarded through a simple saturation cut. Although a full scale of 50 mV is used, the pulses are offset from the centre of this scale by 20 mV. Hence, bins with amplitude greater than 45 mV will saturate the digitiser.

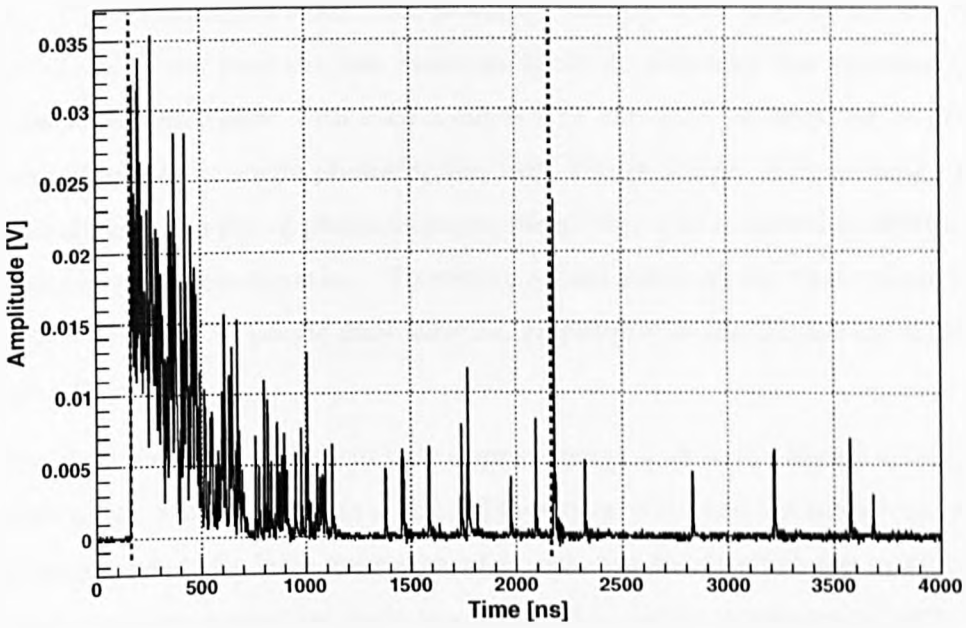

Figure 5.23: Example of Incorrect Hardware Triggering. The pulse from the BC501A liquid scintillator has coincided with the end of an event seen in the NaI(Tl) crystal. The integration window the reduction code uses to determine the total pulse area is shown by the dotted lines. The reduction code identifies the beginning of the pulse correctly. As the time of flight should be close to 0 ns, these pulses cannot be in coincidence.

As a result, amplitudes above 44.5 mV are excluded from the analysis, as indicated in Figure 5.22(a).

Even though the DAQ is triggered on a two-fold coincidence signal, it is surprising to witness some events falling outside of this coincidence window as shown in Figure 5.22(b). Further investigation shows that this is not a problem with the pulse finding algorithm described in Section 5.3. Rather, these events are caused when the DAQ triggers on the end of an event, an example of which is shown in Figure 5.23. The reduction code, having no knowledge of the point at which the DAQ triggers, finds the beginning of the pulse correctly. A veto can be added to the hardware electronics shown in Figure 5.3, to reject a coincidence signal after a certain delay. However, the relatively small number of such events means that a simple cut on the coincidence in software is sufficient, illustrated by the area contained within the red box in Figure 5.22(b).

As discussed in Section 5.5.3, an accurate baseline can be determined by recalculat-

ing the mean after excluding any pulses that exceed a threshold of 3σ from the original mean. The remaining bins are then scanned, and any with amplitudes less than three standard deviations from the new mean are ignored. Although this improves the signal-to-noise ratio, the danger with such a cut is that the value of 3σ could be greater than the amplitude of the single photoelectron from Figure 5.8(a). As low energy pulses will only result in a handful of photoelectrons spread over a time period of 2000 ns, this can lead to energy underestimation. Therefore, a final low level cut that rejects any events with $3\sigma > 0.005987$ V (single photoelectron amplitude) is also implemented, as shown in Figure 5.22(c).

The final scatter plot of mean time against energy is shown in Figure 5.22(d), after the solution to the baseline problem described in Section 5.5.3 and the initial cuts above have been implemented. No large improvement is seen over the result shown in Figure 5.17(d), although on closer inspection there has been a very minor improvement with the spread of mean time at low energies.

Although little improvement is seen, it is important to note that the main purpose of these cuts is not to reduce the spread of mean times at low energies. This is already adequately done by recalculating the baseline. These cuts help to reject events that would otherwise decrease the efficiency of higher level cuts. These higher level cuts will now be discussed.

5.7 Neutron-Gamma Discrimination in BC501A Detector

A secondary detector is required to identify neutrons that scatter off the target nuclei at the nuclear recoil energies given by Eq. (3.15). As the main background is from gamma-rays, a detector material with a high discrimination power is a major requirement. The characteristics of the BICRON Corporation BC501A organic liquid scintillator ($C_6H_4(CH_3)_2$), equivalent to Nuclear Enterprises NE213, are well-suited for this purpose. The properties of BC501A are detailed in Table 5.4, and the scintillation mechanism in organic liquids is outlined in Section 3.1.

Calibration of the detector with a ^{137}Cs source is shown in Figure 5.24. Energy calibration is needed to investigate the characteristics of BC501A in detail, and hence optimise the analysis. The response of BC501A is not linear at low energies [165], but this does

Table 5.4: Properties of BC501A Liquid Scintillator Relevant to its Scintillation. Values taken from [158, 164].

Density		0.874	g/cm^3
Hydrogen-to-Carbon Ratio		1.212	
Flash Point		299	K
Peak Emission Wavelength		425	nm
Decay Times	τ_1	3.16	ns
	τ_2	32.3	ns
	τ_3	270	ns
Absolute Light Yield		13	photons/keV

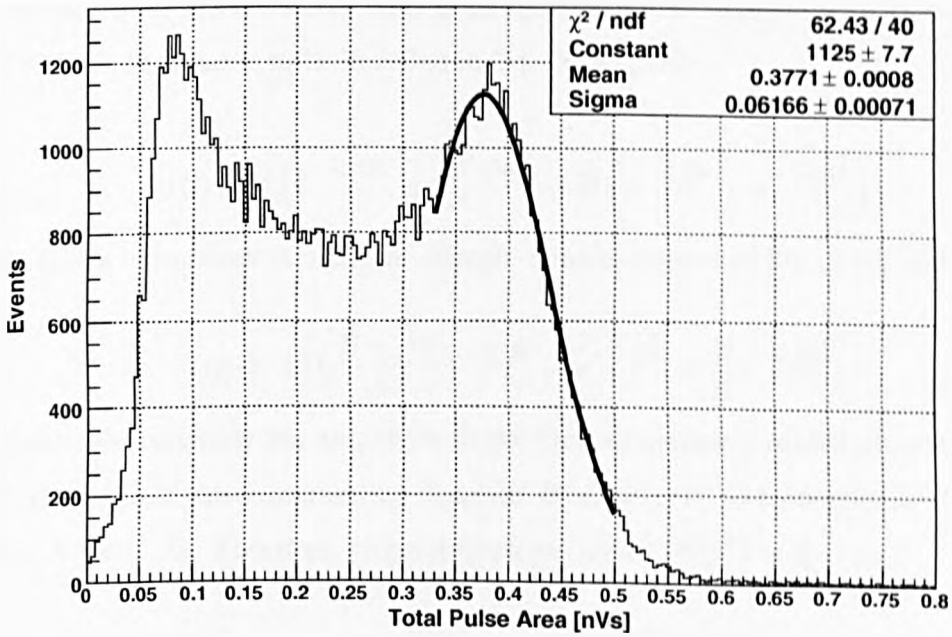

Figure 5.24: Calibration of BC501A Detector with 662 keV Gamma Line from ^{137}Cs Source. A Gaussian function is fitted to the peak corresponding to the gamma line.

not affect measurements on the high-energy scattered neutrons that are detected in this work.

5.7.1 Pulse Shape Analysis

An equation for the pulse shape can be obtained by combining the response function of the readout system and light detector, with the exponential decay spectrum of the material [158]. The intensity of this pulse $I(t)$ can be written as a function of two exponentials [166]:

$$I(t) = A\left(e^{-\frac{(t-t_0)}{\tau_e}} - e^{-\frac{(t-t_0)}{\tau_1}}\right) \tag{5.12}$$

where τ_e is the RC time constant of the data acquisition electronics, τ_1 is the decay time constant of the scintillating medium, and A is a normalisation constant. Due to the loose definition of the pulse start time given in Section 5.3, an additional parameter for time reference t_0 is defined.

It is clear from fits to the typical gamma and neutron pulses in Figures 5.25 and 5.26 respectively, that the two exponential terms in Eq. (5.12) do not give satisfactory results. It is evident from Table 5.4 that there is an additional slow component, with a decay time τ_2 of 32.3 ns, that needs to be included in Eq. (5.12) [166]:

$$I(t) = A\left(e^{-\frac{(t-t_0)}{\tau_e}} - e^{-\frac{(t-t_0)}{\tau_1}}\right) + B\left(e^{-\frac{(t-t_0)}{\tau_e}} - e^{-\frac{(t-t_0)}{\tau_2}}\right) \tag{5.13}$$

where B is a normalisation constant. Simple re-arrangement of Eq. (5.13) yields:

$$I(t) = A\left[\left(\frac{B+A}{A}\right)e^{-\frac{(t-t_0)}{\tau_e}} - e^{-\frac{(t-t_0)}{\tau_1}} - \frac{B}{A}e^{-\frac{(t-t_0)}{\tau_2}}\right] \tag{5.14}$$

Due to the relatively low amplitude of the slow component's contribution to the waveform, the value of the normalisation constant B is expected to be negligible compared to that of A ($B \ll A$). Therefore, to good approximation, $\left(\frac{B+A}{A}\right) \approx \frac{A}{A} = 1$:

$$I(t) \approx A\left(e^{-\frac{(t-t_0)}{\tau_e}} - e^{-\frac{(t-t_0)}{\tau_1}} - \frac{B}{A}e^{-\frac{(t-t_0)}{\tau_2}}\right) \tag{5.15}$$

The results of the fits of the simplified approximation given in Eq. (5.15) to typical gamma and neutron pulses are shown in Figures 5.25 and 5.26 respectively. This results

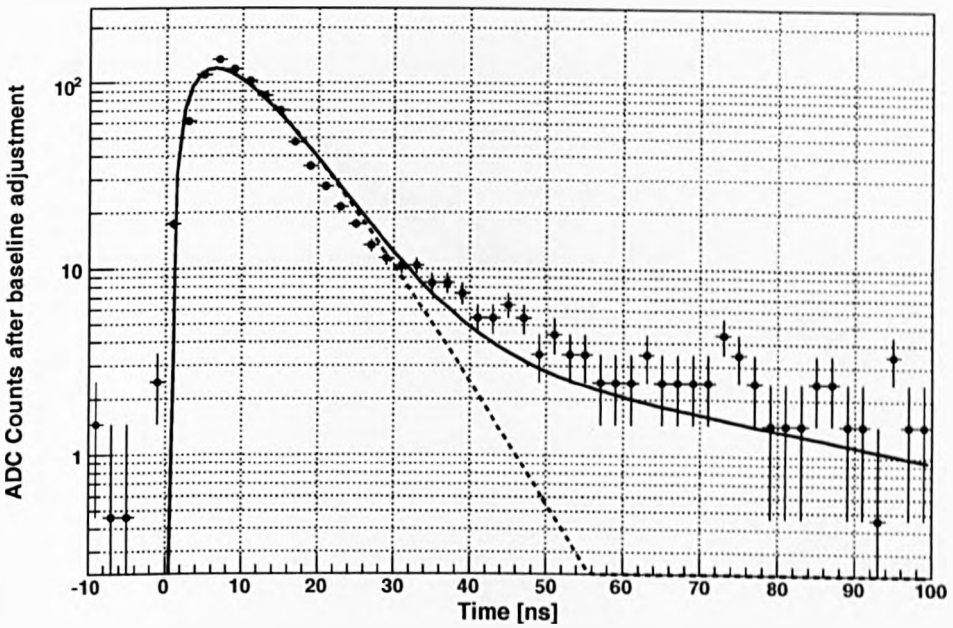

Figure 5.25: Decay Time Spectrum of a Typical 600 keV Electron Recoil in BC501A Detector. The waveform is plotted after the baseline correction outlined in Section 5.3 is performed. The results of the fits performed with Eq. (5.12) and Eq. (5.15) are shown by the dashed and solid line respectively. Parameters derived from the 3-exponential fit (Eq. (5.15)) are detailed in Table 5.5. Energy scale calibration is performed with the 662 keV line from a ^{137}Cs source (Figure 5.24).

in a more accurate reproduction of the pulse shape. Resultant fit parameters are given in Table 5.5.

From Table 5.5, the decay time of the slow component τ_2 for the electron recoil shown in Figure 5.25 agrees with the manufacturer's value within errors. The magnitude of the error on τ_2 is a significant fraction of the value obtained due to the low counts in the regime dominated by the slow component (> 30 ns).

The decay times determined for the slow component exceed the actual decay constant, given in Table 5.4, by a considerable amount. This is due to contamination from the further fluorescence component τ_3 of lifetime 270 ns, which is not included in the fit. The discrepancy between these results, and those obtained by [166] lies in the bad coupling between the BC501A detector and hardware trigger electronics. The evidence of this is seen by oscillations in ADC counts in the tail region of the pulses shown in Figures 5.25

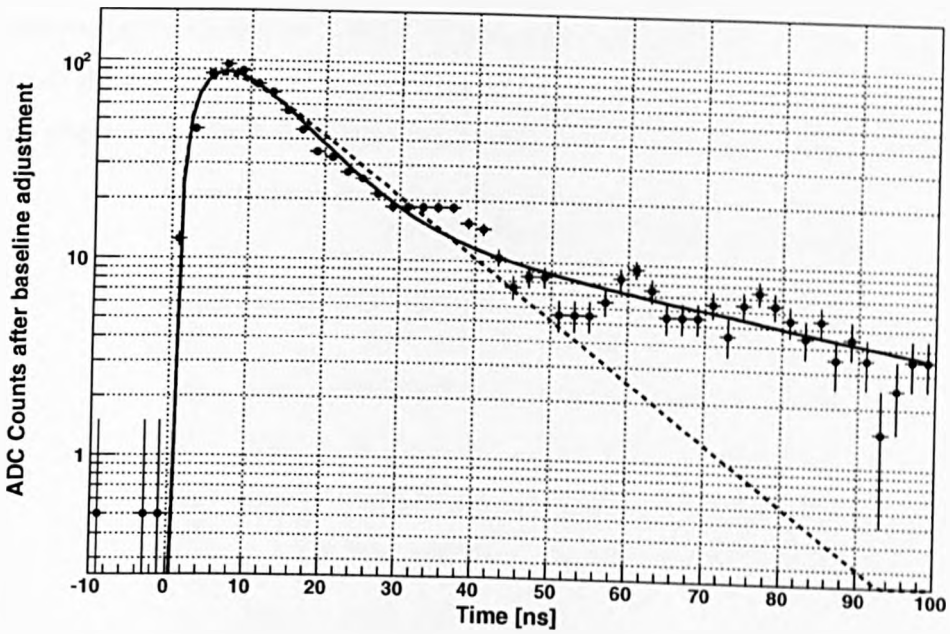

Figure 5.26: Decay Time Spectrum of a Typical 600 keV Nuclear Recoil in BC501A Detector. As in Figure 5.25, the waveform is plotted after the baseline correction outlined in Section 5.3 is performed. The results of the fits performed with Eq. (5.12) and Eq. (5.15) are shown by the dashed and solid line respectively. Parameters derived from the 3-exponential fit (Eq. (5.15)) are detailed in Table 5.5. Energy scale calibration is performed with the 662 keV line from a ^{137}Cs source (Figure 5.24).

and 5.26.

The ratio of the intensities of the slow to fast components $\left|\frac{B}{A}\right|$ provides a measure of the discrimination power, making use of the characteristic enhanced emission of the slow component in BC501A. It is clear from Table 5.5 that gammas and neutrons can be distinguished with this ratio, even though the result for electron recoils does not agree with that from [166] for the reasons outlined above.

The fitting of each pulse is a time consuming procedure due to the six free parameters in Eq. (5.15). The time taken for a fit to successfully converge can be improved by restricting parameters, or deriving average values for some and fixing them. The latter method is used by [166]. However, if the discriminating factor is the ratio of the intensities of the slow to fast components, the same should hold for the ratio of the slow component to the total intensity of the pulse.

Table 5.5: Resultant Fit Parameters for Scintillation Pulses from BC501A Detector. The parameters are obtained as a result of fits performed with Eq. (5.15) to typical 600 keV electron (Figure 5.25) and nuclear (Figure 5.26) recoils. These are compared with the values obtained by [166] for a three-exponential fit to a sample of electron recoils.

		Electron Recoils		Nuclear Recoils
		Eq. (5.15)	[166]	Eq. (5.15)
A		1351 ± 6	Free	1278 ± 2
t_0	[ns]	0.846 ± 0.017	0.31	0.842 ± 0.026
τ_e	[ns]	6.24 ± 0.34	5.578	6.16 ± 0.69
τ_1	[ns]	4.93 ± 0.28	4.887	5.22 ± 0.55
$\left\|\frac{B}{A}\right\|$		0.0043 ± 0.0004	0.0166	0.0156 ± 0.0012
τ_2	[ns]	54.3 ± 17.9	34.276	56.5 ± 4.0

Therefore, by integrating over the tail of a pulse and dividing by the total pulse area, as shown in Figure 5.27, neutron and gamma events are separated. The ratio of tail $P_{\rm nr}$ to total pulse area $A_{\rm nr}$ for nuclear recoils will be closer to unity when compared with electron recoils of the same energy $\frac{P_{\rm er}}{A_{\rm er}}$. This can be inferred from Table 5.5, where the $|\frac{B}{A}|$ ratio is smaller for electron recoils. In other words:

$$\frac{P_{\rm nr}}{A_{\rm nr}} > \frac{P_{\rm er}}{A_{\rm er}} \tag{5.16}$$

5.7.2 Implementation of Discrimination Technique

A pulse finding algorithm for BC501A waveforms has been developed and programmed into the analysis code. Initially, the position and amplitude of the maximum bin is found. For the pulses in Figure 5.27, this occurs 140 ns after the start of data acquisition. Then, starting at 20 ns prior to the position of the maximum bin, the time of the first bin to exceed 10% of the maximum bin's amplitude is found. This is the start of the pulse, which occurs at 134 ns for both pulses in Figure 5.27. The end of the waveform is defined as being 100 ns after the position of the maximum bin (at 240 ns in Figure 5.27). The waveform is integrated between these boundaries to find the total pulse area.

The lower integration boundary for the area of the tail is defined as being a certain

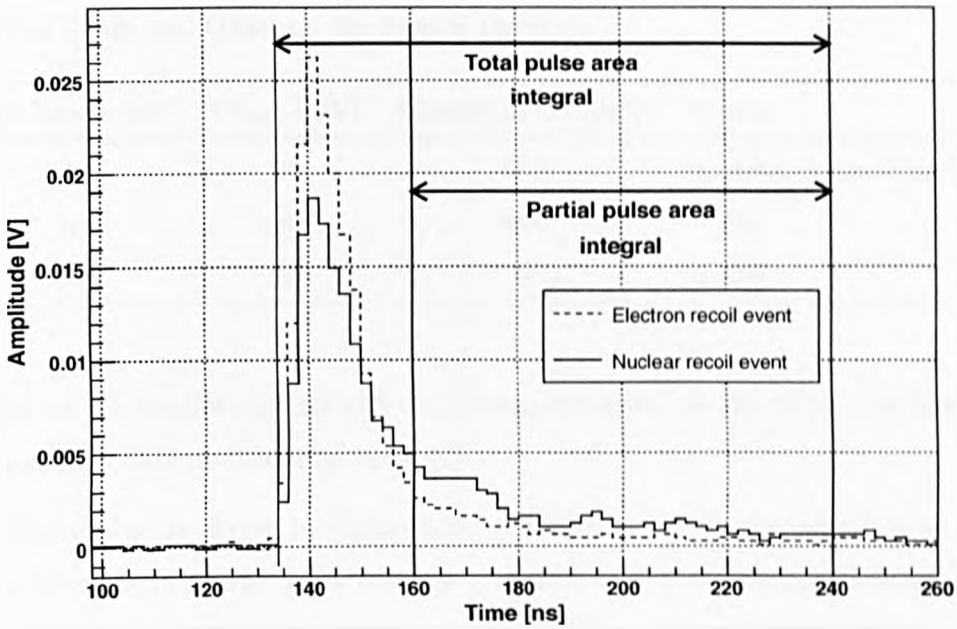

Figure 5.27: Pulses from Nuclear and Electron Recoils in BC501A Detector. The ratio of the partial-to-total area is used to discriminate nuclear and electron events. Fits to the decay time spectra of these sample pulses are shown in Figure 5.25 and 5.26. As shown here, for the same energy, this ratio will be closer to 1 for nuclear recoils. The lower partial integration boundary shown occurs 20 ns after the maximum peak position. Energy scale calibration is performed with the 662 keV gamma line from a ^{137}Cs source (Figure 5.24).

time period after the position of the maximum bin. In Figure 5.27, this occurs at 160 ns, which is 20 ns after the maximum bin position. The upper integration boundary for this partial pulse area is the same as that for the whole pulse. The waveform is integrated between these boundaries, using the formula given in Eq. (5.7), to determine the partial pulse area.

The discrimination technique defined by Eq. (5.16) is tested by exposing the BC501A detector to gamma-ray and neutron sources. PMT pulses from the BC501A detector are sent to a two-way 50 Ω power divider. This splits the signal into two, resulting in a reduction in amplitude by the same factor. One of the resultant pulses is sent to the Acqiris digitizer, while the other is sent to a hardware discriminator. If the maximum pulse height satisfies the hardware threshold (5 mV for all sources, 3 mV for the background run), a NIM logic-pulse is sent to the Acqiris digitizer, acting as the external trigger. Full

Table 5.6: Saturation Cuts Employed during Analysis of BC501A Data as a Function of the Full Range and Offset on the Acqiris Digitizer.

Full Range [mV]	Offset [mV]	Saturation Cut [mV]	Source
50	20	44.5	neutron beam & background
100	40	89.0	^{137}Cs
200	80	178.0	AmBe

ranges on the Acqiris digitizer and the corresponding offline saturation cuts performed on the recorded data are listed in Table 5.6.

The results are shown in Figure 5.28. An initial limit for the partial area integral of 30 ns after the maximum peak position is chosen. An upper horizontal band of neutrons is hinted at for data taken with the shielded AmBe neutron source (Figure 5.28(c)). The presence of this band is confirmed with data from the 2.45 MeV deuterium-deuterium neutron beam (Figure 5.28(d)). Only the lower gamma-ray event band is visible in background (Figure 5.28(a)) and ^{137}Cs data (Figure 5.28(b)).

It is interesting to note that, even with the neutron beam, a large gamma background is still apparent in Figure 5.28(d). This emphasises the need for good neutron-gamma discrimination in this experiment.

5.7.3 Effect of Collimating the Neutron Source

It is evident from Figure 5.1 that neutrons from the beam are collimated to some extent. As the neutron generator produces an isotropic distribution of mono-energetic neutrons, the concrete castle serves to shield the rest of the laboratory. This prevents neutrons scattering off other bodies into the crystal.

Further collimation may cause an improvement in results, by directing all neutrons toward the crystal. Two layouts are tested. The first uses sheets of wax similar to those seen in Figure 5.1, with the exception of a 32 mm diameter hole drilled through them. The wax should provide extra shielding, only allowing those neutrons that are on a direct path to the crystal to pass unhindered. The second layout involves decreasing the diameter of the hole further by introducing a 30 mm external diameter, 3 mm thick, iron pipe into the framework. Schematics for both setups are shown in Figure 5.29.

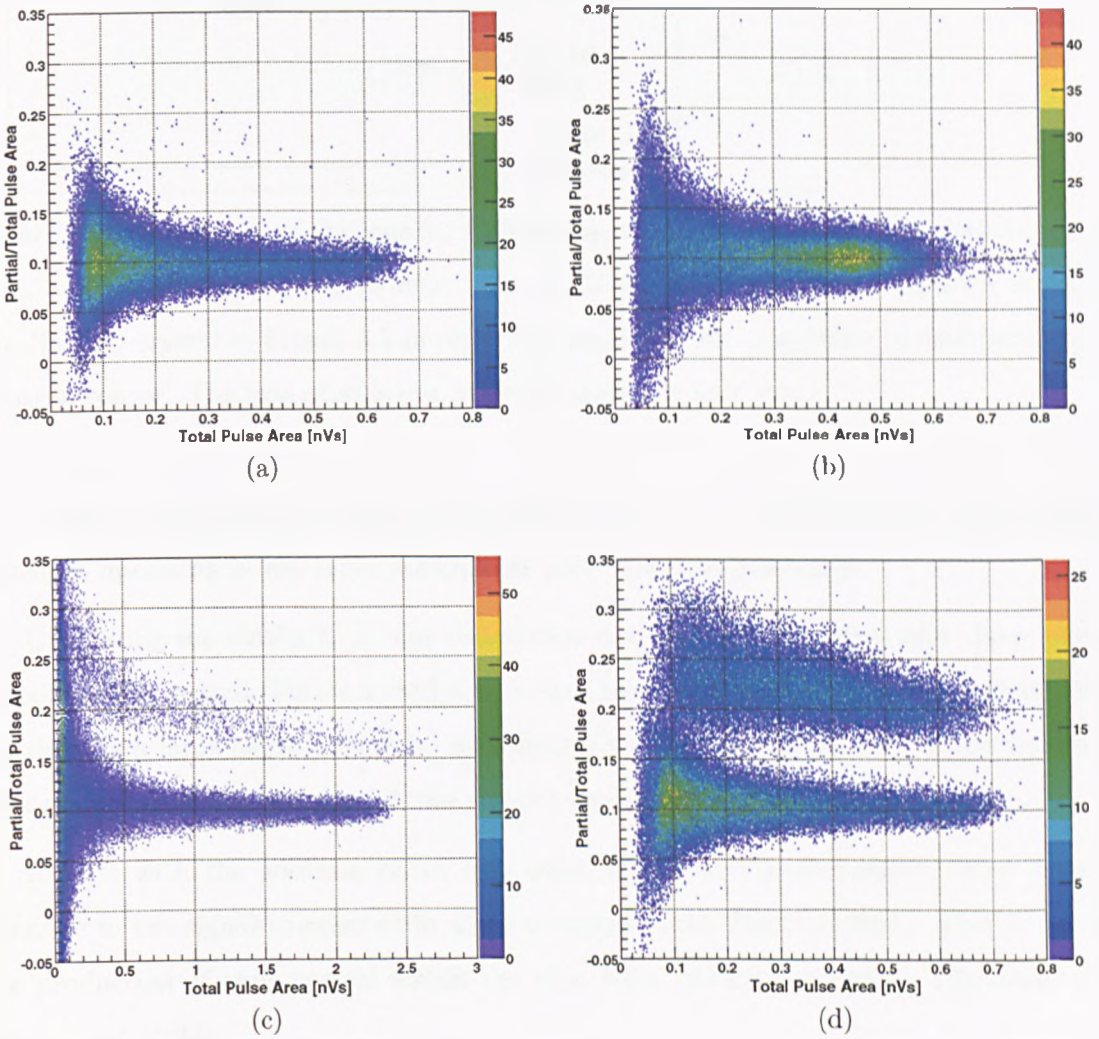

Figure 5.28: Scatter Plots of Partial-to-Total Pulse Area Ratio vs. Total Pulse Area in the BC501A Detector for: (a) background events; (b) ^{137}Cs gamma-ray source; (c) shielded AmBe neutron source; and (d) 2.45 MeV deuterium-deuterium neutron beam. The 662 keV gamma line is visible in (b) at approximately 0.45 nVs total pulse area. An upper band of neutron energies is evident in (c) and (d). Initial and final limits of 30 ns and 100 ns after the maximum peak position are implemented for the partial area integral.

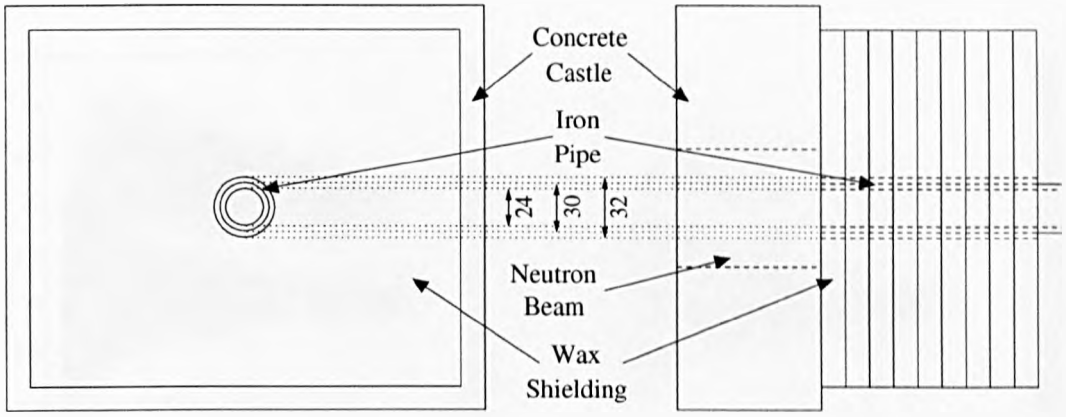

Figure 5.29: Schematic of Options for Collimating the Neutron Beam. Dimensions are in mm, and the diagram is not to scale. The BC501A liquid scintillator detector replaces the NaI(Tl) crystal in Figure 5.1 in order to investigate the possibility of collimating the neutron source. The iron pipe is not present during the first run.

To assess the effects of these two layouts, the crystal is replaced with the BC501A detector, operating in the same principle as that described previously.

Comparing the results from wax collimation only in Figure 5.30(a), with those where no collimation is used (Figure 5.28(d)), it is clear that there is some degree of neutron loss. As there is a large gamma background inherent to this experiment, and fewer neutrons that emerge from the beam reach the crystal, the signal-to-noise ratio decreases.

Results with the addition of an iron pipe, shown in Figure 5.30(b), show a large decrease in the signal-to-noise ratio when compared with Figure 5.28(d). This is due to the production of gamma-rays within the pipe from incident neutrons. Therefore, this setup is not viable.

5.7.4 Determination of Pulse Area Integration Boundaries

Being conservative, from Figure 5.28(d), nuclear and electron recoils can be separated at total pulse areas greater than 0.3 nVs. Using the 662 keV calibration peak in Figure 5.24, this area corresponds to a deposited recoil energy of approximately 530 keVee.

For the reasons outlined in Section 3.6.1, the scintillation light from nuclear recoils is quenched in all scintillating materials. BC501A is not an exception, and the quenching factor has been found to be non-linear [167]:

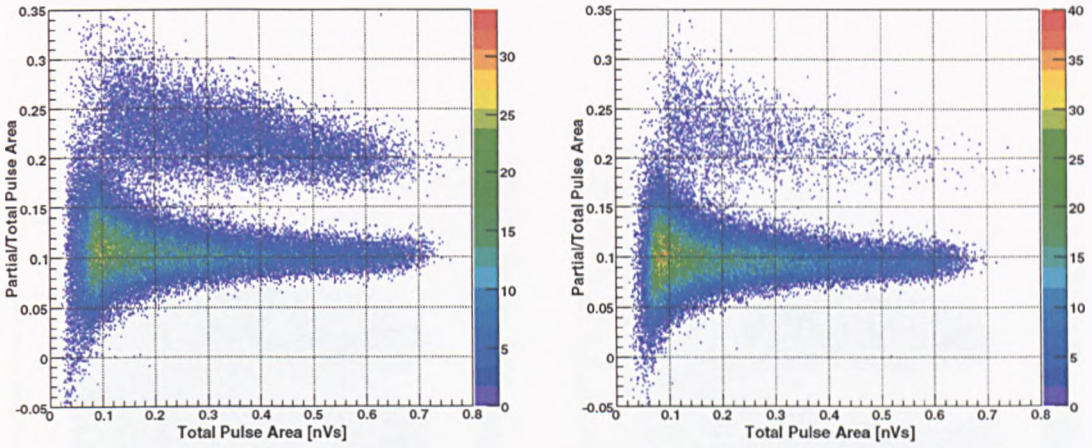

(a) (b)

Figure 5.30: Effect of Collimation on Pulse Shape Discrimination in BC501A Detector: (a) with wax only; and (b) with iron-pipe and wax collimation. Data were taken with the 2.45 MeV deuterium-deuterium neutron beam. This can be compared with Figure 5.28(d), where no attempt to collimate the neutrons is made. This shows that collimation leads to an increase in gamma-rays, implying that no attempt to collimate the beam should be made when conducting the experiment.

$$E_{\mathrm{ee}}\,[\mathrm{MeV}] = (0.034 \pm 0.003) E_{\mathrm{nr}}^{2}\,[\mathrm{MeV}] + (0.311 \pm 0.011) E_{\mathrm{nr}}\,[\mathrm{MeV}] - (0.109 \pm 0.006) \quad (5.17)$$

where E_{ee} is the electron equivalent energy observed, and E_{nr} is the actual nuclear recoil energy deposited in the liquid scintillator. In order to rearrange Eq. (5.17) in terms of E_{ee}, the quadratic is solved to give:

$$E_{\mathrm{nr}}\,[\mathrm{MeV}] = \sqrt{22.4 + 27.2 E_{\mathrm{ee}}\,[\mathrm{MeV}]} - 4.57 \quad (5.18)$$

which gives the only positive answer. Hence, a deposited energy of 530 keVee is equivalent to a nuclear recoil of energy 1.5 MeVnr. Therefore, with reference to Figure 5.28(d), a scattering neutron must deposit a minimum nuclear recoil energy of 1.5 MeVnr to enable successful discrimination. Otherwise, it would be rejected.

By changing the pulse partial area integration boundaries, it may be possible to increase the resolution between neutron and gamma events, and hence decrease the energy threshold for discrimination. The start of the tail is varied between 10 and 50 ns after the

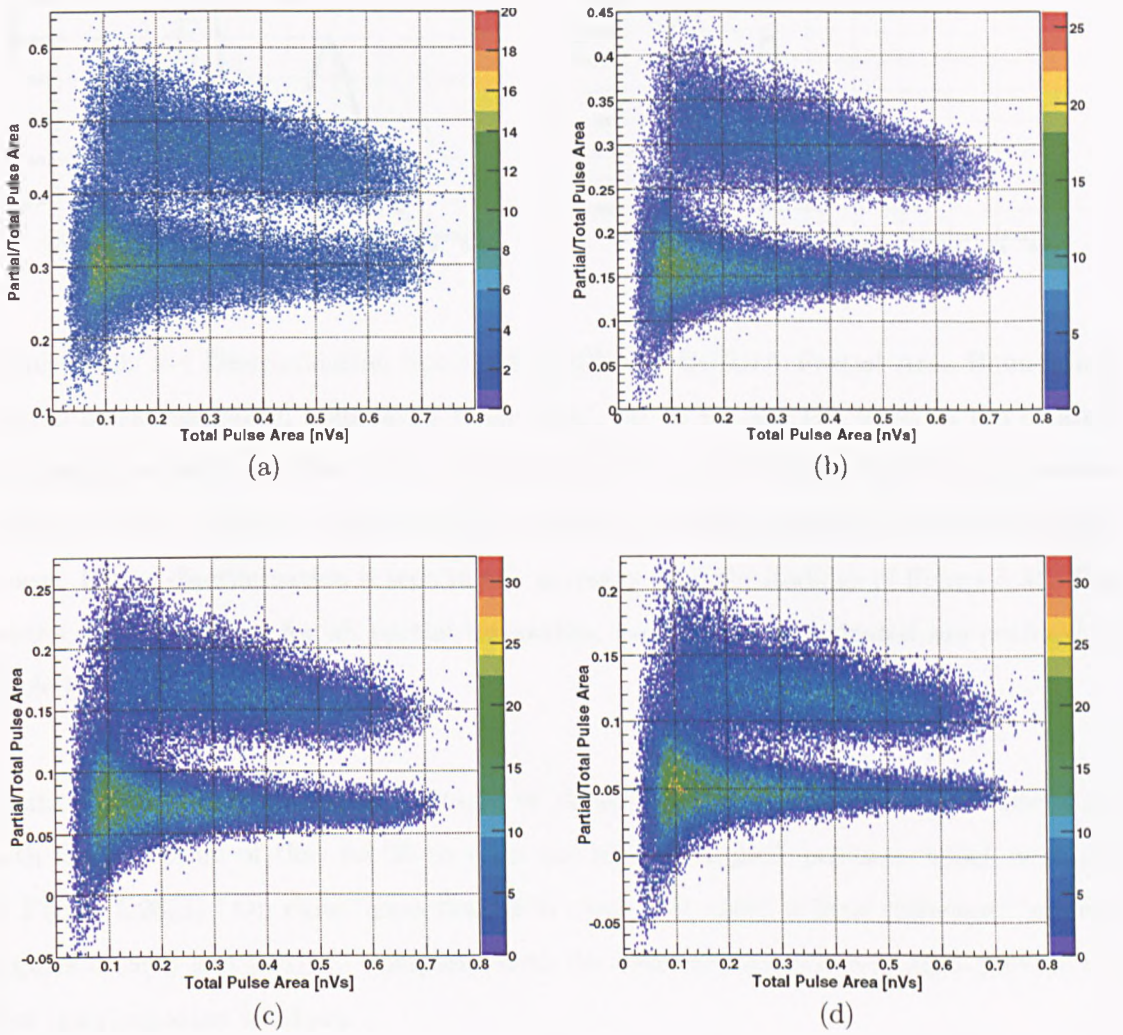

Figure 5.31: Comparison of Different Partial Area Boundaries for BC501A Pulses. Partial pulse integration boundaries range from: (a) 10 ns; (b) 20 ns; (c) 40 ns; and (d) 50 ns to 100 ns after the maximum peak position. Data is taken with the 2.45 MeV deuterium-deuterium neutron beam. Pulse shape discrimination for the partial pulse integration boundary from 30 ns to 100 ns after the maximum peak position is shown in Figure 5.28(d). The best separation between electron and nuclear recoils is attained in (b).

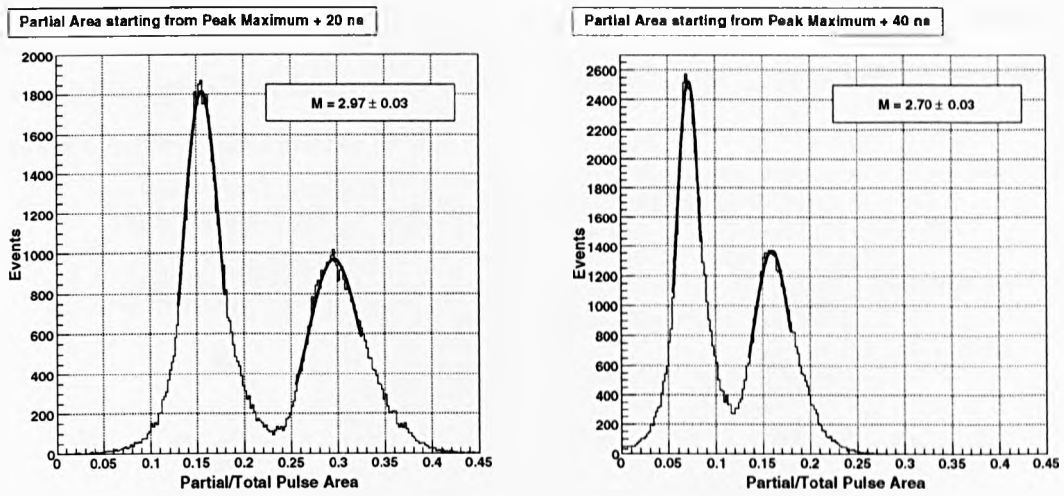

(a) (b)

Figure 5.32: n-γ Discrimination Spectra for Different BC501A Partial Area Boundaries. Partial pulse integration boundaries range from: (a) 20 ns; and (b) 40 ns to 100 ns after the maximum peak position. Data was taken with the 2.45 MeV deuterium-deuterium neutron beam. A figure of merit M (Eq. (5.19)) is used to quantify the discrimination power. Better discrimination is seen in (a), agreeing with the findings of Figure 5.31. The results of this analysis for all partial integration boundaries investigated are outlined in Table 5.7.

position of the maximum peak, in stages of 10 ns. The results are shown in Figure 5.31, with the exception of that for 30 ns after the maximum peak position, which is shown in Figure 5.28(d). On close inspection, it is clear that there is little difference between Figures 5.28(d) and 5.31(b). Compared with the other results, however, they provide the best discrimination windows.

A figure of merit M is used to quantify the neutron-gamma discrimination power [158]:

$$M = \frac{(\bar{x}_{\mathrm{n}} - \bar{x}_{\gamma})}{(\sigma_{\mathrm{n}} + \sigma_{\gamma})} \tag{5.19}$$

where $\bar{x}_{\mathrm{n}}$ and $\bar{x}_{\gamma}$ are the mean positions of the neutron and gamma peaks respectively. The full width half maxima of the neutron and gamma peaks are given by σ_{n} and σ_{γ} respectively.

One dimensional histograms of the the partial-to-total pulse area ratio for the data in Figures 5.28(d) and 5.31 result in two peaks as shown in Figure 5.32. Fitting Gaussians to these peaks and applying Eq. (5.19), M-factors are calculated as shown in Table 5.7. An

Table 5.7: Analysis on Different Partial Integration Boundaries for BC501A Pulses. The greater the value of the figure of merit M, given by Eq. (5.19), the better the discrimination between nuclear and electron recoils.

Intial Integration Boundary [ns]		Electron Recoil Peak	Nuclear Recoil Peak	M
10	$\bar{x}$	0.2990 ± 0.0002	0.4518 ± 0.0003	2.15 ± 0.02
	σ	0.0324 ± 0.0003	0.0386 ± 0.0005	
20	$\bar{x}$	0.1555 ± 0.0001	0.2961 ± 0.0003	2.97 ± 0.03
	σ	0.0189 ± 0.0002	0.0284 ± 0.0004	
30	$\bar{x}$	0.1030 ± 0.0001	0.2155 ± 0.0003	2.90 ± 0.03
	σ	0.0149 ± 0.0002	0.0239 ± 0.0003	
40	$\bar{x}$	0.0715 ± 0.0001	0.1596 ± 0.0002	2.70 ± 0.03
	σ	0.0125 ± 0.0002	0.0201 ± 0.0003	
50	$\bar{x}$	0.0482 ± 0.0001	0.1161 ± 0.0002	2.49 ± 0.04
	σ	0.0108 ± 0.0001	0.0165 ± 0.0004	

initial pulse partial area integration boundary of 20 ns after the position of the maximum peak provides the best resolution power. Closer inspection of Figure 5.31(b) shows that a conservative minimum pulse total area cut can comfortably be imposed at 0.25 nVs. This results in the reduction of the energy threshold to 440 keVee. Using Eq. (5.18), this is equivalent to a nuclear recoil energy of 1.3 MeVnr.

5.8 Time of Flight

As mentioned in Section 3.6.2, a deuterium-deuterium neutron beam produces an isotropic distribution of 2.45 MeV neutrons (Eq. (3.19)). As the rest mass of these neutrons is far greater than their kinetic energy, they are non-relativistic. By contrast, gamma-rays are massless, and hence highly relativistic. With reference to Figure 5.1, after interacting with the crystal, the non-relativistic neutrons used in this experiment will take longer to reach the secondary BC501A detector when compared with gammas. We quantify this by deriving the time of flight formula from first principles:

$$t\,[\mathrm{s}] = 3.336 \times 10^{-9} \cdot s\,[\mathrm{m}] \sqrt{\frac{m_{\mathrm{n}}\,[\mathrm{MeV}]}{2(E_{\mathrm{n}}\,[\mathrm{MeV}] - E_R\,[\mathrm{MeV}])}} \tag{5.20}$$

where s is the distance travelled by the neutron, m_{n} is its mass, E_{n} is its initial energy before interacting and E_R is the energy deposited in the crystal. As E_R is less than E_{n} by more than an order of magnitude, it can be ignored. Therefore, Eq. (5.20) can be rewritten to good approximation:

$$t\,[\mathrm{s}] \approx 3.336 \times 10^{-9} \cdot s\,[\mathrm{m}] \sqrt{\frac{m_{\mathrm{n}}\,[\mathrm{MeV}]}{2E_{\mathrm{n}}\,[\mathrm{MeV}]}} \tag{5.21}$$

yielding a value of 38 ns for the time of flight.

In Figure 5.33(b), two peaks are visible at approximately 0 and 40 ns corresponding to electrons and neutrons respectively. The time of flight differs slightly from that expected, due to a time delay between the cables carrying the signal from the BC501A detector and NaI(Tl) crystal. This systematic error does not make any difference to the final result, as it is the difference between the peaks, and not the positions, that matter.

An additional explanation can be provided from the neutron scattering simulations performed, as outlined in Section 5.2. Although the neutron peaks in Figure 5.34 occur at approximately 38 ns, the distribution is smeared at larger time differences. This is due to the fact that the distance s in Eq. (5.20) and Eq. (5.21) is that measured between the centre of the crystal and the face of the secondary detector. An incident neutron can interact anywhere in the 8 cm depth of liquid scintillator that it traverses. Substituting a value of $s = 88$ cm into Eq. (5.21) results in an upper limit of 42 ns for the time of flight. From Figure 5.34, a sharp decline is witnessed in the number of events that contribute to the simulated neutron peaks after 42 ns.

Simulated events that scatter once in the target crystal are represented by the shaded histograms in Figure 5.34. There is a wide gap between the gamma and neutron peaks as no other particles are scattered or produced in this experiment that would result in an intermediate time of flight. Additionally, as the time of flight increases from that of the neutron peak, the number of events decreases. The shape of this decrease is a result of events that interact with wax shielding, and scatter into the secondary detector at later times.

Due to the large background from gamma-rays, it is difficult to fit a Gaussian function to the measured neutron peak in Figure 5.33(b). However, after cutting on neutron

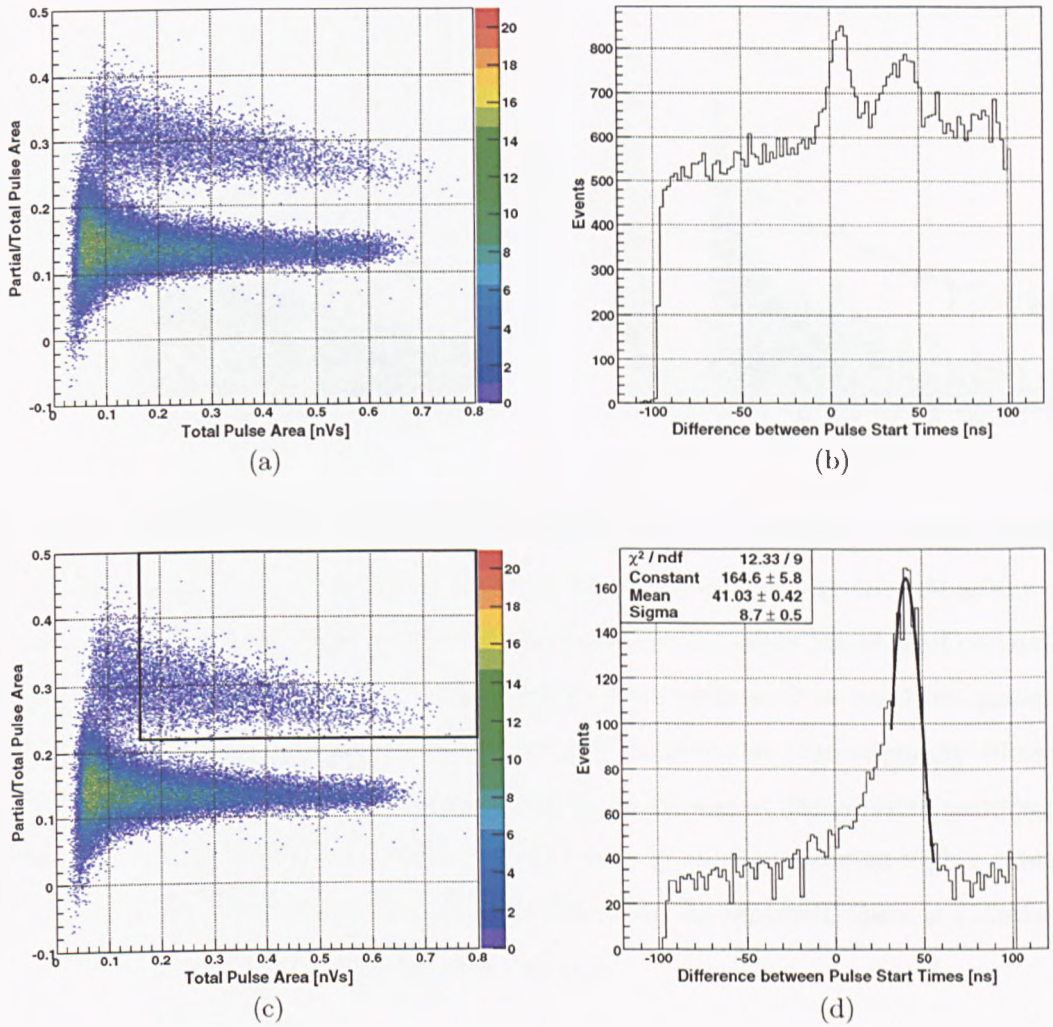

Figure 5.33: Pulse Shape Discrimination (PSD) and Time of Flight Cuts for 10 keVnr: (a) PSD in BC501A detector; (b) Time of Flight between NaI(Tl) crystal and BC501A detector; (c) Implementation of PSD cut in BC501A detector, where events that lie within the black box are accepted; and (d) Time of Flight distribution after cut shown in (c) is performed. It now becomes possible to fit a Gaussian function to the neutron peak in (d).

events in the BC501A detector, as described in Section 5.7 and shown in Figures 5.33(a) and 5.33(c), the neutron peak becomes clearly visible in Figure 5.33(d).

Only events within the black box in Figure 5.33(c) pass the discrimination cut in the BC501A detector. A Gaussian function is fit to the neutron peak in Figure 5.33(d), and events that lie half a standard deviation from the mean pass the time of flight cut.

Although the background has been supressed to a great extent in Figure 5.33(d), it

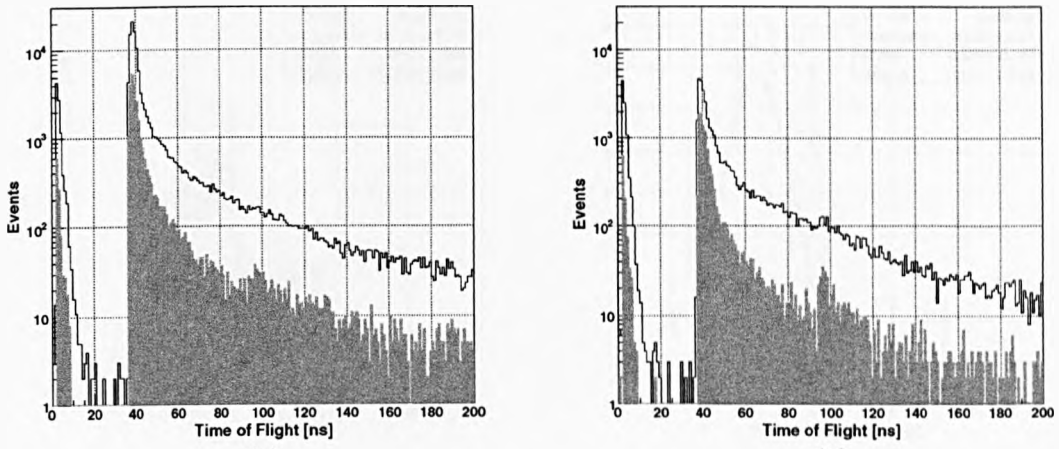

Figure 5.34: Simulated Time of Flight Distributions between NaI(Tl) Crystal and BC501A Detector for Scattering Angles associated with (a) 10 keVnr; and (b) 100 keVnr energy depositions. The unshaded histogram includes all events, while the shaded one only consists of single scattered events in the crystal. The peaks at 0 ns are from gamma-rays produced by inelastic scattering in the crystal. The peaks at approximately 40 ns represent neutrons elastically scattering off nuclei in the crystal at the correct scattering angle to interact with the BC501A detector. A decrease in events is seen at higher times from scattering of neutrons off nuclei in the wax shielding. As expected, there is a distinct lack of events between these two peaks in (a) and (b).

has not been completely removed. This is because the pulse shape discrimination cut on BC501A events described in Section 5.7 is not 100% efficient. Close inspection of background events in Figure 5.28(a) and gamma-rays from a ^{137}Cs source in Figure 5.28(b) show that some events do appear in the neutron band. These events serve to reduce the signal-to-background ratio, and as such, demonstrate the importance of a second cut on the time of flight.

On a side note, data are cut at a lower energy threshold than the conservative figure of 440 keVee that was set in Section 5.7.4. Using the ^{137}Cs calibration plot in Figure 5.24, cutting at areas greater than 0.16 nVs, as shown in Figure 5.33(d), is equivalent to a minimum energy threshold of 280 keVee. Using Eq. (5.18), this corresponds to a nuclear recoil energy of 910 keVnr, which helps to improve the efficiency of the cut.

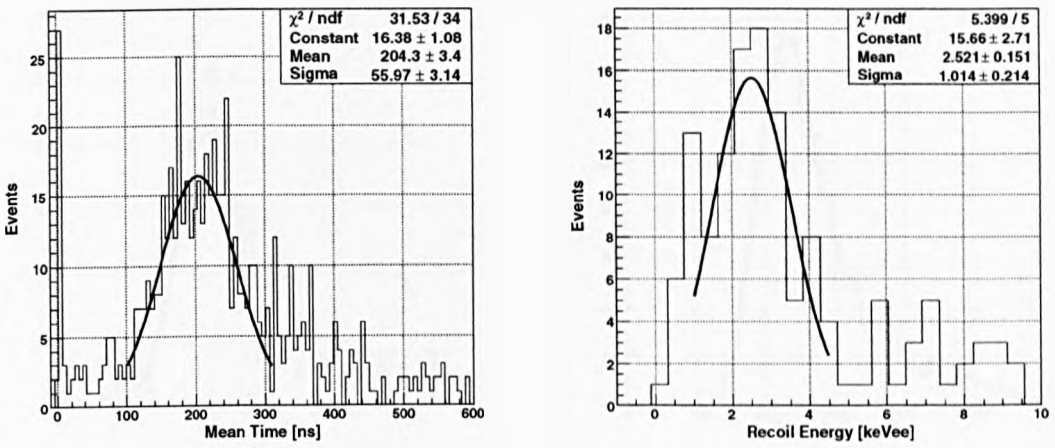

Figure 5.35: (a) Mean Time of pulses from 10 keVnr Na recoils in the NaI(Tl) crystal; and (b) Recoil energy in electron equivalent scale after events that lie more than half a standard deviation from the mean in (a) are cut out. The result in (b) indicates that the quenching factor for 10 keVnr recoils is 25.21%.

5.9 Pulse Shape Discrimination in NaI(Tl)

A variety of pulse shape discrimination techniques can be employed to discriminate low energy nuclear and electron recoils in inorganic crystal scintillators. Discrimination using mean time, neural networks and log likelihood have been investigated in CsI(Tl) crystals [168]. No significant difference in efficiencies between the techniques was observed. The scintillation mechanism of CsI(Tl) is similar to that of NaI(Tl), so there is no reason to believe that the same result would not be true for NaI(Tl). Therefore, mean time is used for nuclear-electron recoil discrimination as it is the easiest to implement.

The reduction code calculates the mean time for each event with Eq. (5.9). After all the cuts outlined above are performed on the nuclear recoil data, a histogram of the mean time is plotted for each nuclear recoil energy. The mean time distribution at 10 keVnr for nuclear recoils is shown in Figure 5.35(a). Cutting out events that lie half a standard deviation from the mean, the electron equivalent recoil energy is plotted, as shown in Figure 5.35(b).

To show that this technique can be used to discriminate neutrons from gamma-rays, the mean time distribution of electron recoils must also be assessed at the same energy scales. As outlined in Section 5.5, Compton scatter events induced by the back-to-back

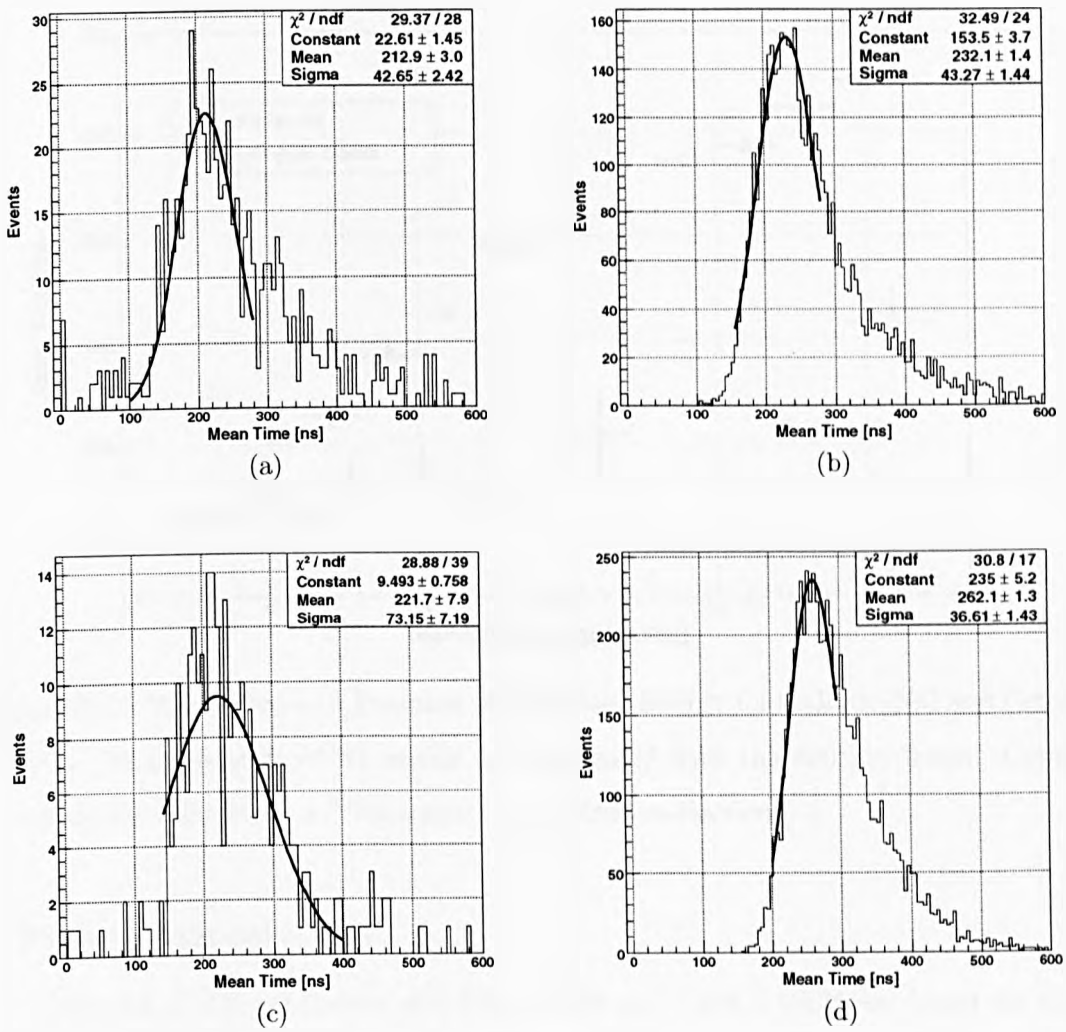

Figure 5.36: Typical Mean Time Distributions for: 6.98 to 8.36 keVee (a) nuclear, and (b) electron recoils; and 15.19 to 16.95 keVee (c) nuclear, and (d) electron recoils.

511 keV gamma-ray emission from a ^{22}Na source can be exploited to determine the mean time at these low energies. Then Eq. (5.19) can be used to quantify the separation, and hence evaluate the discrimination power at various energies.

Mean time distributions for 40 and 80 keVnr nuclear recoils are shown in Figures 5.36(a) and 5.36(c) respectively. The electron equivalent energy for these two distributions is derived by fitting a Gaussian function to the final energy recoil distribution, as shown in Figure 5.35(b) for 10 keVnr nuclear recoil energy. The error on this fit represents the range of energies that are included in the mean time distributions. Cutting on this energy range on data taken with a ^{22}Na source yields similar mean time distributions, as shown

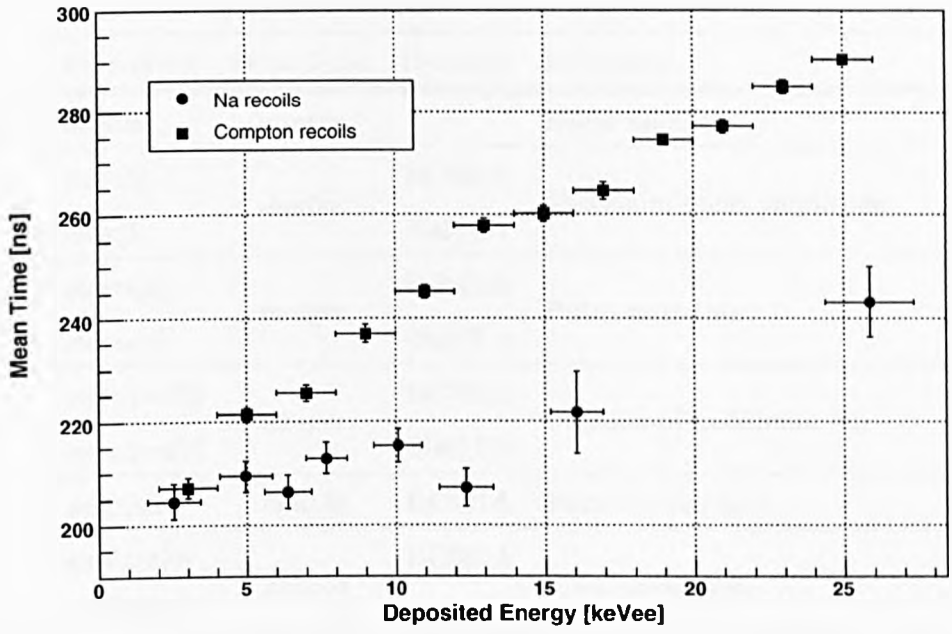

Figure 5.37: Mean Time as a Function of Deposited Energy for Sodium (Na) and Compton Recoils. Measurements of Na recoils are performed with the neutron beam. Compton electrons are induced by a ^{22}Na source, as outlined in Section 5.5.

in Figures 5.36(b) and 5.36(d).

Using Eq. (5.19), M-factors of 0.223 ± 0.039 and 0.368 ± 0.077 are found for 40 and 80 keVnr nuclear recoil energies respectively. At higher energies, the discrimination power between electron and nuclear recoils increases. This is shown more clearly in Figure 5.37, where the values of mean time for Compton and sodium recoils are plotted against electron equivalent energy. Mean time values for electron recoils are evaluated in 2 keVee wide energy bins, with approximately 6000 events in each bin. Values for nuclear recoils come from the data taken with the neutron beam at each scattering angle.

The mean time values for sodium recoils stay roughly constant with energy, compared with those from Compton scatters, which increase. Figure 5.37 indicates that, at energies below 10 keVee, it becomes difficult to distinguish electron and nuclear recoils. This directly affects the sensitivity of dark matter experiments that use sodium iodide as the target material.

The trend seen is a result of the emission of fewer photons at lower energies. The value obtained by Eq. (5.9) is dependent on the amplitude and position of digitised peaks.

Table 5.8: Final Waveform Parameters Calculated by Reduction Code.

Parameter	Data Type	Detector	Definition
evnum	integer	–	Event number
max[0]	double	BC501A	Maximum pulse amplitude
max[1]		NaI(Tl)	
starta[0]	integer	BC501A	Pulse start time
starta[1]		NaI(Tl)	
max_pos[0]	integer	BC501A	Position of maximum bin
max_pos[1]		NaI(Tl)	
surf_part	double	BC501A	Partial pulse area
surf_tot[0]	double	BC501A	Total pulse area
surf_tot[1]		NaI(Tl)	
sigma	double	NaI(Tl)	Standard deviation of the baseline
tau	double	NaI(Tl)	Mean time

The greater the number of peaks, the more the difference in mean time between electron and nuclear recoils as there is more information to feed into this equation. With fewer photons, discriminating gamma-rays from neutrons becomes harder.

5.10 Quenching Factor Measurements of Na Recoils

Over the course of the experiment, the waveform parameters determined by the reduction code and listed in Table 5.3 have been improved and expanded upon. The waveform parameters calculated by the reduction code for the data files containing quenching factor measurements are listed in Table 5.8. Additionally, a brief summary of all the cuts implemented on these files during the analysis, as discussed in this chapter, is presented in Table 5.9.

The quenching factor is defined in Eq. (3.21) in terms of the measured detector response E_{Ree} and the calculated nuclear recoil energy as a function of scattering angle E_R from Eq. (3.15). From Eq (3.21), the error in the quenching factor ΔQ is:

Table 5.9: Summary of Cuts in Chronological Order. Definitions are given in terms of the waveform parameters listed in Table 5.8. References are given to the relevant sections where the cut is discussed, and figures showing examples of implementation.

Name	Definition	Section	Figure
Saturation	max[0] < 0.0445 V max[1] < 0.0445 V	5.6	5.22(a)
Coincidence	320 ns < starta[0] < 440 ns 320 ns < starta[1] < 440 ns	5.6	5.22(b)
Baseline	3 × sigma < 0.005987 V	5.6	5.22(c)
PSD in BC501A	$\frac{\text{surf\_part[0]}}{\text{surf\_tot[0]}} > 0.23$ surf_tot[0] > 0.14 nVs	5.7	5.33(c)
Time of Flight	Gaussian fit to (starta[0] − starta[1]): mean $\pm\frac{\sigma}{2}$	5.8	5.33(d)
PSD in NaI(Tl)	Gaussian fit to tau: mean $\pm\frac{\sigma}{2}$	5.9	5.35(a)

$$\Delta Q = \sqrt{\left(\frac{1}{E_R}\Delta E_{Ree}\right)^2 + \left(\frac{E_{Ree}}{E_R^2}\Delta E_R\right)^2} \tag{5.22}$$

where ΔE_{Ree} and ΔE_R are the errors on the measured and calculated nuclear recoil energies respectively. The value of ΔE_{Ree} is the statistical error associated with the Gaussian fit to the measured detector response. An example of such a fit at 10 keVnr energy is shown in Figure 5.35(b).

As E_R is dependent on the scattering angle, its associated error ΔE_R is obtained from the $\cos\theta$ term in Eq. (3.15). As the scattering angle is inferred by measuring the distances between the neutron source, NaI(Tl) crystal and BC501A secondary detector through the cosine rule (Eq. (5.2)), the error on the cosine of the scattering angle $\Delta(\cos\theta)$ is given by:

$$\Delta(\cos\theta) = \sqrt{\left(\frac{c}{ab}\Delta c^2\right) + \left[\left(\frac{1}{2a} - \frac{a}{2b^2} - \frac{c^2}{2ab^2}\right)\Delta b\right]^2 + \left[\left(\frac{1}{2b} - \frac{b}{2a^2} - \frac{c^2}{2a^2b}\right)\Delta a\right]^2} \tag{5.23}$$

where a is the distance between the crystal and neutron source, b is that between the crystal and BC501A detector, and c is that between the BC501A detector and neutron source. It is reasonable to state that the accuracy of each of these measured distances

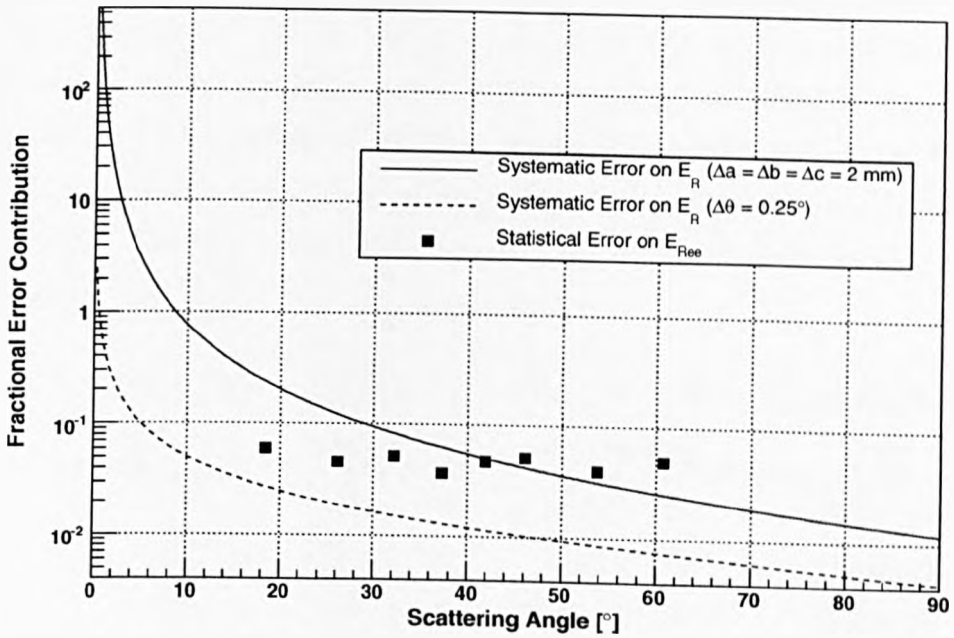

Figure 5.38: Fractional Contributions from Systematic Errors on the Nuclear Recoil Energy E_R and Statistical Errors on the Measured Energy Response E_{Ree} as a Function of the Scattering Angle. A marked increase in the contribution from the systematic error is seen at low scattering angles θ. The situation can be improved through accurate angle measurement rather than using the cosine rule, providing a finer angular resolution. With reference to Eq. (3.15), E_R is proportional to $\cos\theta$, implying that the systematic error will dominate at lower energies.

is ± 2 mm. Therefore, from Eq. (3.15), the magnitude of the error on the recoil energy $|\Delta E_R|$ can be written as:

$$|\Delta E_R| = \frac{\partial E_R}{\partial(\cos\theta)}\Delta(\cos\theta) = \frac{2m_A E_{\rm n} m_{\rm n}}{(m_A + m_{\rm n})^2}\Delta(\cos\theta) \tag{5.24}$$

where m_A is the mass of the target nucleus, $E_{\rm n}$ is the energy of the incident neutrons from the beam and $m_{\rm n}$ is the neutron mass. The value for $\Delta(\cos\theta)$ from Eq. (5.23) can be substituted into Eq. (5.24), which in turn gives the value for ΔE_R in Eq. (5.22).

It is clear from Figure 5.38 that, while the fractional contribution from the statistical error remains the same, that from the systematic error increases with decreasing scattering angles. From Eq. (3.15), the nuclear recoil energy E_R is proportional to $\cos\theta$, thus implying that at lower energies there is a marked increase in the systematic error. This is in part

Table 5.10: Quenching Factors of Na Recoils relative to those of gamma-rays of the same energy. Systematic errors contribute to the uncertainty on the recoil energy E_R. Statistical uncertainties contribute to the error on the measured energy E_{vis}. The fractional contribution from statistical errors remains roughly constant at ≈ 0.05 over the full energy range. A marked increase in the contribution from the systematic error is seen at low θ, where $E_R < 20$ keVnr. Systematic and statistical errors are combined with Eq. (5.22) to obtain the uncertainty on the quenching factor.

Scattering Angle θ [°]	Recoil Energy E_R [keVnr]	Measured Energy E_{vis} [keVee]	Quenching Factor Q [%]
18.4	10.0 ± 2.5	2.52 ± 0.15	25.2 ± 6.4
26.1	20.0 ± 2.4	4.96 ± 0.23	24.8 ± 3.2
32.1	30.0 ± 2.4	6.37 ± 0.33	21.2 ± 2.0
37.3	40.0 ± 2.3	7.67 ± 0.28	19.2 ± 1.3
41.9	50.0 ± 2.3	10.08 ± 0.48	20.2 ± 1.3
46.1	60.0 ± 2.2	12.35 ± 0.64	20.6 ± 1.3
53.8	80.0 ± 2.1	16.07 ± 0.64	20.1 ± 1.0
60.7	100.0 ± 2.1	25.86 ± 1.28	25.9 ± 1.4

due to the use of the cosine rule as a tool to measure the scattering angle. A more accurate determination of θ results in a significant improvement, of as much as an order of magnitude at lower scattering angles, as shown in Figure 5.38.

From the results in Figure 5.39 and Table 5.10, it is clear that the systematic error begins to become a problem at nuclear recoil energies less than 20 keVnr. Although it may be possible to take a measurement at 5 keVnr, especially as the light yield seems to increase at nuclear recoil energies less than 40 keVnr, the magnitude of the systematic error at this scattering angle, from Figure 5.38, would be too large to obtain a sensible result. Therefore, the limiting factor in this experiment is not the light yield, but the error associated with the scattering angle.

Another source of error on the determination of the scattering angle comes from the size of the crystal. The assumption made is that all events will interact in the centre of the 2-inch diameter crystal. However, as is evident from the lack of collimation in the detector

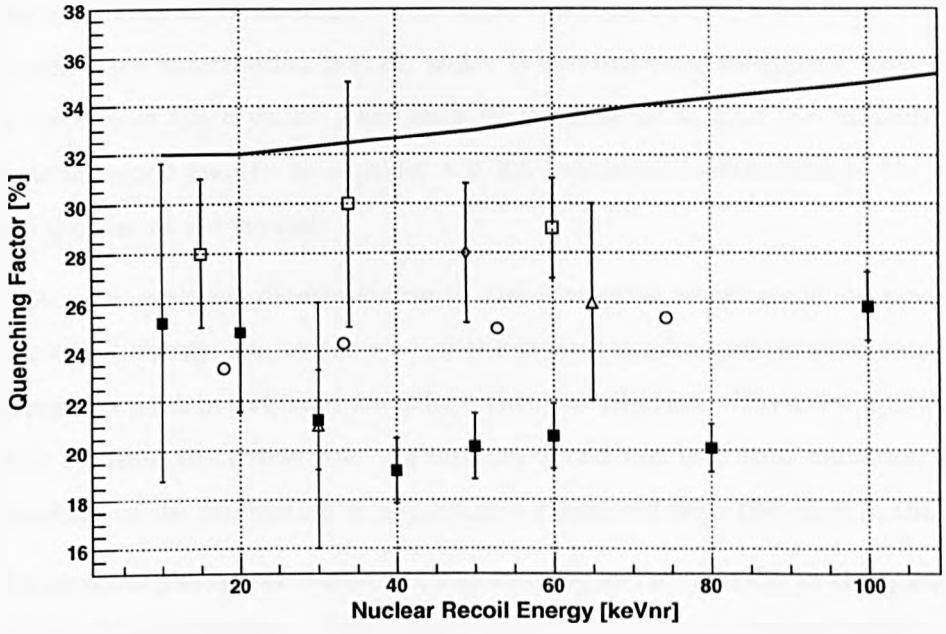

Figure 5.39: Quenching Factor of Sodium (Na) Recoils in NaI(Tl). Experimental results from this work (closed black squares), Simon et al. [169] (open diamond), Gerbier et al. [163] (open circles), Tovey et al. [170] (open triangles) and Spooner et al. [171] (open squares) are shown. Additionally, the preliminary theoretical estimation of the upper limit from Hitachi [141] is represented by the solid black line. Error bars represent combined systematic and statistical errors. The smaller error bar at 30 keVnr is associated with the uncertainty on the quenching factor measured in this experiment.

arrangement shown in Figure 5.1, this is not an accurate description of the only region where a neutron can interact. As a result, it is possible to record a range of recoil energies rather than that defined by the scattering angle. As the geometry of the experiment has been accurately reconstructed in a GEANT4 simulation, an idea of the possible range of deposited energies can be inferred from Figure 5.5(b). This shows the results from the 10 keVnr neutron scattering simulation. Detector resolution has not been factored into the simulation, so the broadness of the peak is due solely to interactions taking place throughout the crystal, rather than in its centre.

From Figure 5.5(b) the error on the mean of the Gaussian fit to the Na recoil peak is 0.03 keVnr. For $E_R = 10$ keVnr, this translates to a fractional contribution to the error on the recoil energy of 0.003. This can be compared with the fractional error contribution from

the use of the cosine rule to determine the angle, as shown in Figure 5.38 and Table 5.10. At the scattering angle associated with 10 keV nuclear recoils (18.4° from Table 5.10), the fractional error contribution is 0.25, which is two orders of magnitude greater than that from the size of the crystal. This leads to the conclusion that the measurement of the angle is not good enough to consider a 0.003 fractional contribution to the error on E_R due to the size of the crystal.

If a more accurate determination of the scattering angle could be made, the error on the recoil energy due to the size of the crystal would start to dominate. Therefore, collimation would be required to reduce this contribution. However, under the present method of using the cosine rule, collimation would not lead to a reduction of errors, as the position of the interaction is insignificant compared with the error in the angle.

There are a number of features of Figure 5.39, including a dip in the quenching factor between 20 and 100 keVnr. The exact nuclear recoil energy at which this feature occurs is difficult to ascertain due to the similar quenching factors and errors over this energy range. The dip and subsequent rise in the quenching factor at decreasing nuclear recoil energies is also seen in germanium crystals [172] and liquid xenon [173]. Although this trend is not seen with some other results for these materials (see [174] for germanium and [175] for xenon), there is an indication that an underlying process is responsible for these observations. It is important to point out the subsequent rise in the quenching factor of xenon by [173] is witnessed at a lower nuclear recoil energy than that reached by [175], thus these results are not in contradiction with each other.

From Figure 5.39, the quenching factor of sodium recoils in NaI(Tl) varies between 19% to 26% in the range 10 to 100 keVnr nuclear recoil energy. This is in good agreement with previous experimental results [163, 169–171]. From Figure 5.35(b), a scintillation efficiency of $25.2 \pm 6.4\%$ has been determined for 10 keVnr Na recoils in NaI(Tl), which is currently the lowest energy measured.

5.11 Summary

As the first scintillators used as target media in direct dark matter search experiments, NaI(Tl) crystals remain a popular choice due to their high light yield and pulse shape differences between nuclear and electron recoils. They remain the best at determining spin-

dependent WIMP-nucleon limits and are the only detector material in which a consistent annual modulation signal has been witnessed.

A 2-inch NaI(Tl) crystal has been exposed to 2.45 MeV mono-energetic neutrons produced by a deuterium-deuterium beam to measure the quenching factor of sodium recoils, of energies between 10 and 100 keVnr, in NaI(Tl). The quenching factor is the ratio of light from a nuclear recoil to that from an electron recoil of the same energy. This is an important measurement for dark matter detectors as energy calibration is commonly performed with a source of gamma-rays, inducing electron recoils in the target. WIMPs will scatter elastically off target nuclei, in the same way as neutrons, and therefore this correction factor is required so that the differential event rate calculated gives an accurate limit on WIMP-nucleon cross-sections.

As the nuclear recoil energy is dependent on scattering angle, a secondary detector of BC501A liquid scintillator is placed around the crystal. Neutrons of a known initial energy scatter off sodium nuclei in the target, and interact with the secondary detector. If calibration is performed with a gamma source, an electron equivalent energy scale can be established. The ratio of the measured detector response to the nuclear recoil energy given by the angular position of the secondary detector with respect to the target is the quenching factor.

Simulations indicate that the energy distribution from multiple scatter events is featureless, and hence these do not provide a significant background to this experiment.

Prior to the measurement itself, the determination of NaI(Tl) and BC501A scintillation pulse properties is required. Digitised waveforms are scanned by reduction code software that has been programmed within the ROOT framework. Pulse parameters are extracted and analysed so that they can be improved upon.

A variety of algorithms have been tested on NaI(Tl) data taken during its exposure to gamma-rays from a ^{22}Na source. Of these, the most accurate reproduction of the original pulse is achieved through the removal of any inherent noise in the baseline. This process requires the code to find the mean of first 200 ns of a waveform, which lies in the pre-trigger time period. The process is then repeated, excluding any amplitudes that lie three standard deviations from the initial mean. The new mean gives a more accurate value for the baseline, and the rest of the waveform is scanned to remove any bins that lie less than three standard deviations from it.

During the quenching factor experiment, events are recorded if pulses from the NaI(Tl) crystal and BC501A scintillator are coincident within 100 ns of each other. Energy calibration is performed with the 122 keV gamma line emitted by a ^{57}Co source every three hours. The light collection efficiency is improved through optical coupling of the PMT glass window with that of the encapsulated crystal, and clamping them together minimises any drift in detector response. Initial software cuts on the waveforms include removing saturated and false coincident events, and those where three standard deviations from the mean noise level exceed the single photoelectron amplitude.

As there is a large gamma background associated with this experiment, gamma-neutron pulse shape discrimination in BC501A is the first higher level cut performed. As the fractional intensity of the slow component will be higher for nuclear recoils, the partial-to-total pulse area ratio is used as a discriminant. The best separation between nuclear and electron recoils is achieved when the initial partial area pulse integration boundary lies 20 ns after the peak position. Electron and nuclear interactions can be successfully separated down to recoil energies of 280 keVee.

Neutrons are expected to arrive at the secondary detector 38 to 42 ns after recoiling off a sodium nucleus. This is confirmed from simulation results, and a Gaussian function is fit to the time of flight distribution. Events that lie half-a-standard deviation from the mean are excluded from the analysis.

The final cut is that of pulse shape discrimination in NaI(Tl) itself, using the mean time. Below 10 keVee, neutron and gamma separation becomes difficult as there are fewer photons emitted at these energies, and hence little difference between these pulses.

A quenching factor of $25.2 \pm 6.4\%$ has been measured for 10 keVnr sodium recoils, which is currently the lowest energy attained. Measurements are limited by the increasing systematic errors at lower scattering angles, making a measurement at 5 keVnr infeasible. The results are in good agreement with those from other experiments, and show an average value of 22.1% at energies less than 50 keVee. However, a dip in the quenching factor is seen at nuclear recoil energies between 20 and 100 keVnr, which has not been witnessed before. Possible reasons for this may lie in the energy of electrons induced by a recoiling sodium nucleus at these nuclear recoil energies.

Chapter 6

The Response of NaI(Tl) to Electron Recoils

As previously mentioned, dark matter detectors are calibrated with gamma-ray emitting radioisotopes, and a linear energy response is assumed. However, the light yield varies by the order of a few percent over a range of energies in NaI(Tl) [146]. Additionally, a significant drop in light yield is seen at the K- and L-shell absorption edges of the target materials in crystal scintillators. In contrast, semiconductor detectors exhibit good proportionality down to low energies.

The photon response is directly proportional to the electron response, which is independent of scintillator size and shape [125]. With reference to Figure 3.6, photoelectrons ejected by incident gamma-rays of energy just above that of the iodine K-shell have very little kinetic energy. As the electron response decreases linearly at electron energies lower than 20 keV [176], the light yield from the interactions induced by these photoelectrons is small. Thus, the photon response is suppressed for incident gamma-rays with energies just above that of the K-shell. Just below this energy, K-shell ionisation is not kinematically possible, so L-shell ionisation takes place, and the probabilities given in Figure 3.6 change accordingly. As the L-shell binding energy is lower, photoelectrons are ejected with higher kinetic energies, and this causes the light yield to increase. The same argument can be applied to incident photons of energy close to that of the L-shell.

Therefore, a significant drop in the response of a NaI(Tl) crystal is expected at the K- and L-shell binding energies. With reference to Figure 3.5(a), the cross-section for Compton scattering begins to dominate at incident gamma-ray energies greater than ap-

proximately 200 keV. If a photon deposits its entire energy in a target, the scattered gamma-ray at these energies will eventually undergo photoelectric absorption. However, the higher the incident energy, the greater the relative energy loss from elastic scattering, implying that the photoelectrons ejected from photoelectric absorption carry a smaller fraction of the total energy. Therefore, linearity is gradually restored with increasing incident gamma-ray energy.

Unlike the electron response, the photon response is dependent on scintillator geometry, due to variations in the probability of multiple scattering events. In other words, full-energy absorption is more likely in larger crystals than smaller ones as there is a lower chance of escape.

The non-linear response of NaI(Tl) to photons is initially investigated by exposing the crystal to gamma-ray sources of various energies. The Compton Coincidence Technique (CCT) [176, 177] is then used to investigate the response to electrons. The experiments were conducted with the aid of Dr. Pawel Majewski at the University of Sheffield.

6.1 Response to Gamma-Ray Sources

Traditionally, experiments looking into the response of NaI(Tl) crystals to electron recoils have used a variety of gamma-ray sources, covering a vast range of deposited energies, to compare light yields. As a starting point, the NaI(Tl) crystal on which quenching factor measurements were performed as described in Chapter 5, is exposed to the X-ray and gamma sources listed in Table 6.1.

Incident gamma-rays with energy less than the 29.67 keV Xe K_α X-rays from ^{129}I will be absorbed by the aluminium encasing that surrounds the crystal. Therefore, measurements of the photon response of NaI(Tl) below these energies are not possible with the current crystal geometry illustrated in Figure 5.2. Beryllium foil is commonly used as an alternative encasing. However, the extraction and subsequent re-encasing of a hygroscopic crystal is difficult, and requires special equipment. Therefore, this procedure is not performed here.

A total of 100000 events are taken for each source. The reduction code designed for the quenching factor experiment, as outlined in Section 5.3, is used to determine pulse areas. A Gaussian function is fit to the photopeaks to give a mean pulse area A_γ. This is

Table 6.1: X-Ray and Gamma Sources for Investigating NaI(Tl) Response. Gamma-rays and X-rays below the energy of ^{129}I will be absorbed by the aluminium that encases the crystal.

Energy [keV]	Photons	Source
29.67	Xe K_α X-rays	^{129}I
30.85	Cs K_α X-rays	^{133}Ba
32.06	Ba K_α X-rays	^{137}Cs
59.54	γ-rays	^{241}Am
80.90	γ-rays	^{133}Ba
122.06	γ-rays	^{57}Co
356.02	γ-rays	^{133}Ba
511.00	γ-rays	^{22}Na
661.66	γ-rays	^{137}Cs

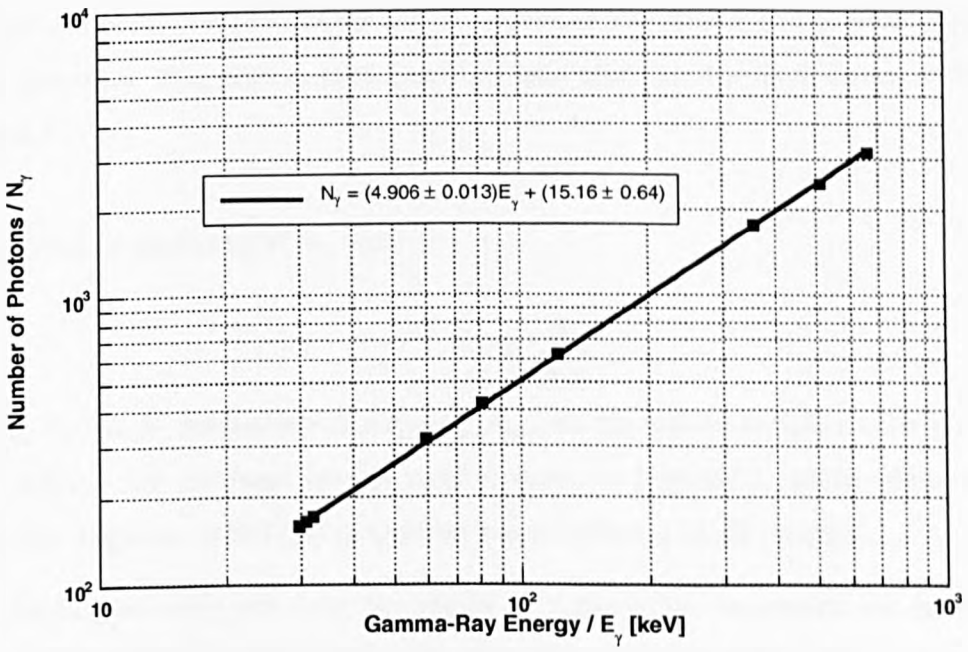

Figure 6.1: Measured Photon Response using the Standard Integral Technique. Gaussian fits are performed on the resultant photopeaks for the sources listed in Table 6.1, and the mean values are substituted into Eq. (6.1) to yield the number of photons N_γ. The straight line fit seems to indicate that the response of NaI(Tl) to gamma-rays is linear.

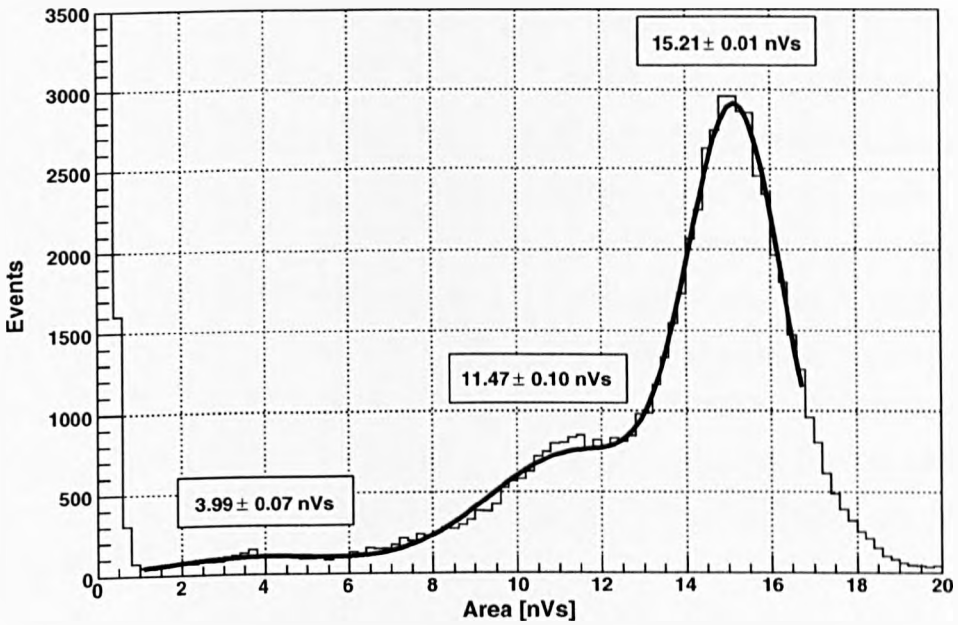

Figure 6.2: Photoelectric Absorption of 122 keV Gamma-Rays in NaI(Tl) Crystal. As with Figure 5.9(b), three peaks are visible, corresponding to 29.11 keV X-ray absorption at 3.99 nVs, 88.89 keV photoelectron absorption at 11.47 nVs and 122 keV combined X-ray and photoelectron absorption. A combined 3 Gaussian fit has been performed on this spectrum. The photon yield from the total absorption peak is shown in Figures 6.1 and 6.4.

converted to photon yield N_γ with:

$$N_\gamma = \frac{A_\gamma}{A_{\text{spe}}} \tag{6.1}$$

using the single photoelectron response A_{spe} for the photomultiplier tube given in Figure 5.8(a). The resultant photon yield is shown in Figure 6.1, which seems to indicate that the response of NaI(Tl) to electron recoils is linear at all energies.

As an interesting side note, the results of photoelectric absorption can be clearly seen in the cobalt-57 (^{57}Co) spectra shown in Figures 5.9(b) and 6.2. As mentioned in Section 3.5.1, the photoelectric absorption of an incident gamma-ray of energy greater than the K-shell binding energy of iodine (33.17 keV) can result in a number of subprocesses as summarised in Figure 3.6. For a 122 keV gamma-ray from a ^{57}Co source, the most likely process is that of interaction with the K-shell, leading to the ejection of a photoelec-

tron of energy $E_\gamma - 33.17$ keV, where $E_\gamma = 122$ keV. This is followed by the subsequent de-excitation of an electron from the L-shell resulting in a 28.61 keV X-ray.

The largest peak in Figure 6.2, at an area of 15.21 nVs, corresponds to the combined absorption of the photoelectron and X-ray, and hence 122 keV energy deposition. However, the X-ray can escape, leaving only the photoelectron to be detected, and this is the origin of the peak seen at 11.47 nVs. From Figure 3.6, this corresponds to a photoelectron of energy 88.89 keV. As calculated in Section 5.4.2, the typical penetration depth of a 122 keV gamma-ray in a NaI(Tl) crystal is 2.7 mm. As this is so close to the surface of the crystal, it is possible for the emitted photoelectron to be absorbed by the aluminium encasing rather than the crystal itself. This gives rise to the low energy peak at 3.99 nVs, which is a convolution of all the possible X-ray energies outlined in Figure 3.6. The weighted average of these energies is 29.11 keV.

Although a linear fit to the calculated results in Figure 6.1 appears to be excellent, this technique can hide small deviations from a proportional response. Plotting the photon responses relative to that from a control source can reveal such deviations [178]. The 662 keV line from caesium-137 (^{137}Cs) is normally chosen for such a purpose as it is a common laboratory source which emits a gamma-ray of sufficient energy such that interactions will occur in the bulk of the crystal rather than on the surface.

Light yields from the sources in Table 6.1 are calculated with Eq. (4.2), and compared with that from the ^{137}Cs calibration spectrum shown in Figure 6.3. The photopeak from interactions with 32.06 keV Ba K_α X-rays is also evident from the ^{137}Cs energy spectrum. The β^- decay of ^{137}Cs results in the production of the stable barium-137 (^{137}Ba) isotope. Gamma-rays emitted during this decay can interact with residual ^{137}Ba atoms from previous decays, and the subsequent excitation and de-excitation of electrons results in the production of these X-rays, which in turn can interact with the crystal. The older the source, the greater the number of ^{137}Ba atoms, and hence the more prominent the photopeak.

The resultant distribution of relative light yields is illustrated in Figure 6.4. Due to the lack of radioactive sources available in the laboratory, only a few data points could be taken. However, the results are consistent with those from other groups, and a dip in the photon response is seen around the iodine K-shell binding energy of 33.17 keV.

As expected, smaller deviations from unity are seen at higher energies. This is due to

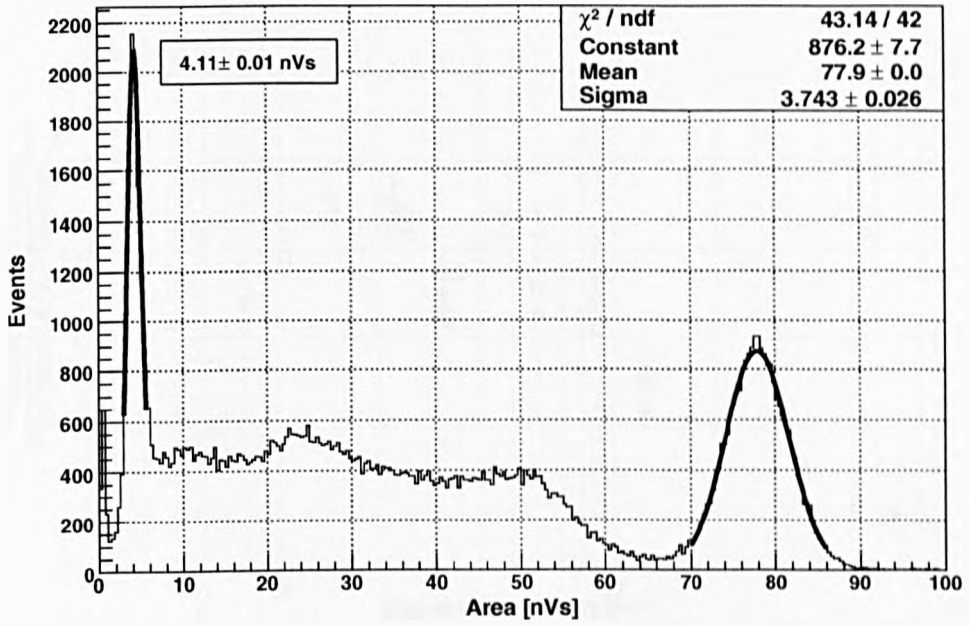

Figure 6.3: Calibration of NaI(Tl) Crystal with ^{137}Cs Source. A second fit is performed on the Ba K_α X-rays from gamma-ray interactions with ^{137}Ba present on the source. Gamma-rays arise from the β^- decay $^{137}\mathrm{Cs} \rightarrow {}^{137}\mathrm{Ba} + \mathrm{e}^- + \bar{\nu}_\mathrm{e}$, where the daughter ^{137}Ba is stable. Gamma-rays emitted from ^{137}Cs interact with residual ^{137}Ba atoms, causing the excitation and subsequent de-excitation of electrons, resulting in the emission of an X-ray of energy 32.06 keV. In turn, this X-ray can interact with the NaI(Tl) crystal. Over time, the concentation of ^{137}Ba increases, and hence, this line becomes visible.

the cross-section for Compton scattering dominating that for photoelectric absorption at incident gamma-ray energies above 200 keV, as shown in Figure 3.5(a). Therefore, at these energies, total absorption of incident gamma-rays will tend to occur after multiple scatters, during which energy is transferred to target electrons. Eventually the gamma-ray will lose all its energy through photoelectric absorption, although the fraction of initial energy lost in this process will be smaller at higher incident gamma-ray energies. Therefore, the electron response, rather than the photon response, begins to dominate.

6.2 Electron Response Non-Linearity

A gamma-ray interacting in a NaI(Tl) crystal has a number of possible energy loss interactions, which are summarised in Section 3.5.1. Although it is evident from Figure 3.5(a)

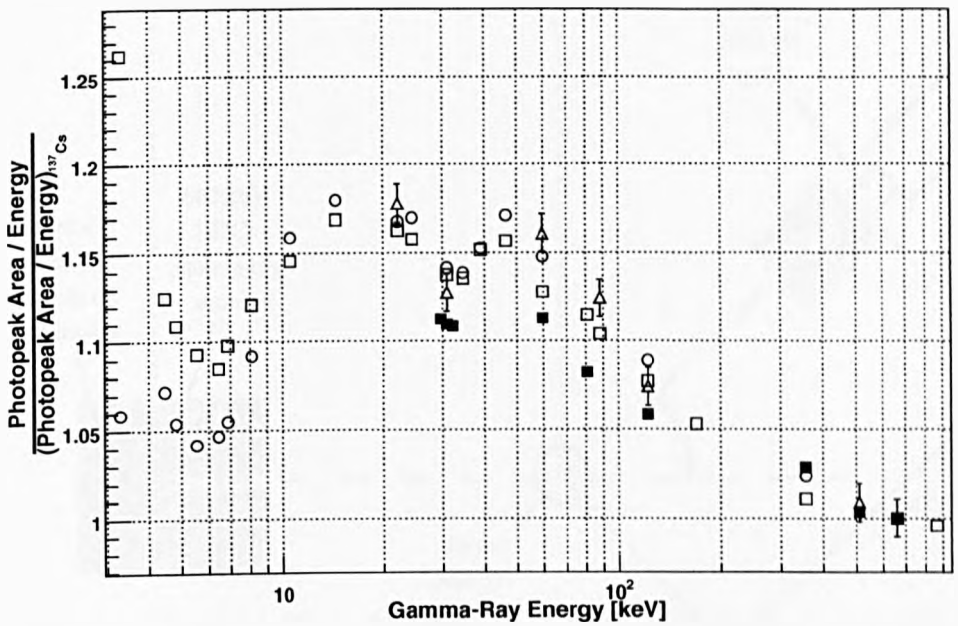

Figure 6.4: Measured Photon Response shown using the Alternative Integral Technique. In comparison with Figure 6.1, small deviations from a linear response are now visible. In some cases, the discrepancy can be as much as 18%. Dips in photon response at the iodine L- (5.19 keV) and K-shells (33.17 keV) are also evident. Experimental results from this work (closed black squares), Aitken et al. [146] (open circles and squares representing two different crystals) and Rooney & Valentine [125] (open triangles) are shown. All values are normalised to the response to 661.66 keV gamma-rays from ^{137}Cs, and the crystal used by Rooney & Valentine [125] is similar in size to that used in this work.

that the cross-sections for different processes dominate at different energies, photoelectric absorption and Compton scattering are kinematically possible at all photon energies.

Considering the 662 keV gamma-ray emitted from a ^{137}Cs source, the cross-section for Compton scattering is higher than that for photoelectric absorption in NaI(Tl), as illustrated in Figure 3.5(a). However, in a small crystal, it is likely that the gamma-ray may scatter off an electron and escape from the detector, leaving behind a relatively small energy deposit. It is more likely that events in which the gamma-ray is totally absorbed in such crystals are due to immediate photoelectric absorption. In larger crystals, the gamma-ray can scatter one or more times before eventually undergoing photoelectric absorption.

These two processes will transfer different amounts of energy to the target electrons

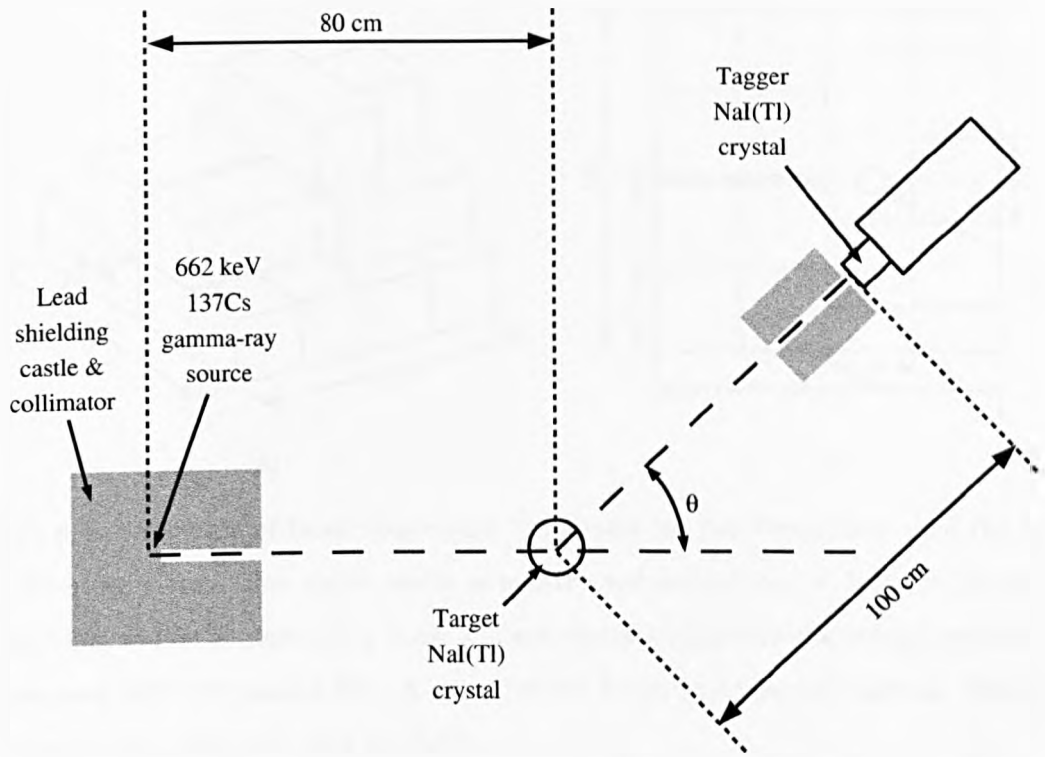

Figure 6.5: Schematic View of the Detector Arrangement used to Measure Electron Response in NaI(Tl).

and, as mentioned previously, a different response will be seen as the electron response is non-linear in NaI(Tl) [176]. Therefore, the procedure outlined in Section 6.1 and results shown in Figure 6.4 are inherently biased on the geometry of the scintillator. Consequently, measuring the electron response, rather than the photon response, provides a way of investigating non-linearity in NaI(Tl) independent of crystal geometry.

6.2.1 Compton Coincidence Technique

There are a number of methods by which the electron response in scintillators can be measured. The electron response can be separated from measured gamma-ray response data [147, 179]. This requires the very accurate determination of electron energy distributions as a function of the intial gamma-ray energy, and these spectra are normally generated from Monte Carlo simulations. Alternatively, the direct measurement of electron response can be performed with external electron sources [180]. However, being charged particles, the mean free path of electrons in NaI(Tl) is relatively small, and therefore surface effects will add extra complications to any measurements at low incident energies.

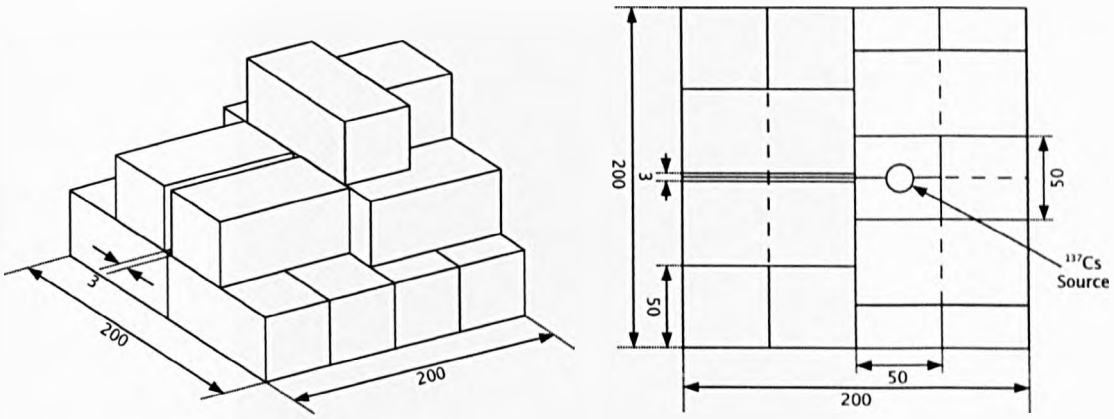

(a) (b)

Figure 6.6: Schematic of Lead Castle and Collimator in: (a) Perspective; and (b) Bird's eye cut-away views. The entire castle is constructed from 5 cm × 5 cm × 10 cm lead bricks. The source is placed in a 5 cm × 5 cm cavity to improve the energy resolution of the emitted 662 keV gamma line. A slit of width 3 mm provides collimation. The design is based on the collimator used by [181].

To combat these problems, the electron response can be measured with the Compton Coincidence Technique (CCT) [177], in which energetic electrons can be produced from Compton scattered gamma-rays. The experimental procedure is similar to that for the quenching factor measurements described in Chapter 5 and a schematic view of the detector arrangement is shown in Figure 6.5. As with the arrangement for the quenching factor measurements, the target NaI(Tl) crystal and photomultiplier tube are coupled together with silicone oil and fixed into the clamp shown in Figure 5.12.

A strong ^{137}Cs gamma-ray source (activity of 60 MBq) is placed within a dual-purpose lead castle and collimator, the design of which is shown in Figure 6.6. It is based on the collimator used by [181], which was found to reduce internal scattering. Scattering that occurs close to the source results in a broadening of the gamma line, and this is minimised by placing the source within a cavity as shown in Figure 6.6(b). This results in the trapping of some of the scattered gamma-rays and the reduction of the intensity of radiation incident on the internal surface of the collimator. The size of the slit is 3 mm.

With reference to Figure 6.5, 662 keV gamma-rays that scatter off target electrons are detected with a second 1-inch diameter NaI(Tl) crystal, known as the tagger. Assuming that there is only one interaction in the target, the kinetic energy of the recoil electron as

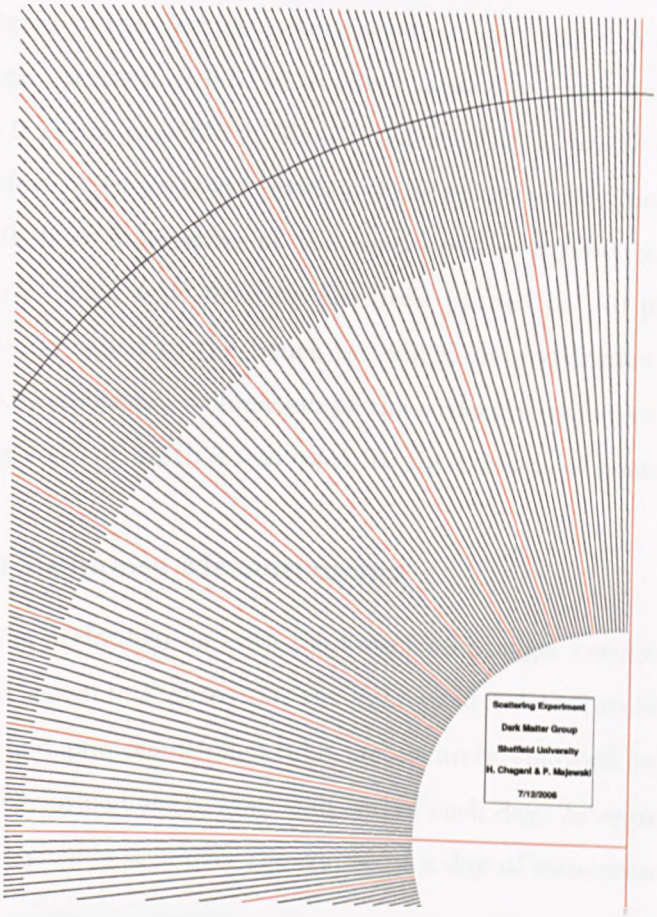

Figure 6.7: Scale Drawing depicting Experimental Angular Accuracy. A ROOT [162] macro was programmed to accurately draw the angles around the centre of the NaI(Tl) crystal, positioned at the intersection with two lines in the bottom-right corner, with separations of 0.5°. This was then printed onto A0 paper, laminated, and taped to the experimental bench. As an aid red lines are present every 10°, and an arc of radius 1 m is drawn to help in the positioning of the tagger.

a function of the scattering angle is given by Eq. (3.11), the distribution of which is shown in Figure 3.9.

This technique allows for direct measurements of the electron response within the bulk of the crystal, thus avoiding the complications that arise from surface effects. Additionally, the electron energy can be varied by simply changing the scattering angle, meaning that the measured electron response can consist of any number of energies sampled from the Compton continuum.

As Compton scattering dominates at incident gamma-ray energies larger than 200 keV (Figure 3.5(a)), the 662 keV line from ^{137}Cs is suitable. It is apparent from Figure 3.9,

the energy transferred to the electron is very sensitive to changes in the scattering angle. In fact, a minimum precision of 0.5° is required, and it is clear from the discussion in Section 5.10 that it is not possible to obtain this level of accuracy with the cosine rule (Eq. (5.2)). Therefore, a simple scale drawing of the setup is constructed with the ROOT package [162], with lines originating at the centre of the crystal, spaced 0.5° apart as shown in Figure 6.7. This scale drawing has been printed on A0 paper, laminated for added protection, and taped to the bench on which the experiment is conducted. As shown in Figure 6.5, additional collimation of the scattered gamma-ray is achieved with lead bricks, leaving a slit of width 3 mm open for the passage of gamma-rays.

6.2.2 Electron Response Measurements

Energy calibration is performed on both the target and tagger crystals with the 662 keV line from ^{137}Cs. As shown in Figure 5.11, the light yield is found to be fairly stable when the target crystal and photomultiplier tube are securely clamped together. Therefore, calibration is only performed at the start and end of each day. As expected, no significant degradation in light yield is seen over the course of a day of measurements.

The hardware trigger electronics used here and those for measuring the quenching factor, illustrated in Figure 5.3, share many similarities. The BC501A detector is replaced with the NaI(Tl) tagger. Furthermore, the 100 ns time window is reduced to 30 ns, the minimum setting on each discriminator, as the time of flight for gamma-rays is expected to be immediate.

Slight changes are made to the reduction code described in Section 5.3 for use in this analysis. With reference to Table 5.8, the partial pulse area (surf_part) is no longer calculated. Additionally, the baseline calculation problem highlighted in Section 5.5.3 is not present with the tagger crystal, and hence its standard deviation (sigma) is not derived. There is also no requirement for gamma-neutron discrimination, so the mean time (tau) is excluded. The new parameters calculated by the altered reduction code are given in Table 6.2.

Initial cuts are made on the data as described in Section 5.6, with some key differences. As the pulses expected in both crystals are of relatively high energy compared with that measured during the quenching factor experiment, both channels on the digitiser are set to a range of 200 mV. This results in a saturation cut of 178 mV rather than 44.5 mV shown

Table 6.2: Waveform Parameters Calculated by Reduction Code for Electron Response Measurements.

Parameter	Data Type	Detector	Definition
evnum	integer	-	Event number
max[0]	double	tagger	Maximum pulse amplitude
max[1]		target	
starta[0]	integer	tagger	Pulse start time
starta[1]		target	
max_pos[0]	integer	tagger	Position of maximum bin
max_pos[1]		target	
surf_tot[0]	double	tagger	Total pulse area
surf_tot[1]		target	
sigma	double	target	Standard deviation of the baseline

in Figure 5.22(a). Additionally, the narrowing of the digitiser logic signals results in a more stringent cut on the start times of scintillation pulses than that shown in Figure 5.22(b). Events are still cut when 3σ exceeds the single photoelectron amplitude of 5.987 mV in the target crystal, as illustrated in Figure 5.22(c).

A higher level cut is then performed on the time of flight. As mentioned previously, the time of flight is expected to be immediate as gamma-rays are relativistic particles. Evidence of this can be seen in Figure 6.8(a), where the start time of the pulse in the tagger is subtracted from that in the target. As with Figure 5.33(b), the mean of the peak is clearly not at 0 ns exactly. This can be explained with the presence of a delay due to the cable leading to the tagger (BC501A detector in Chapter 5) being slightly longer than that attached to the target crystal. The problem is further compounded by the 2 ns timing resolution of the digitiser, which is fairly large on the scale of this experiment. However, this remains a systematic error that can simply be corrected by manually taking the position of the peak into account. As can be seen from Figure 6.8(a), the peak is very sharp and tall compared with the background, so this method proves little problem. A Gaussian fit is performed on the peak, and cut boundaries are set one standard deviation from the mean. The results of this cut on the energy distribution of electron recoils in the

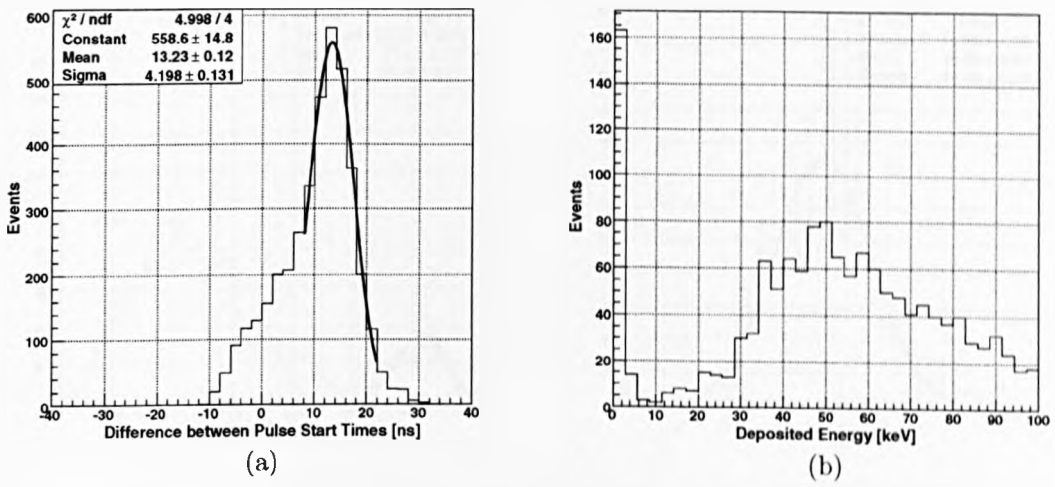

Figure 6.8: Effect of (a) Time of Flight Cut on the (b) Electron Energy Distribution in the Target NaI(Tl) Crystal. Data taken at a scattering angle associated with 41.5 keVee electron energy deposition in the target. Cut boundaries are set one standard deviation from the mean in (a). Although a peak becomes visible in (b) after this cut, the signal-to-background ratio is still too low to permit a Gaussian fit on this distribution.

target crystal is shown in Figure 6.8(b).

It is evident from Figure 6.8(b) that, even after a cut on the time of flight, fitting a Gaussian function to the peak that has emerged is problematic. From looking at the energy distribution of these events in the tagger, as shown in Figure 6.9(a), a Compton continuum followed by a photopeak at approximately 615 keV are visible. The Compton continuum is formed by gamma-rays that do not make a full energy deposition in the tagger once they have scattered off electrons in the target crystal. Instead, they may have scattered once or twice before leaving the secondary detector. Although such events are part of the signal, and therefore can be included in the analysis, the continuum is also comprised of other events. These include multiple scatters in the target, where an incident gamma-ray may deposit energy on two or more target electrons, scatter towards the tagger, and deposit its remaining energy there. Such scattered gamma-rays will enter the tagger with less incident energy, and hence result in a lower energy deposition. By excluding the Compton continuum from the analysis, these events can be removed, resulting in a clearer peak in the deposited energy distribution from the target shown in Figure 6.9(b). Cut boundaries on the photopeak from the tagger in Figure 6.9(a) are set one standard

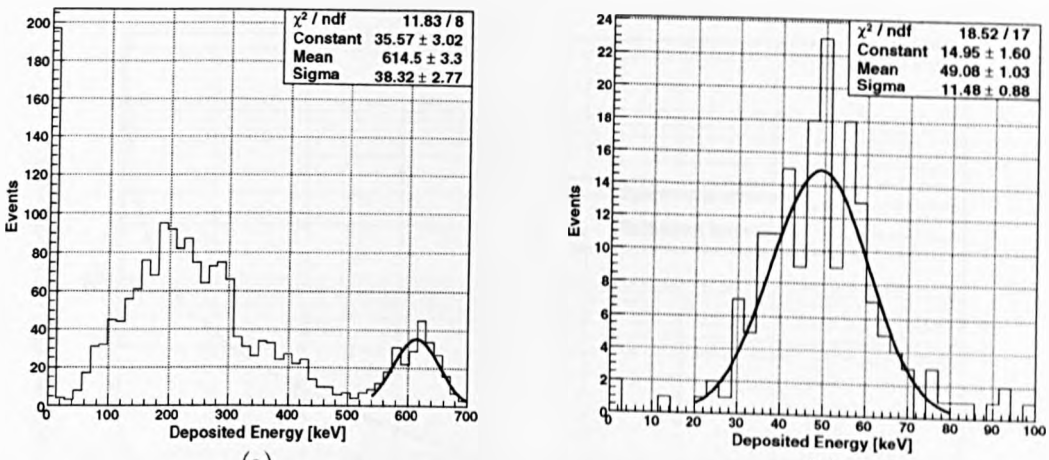

(a) (b)

Figure 6.9: Effect of (a) Cut on Deposited Energy in the Tagger on the (b) Electron Energy Distribution in the Target NaI(Tl) Crystal. Data taken at a scattering angle associated with 41.5 keVee electron energy deposition in the target. Cut boundaries are set one standard deviation from the mean in (a). Compared with Figure 6.8(b), the peak becomes clearer in (b), allowing a Gaussian fit to be performed.

deviation from the mean.

The electron response R_e relative to calibration with a 662 keV gamma source is expressed as:

$$R_e = \frac{E_{vis}(R_\gamma)}{E_e(\theta)} \tag{6.2}$$

where E_{vis} is the measured electron energy, dependent on the response to the calibration source R_γ, and E_e is the actual energy transferred to the electron given by Eq (3.11), which is dependent on the scattering angle θ. The error associated with E_{vis} is statistical, and given by the Gaussian fits performed to the electron energy distribution in the target after all cuts, as shown in Figure 6.9(b). Systematic errors dominate E_e in the form of the inherent error on θ from the finite resolution of the scale drawing in Figure 6.7. The error in the electron energy ΔE_e is given by:

$$\Delta E_e = \frac{\partial E_e}{\partial \theta}\Delta\theta = \frac{\frac{E_\gamma^2}{m_e c^2}\sin\theta}{\left[1 + \frac{E_\gamma}{m_e c^2}(1-\cos\theta)\right]^2}\Delta\theta \tag{6.3}$$

where $m_e c^2$ is rest mass energy of the electron and $\Delta\theta$ is the error in the scattering angle

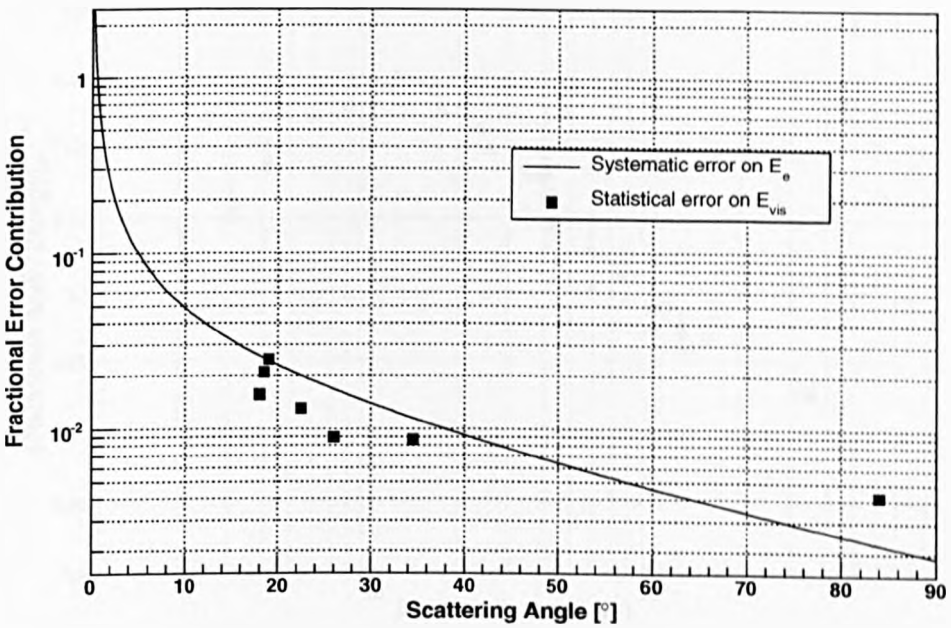

Figure 6.10: Fractional Contributions from Systematic Errors on the Electron Energy E_e and Statistical Errors on the Visible Energy E_{vis} as a Function of the Scattering Angle. A marked increase in the contribution from the systematic error is seen at low scattering angles θ. As seen in Eq. (3.11), E_e is proportional to θ. Therefore, if the contribution from statistical errors remains in the same region over all scattering angles, the systematic error will dominate at lower energies. As such, a more accurate procedure of determining the angle is required to probe these electron energies.

in units of radians. From Figure 6.7, it can be said with confidence that the error in the scattering angle is 0.25° (0.0044 radians). The fractional contribution in terms of scattering angle given by this systematic error is shown in Figure 6.10.

A marked increase in the fractional contribution from systematic errors on the the electron energy can be seen at low scattering angles in Figure 6.10. This can be compared with the statistical error in the same figure, which remains roughly constant. From Eq (3.11), the scattering angle is proportional to the energy, and thus it can be inferred that at lower electron energies, the systematic error will dominate. This can only be combated by using a more accurate method with which to determine the scattering angle. To improve the statistical error, the time frame for data collection should be extended.

Results from this experiment, which are given in Figure 6.11, are consistent with those

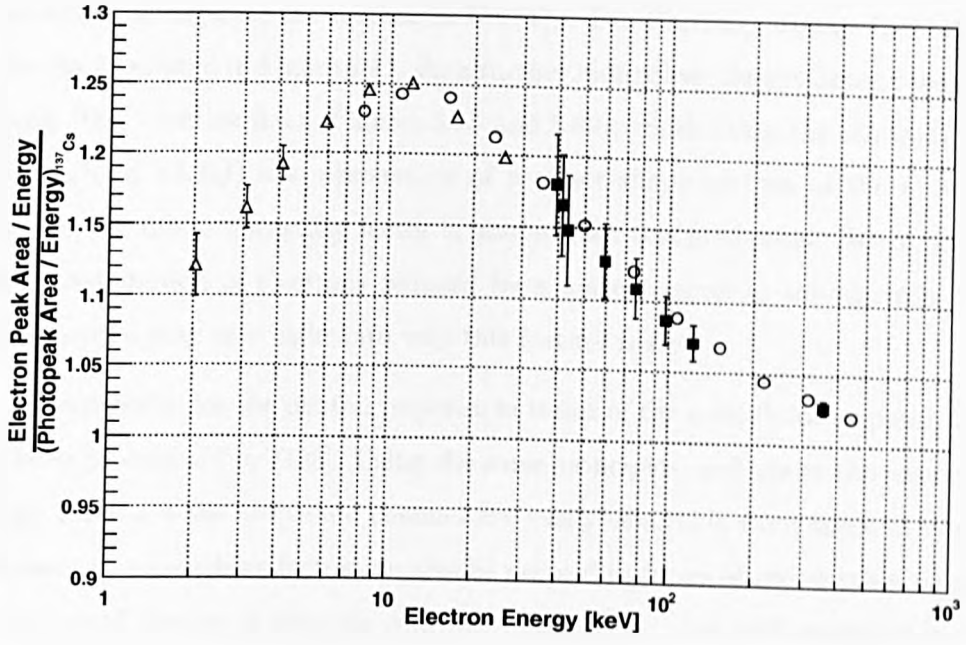

Figure 6.11: Measured Electron Response as a Function of Electron Energy. Experimental results from this work (closed black squares) and Rooney & Valentine [176] (open circles for points taken with ^{137}Cs and triangles for those taken with ^{99m}Tc) are shown. All values are normalised to each other at 662 keV.

from [176]. However, the magnitude of errors on each point do not compare favourably for the reasons outlined above. Nevertheless, the general trend of decreasing response with increasing electron energy after 20 keV is seen. Taking measurements at lower energies would require a more accurate determination of the scattering angle. At energies below 10 keV, this becomes difficult with a ^{137}Cs source. From Eq. (3.11), the resolution on the electron response energy can be improved in this region with the use of a gamma-ray source of lower energy. This is the reason why Ref. [176] use the 141 keV gamma line from technetium-99m (^{99m}Tc) in their measurements.

6.3 Implications for Quenching Factor Measurements

Lindhard theory [139, 140] (outlined in Section 3.6.3) assumes that the electronic energy loss, being the one that induces scintillation light, of a nuclear recoil can be separated from the non-radiative transfers of the atomic channel. Although this is an oversimplification [143], a more fundamental reason as to why the shape of the Lindhard curve

in Figure 3.15 does not match that of the measured quenching factor in Figure 5.39 may come from the response of electrons in NaI(Tl). The electron response in NaI(Tl) is non-linear, as illustrated in Figure 6.11. As a further indication, the predicted upper limit from Hitachi [141] (Section 3.6.4, Figures 3.15 and 5.39), which takes the electronic quenching factor q_e (Eq. (3.31)) into account, is of a closer shape to that of the measured data. However, the dip in quenching factor is absent from this prediction. Hence, matching the energy distribution of electrons induced by a nuclear recoil to the electron response at these energies may shed light into why this feature is seen.

An expression for the photon response in terms of the scintillator response to electrons has been determined by [125]. Using the same principles, and under the assumption that energy losses via the electronic channel are easily separable from those of non-radiative processes, the quenching factor can also be derived in terms of the electron response. The nuclear recoil energy in electron equivalent scale E_{Ree} that was measured in Chapter 5 can be expressed as:

$$E_{Ree}(E_R) = \int_0^\infty \Psi(E_R, E_e)\, E_{vis}(E_e, R_\gamma)\, dE_e \tag{6.4}$$

where $\Psi(E_R, E_e)$ is the energy distribution of electrons induced by the recoiling nucleus of energy E_R and other secondary collisions. The measured energy E_{vis} of electrons of energy E_e in terms of the photon response to the calibration source R_γ is given in Eq. 6.2. Substituting E_{Ree} from Eq. (3.21) and E_{vis} from Eq. (6.2) into Eq. (6.4) yields:

$$Q(E_R) = \frac{1}{E_R} \int_0^\infty \Psi(E_R, E_e)\, R_e(E_e, R_\gamma)\, E_e\, dE_e \tag{6.5}$$

where Q is the quenching factor of nuclear recoils of energy E_R, and R_e is the electron response in terms of E_e.

The measured electron response R_e can be taken from Figure 6.11, and Monte Carlo simulations can be used to determine $\Psi(E_R, E_e)$. If the electron energy distribution from each simulated event is presented in the form of a histogram of n bins, a discrete set of electron energies can be obtained that are dependent on the bin size. Therefore, $\Psi(E_R, E_e)$ can be discretised to:

$$\Psi(E_R, E_e) = \sum_{i=0}^{n} \Psi(E_R, E_i)\, \delta(E_e - E_i) \tag{6.6}$$

where $\Psi(E_R, E_i)$ is the probability per event that a nuclear recoil of energy E_R will produce an electron of energy E_i. The Dirac delta function $\delta(E_e - E_i)$ returns a zero value if E_e does not lie within the boundaries of bin i. Substituting Eq. (6.6) into Eq. (6.5) and solving the integral yields:

$$Q(E_R) = \frac{k}{E_R} \sum_{i=0}^{n} \Psi(E_R, E_e)\, R_e(E_i, R_\gamma)\, E_i \tag{6.7}$$

where k is a normalisation factor.

Unfortunately, although the SRIM/TRIM [142] Monte Carlo program does provide information on the total electronic energy loss as a nucleus moves through a target material, the energies supplied to individual electrons are not recorded. Therefore, it is not currently possible to obtain an electronic energy distribution to substitute into Eq. (6.7).

A hint of a dip in the response of liquid xenon to photons at the xenon K-shell (34.56 keV) is witnessed by [182]. Due to the physical constraints imposed when operating cryogenic liquid detectors, it becomes difficult for gamma-rays of energy less than 30 keV to successfully traverse through the vacuum chambers surrounding the liquid. Therefore, measurements below this energy are not possible. However, such a result indicates that the dip in the quenching factor of liquid xenon at low nuclear recoil energies [173] could be due to the same reasons as those for NaI(Tl).

6.4 Summary

The results from exposure to various X-ray and gamma sources indicate that there is a dip in the photon response of the 2-inch NaI(Tl) crystal at the K-shell binding energy of iodine. The position of this dip is in agreement with results from other groups and can be clearly seen when the alternative, rather than standard, integral technique is used.

As photon response measurements are inherently biased on the geometry of the scintillator, it is better to investigate the electron response, which is independent of detector shape and size. These were performed on the NaI(Tl) crystal using the Compton Coincidence Technique, and the results at high energy agree with those published. Measurements at lower energies were not feasible due to the increasing systematic errors with decreasing scattering angle.

The non-linearity of electron response in NaI(Tl) may provide an explanation for the dip in the quenching factor of sodium recoils. This is under the simple assumption that electronic and atomic energy losses experienced by a recoiling nucleus moving through a target may be separated. As scintillation light is a result of energy loss through the electronic channel, the energy transferred to individual electrons can be used to predict the quenching factor. However, at present there is no way to obtain an electron energy distribution in such processes from the available Monte Carlo simulations.

Chapter 7

Conclusion

The aim of every direct dark matter search detector is discovery. Failing this, experiments produce limits in interaction cross-section against particle mass phase space. The lower the limit, the better the sensitivity of the detector. Experimental limits are determined from the expected differential event rate for WIMP-nucleon interactions, which is dependent on many factors including background rate and quenching factor.

To minimise the exposure of the ZEPLIN-II direct search detector to cosmic rays, it has been placed in a mine with rock overburden equivalent to 2800 mwe. Backgrounds from external radiation at this depth have been reduced through the commissioning of passive gamma and neutron shielding, and an active liquid scintillator veto, as discussed in this thesis.

The impregnation of gadolinium in paraffin wax, and the casting of this into blocks, is outlined in this thesis. This is the first time such a procedure has been conducted to construct shielding for a dark matter detector. Due to its high thermal neutron capture cross-section, neutrons incident on gadolinium nuclei within the shielding will be absorbed, resulting in multiple gamma-ray emission. The detection of gamma-rays in the target can be distinguished from nuclear recoils through simultaneous measurements of ionisation and scintillation light as described in this thesis. Therefore, the neutron background, which can mimic a signal from a dark matter particle, is significantly reduced.

The passive shielding works in tandem with the active veto, the commissioning and calibration of which is discussed in detail in this thesis. Background rejection efficiencies of 31% and 54% have been determined for gamma-rays and neutrons respectively, in good agreement with an analysis on a different set of data and results from simulations. It has

also been shown that gadolinium nitrate hexahydrate on the inner veto wall results in the capture of neutrons in the americium beryllium data files. The delayed emission of gamma-rays is detected by the veto. The rejection efficiency for gamma-rays is roughly 60% of that for neutrons, as organic liquid scintillators are primarily neutron detectors. However, the number of gamma-rays emitted from this reaction is large enough to imply that gadolinium impregnation has resulted in an increased neutron background rejection efficiency. The probability of the veto accepting a dark matter event in the target has been calculated as 99.15%.

The quenching factor of sodium recoils in sodium iodide (NaI(Tl)) has been measured down to 10 keVnr nuclear recoil energy. The quenching factor, ratio of scintillation light from a nuclear recoil to that of an electron recoil, for 10 keVnr sodium recoils is 25.2±6.4%. At the time of writing, this is the lowest energy at which the quenching factor has been probed in NaI(Tl). In the energy regime of interest for dark matter searches, in other words recoil energies below 50 keVnr, an average value of 22.1% has been derived. The results compare favourably with those from other groups.

However, a dip in the quenching factor is witnessed at nuclear recoil energies between 20 and 100 keVnr, which is in contrast to results from other experiments. The measurement performed here is the most comprehensive study of the quenching factor of sodium recoils in NaI(Tl) to date in the low energy regime. It is therefore possible that such a feature could have been hidden from the other experiments, as there are fewer data points available to witness this pattern at these energies.

The reason for such a dip must lie in the mechanism for production of scintillation light from a recoiling nucleus. In the simplest case, Lindhard theory assumes that a recoiling nucleus can deposit energy through the electronic and atomic channels as it moves through a target medium. Atomic channels lead to non-radiative energy losses, while energy transferred to electrons can lead to photoemission through their subsequent de-excitation. For a sodium nucleus traversing a sodium target, Lindhard theory dictates that the quenching factor increases rapidly with recoil energy at first, before plateauing. Results from the Monte Carlo programs for ion transport in matter, SRIM and TRIM, which are also presented in this thesis, show that the quenching factor as a function of nuclear recoil energy for sodium recoils in NaI(Tl) follows the shape of that from Lindhard theory. However, it plateaus at a lower value, which is likely to be the result of collisions

with iodine nuclei that are predicted to have a lower quenching factor.

However, neither of these theoretical curves matches the shape of the experimental results. This is because neither Lindhard theory or SRIM/TRIM consider the effect of electron quenching. Using the energy loss data from SRIM/TRIM for electrons, the quenching of electron recoils can be obtained, and the corrected curve bears a better resemblance to that from the measurements in this thesis.

Yet the appearance of a dip remains unexplained. To understand why such a feature is seen, the non-linear response of NaI(Tl) to gamma-rays should be considered. The photon response has been shown to dip at the iodine K-shell binding energy not only in this thesis, but by other groups. This is a direct consequence of the non-linear electron response. Gamma-rays that deposit their entire energy E_γ in a single interaction, through photoelectric absorption with the K-shell, result in the emission of a photoelectron. This photoelectron has an energy of $E_\gamma - 33.17$ keV, where 33.17 keV is the electron binding energy of the iodine K-shell. Gamma-rays of energy just above 33.17 keV will result in the emission of very low energy photoelectrons. As the electron response is relatively small at such low energies, there is a coincident dip in the scintillation light from these gamma-rays. An attempt to measure the electron response as a function of energy has been made in this thesis, and although it is in good agreement with the only similar measurement to date, growing systematic errors prevented any further measurements. Therefore, the characteristic fall in response between 10 and 20 keV electron energy has not been reproduced.

The same principle can be applied to the energy transferred to electrons when a recoiling nucleus traverses a target medium. In order to see how important a factor this is, a Monte Carlo simulation is required to obtain energy distributions of individual electrons at varying recoil energies. With a high statistics sample, probabilities for the energies transferred to individual electrons can be determined, and the quenching factor can be predicted through photon response measurements. Unfortunately, information pertaining to the energy given to individual electrons is lost when using SRIM/TRIM as a simulator.

Implications for this stretch beyond that for sodium iodide. A dip is also witnessed in the quenching factor for xenon by a different group. The photon response of xenon is also seen to dip at the electron binding energy of the xenon K-shell. There is currently no measurement of the electron response in liquid xenon.

References

[1] A. Liddle, *"An Introduction to Modern Cosmology"*, John Wiley & Sons (1998)
S. Dodelson, *"Modern Cosmology: Anisotropies and Inhomogeneities in the Universe"*, Academic Press, 2nd edition (2003)

[2] M. L. Humason, Proc. Nat. Acad. Sci. **15** (1929) 167
E. Hubble, Proc. Nat. Acad. Sci. **15** (1929) 168

[3] V. M. Slipher, Proc. Amer. Phil. Soc. **56** (1917) 403

[4] D. N. Spergel *et al.*, WMAP Collaboration, Astrophys. J. Suppl. **170** (2007) 377

[5] J. C. Mather *et al.*, Astrophys. J. **420** (1994) 439

[6] A. H. Guth, Phys. Rev. D **23** (1981) 347
A. Albrecht & P. J. Steinhardt, Phys. Rev. Lett. **48** (1982) 1220
A. D. Linde, Phys. Lett. B **108** (1982) 389

[7] V. C. Rubin & W. K. Ford, Jr., Astrophys. J. **159** (1970) 379
V. C. Rubin, N. Thonnard & W. K. Ford, Jr., Astrophys. J. **238** (1980) 471

[8] K. G. Begeman, A. H. Broeils & R. H. Sanders, Mon. Not. Roy. Astron. Soc. **249** (1991) 523

[9] Y. Sofue & V. Rubin, Ann. Rev. Astron. Astrophys. **39** (2001) 137

[10] S. R. Kulkarni, L. Blitz & C. Heiles, Astrophys. J. **253** (1982) L63

[11] J. R. Brownstein & J. W. Moffat, Astrophys. J. **636** (2006) 721

[12] R. A. Cabanac *et al.*, Astron. Astrophys. **436** (2005) L21

[13] D. Clowe *et al.*, Astrophys. J. **648** (2006) L109

[14] J. R. Brownstein & J. W. Moffat, Mon. Not. Roy. Astron. Soc. **382** (2007) 29

[15] N. Palanque-Delabrouille, New Astron. Rev. **45** (2001) 395

[16] K. Jedamzik, Phys. Rept. **307** (1998) 155

[17] D. N. Schramm & M. S. Turner, Rev. Mod. Phys. **70** (1998) 303

[18] S. Burles & D. Tytler, Astrophys. J. **499** (1998) 699
S. Burles & D. Tytler, Astrophys. J. **507** (1998) 732

[19] T. M. Bania, R. T. Rood & D. S. Balser, Nature **415** (2002) 54

[20] P. Bonifacio, Astron. Astrophys. **390** (2002) 91

[21] D. Tytler *et al.*, Phys. Scripta **T85** (2000) 12

[22] S. Burles, K. M. Nollett & M. S. Turner, Astrophys. J. Lett. **552** (2001) L1

[23] A. C. S. Readhead *et al.*, Astrophys. J. **609** (2004) 498

[24] C. L. Kuo *et al.*, ACBAR Collaboration, Astrophys. J. **600** (2004) 32

[25] A. Pich, IFIC/07-27, FTUV/07-0529; available from <arXiv:0705.4264>, May 2005

[26] B. R. Martin & G. Shaw, *"Particle Physics"*, John Wiley & Sons, 2nd edition (1997)

[27] W.-M. Yao *et al.*, J. Phys. G **33** (2006) 1

[28] V. A. Bednyakov, N. D. Giokaris & A. V. Bednyakov, JINR ATLAS Physics Workshop; available from <arXiv:hep-ph/0703280>, March 2007

[29] P. W. Higgs, Phys. Lett. **12** (1964) 132
P. W. Higgs, Phys. Rev. **145** (1966) 1156

[30] P. Verkerk *et al.*, Phys. Rev. Lett. **68** (1992) 1116

[31] G. Bertone, D. Hooper & J. Silk, Phys. Rept. **405** (2005) 279

[32] R. Haag, J. T. Lopuszànski & M. Sohinus, Nucl. Phys. B **88** (1975) 257

[33] G. R. Farrar & P. Fayat, Phys. Lett. B **76**(1978) 575

[34] H. E. Haber, Nucl. Phys. Proc. Suppl. **62** (1998) 469

[35] D. J. Miller, R. Nevzorov & P. M. Zerwas, Nucl. Phys. B **681** (2004) 3

[36] L. Hall, J. Lykken & S. Weinberg, Phys. Rev. D **27** (1983) 2359

[37] M. Dine & A. E. Nelson, Phys. Rev. D **48** (1993) 1277

[38] S. Y. Choi *et al.*, Eur. Phys. J. C **22** (2001) 563

[39] A. Bottino *et al.*, Nucl. Phys. Proc. Suppl. **31** (1993) 359

[40] J. L. Feng, A. Rajaraman & F. Takayama, Phys. Rev. Lett. **91** (2003) 011302
J. L. Feng, A. Rajaraman & F. Takayama, Phys. Rev. D **68** (2003) 063504

[41] Y. Fukuda *et al.*, Phys. Rev. Lett. **86** (2001) 5651
Q. R. Ahmad *et al.*, Phys. Rev. Lett. **87** (2001) 071301
Q. R. Ahmad *et al.*, Phys. Rev. Lett. **89** (2002) 011301

[42] R. Davis, Jr., D. S. Harmer & K. C. Hoffman, Phys. Rev. Lett. **20** (1968) 1205

[43] S. D. M. White, C. S. Frenk & M. Davis, Astrophys. J. **274** (1983) L1

[44] J. Lesgourgues & S. Pastor, Phys. Rept. **429** (2006) 307

[45] G. G. Raffelt, J. Phys. A **40** (2007) 6607

[46] R. D. Peccei & H. R. Quinn, Phys. Rev. Lett. **38** (1977) 1440

[47] E. J. Chun, H. B. Kim & D. H. Lyth, Phys. Rev. D **62** (2000) 125001

[48] L. Roszkowski, Pramana **62** (2004) 389

[49] E. Kolb & R. Slansky, Phys. Lett. B **135** (1984) 378
G. Servant & T. M. P. Tait, Nucl. Phys. B **650** (2003) 391

[50] S. Chang, C. Corianò & A. E. Faraggi, Nucl. Phys. B **477** (1996) 65
D. J. H. Chung, E. W. Kolb & A. Riotto, Phys. Rev. D **59** (1999) 023501

[51] P. F. Smith & J. D. Lewin, Phys. Rept. **187** (1990) 203

[52] M. W. Goodman & E. Witten, Phys. Rev. D **31** (1985) 3059

[53] F. Aharonian *et al.*, HESS Collaboration, Phys. Rev. Lett. **97** (2006) 221102

[54] A. Achterberg *et al.*, AMANDA Collaboration, Astropart. Phys. **26** (2006) 129

[55] J. Carr, G. Lamanna & J. Lavalle, Rep. Prog. Phys. **69** (2006) 2475

[56] H. Baer, T. Krupovnickas & X. Tata, JHEP **0307** (2003) 020

[57] M. Battaglia, I. Hinchliffe & D. Tovey, J. Phys. G **30** (2004) R217
M. M. Nojiri, G. Polesello & D. R. Tovey, JHEP **0603** (2006) 063

[58] A. Djouadi, Acta. Phys. Polon. B **37** (2006) 925
M. Battaglia & M. E. Peskin, Proc. 2005 ILC Workshop (2005) 0709; available from <arXiv:hep-ph/0509135>, September 2005

[59] N. J. C. Spooner, to be published in JPSJ; available from <arXiv:0705.3345>, May 2007

[60] J. D. Lewin & P. F. Smith, Astropart. Phys. **6** (1996) 87

[61] D. P. Snowden-Ifft, C. J. Martoff & J. M. Burwell, Phys. Rev. D **61** (2000) 101301

[62] A. Kurylov & M. Kamionkowski, Phys. Rev. D **69** (2004) 063503

[63] G. Jungman, M. Kamionkowski & K. Griest, Phys. Rept. **267** (1996) 195

[64] J. Engel, Phys. Lett. B **264** (1991) 114

[65] G. Fricke *et al.*, Atomic Data and Nuclear Data Tables **60** (1995) 177

[66] J. J. Quenby *et al.*, Phys. Lett. B **351** (1995) 70

[67] J. Amaré *et al.*, Proc. 6th Int. Workshop on the Identification of Dark Matter (2006) 237

[68] R. Bernabei *et al.*, Phys. Lett. B **424** (1998) 195

[69] K. Fushimi *et al.*, Astropart. Phys. **12** (1999) 185

[70] B. Ahmed *et al.*, Astropart. Phys. **19** (2003) 691

[71] G. J. Alner *et al.*, UKDMC, Phys. Lett. B **616** (2005) 17

[72] R. Bernabei *et al.*, J. Phys.: Conf. Ser. **39** (2006) 82

[73] H. S. Lee *et al.*, KIMS Collaboration, Phys. Lett. B **633** (2006) 201

[74] S. Cebrían *et al.*, Astropart. Phys. **21** (2004) 23

[75] J. Amaré *et al.*, Proc. 5th Int. Workshop on the Identification of Dark Matter (2004) 384

[76] G. Angloher *et al.*, Nucl. Instrum. Methods Phys. Res. A **520** (2004) 108

[77] H. Kraus *et al.*, Proc. 6th Int. Workshop on the Identification of Dark Matter (2006) 668

[78] R. Bernabei *et al.*, New J. Phys. **2** (2000) 15
R. Bernabei *et al.*, Nucl. Instrum. Methods Phys. Res. A **482** (2002) 728

[79] G. J. Alner *et al.*, UKDMC, Astropart. Phys. **23** (2005) 444

[80] A. Takeda *et al.*, Proc. 6th Int. Workshop on the Identification of Dark Matter (2006) 243

[81] N. J. T. Smith *et al.*, in preparation

[82] D. Y. Akimov *et al.*, Astropart. Phys. **27** (2007) 46

[83] E. Aprile *et al.*, XENON Collaboration, to be published in Phys. Rev. Lett.; available from <arXiv:0706.0039>, May 2007

[84] R. Brunetti *et al.*, New Astron. Rev. **49** (2005) 265

[85] M. G. Boulay & A. Hime; available from <arXiv:astro-ph/0411358>, November 2004

[86] M. Laffranchi & A. Rubbia, to be published in Proc. 3rd Symposium on Large TPCs for Low Energy Rare Event Detection, available from <arXiv:hep-ph/0702080>

[87] J. A. Nikkel, W. H. Lippincott & D. N. McKinsey, Int. J. Mod. Phys. A **20** (2005) 3113

[88] D. S. Akerib *et al.*, CDMS Collaboration, Phys. Rev. Lett. **93** (2004) 211301

[89] P. C. F. Di Stefano *et al.*, New. Astron. Rev. **49** (2004) 251

[90] G. J. Alner *et al.*, Nucl. Instrum. Methods Phys. Res. A **555** (2005) 173

[91] T. Tanimori *et al.*, Phys. Lett. B **578** (2004) 241

[92] T. Morlat *et al.*, to be published in Phys. Lett. B; available from <arXiv:0704.2037>, April 2007

[93] M. Barnabé-Heider *et al.*, PICASSO Collaboration, Nucl. Instrum. Methods Phys. Res. A **555** (2005) 184

[94] J. Collar *et al.*, COUPP Collaboration, FERMILAB-PROPSAL-0961 (2007)

[95] K. Borer *et al.*, Nucl. Instrum. Methods Phys. Res. A **520** (2004) 112

[96] D. R. Tovey *et al.*, Phys. Lett. B **488** (2000) 17

[97] H. S. Lee *et al.*, KIMS Collaboration, Phys. Rev. Lett. **99** (2007) 091301

[98] G. Angloher *et al.*, Astropart. Phys. **23** (2005) 325

[99] V. Sanglard, *et al.*, EDELWEISS Collaboration, Phys. Rev. D **71** (2005) 122002

[100] P. Benetti *et al.*, WARP Collaboration, Astropart. Phys. **28** (2007) 495

[101] G. J. Alner *et al.*, Astropart. Phys. **28** (2007) 287

[102] D. S. Akerib *et al.*, CDMS Collaboration, Phys. Rev. Lett. **96** (2006) 011302

[103] R. Bernabei *et al.*, DAMA Collaboration, Phys. Lett. B **480** (2000) 23

[104] R. Gaitskell, V. Mandic & J. Filippini, *"Dark Matter Limit Plot Generator"*; available from http://dmtools.berkeley.edu/limitplots/

[105] A. Benoit *et al.*, EDELWEISS Collaboration, Phys. Lett. B **616** (2005) 25

[106] G. J. Alner, ZEPLIN-II Collaboration, Phys. Lett. B **653** (2007) 161

[107] D. S. Akerib, CDMS Collaboration, Phys. Rev. D **73** (2006) 011102

[108] M. Barnabé-Heider *et al.*, Phys. Lett. B **624** (2005) 186

[109] T. A. Girard *et al.*, Phys. Lett. B **621** (2005) 233

[110] P. Harihar *et al.*, Nucl. Instrum. Methods Phys. Res. A **336** 176

[111] G. J. Davies *et al.*, Phys. Lett. B **322** (1994) 159

[112] R. Hofstadter, Phys. Rev. **74** (1948) 100

[113] R. G. Kaufman, W. B. Hadley & H. N. Hersh, IEEE Trans. Nucl. Sci. **17** (1970) 82

[114] S. Koički, A. Koički & V. Ajdačić, Nucl. Instrum. Methods **108** (1973) 297

[115] S. Kubota *et al.*, Phys. Rev. B **20** (1979) 3486

[116] E. S. Peterson, B. J. Schwartz & C. B. Harris, J. Chem. Phys. **99** (1993) 1693

[117] T. Doke *et al.*, Jpn. J. Appl. Phys. **41** (2002) 1538

[118] P. Moutard *et al.*, J. Chem. Phys. **88** (1988) 7485

[119] A. Hitachi *et al.*, Phys. Rev. B **27** (1983) 5279

[120] S. Kubota *et al.*, Phys. Rev. B **17** (1978) 2762

[121] E. Aprile *et al.*, Phys. Rev. Lett. **97** (2006) 081302

[122] K. Ni *et al.*, Nucl. Instrum. Methods. Phys. Res. A **551** (2005) 356

[123] M. Moszyński *et al.*, IEEE Trans. Nucl. Sci. **46** (1999) 880

[124] M. J. Berger *et al.*, *"XCOM: Photon Cross Sections Database"*; available from http://physics.nist.gov/PhysRefData/Xcom/Text/XCOM.html

[125] B. D. Rooney & J. D. Valentine, IEEE Trans. Nucl. Sci. **44** (1997) 509

[126] G. Zavattini *et al.*, Nucl. Instrum. Methods Phys. Res. A **401** (1997) 206

[127] J. Chang, *"ENDFPLOT-2.0: Online Graph Plot for Neutron Cross-Section"*; available from http://atom/kaeri.re.kr/endfplot.shtml

[128] H. H. Barschall & M. H. Kanner, Phys. Rev. **58** (1940) 590
H. O. Cohn & J. L. Fowler, Phys. Rev. **114** (1959) 194
D. Lister & A. Sayres, Phys. Rev. **143** (1966) 745

[129] P. K. Lightfoot *et al.*, Nucl. Instrum. Methods Phys. Res. A **522** (2004) 439
Y. Ding *et al.*, Nucl. Instrum. Methods Phys. Res. A **584** (2008) 238

[130] S. Masaoka *et al.*, Nucl. Instrum. Methods Phys. Res. A **513** (2003) 538

[131] D. A. Abdushukurov *et al.*, Nucl. Instrum. Methods Phys. Res. B **84** (1994) 400

[132] J. B. Birks, *"The Theory and Practice of Scintillation Counting"*, Permagon Press (1964)

[133] M. Moszyński *et al.*, Nucl. Instrum. Methods Phys. Res. A **568** (2006) 739

[134] G. M. Seidel, R. E. Lanou & W. Yao, Nucl. Instrum. Methods Phys. Res. A **489** (2002) 189

[135] N. Ishida *et al.*, Nucl. Instrum. Methods Phys. Res. A **384** (1997) 380
V. N. Solovov *et al.*, Nucl. Instrum. Methods Phys. Res. A **516** (2004) 462

[136] É. L. Vinograd *et al.*, Atomic Energy **52** (1981) 277

[137] R. B. Murray & A. Meyer, Phys. Rev. **122** (1961) 815
J. W. Blue & D. C. Liu, IRE Trans. Nucl. Sci. **9** (1962) 48

[138] R. Voltz *et al.*, J. Chem. Phys. **45** (1966) 3306

[139] J. Lindhard, M. Scharff & H. E. Schiøtt, Mat. Fys. Medd. Dan. Vid. Selsk. **33** (1963) 14

[140] J. Lindhard *et al.*, Mat. Fys. Medd. Dan. Vid. Selsk. **33** (1963) 10

[141] A. Hitachi, private communication

[142] J. F. Ziegler, J. P. Biersack & U. Littmark, "SRIM/TRIM version 2006.02"; available from http://www.srim.org

[143] I. S. Tilinin, Phys. Rev. A **51** (1995) 3058

[144] A. Hitachi, Astropart. Phys. **24** (2005) 247

[145] T. Doke, E. Shibamura & S. Kubota, J. Phys. Soc. Jpn. **68** (1999) 2433

[146] D. Aitken *et al.*, IEEE Trans. Nucl. Sci. **14** (1967) 468

[147] L. R. Wayne *et al.*, Nucl. Instrum. Methods Phys. Res. A **411** (1998) 351

[148] J. D. Valentine, B. D. Rooney & P. Dorenbos, IEEE Trans. Nucl. Sci. **45** (1998) 1750

[149] L. F. Ferreira *et al.*, Nucl. Instrum. Methods Phys. Res. A **516** (2004) 486

[150] A. Mangiarotti *et al.*, Nucl. Instrum. Methods Phys. Res. A **580** (2007) 114

[151] Electron Tubes Ltd., Bury Street, Ruislip, Middlesex HA4 7TA, United Kingdom; http://www.electrontubes.com

[152] G. J. Alner *et al.*, to be published in Nucl. Instrum. Methods Phys. Res. A; available from <arXiv:astro-ph/0703362>, March 2007

[153] Acqiris Europe, 18 Chemin des Auix, 1228 Plan-les-Ouates, Geneva, Switzerland; http://www.acqiris.com

[154] DuPont Performance Elastomers S.A., 2 Chemin du Pavillon, Le Grand-Saconnex, Geneva, Switzerland; http://www.dupontelastomers.com

[155] Y. Kishimoto, AIP Conf. Proc. **785** (2005) 193

[156] E. J. Daw, Proc. 6th Int. Workshop on the Identification of Dark Matter (2006) 576

[157] M. J. Carson *et al.*, Nucl. Instrum. Methods Phys. Res. A **548** (2005) 418
C. Bungau *et al.*, Astropart. Phys. **23** (2005) 97
P. F. Smith *et al.*, Astropart. Phys. **22** (2005) 409

[158] G. F. Knoll, "Radiation Detection and Measurement", New York, USA: John Wiley & Sons (2000)

[159] H. Chagani *et al.*, Proc. 6th Int. Workshop on the Identification of Dark Matter; available from <arXiv:physics/0611156>, November 2006

[160] H. Chagani *et al.*, 2008 JINST **3** P06003

[161] S. Agostinelli *et al.*, GEANT4 Collaboration, Nucl. Instrum. Methods Phys. Res. A **506** (2003) 250

[162] R. Brun & F. Rademakers, Nucl. Instrum. Methods Phys. Res. A **389** (1997) 81

[163] G. Gerbier *et al.*, Astropart. Phys. **11** (1999) 287

[164] F. Arneodo *et al.*, ICARUS Collaboration, Nucl. Instrum. Methods Phys. Res. A **418** (1998) 285

[165] G. Dietze, IEEE Trans. Nucl. Sci. **NS-26** (1979) 398

[166] S. Marrone *et al.*, n_TOF Collaboration, Nucl. Instrum. Methods Phys. Res. A **490** (2002) 299

[167] J. H. Lee & C. S. Lee, Nucl. Instrum. Methods Phys. Res. A **402** (1998) 147

[168] S. C. Wu *et al.*, Nucl. Instrum. Methods Phys. Res. A **523** (2004) 116

[169] E. Simon *et al.*, Nucl. Instrum. Methods Phys. Res. A **507** (2003) 643

[170] D. R. Tovey *et al.*, Phys. Lett. B **433** (1998) 150

[171] N. J. C. Spooner *et al.*, Phys. Lett. B **321** (1994) 156

[172] C. Chasman, K. W. Jones & R. A. Ristinen, Phys. Rev. Lett. **15** (1965) 245

[173] V. Chepel *et al.*, Astropart. Phys. **26** (2006) 58

[174] A. R. Sattler, F. L. Vook & J. M. Palms, Phys. Rev. **143** (1966) 588

[175] E. Aprile *et al.*, Phys. Rev. D **72** (2005) 072006

[176] B. D. Rooney & J. D. Valentine, IEEE Trans. Nucl. Sci. **43** (1996) 1271

[177] J. D. Valentine & B. D. Rooney, Nucl. Instrum. Methods Phys. Res. A **353** (1994) 37

[178] D. Engelkemeir, Rev. Sci. Instrum. **27** (1956) 589

[179] A. J. L. Collinson & R. Hill, Proc. Phys. Soc. **81** (1963) 883

[180] F. T. Porter, Nucl. Instrum. Methods **39** (1966) 35

[181] F. T. Farmer & M. P. Collins, Phys. Med. Biol. **19** (1974) 808

[182] M. Yamashita *et al.*, Nucl. Instrum. Methods Phys. Res. **535** (2004) 692